New approach methodologies (NAMs) to understand and predict drug-induced effects on bile acid homeostasis and cholestasis

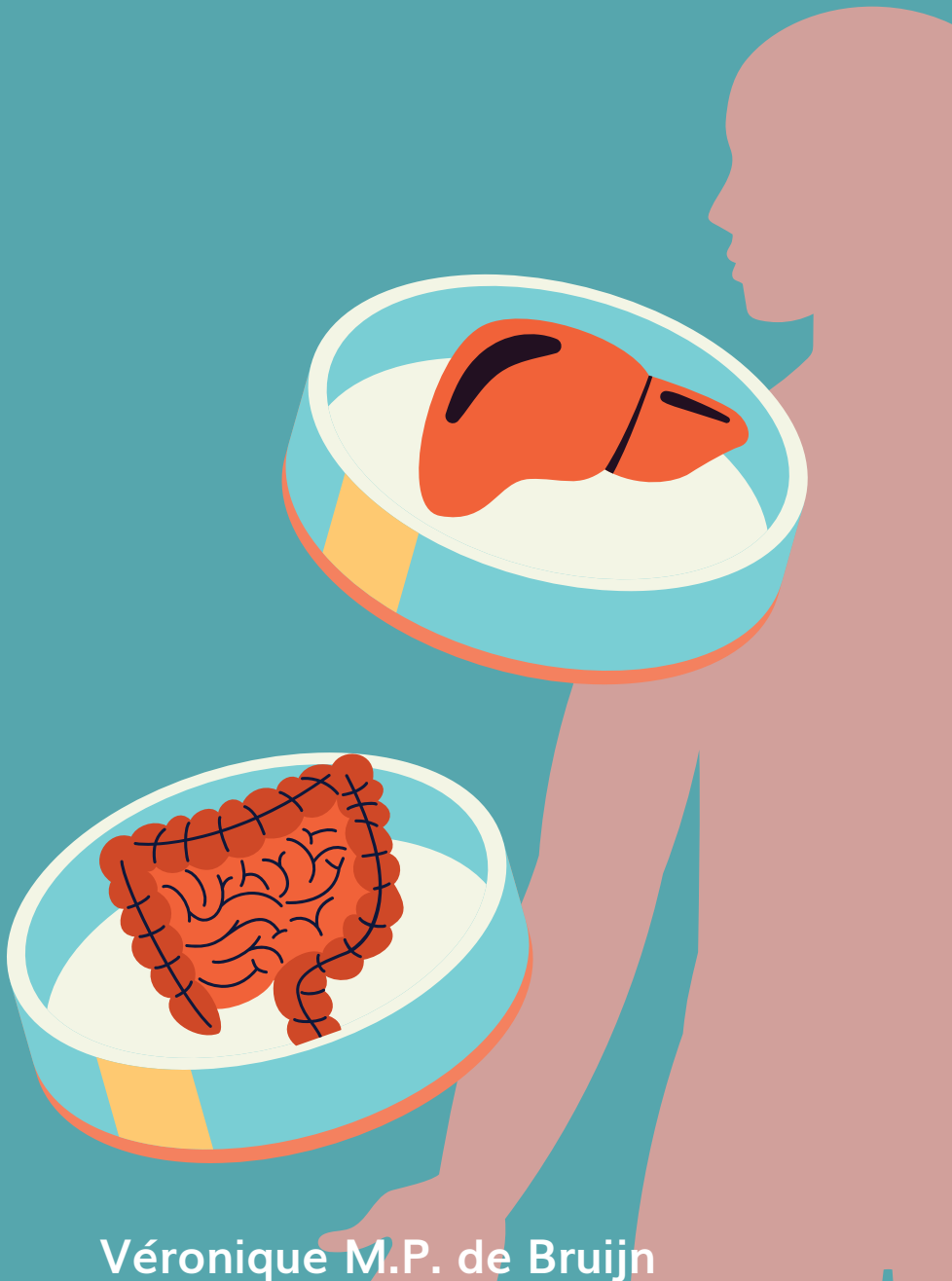

Véronique M.P. de Bruijn

Propositions

1. The cholestatic risk of drugs can only be evaluated taking kinetics into account. (this thesis)

2. The *in vitro* to *in vivo* scaling of carrier-mediated transport requires well-characterized *in vitro* models. (this thesis)

3. Using biodegradable plastic disposables reduces the environmental footprint of laboratory research.

4. Tuning nitrogen fertilization strategies to crop demand is the most cost-effective way to reduce nitrogen depositions in the agricultural sector.

5. Active membership in sport, cultural or charity associations improves coherence in society.

6. Self-doubt is both a strength and a weakness.

Propositions belonging to the thesis, entitled
New approach methodologies (NAMs) to understand and predict drug-induced effects on bile acid homeostasis and cholestasis
Véronique M.P. de Bruijn
Wageningen, 9 January 2024

New approach methodologies (NAMs) to understand and predict drug-induced effects on bile acid homeostasis and cholestasis

Véronique M.P. de Bruijn

Thesis committee

Promotors

Prof. Dr I.M.C.M. Rietjens
Professor of Toxicology
Wageningen University & Research

Dr H. Bouwmeester
Associate professor, Toxicology
Wageningen University & Research

Other members:

Dr M. Strikwold, Van Hall Larenstein University of Applied Sciences, Leeuwarden
Prof. Dr R.F. Witkamp, Wageningen University & Research
Prof. Dr P. Olinga, University of Groningen
Prof. Dr J. Keijer, Wageningen University & Research

This research was conducted under the auspices of VLAG Graduate School (Biobased, Biomolecular, Chemical, Food and Nutrition sciences)

New approach methodologies (NAMs) to understand and predict drug-induced effects on bile acid homeostasis and cholestasis

Véronique M.P. de Bruijn

Thesis

submitted in fulfilment of the requirements for the degree of doctor
at Wageningen University
by the authority of the Rector Magnificus,
Prof. Dr A.P.J. Mol,
in the presence of the
Thesis Committee appointed by the Academic Board
to be defended in public
on Tuesday 9 January 2024
at 4 p.m. in the Omnia Auditorium.

Véronique M.P. de Bruijn

New approach methodologies (NAMs) to understand and predict drug-induced effects on bile acid homeostasis and cholestasis, 237 pages.

PhD thesis, Wageningen University, Wageningen, the Netherlands (2024)

With references, with summary in English and Dutch

ISBN: 978-94-6447-971-3

DOI: https://doi.org/10.18174/641488

Table of contents

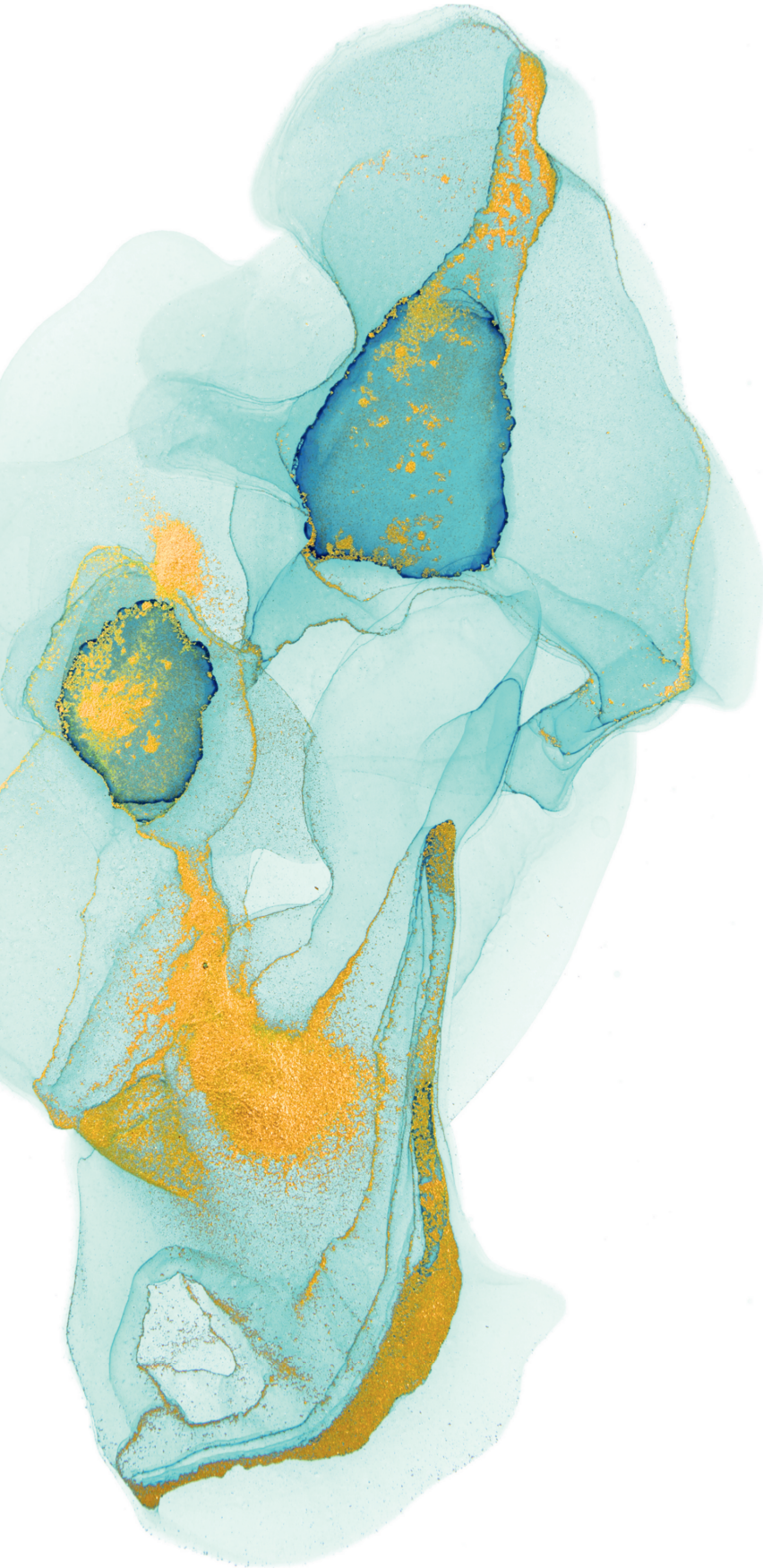

Chapter 1

General introduction

1.1 Bile acids as signaling molecules

Bile acids are the major functional components of bile, and have been known to serve as emulsifiers of dietary lipids and lipid-soluble vitamins for a long time (Hofmann, 1961). Bile acids are found throughout the whole body, but mainly in the liver, gall bladder and intestine (Jantti et al., 2014; Monteiro-Cardoso et al., 2021). Besides their role as emulsifiers in the intestinal lumen, bile acids are increasingly recognized as important hormone-like signaling molecules regulating lipid, glucose and energy metabolism and innate and adaptive immune functions in the whole body (Jia et al., 2023; Hylemon et al., 2009). Bile acids exert these signaling functions via binding to numerous nuclear receptors, such as the farnesoid X receptor (FXR, NR1H4), the G protein-coupled bile acid receptor (TGR5, GPBAR1), vitamin D receptor (VDR, NR1I1) and pregnane X receptor (PXR, NR1I2) (Guo et al., 2003; Makishima et al., 2002; Anstee et al., 2013). Two major pathways include those regulated via FXR and TGR5 (Fiorucci et al., 2009). FXR is highly expressed in the gastrointestinal tract (Chiang and Ferrell, 2022). FXR tightly controls bile acid homeostasis by regulation the expression of genes related to bile acid synthesis, secretion and absorption. FXR also acts as a metabolic sensor in glucose metabolism, lipid and energy metabolism (Chiang, 2017), and regulates cell proliferation and inflammation (Fiorucci et al., 2011). Furthermore, FXR-deficient mice were shown to have increased colon cell proliferation rates and subsequent tumorigenesis compared to wildtype mice, indicating that FXR has anti-tumorigenic properties (Maran et al., 2009). TGR5 is not only expressed throughout the intestinal epithelium, but also in monocytes and macrophages, liver sinusoidal endothelial cells and Kupffer cells, but not in hepatocytes (Chiang and Ferrell, 2022). TGR5 regulates amongst others energy homeostasis, intestinal integrity, insulin secretion, cell proliferation and inflammation (Ticho et al., 2019; Guo et al., 2016).

Bile acids are involved in the crosstalk between the host and the gut microbiome in the intestinal lumen. The gut microbiome is a dynamic ecosystem that plays a pivotal role in shaping various aspects of human physiology and heath (Visconti et al., 2019). Comprising more than 100 trillion microorganisms, the microbiome forms a symbiotic relationship with the host, influencing essential functions ranging from digestion to immune response modulation (Comess and Abad-Jorge, 2023). Several microbial species in the microbiome possess the ability to modify bile acid structures. These modifications result in different bile acid species with different kinetic and signaling properties. For example, the first bacterial modification step is deconjugation of bile acids. Deconjugation improves membrane-permeability and thereby intestinal reuptake of bile acids (Fuchs and Trauner, 2022). Furthermore, the affinity for the nuclear receptors depends on the type of bile acid formed, since some types of bile acids are more potent ligands for nuclear receptors than others (Zhang et al., 2023; Jia et al., 2018). Combined, the gut microbiome has a substantial effect on the fate and type of bile acids formed and thereby on the downstream targets of the nuclear receptors targeted by bile acids. In turn, bile acids prevent bacterial overgrowth in the intestine due to their antimicrobial capacities (Wigg et al., 2001). The multitude of physiological processes controlled by bile acid signaling along the gut-liver axis and beyond highlight the crucial role of bile acids and bile acid homeostasis for host health.

1.2 Enterohepatic circulation of bile acids

Bile acids undergo enterohepatic recycling via bile acid secretion from the liver, transport to the intestine, intestinal reabsorption and return to the liver (Jia et al., 2018). The enterohepatic circulation of bile acids and the transporters involved are schematically depicted in Figure 1. Primary bile acids, including cholic acid (CA) and chenodeoxycholic acid (CDCA), are *de novo* synthesized in the liver via cytochrome P (CYP) 450-mediated oxidation of cholesterol (Schwarz, 2004)(Figure 2). Bile acid synthesis occurs via two biosynthetic pathways, namely the "classical" and "alternative" pathway. The largest quantity of bile acids is produced through the classical pathway in which CYP7A1 is the rate-limiting enzyme (Duane and Javitt, 1999; Chiang and Ferrell, 2020). The primary bile acids that are formed depend on the species. CA and CDCA are the major primary bile acids found in humans, while rodents additionally synthesize α-muricholic acid (α-MCA) and β-muricholic acid (β-MCA) (Garcia-Canaveras et al., 2012). Subsequently, CA and CDCA are conjugated with glycine or taurine, leading to the formation of glycocholic acid (GCA), taurocholic acid (TCA), glycochenodeoxycholic acid (GCDCA) and taurochenodeoxycholic acid (TCDCA). Importantly, conjugation impairs the ability of bile acids to cross the membranes passively, and therefore carriers are needed to facilitate bile acid transport over the cellular membranes in the liver and intestine (Fuchs and Trauner, 2022). The conjugated bile acids are secreted from the hepatocyte into the bile canaliculus via the canalicular bile salt export pump (BSEP, ABCB11). Some bile acids are sulfated or glucuronidated in the liver via sulfotransferases (SULTs) and UDP-glucuronosyltransferases (UGTs) (Kirkpatrick et al., 1988). Subsequently, they are conjugated with taurine or glycine and secreted into the bile via multidrug resistance-associated protein 2 (MRP2, ABCC2) (Meier and Stieger, 2002). Alternatively, bile acids can be secreted to the systemic (blood) circulation through basolateral export systems that are mediated by members of the multidrug resistance protein (MRP3/4, ABCC3/4) and the organic solute transporter subunit alpha (OSTα)-OSTβ complex. Basolateral efflux plays a minor role under healthy conditions, but under certain pathological conditions basolateral efflux is increased as a compensatory mechanism to counteract intrahepatic bile acid accumulation (*i.e.* cholestasis) (Vinken et al., 2013).

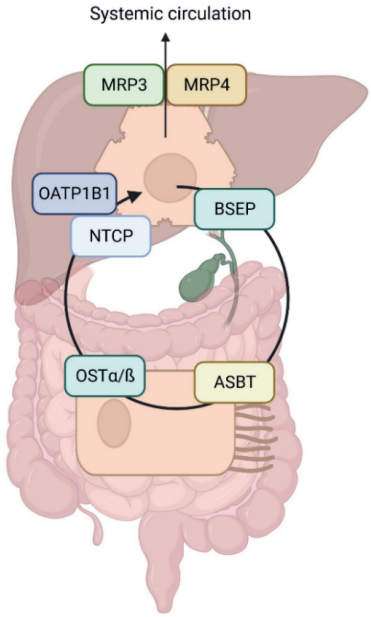

Figure 1 Enterohepatic circulation of bile acids. BSEP=bile salt export pump, ASBT=apical sodium-dependent bile acid transporter, OSTα/β=organic solute transporter α/β, NTCP=sodium/taurocholate cotransporting polypeptide, OATP1B1= organic anion transporting polypeptide 1B1, MRP3/4=multidrug resistance protein 3/4. Figure created with BioRender.com

In humans, around half of the bile acids that are secreted into the bile duct are stored in the gall bladder, while the remaining bile acids are directly transported to the intestinal duodenum (Hofmann, 1999). The gallbladder contracts in response to a meal and bile acids are released into the intestinal lumen. Here, around 95% of bile acids are reabsorbed and transported back to the liver via the portal vein (Chiang, 2009). Bile acid reabsorption predominantly occurs through the activity of the apical sodium-dependent bile acid transporter (ASBT, SLC10A2) in the distal ileum. Bile acids that escape ileal reabsorption are deconjugated by microbial bile salt hydrolases (BSH) and then transformed by the gut microbiome to secondary bile acids. CDCA and CA are converted to lithocholic acid (LCA) and deoxycholic acid (DCA) through 7α-dehydroxylation (Chiang, 2009). Alternatively, CDCA can be converted to ursodeoxycholic acid (UDCA) through an epimerization reaction. The majority of CA, CDCA, DCA, and to some extent UDCA, are then reabsorbed in the intestine and transported back to the liver, whereas most of the LCA is excreted in feces (Chiang, 2009; Hofmann, 1994). Reabsorbed bile acids are transported via the portal vein to the liver, where their uptake is facilitated mainly by sodium/taurocholate cotransporting polypeptide (NTCP, SLC10A1) and to a lesser extent by the members of the organic anion transporting polypeptide (OATP) family. A small amount of circulating bile acids is secreted via the kidneys through urinary excretion (Humbert et al., 2012).

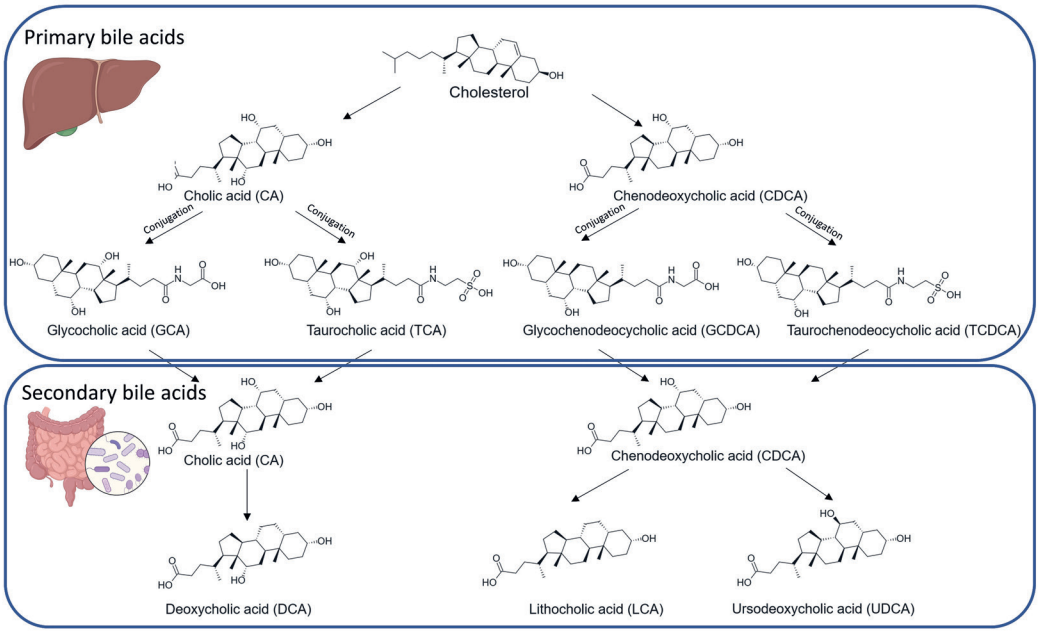

Figure 2 Bile acid metabolism in humans. In the liver, bile acid metabolism mainly produces two primary bile acids, cholic acid (CA) and chenodeoxycholic acid (CDCA). Before secretion, bile acids are conjugated with glycine or taurine. Secondary bile acids are generated through microbial modifications in the intestine, including deoxycholic acid (DCA), lithocholic acid (LCA) and ursodeoxycholic acid (UDCA).

1.3 (Drug-induced) disruption of the bile acid homeostasis

Next to their physiological functions, bile acids can be cytotoxic with pathological consequences. Their detergent properties can disturb cell membranes by solubilizing membrane lipids (Perez and Briz, 2009). These potential adverse health outcomes illustrate why bile acid concentrations need to be tightly regulated. Aside from direct effects on cellular components, changes in the bile acid homeostasis can alter nuclear receptor-mediated signaling and the microbiome's composition and functionality. A disruption of the bile acid homeostasis and signaling has been related to various diseases, such as cholestasis, inflammatory bowel disease and metabolic diseases including obesity, diabetes and metabolic-associated fatty liver disease (MAFLD) (Arab et al., 2017; Fuchs and Trauner, 2022). Various risk factors can contribute to the onset of these diseases, including genetics, diet, infectious diseases, but also exposure to drugs or other chemicals (Vilas-Boas et al., 2019; Jansen and Sturm, 2003; Gijbels et al., 2019; Younossi et al., 2018; Sobczak et al., 2014; Ghouri et al., 2020).

Cholestasis refers to impaired hepatic bile acid secretion and subsequent hepatic bile acid accumulation and increased bile acid levels in the systemic blood circulation. Symptoms of cholestasis include jaundice, pruritus and fever (Sundaram and Bjornsson, 2017). It is well known that some drugs can induce cholestasis. An analysis of 1100 adverse drug reactions in Danish persons revealed that about 16% of all reported hepatic adverse drug reactions were classified as cholestasis responses (Friis and Andreasen, 1992). Where the liver is the main organ involved in cholestasis pathology, the pathology of metabolic diseases is multifaceted and involves a combination of metabolic disturbances

and proinflammatory events in multiple organs (Rodriguez-Duque et al., 2023). A disruption of bile acid homeostasis is one of the many physiological functions that are disturbed in these pathologies. MAFLD, previously known as non-alcoholic fatty liver disease, is becoming the most common chronic liver disorder in the world (Eslam et al., 2020). Several studies have reported an increase of total serum and fecal bile acids in patients with MAFLD (Ferslew et al., 2015; Mouzaki et al., 2016; Jiao et al., 2018). Compositional changes in the bile acid pool have been linked to disease progression. With the disease progression of MAFLD, the ratios of primary to secondary and conjugated to unconjugated bile acids increase (Jahn and Geier, 2018; Puri et al., 2018). Notably, increased concentrations of conjugated CA species in serum is associated with liver fibrosis (Puri et al., 2018). This gradual shift from predominantly conjugated CDCA species to CA species in serum might result in a less potent activation of FXR, because CA is a weaker FXR agonist than CDCA (Cai et al., 2022). Through a reduced FXR activity, alterations in lipid and glucose metabolism and inflammation might occur, which are all involved in MAFLD pathology. The exact mechanism of MAFLD pathology remains to be elucidated, but it is well established that a disruption of bile acid homeostasis is involved in MAFLD pathology.

It is well understood that certain drugs can contribute to the onset and progression of diseases in which a disturbed bile acid homeostasis plays a role, such as cholestasis or MAFLD. Not only drugs, but also environmental contaminants have been associated with an altered bile acid homeostasis. Trichloroethylene (TCE) is an example of an environmental contaminant which was shown to alter bile acid levels in humans. Non-targeted metabolomics analysis revealed that 80 workers exposed to TCE had lower levels of certain plasma bile acids than 95 unexposed controls (Walker et al., 2016). TCE is a widely used industrial solvent and common organic contaminant in groundwater. TCE is classified as carcinogenic to humans by the International Agency for Research on Cancer (IARC, 2014) and as both a carcinogenic and non-carcinogenic health hazard by the US Environmental Protection Agency (EPA) (Chiu et al., 2013). Besides kidney and liver cancer (Charbotel et al., 2006), TCE exposure has been linked to immune dysfunction (Cooper et al., 2009), renal and liver toxicity (Bruning and Bolt, 2000; Brautbar and Williams, 2002). The role of a disturbed bile acid homeostasis in TCE-induced toxicity remains to be established, but this example indicates that alterations to bile acid homeostasis are probably involved in several, not fully understood pathologies. A disruption of bile acid homeostasis may thus be a valuable indicator of certain adverse health outcomes. Upon gaining a better understanding of the relationship between specific disruptions in bile acid homeostasis and adverse health outcomes, measurements of the bile acid concentration and composition might complement the currently available methods used within the toxicological risk assessment.

At the current state-of-the-art such toxicological risk assessments still heavily rely on animal testing. Over the last decades, controversy has arisen about the use of data derived from animal-based strategies, because of ethical, economical and legislative issues. Furthermore, experimental animals do not adequately represent human physiology and may not cover human pathologies. Large differences in bile acid pool composition and the hydrophobicity of species specific bile acids between experimental animal species and humans have been observed (Sangaraju et al., 2022; Garcia-Canaveras et al., 2012). Also anatomical differences, such as the absence of a gallbladder in rats, hamper the translation of findings in preclinical animals to the human situation (Higashiyama et al., 2018). Therefore, the human relevance of laboratory animal study related data on chemical-induced

bile acid homeostasis perturbations (or the absence thereof) might be limited. This drives the need for alternative testing strategies to replace, reduce and refine (3Rs) the use of experimental animals (Russell and Burch, 1959). These alternative testing strategies are referred to as New Approach Methodologies (NAMs). Within this context, *in vitro* cell based assays are of use to obtain concentration-response curves for several endpoints, such as cytotoxicity or transporter-inhibition. Yet, for a toxicological risk assessment, *in vivo* dose-response curves are required. Here, physiologically-based kinetic (PBK) modeling provides a useful tool to bridge the gap between *in vitro* concentration-response or potency information and *in vivo* dose-response data (Louisse et al., 2017). A PBK model is a set of mathematical equations that predicts the behavior of drugs or chemicals within the human body. These models are designed to simulate how a chemical is absorbed, distributed, metabolized, and excreted (ADME) in various organs over time. PBK models are valuable tools for assessing the potential toxicity or risk associated with exposure to a chemical at a certain external dose level, as they allow researchers to estimate the concentration of a chemical in different organs.

1.4 Aim of the thesis

The aim of the current thesis was to develop and apply reliable human cell based *in vitro* models and physiologically based kinetic (PBK) models to better understand and predict drug-induced disruption of bile acid homeostasis with an emphasis on cholestasis. Upon gaining a better understanding of the relationship between specific disruptions in bile acid homeostasis and adverse outcomes, measurement of these disruptions *in vitro* can serve as an indicator of toxicity or potency for selected adverse outcomes. PBK modeling is needed to translate *in vitro* toxicity or potency to *in vivo* risk. A proof-of-principle was provided focusing on the endpoint cholestasis and data-rich chemicals (drugs).

1.5 The role of BSEP-inhibition in the development of cholestasis

Bile acids are very efficiently recycled through the body, with only around 5% of the bile acids that are secreted from the liver into the intestine leaving the body via the feces (Chiang, 2009). For this reason, (carrier-mediated) transport processes are a crucial part of bile acid homeostasis and they were extensively studied in this PhD dissertation. The ATP-binding cassette (ABC) carrier BSEP actively mediates the efflux of bile acids from hepatocytes into bile canaliculi (Boyer, 2013). BSEP plays a central role in maintaining bile acid homeostasis and preventing the accumulation of cytotoxic bile acids within hepatocytes. Disruption of BSEP-functionality hampers hepatic bile acid efflux. To (partially) counteract toxic bile acid accumulation in hepatocytes, these cells undergo adaptive changes in transporter expression under the tight regulation of FXR upon increased intracellular bile acid concentrations. Expression of the bile acid uptake transporter NTCP is reduced, and the expression of basolateral efflux transporters MRP3/4 are increased. When the adaptive response is not sufficient, bile acids accumulate in hepatocytes to toxic levels and cause cholestasis (Vinken et al., 2013). Illustratively, individuals with genetic disorders like progressive familial intrahepatic cholestasis 2 (PFIC2) or benign recurrent intrahepatic cholestasis 2 (BRIC2) face an increased susceptibility to develop cholestasis. Both PFIC2 and BRIC2 are caused by polymorphisms of the BSEP-coding gene

which leads to a malfunctioning BSEP protein. PFIC2 and BRIC2 are estimated to occur in about 1 per 50,000 to 1 per 100,000 childbirths (Geethalakshmi and Mageshkumar, 2014). Notably, BRIC2-carriers generally retain a basal BSEP functionality, whereas the BSEP transporter in PFIC2 carriers is typically not detected or appears abnormal using immunostaining (Jansen et al., 1999; Strautnieks et al., 2008; Evason et al., 2011). The severity of PFIC2 often necessitates liver transplantation due to the emergence of cholestasis, progressive hepatic fibrosis, cirrhosis, and end-stage liver disease (Srivastava, 2014). These polymorphisms clearly illustrate that a proper BSEP functionality is crucial for maintaining healthy (hepatic) bile acid levels.

Certain drugs have the ability to (non-)competitively inhibit BSEP-mediated hepatic bile acid efflux. Drugs with a BSEP-inhibitory potency pose an increased risk to development of cholestasis (Morgan et al., 2013). Therefore, the European Medicines Agency (EMA) recommends that new drugs that are cleared from the body by the liver should be investigated for their potential to inhibit BSEP (EMA Committee for Human Medicinal Products, 2012). In the USA, the Federal Drug Administration (FDA) guidance also recommends the consideration of BSEP inhibition studies when appropriate (FDA, 2022).

1.6 Adverse outcome pathway of cholestasis

In recent years, lots of efforts have been placed on the development of Adverse Outcome Pathways (AOPs) as a conceptual framework to support the construction of non-animal based testing approaches for chemical safety assessment. AOPs consist of a molecular initiating event (MIE), one or more key event(s) (KEs) and an adverse outcome (AO), which represent responses at different levels of biological organization. The general principle of AOPs is that a limited set of KEs can sufficiently describe and predict a toxicological response. The identified KEs can be studied using *in vitro* or *in silico* approaches, thus allowing for a mechanistically-based non-animal toxicological risk assessment (De Vries et al., 2021). BSEP-inhibition has been recognized as a MIE in the AOP of cholestasis (Vinken et al., 2013) (Figure 3). BSEP-inhibition, but also MIEs like tight junction disruption, altered membrane fluidity, compromised cytoskeleton and/or disturbed vesicle transport lead to bile acid accumulation in the hepatocyte. This triggers two types of cellular effects: a) cellular effects related to deteriorative processes, such as inflammation, oxidative stress and cell death (yellow box) and b) adaptive responses aiming to eliminate bile acids from the hepatocyte and prevent further accumulation (pink box). The adaptive responses are tightly regulated by FXR, PXR and the constitutive androstane receptor (CAR, NR1I3) and compromises upregulation of basolateral efflux transporters (MRP3/4), reduced expression of the uptake transporters NTCP and OATP1B1 and a reduced synthesis of bile acids by CYP7A1. The high hepatic bile acid levels result in increased serum concentrations of alkaline phosphatase (ALP), 5'-nucleotidase (5'-NT), gamma-glutamyl transferase (GGT), alanine aminotransferase (ALT) and aspartate aminotransferase (AST), because of bile acid induced membrane damage to hepatocytes (Padda et al., 2011; Hofmann, 2009). The major components of bile are bilirubin and bile acids. Due to the reduced bile flow, bilirubin accumulates in the hepatocytes (Shah and John, 2018). Too high serum bilirubin concentrations (hyperbilirubinemia) are related to jaundice, while too high serum bile acid concentrations are thought to lead to pruritus (Padda et al., 2011; Kuntz and Kuntz, 2008). Ultimately, all these processes lead to the AO cholestasis. It should be taken into

account that alternative mechanisms than those presented in the AOP presented in Figure 3 can also lead to cholestasis; the AOP does not fully cover all aspects involved in human physiology (Leist et al., 2017).

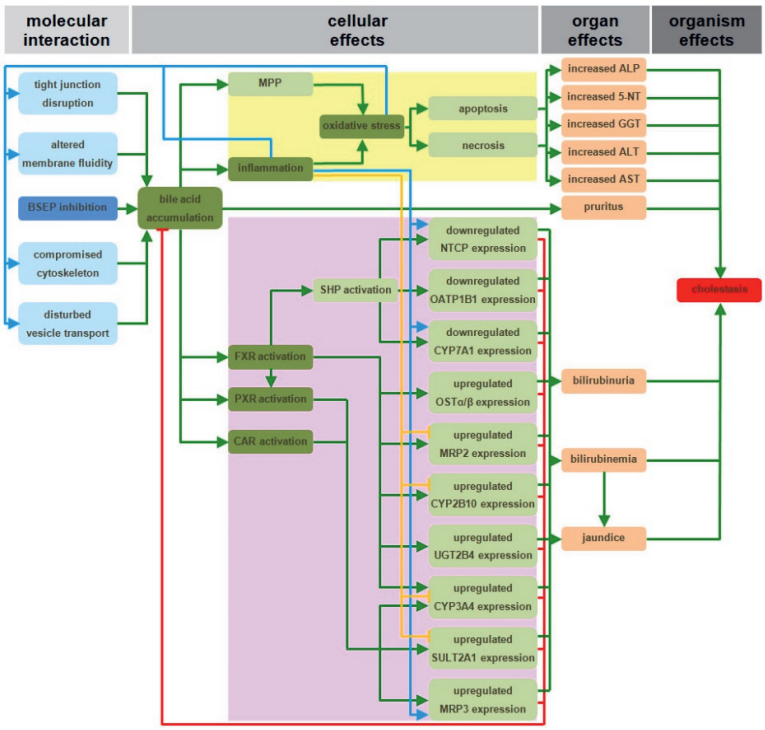

Figure 3 Adverse outcome pathway for cholestatic liver injury induced by inhibition of Bile Salt Export Pump. Figure obtained from: https://aopwiki.org/aops/27

1.7 Health consequences of ASBT-inhibition

Bile acid absorption from the intestinal lumen is a crucial process of the enterohepatic circulation. The majority of the bile acid absorption is mediated by ASBT in the distal ileum. Unconjugated bile acids with high pKa can be transported via passive diffusion into the enterocytes, but this represents only a small quantity of the total bile acids taken up (Alrefai and Gill, 2007). ASBT-mediated transport is coupled with the co-transport of sodium ions. Once inside the enterocytes, the bile acids are transported across the cells by binding to ileal bile acid binding protein (I-BABP) and via OSTα/β secreted into the portal vein (Lu et al., 2022). OSTα/β is independent of sodium and not sensitive to pH, kalium, chlorine or ATP depletion, which indicates that the bile acid efflux from enterocytes is facilitated diffusion (Soroka et al., 2010).

Drugs that inhibit ASBT are interesting leads within drug discovery, as there is a need to develop drugs that mitigate elevated systemic concentrations of bile acids, as is the case in cholestasis. The selective ASBT inhibitor odevixibat has been approved for treatment of the before mentioned genetic disorder PFIC (see section 1.5) (Deeks, 2021). Individuals with PFIC typically have high levels of

circulating bile acids, and for them a reduced intestinal absorption can be beneficial. However, a reduction or inhibition of ASBT-mediated transport can have adverse health effects for otherwise healthy individuals. Also in preclinical and clinical studies on inflammatory bowel disease, reduced bile acid uptake was observed, which was typically accompanied by decreased ASBT expression (Fitzpatrick and Jenabzadeh, 2020). Reduced ASBT expression or activity can have several causes, such as inflammatory cytokine induced repression of the ASBT promoter and/or exposure to certain drugs or chemicals, such as odevixibat or the foodborne mycotoxin deoxynivalenol (Wang et al., 2022; Graffner et al., 2016). Through a reduction of (ASBT-mediated) bile acid uptake, the bile acid concentrations in the lumen increase (Graffner et al., 2016). It has been shown that high levels of DCA reduced intestinal integrity in pig colonic crypts (Leschelle et al., 2002) and in rabbit small intestine (Fasano et al., 1990). A reduced intestinal integrity is related to diarrhea, inflammatory bowel disease and MAFLD (Miele et al., 2009; Marasco et al., 2022). When intestinal integrity is reduced, bacterial products translocate more easily to the liver where they can trigger local inflammatory and stress responses (Duan et al., 2022; Sabino et al., 2016). This provides another plausible mechanism involving bile acid mediated signaling in the pathology of MAFLD.

1.8 Antibiotic-induced effects on bile acid homeostasis

Antibiotics are a powerful class of drugs used to treat bacterial infections. Beyond their targeted antimicrobial effects, antibiotics can also induce unintended consequences on various physiological processes within the human body. Antibiotics can alter the diversity of the gut microbiota due to their antimicrobial properties. Several studies report changes in the gut microbiome's composition and the fecal and plasma bile acid pool in rats upon antibiotic administration (Behr et al., 2018; Murali et al., 2021; de Bruijn et al., 2020). In a single blinded randomized controlled trial, 20 obese men with metabolic syndrome were administered the antibiotic vancomycin for 7 days. Vancomycin treatment was shown to decrease the gut microbiome diversity and the bile acid concentration and composition in plasma and feces (Vrieze et al., 2014). In another study strong correlations were found between antibiotic-induced changes in the microbiome and fecal bile acid alterations (Murali et al., 2021). Yet, changes in the microbiome's composition and related bile acid metabolism cannot fully explain the changes observed in the plasma bile acid levels. Therefore, it was speculated that also other mechanisms are involved in the alterations in plasma bile acid levels, for example changes in intestinal bile acid (re)uptake. This hypothesis is supported by the fact that pretreatment of Caco-2 cells with the antibiotic tobramycin inhibited TCA transport across a Caco-2 cell layer (Zhang et al., 2022). In this thesis, further investigations were performed to evaluate the effects of oral antibiotic exposure on host bile acid homeostasis via effects on intestinal bile acid deconjugation and reuptake.

1.9 New approach methodologies to study bile acid homeostasis

In recent years, significant advances have been made to evaluate both the toxicokinetic and toxicodynamic effects of exposure to chemicals or drugs via nonanimal experimentation. In the current thesis the drug-induced effects on bile acid homeostasis were studied using NAMs. Given that carrier-mediated processes are pivotal in the whole-body bile acid homeostasis, first some background

about the kinetics of carrier-mediated transport will be provided. Next, *in vitro* techniques to study inhibition of ASBT- and BSEP-mediated bile acid transport will be introduced.

1.9.1. The kinetics of carrier-mediated transport

Carriers for chemicals are present in virtually all cell membranes and can be divided in two major superfamilies: the ATP-binding cassette (ABC) transporters and the solute carrier (SLC) transporters (Keogh, 2012). The earlier introduced bile acid transporters BSEP and ASBT are examples of an ABC-transporter and SLC-transporter, respectively. ABC transporters are multimembrane-spanning proteins, which use ATP hydrolysis to drive the transport of their substrates against an electrochemical gradient (Tarling et al., 2013). SLC transporters are integrated into the membrane and either facilitate the transport along the electrochemical gradient, or, as is the case for ASBT, the transporter uses the electrochemical gradient of another solute (*i.e.* sodium) for cotransport (Lu et al., 2021).

Carrier-mediated transport can be described by the same mathematical equation as enzyme kinetics, namely the Michaelis Menten equation (van Ginneken and Russel, 1989). The transport rate increases with increasing concentrations, until the carrier is saturated and the maximal transport rate is achieved (V_{max}). The affinity or the Michaelis-Menten constant (K_m) refers to the substrate concentration needed to achieve half maximal transport rate. The following equation can be used to describe the transport rate (Eq.1)(Runge et al., 2006; Cornish-Bowden, 2013):

$$v = \frac{V_{max} \times [S]}{K_m + [S]} \qquad \text{Eq.1}$$

Where v is the transport rate, V_{max} the maximal transport rate, [S] the substrate concentration and K_m the Michaelis Menten constant. V and V_{max} are expressed in the same unit, typically pmoles/min, and K_m and [S] are expressed in the same unit, typically µM. The units depend on the experimental conditions.

Chemicals or drugs can inhibit transport processes by competitively binding to the carrier and/or reducing the carrier's expression/activity (non-competitive inhibition). Several *in vitro* assays have been developed to study the potential interaction of drugs or chemicals and transporters. These systems provide estimates of the half-maximal inhibitory concentration (IC_{50}) or the inhibitory constant (K_i). K_i can be incorporated in the Michaelis-Menten equation to describe the transport rate in the presence of a certain concentration of the inhibitor. For a competitive inhibitor, this leads to the following equation (Cornish-Bowden, 2013) (Eq. 2):

$$v = \frac{V_{max} \times [S]}{K_m \times (1 + \frac{[I]}{K_i}) + [S]} \qquad \text{Eq. 2}$$

Where v is the transport rate, V_{max} the maximal transport rate, [S] the substrate concentration and K_m the Michaelis Menten constant, [I] the inhibitor concentration and K_i the inhibitory constant. V and V_{max} are expressed in the same unit, typically pmoles/min, and K_m, [S], K_i and [I] are expressed in the same unit, typically µM. The units depend on the experimental conditions.

1.9.2. *In vitro* models to study drug-induced inhibition of ASBT-mediated transport

The available *in vitro* assays to study drug-transporter interactions range from relatively simple models to more complex and physiologically relevant models (Cheng et al., 2016). Cells transfected with a

transporter are a relatively simple model. Physiologically relevant systems are able to perform several metabolic and transporter processes, depending on the organ that the cells represent. Transfected cells provide a well-controlled environment with high stability and reproducibility to study solely the transporter of interest, and therefore a "clean" estimate of the kinetic parameters. A physiologically relevant system provides an overall or apparent estimate of the kinetic parameters. *In vitro* models for intestine and liver are discussed in the following section and section 1.9.3, respectively. The consequences of the chosen *in vitro* system for the *in vitro* to *in vivo* extrapolation will be discussed in section 1.9.5.

Several types of cells are suitable for transfection with transporter cDNA to ultimately express the transporters on the membranes. Typically, insect cells from *Spodoptera frugiperda* (Sf9 or Sf21) are transfected with transporter cDNA, but also several mammalian cells are suitable for transfection, such as Chinese Hamster Ovary (CHO), Madin-Darby canine kidney cells (MDCK) and Human Embryonic Kidney (HEK) 293 cells (Notenboom et al., 2018; De Bruyn et al., 2014). When interested in an uptake transporter, such as ASBT, the transfected cells are cultured in a monolayer and after incubation with selected concentrations of the substrate (and inhibitor), the cells are carefully washed and lysed in order to determine the amount of substrate that was taken up (Balakrishnan et al., 2006).

Caco-2 cells encompass a more physiologically relevant model to study intestinal transport. Caco-2 cells are derived from a human colon carcinoma and commonly cultured on permeable filters ("transwells") to study transepithelial transport of chemicals or drugs (Pinto et al., 1983). Comparative studies revealed that Caco-2 transport assays are able to model the passive and transcellular drug transport *in vivo* (Lennernäs et al., 1996; Amidon et al., 1995; Artursson et al., 2001). Accurate estimates of drug transport are important to predict its bioavailability and the systemic concentrations. A proteome study identified 327 proteins that are involved in absorption, distribution, metabolism and excretion in Caco-2 cells, including 112 SLC transporters and 20 ABC transporters (Olander et al., 2016). Even though ASBT protein expression in Caco-2 cells is not conclusively shown, Caco-2 cells are known to transport bile acids in a sodium-dependent way (Bruck et al., 2017; Olander et al., 2016; van der Mark et al., 2014; Chandler et al., 1993). Given that ASBT is a sodium-symporter, this provides strong evidence that ASBT is indeed functionally present in Caco-2 cells. The interpretation of the results obtained using a Caco-2 transport assay can be more complicated than the results from an ASBT-transfected cell system, because the overall transport, and not specifically the ASBT-mediated transport, is measured. The overall transport also incorporates intracellular and basolateral transport. It can be argued that the estimate of overall transport rate rather than an ASBT-specific rate actually improves the accuracy to predict *in vivo* transport, because the overall transport is more relevant to the human *in vivo* situation.

1.9.3. *In vitro* models to study drug-induced inhibition of BSEP-mediated transport

As previously indicated, inhibition of BSEP is the MIE in the AOP of cholestasis. Therefore, lots of efforts have been placed on the development of *in vitro* models to study BSEP-mediated hepatic bile acid efflux. The most simple system includes BSEP-membrane vesicles (Kis et al., 2009). BSEP-membrane vesicles are generated from cells transfected with BSEP. When interested in an efflux transporter, membrane vesicles are often generated to avoid the need to also transfect the cells with

an uptake transporter. Membrane vesicles have an inside-out orientation, allowing substrates to be transported from the incubation fluid into the vesicle. To generate membrane vesicles, transfected cells are disrupted and centrifuged to remove cellular components. The resulting membrane fraction is isolated through ultracentrifugation and suspended in a buffer (Tabas and Dantzig, 2002). To analyze transporter kinetics, vesicles are separated from the incubation fluid, washed and lysed, after which the substrate concentration in the vesicles is quantified using analytical methods (Cheng et al., 2016). Several Sf9 and HEK-derived membrane vesicles are commercially available. The use of membrane vesicles gives a "clean" estimate of solely BSEP-mediated transport.

Several models with increased biological complexity and physiological relevance to study hepatic bile acid transport kinetics are available. With a physiologically relevant hepatocyte(-like) system the net hepatic bile acid efflux is measured. The net efflux provides a holistic estimate of apical bile acid uptake, *de novo* synthesis and basolateral and canalicular efflux. An important characteristic of these models is their ability to perform *in situ* metabolism. *In situ* metabolism is crucial when the metabolite and not the parent compound is the active transport-inhibitor. In some cases, such as troglitazone, the metabolite inhibits BSEP-mediated TCA transport more potently than the parent compound (Funk et al., 2001). Several BSEP-inhibitors are known to also inhibit hepatic uptake transporters. Troglitazone, for example, inhibits BSEP-mediated TCA transport (Funk et al., 2001), but also transport mediated by NTCP (Marion et al., 2007), MRP3 and MRP4 (Morgan et al., 2013). The reduction of net bile acid efflux from physiologically relevant cells can thus not be solely attributed to BSEP-inhibition. In the following paragraphs, three hepatic *in vitro* models with high physiological relevance are introduced. The three models introduced are primary human hepatocytes, HepaRG cells and hepatocyte-like intrahepatic cholangiocyte organoids (ICO-hep). The difference in functionality between these cell models is mainly related to the origin of the cells, *i.e.* a liver biopsy, hepatic carcinoma cells or adult stem cells from a liver biopsy.

Primary human hepatocytes are the gold standard *in vitro* model to study liver cell function for drug development and toxicity testing. Primary human hepatocytes are typically isolated from liver tissue with a two-step collagenase perfusion technique (Hengstler et al., 2000; LeCluyse and Alexandre, 2010). Primary human hepatocytes can be cultured short-term in a suspension, but this is accompanied by rapid dedifferentiation. When cultured in a sandwich configuration, *i.e.* between two layers of extracellular matrix, primary hepatocytes maintain their polarized phenotype for a longer period (Gijbels and Vinken, 2019). Fresh primary human hepatocytes are not readily available, but to overcome this limitation, cryopreserved primary hepatocytes can be obtained commercially. Primary hepatocytes, cultured either in sandwich or suspension, have been successfully used to study drug-mediated inhibition of bile acid transport (Zhang et al., 2016; Oorts et al., 2021).

Alternatively, the hepatic hepatoma cell line HepaRG has been established as a useful surrogate for human hepatocytes for drug metabolism, transport and toxicity studies (Andersson et al., 2012; Guillouzo et al., 2007; Lübberstedt et al., 2011). HepaRG cells were also shown to perform saturable TCA uptake (Le Vee et al., 2013). A recent study showed that HepaRG cells exposed to the prototypical cholestatic drugs bosentan, cyclosporin A, glibenclamide or troglitazone had a reduced basolateral and canalicular TCA efflux compared to HepaRG cells exposed to the noncholestatic

compounds salicylic acid or flumazenil (Le Vee et al., 2022). HepaRG cells are derived from one donor, so the data are reproducible and robust due to the absence of interdonor differences.

Organoid models provide solutions to some of the drawbacks of primary human hepatocytes and HepaRG cells. ICO-heps are of non-cancerous nature and have unlimited availability and indefinite proliferation, which makes them a useful alternative to HepaRG cells or primary human hepatocytes. ICO-heps are derived from liver-derived adult stem cells and differentiated towards a hepatocyte-like phenotype. Upon differentiation, ICO-heps show an increased expression of hepatic markers, such as albumin, CYP enzymes and transporters (Huch et al., 2015). Their ability to emulate human liver functionality to synthesize and secrete bile acids was compared to the ability of HepaRG cells and primary human hepatocytes in this thesis.

1.9.4. Physiologically-based kinetic (PBK) modeling

PBK modeling simulates the kinetics of a compound in different organs using mathematical equations. PBK modeling predicts internal concentrations in the tissue of interest after exposure to a defined external dose level. In the current thesis, a drug's inhibitory constant to inhibit ASBT- or BSEP-mediated transport is determined using various *in vitro* assays depending on the research question. To predict the effects of external drug exposure on *in vivo* whole-body bile acid homeostasis, PBK modeling is applied. The first step towards developing a PBK model is defining its basic structure using a conceptual model. An exemplary conceptual model for the enterohepatic bile acid circulation is displayed in Figure 4. In PBK modeling, the body is assumed to consist of several compartments. Each compartment (represented as boxes in Figure 4) represents an organ or a single region of the body with homogenous concentrations throughout. Typically, organs are specifically depicted if they either strongly influence the kinetics of the compound of interest or when they are the target organ of toxicity. The remaining organs are lumped into "rapidly perfused tissue" and "slowly perfused tissue" (Rietjens et al., 2011). The liver, intestine and gallbladder are crucial for the enterohepatic circulation of bile acids, and therefore, these are specifically depicted in the bile acid PBK model. Input parameters include physiological, physico-chemical and biochemical parameters. Physiological parameters include *e.g.* organ volumes and blood flows to organs. These data are available from literature. Physico-chemical parameters include lipophilicity, pKa, molecular weight and the fraction unbound for plasma protein binding. Physico-chemical data can be obtained experimentally or by *in silico* methods. Physico-chemical parameters are used to predict the partitioning between the tissues and blood or plasma using computer-based (*in silico*) predictions (Rodgers and Rowland, 2006; Berezhkovskiy, 2004). The last type of parameters needed are kinetic parameters describing *e.g.* clearance or intestinal uptake. Primary hepatocytes can be used for clearance measurements and Caco-2 cells are frequently used to assess kinetics of intestinal uptake. Recently, a machine learning approach has become available which is able to predict chemical-specific physico-chemical or kinetic parameters (Pires et al., 2015). Upon gaining sufficient trust in these models for a wide domain of structurally diverse chemicals or a clearly defined applicability domain, *in silico* predictions could replace experimentally determined physicochemical and kinetic parameters. The adequacy of PBK model predictions is generally evaluated against *in vivo* plasma, blood or urinary data. Generally, it is

assumed that when the blood or plasma levels are predicted accurately, the concentrations within organs are also accurately predicted.

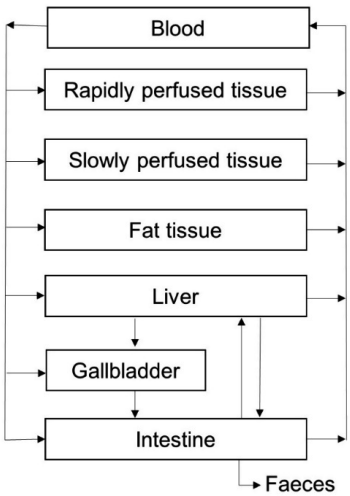

Figure 4 Conceptual model of an exemplary bile acid PBK model

1.9.5. *In vitro* to *in vivo* scaling of carrier-mediated transport kinetics

In order to incorporate kinetic parameters obtained using an *in vitro* model in a PBK model, parameter needs to be expressed in the same unit as the other processes of the model. For example, a V_{max} describing hepatic uptake should have the unit µmoles per entire liver per hour, while the *in vitro* V_{max} is typically obtained in another unit, *e.g.* pmoles per a million hepatocytes per minute or pmoles per mg protein per minute. Different approaches exist to derive the scaling factor for *in vitro* to *in vivo* scaling of carrier-mediated transport.

Firstly, the *in vitro* kinetic parameters can be scaled empirically by comparing the predicted and observed concentration-time profile in plasma or blood and finding the scaling factor that results in the best fit. Even though this approach is not mechanistically sound, it is the most straight-forward way to correct for differences between the *in vitro* and *in vivo* situation, especially when the nature of these differences is not fully understood. Many factors can contribute to differences between the *in vitro* and *in vivo* transport rate, for example, differences in membrane potential or additional transport mechanisms that are present *in vivo* but not in the *in vitro* system, *e.g.* an additional carrier (Noorlander et al., 2021).

A physiological scaling factor can be used to obtain a scaling factor with a mechanistic and/or theoretical basis. A physiological scaling factor includes the number of cells in the tissue of interest or the membrane/total protein content of the tissue of interest. This approach is common for scaling metabolic clearance data obtained using *e.g.* microsomes or S9 fractions, and is also applied for metabolic clearance obtained using primary hepatocytes (Pelkonen and Turpeinen, 2007). The underlying assumption of the physiological scaling approach is that transporter abundance and activity *in vitro* and *in vivo* are equal. When this assumption is not valid, a relative expression factor (REF) or relative activity factor (RAF) can be used to correct for differences in expression or activity, respectively. For the REF approach, gene expression or transporter abundance is measured in the *in*

vitro model and in primary tissue samples. Next, the REF is determined as a quotient that corrects for these differences in gene expression or transporter abundance. Some authors measure gene expression, but abundance measurements are preferrable, because expression does not mean that the protein is transcribed. With the increasing popularity of quantitative targeted proteomics (Prasad et al., 2019), measuring transporter abundances has become more attainable over the last years and the REF approach has been increasingly applied (Nozaki and Izumi, 2020; Deng et al., 2021; Sachar et al., 2020; Vildhede et al., 2016). An alternative approach is the establishment of a relative activity factor (RAF). In order to determine a RAF, the transport rates of a probe substrate *in vitro* and *in vivo* are obtained and used as a quotient that corrects for these differences in activity.

1.10 Outline of the thesis

Chapter 1 gives an introduction on the potential health consequences of (drug-induced) disruption of bile acid homeostasis, techniques to study BSEP- or ASBT-mediated transport inhibition *in vitro* and translation of these findings to the *in vivo* situation and formulates the aim of the thesis: to develop reliable human cell based *in vitro* models and physiologically based kinetic (PBK) models to better understand and predict drug-induced disruption of bile acid homeostasis with emphasis on cholestasis.

Chapter 2 compares the capacity of three different hepatic *in vitro* systems to emulate human liver functionality to synthesize and secrete bile acids. Bile acid synthesis rates and profiles, responsiveness to selected BSEP-inhibitors and selected target genes were analyzed for: hepatocyte-like intrahepatic cholangiocyte organoids (ICO-heps), sandwich cultured human hepatocytes (SCHH) and HepaRG cells (HepaRGs). To this end, basal bile acid production of sandwich cultured human hepatocytes (SCHHs), HepaRG cells and hepatocyte-like intrahepatic cholangiocyte organoids (ICO-heps) were analyzed, and the effect of the known BSEP-inhibitors bosentan and lopinavir on bile acid disposition in SCHHs and HepaRG cells was quantified. RT-qPCR of selected target genes involved in maturation status, synthesis, transport and conjugation of bile acids was performed to mechanistically underpin the observed differences in bile acid homeostasis.

Chapter 3 develops a PBK model that provides a tool to predict dose-dependent bile acid accumulation in humans upon treatment with the BSEP inhibitor bosentan. To this end, three PBK submodels were developed, consisting of a PBK model for a) bosentan, b) RO 47-8634 (the active metabolite of bosentan) and c) bile acids. The bile acid PBK model was developed using glycochenodeoxycholic acid (GCDCA) as an exemplary bile acid. The bosentan and RO 47-8634 PBK models were used to predict their concentrations at the target organ for BSEP inhibition, *i.e.* the liver. The PBK model kinetic parameters for BSEP-mediated transport were obtained from a literature study reporting BSEP-mediated GCDCA uptake in membrane vesicles. The scaling factor required to convert the *in vitro* kinetic data to the *in vivo* situation was based on the relative BSEP expression in the membrane vesicles and *in vivo* tissue (REF approach). The effects of *in vivo* variabilities in transporter abundance and bile acid pool size on plasma and liver bile acids were also simulated.

Chapter 4 simulates the effects of ASBT-inhibition on systemic plasma levels. The model from the previous chapter was extended to describe not only GCDCA, but also GCA and GDCA and a generic unconjugated bile acid. Hepatic bile acid uptake was described as a permeability-limited, NTCP-mediated process. The kinetic parameters and scaling factor for *in vitro* to *in vivo* scaling of NTCP-mediated transport were obtained from literature and based on a transfected cell system combined with the REF approach for scaling. The kinetic parameters for ASBT-mediated transport were obtained experimentally using Caco-2 cells. Empirical *in vitro* to *in vivo* extrapolation was applied for ASBT-mediated transport. Odevixibat, a reversible ASBT-inhibitor, was used as a model compound.

Chapter 5 applies the newly developed PBK model to investigate the effect of the antibiotic tobramycin on bile acid homeostasis. Inhibition of intestinal transport was measured using Caco-2 cells. Inhibition of intestinal deconjugation was based on previous studies using fecal static batch incubations.

Chapter 6 applies the newly developed PBK model to predict the drug-induced hepatic bile acid accumulation and cholestasis for 15 drugs. These drugs are known to inhibit hepatic bile acid efflux and causally linked to the development of drug-induced liver injury, but classified as common, rare or no cholestatic liver injury. First, generic PBK models were built to predict the hepatic concentrations of these drugs. Next, the PBK model predicted hepatic concentrations were used to predict their inhibitory effect on BSEP-mediated efflux as well as their effects on hepatic bile acid accumulation as a measure for cholestatic potency. The inhibitory constants were obtained from a literature study that used primary hepatocytes in suspension. Predictions were made for different dose levels and also for average as well as sensitive individuals.

Chapter 7 gives an overview of the main findings in this thesis and provides a general discussion on points beyond the scope of the individual chapters. The chapter further discusses the use of PBK models for drug metabolism and bile acids, *in vitro* and *in silico* tools to define PBK input parameters, converting *in vitro* data to the *in vivo* situation, the cholestasis adverse outcome pathway and the relevance of bile acids for adverse outcomes other than cholestasis. To finalize, a discussion is provided about the paradigm shift towards an animal-free risk assessment for cholestasis.

References

Alrefai, W. A. and Gill, R. K. (2007). Bile acid transporters: Structure, function, regulation and pathophysiological implications. *Pharm Res 24*, 1803-1823. doi:10.1007/s11095-007-9289-1

Amidon, G. L., Lennernas, H., Shah, V. P. et al. (1995). A theoretical basis for a biopharmaceutic drug classification: The correlation of in vitro drug product dissolution and in vivo bioavailability. *Pharm Res 12*, 413-420. doi:10.1023/a:1016212804288

Andersson, T. B., Kanebratt, K. P. and Kenna, J. G. (2012). The heparg cell line: A unique in vitro tool for understanding drug metabolism and toxicology in human. *Expert Opin Drug Metab Toxicol 8*, 909-920. doi:10.1517/17425255.2012.685159

Anstee, Q. M., Targher, G. and Day, C. P. (2013). Progression of nafld to diabetes mellitus, cardiovascular disease or cirrhosis. *Nat Rev Gastroenterol Hepatol 10*, 330-344. doi:10.1038/nrgastro.2013.41

Arab, J. P., Karpen, S. J., Dawson, P. A. et al. (2017). Bile acids and nonalcoholic fatty liver disease: Molecular insights and therapeutic perspectives. *Hepatology 65*, 350-362. doi:10.1002/hep.28709

Artursson, P., Palm, K. and Luthman, K. (2001). Caco-2 monolayers in experimental and theoretical predictions of drug transport. *Adv Drug Deliv Rev 46*, 27-43. doi:10.1016/s0169-409x(00)00128-9

Balakrishnan, A., Wring, S. A. and Polli, J. E. (2006). Interaction of native bile acids with human apical sodium-dependent bile acid transporter (hasbt): Influence of steroidal hydroxylation pattern and c-24 conjugation. *Pharm Res 23*, 1451-1459. doi:10.1007/s11095-006-0219-4

Behr, C., Ramirez-Hincapie, S., Cameron, H. J. et al. (2018). Impact of lincosamides antibiotics on the composition of the rat gut microbiota and the metabolite profile of plasma and feces. *Toxicol Lett 296*, 139-151. doi:10.1016/j.toxlet.2018.08.002

Berezhkovskiy, L. M. (2004). Volume of distribution at steady state for a linear pharmacokinetic system with peripheral elimination. *J Pharm Sci 93*, 1628-1640. doi:10.1002/jps.20073

Boyer, J. L. (2013). Bile formation and secretion. *Compr Physiol 3*, 1035-1078. doi:10.1002/cphy.c120027

Brautbar, N. and Williams, J., 2nd (2002). Industrial solvents and liver toxicity: Risk assessment, risk factors and mechanisms. *Int J Hyg Environ Health 205*, 479-491. doi:10.1078/1438-4639-00175

Bruck, S., Strohmeier, J., Busch, D. et al. (2017). Caco-2 cells - expression, regulation and function of drug transporters compared with human jejunal tissue. *Biopharm Drug Dispos 38*, 115-126. doi:10.1002/bdd.2025

Bruning, T. and Bolt, H. M. (2000). Renal toxicity and carcinogenicity of trichloroethylene: Key results, mechanisms, and controversies. *Crit Rev Toxicol 30*, 253-285. doi:10.1080/10408440091159202

Cai, J., Rimal, B., Jiang, C. et al. (2022). Bile acid metabolism and signaling, the microbiota, and metabolic disease. *Pharmacol Ther 237*, 108238. doi:10.1016/j.pharmthera.2022.108238

Chandler, C. E., Zaccaro, L. M. and Moberly, J. B. (1993). Transepithelial transport of cholyltaurine by caco-2 cell monolayers is sodium-dependent. *American Journal of Physiology 264*, G1118-G1125. doi:DOI 10.1152/ajpgi.1993.264.6.G1118

Charbotel, B., Fevotte, J., Hours, M. et al. (2006). Case-control study on renal cell cancer and occupational exposure to trichloroethylene. Part ii: Epidemiological aspects. *Ann Occup Hyg 50*, 777-787. doi:10.1093/annhyg/mel039

Cheng, Y., Woolf, T. F., Gan, J. et al. (2016). In vitro model systems to investigate bile salt export pump (bsep) activity and drug interactions: A review. *Chem Biol Interact 255*, 23-30. doi:10.1016/j.cbi.2015.11.029

Chiang, J. Y. (2009). Bile acids: Regulation of synthesis. *J Lipid Res 50*, 1955-1966. doi:10.1194/jlr.R900010-JLR200

Chiang, J. Y. L. (2017). Bile acid metabolism and signaling in liver disease and therapy. *Liver Res 1*, 3-9. doi:10.1016/j.livres.2017.05.001

Chiang, J. Y. L. and Ferrell, J. M. (2020). Up to date on cholesterol 7 alpha-hydroxylase (cyp7a1) in bile acid synthesis. *Liver Res 4*, 47-63. doi:10.1016/j.livres.2020.05.001

Chiang, J. Y. L. and Ferrell, J. M. (2022). Discovery of farnesoid x receptor and its role in bile acid metabolism. *Mol Cell Endocrinol 548*, 111618. doi:10.1016/j.mce.2022.111618

Chiu, W. A., Jinot, J., Scott, C. S. et al. (2013). Human health effects of trichloroethylene: Key findings and scientific issues. *Environ Health Perspect 121*, 303-311. doi:10.1289/ehp.1205879

Comess, J. E. and Abad-Jorge, A. (2023). Introduction to the gut microbiome and its impact on health and disease. *Topics in Clinical Nutrition 38*, 183-195. doi:10.1097/Tin.0000000000000324

Cooper, G. S., Makris, S. L., Nietert, P. J. et al. (2009). Evidence of autoimmune-related effects of trichloroethylene exposure from studies in mice and humans. *Environ Health Perspect 117*, 696-702. doi:10.1289/ehp.11782

Cornish-Bowden, A. (2013). *Fundamentals of enzyme kinetics*. Vol. John Wiley & Sons.

de Bruijn, V., Behr, C., Sperber, S. et al. (2020). Antibiotic-induced changes in microbiome-related metabolites and bile acids in rat plasma. *Metabolites 10*, doi:10.3390/metabo10060242

De Bruyn, T., Sempels, W., Snoeys, J. et al. (2014). Confocal imaging with a fluorescent bile acid analogue closely mimicking hepatic taurocholate disposition. *J Pharm Sci 103*, 1872-1881. doi:10.1002/jps.23933

De Vries, R. B. M., Angrish, M., Browne, P. et al. (2021). Applying evidence-based methods to the development and use of adverse outcome pathways. *ALTEX 38*, 336-347. doi:10.14573/altex.2101211

Deeks, E. D. (2021). Odevixibat: First approval. *Drugs* 1-6.

Deng, F., Tuomi, S. K., Neuvonen, M. et al. (2021). Comparative hepatic and intestinal efflux transport of statins. *Drug Metab Dispos 49*, 750-759. doi:10.1124/dmd.121.000430

Duan, S., Li, X., Fan, G. et al. (2022). Targeting bile acid signaling for the treatment of liver diseases: From bench to bed. *Biomed Pharmacother 152*, 113154. doi:10.1016/j.biopha.2022.113154

Duane, W. C. and Javitt, N. B. (1999). 27-hydroxycholesterol: Production rates in normal human subjects. *J Lipid Res 40*, 1194-1199.

EMA and (CHMP), C. f. H. M. P. (2012). Guideline on the investigation of drug interactions.

Eslam, M., Sanyal, A. J., George, J. et al. (2020). Mafld: A consensus-driven proposed nomenclature for metabolic associated fatty liver disease. *Gastroenterology 158*, 1999-2014 e1991. doi:10.1053/j.gastro.2019.11.312

Evason, K., Bove, K. E., Finegold, M. J. et al. (2011). Morphologic findings in progressive familial intrahepatic cholestasis 2 (pfic2): Correlation with genetic and immunohistochemical studies. *Am J Surg Pathol 35*, 687-696. doi:10.1097/PAS.0b013e318212ec87

Fasano, A., Budillon, G., Guandalini, S. et al. (1990). Bile acids reversible effects on small intestinal permeability. An in vitro study in the rabbit. *Dig Dis Sci 35*, 801-808. doi:10.1007/BF01536791

FDA (2022). M12 drug interaction studies. *ICH consensus guideline*

Ferslew, B. C., Xie, G., Johnston, C. K. et al. (2015). Altered bile acid metabolome in patients with nonalcoholic steatohepatitis. *Dig Dis Sci 60*, 3318-3328. doi:10.1007/s10620-015-3776-8

Fiorucci, S., Mencarelli, A., Palladino, G. et al. (2009). Bile-acid-activated receptors: Targeting tgr5 and farnesoid-x-receptor in lipid and glucose disorders. *Trends Pharmacol Sci 30*, 570-580. doi:10.1016/j.tips.2009.08.001

Fiorucci, S., Mencarelli, A., Cipriani, S. et al. (2011). Activation of the farnesoid-x receptor protects against gastrointestinal injury caused by non-steroidal anti-inflammatory drugs in mice. *Br J Pharmacol 164*, 1929-1938. doi:10.1111/j.1476-5381.2011.01481.x

Fitzpatrick, L. R. and Jenabzadeh, P. (2020). Ibd and bile acid absorption: Focus on pre-clinical and clinical observations. *Front Physiol 11*, 564. doi:10.3389/fphys.2020.00564

Friis, H. and Andreasen, P. B. (1992). Drug-induced hepatic-injury - an analysis of 1100 cases reported to the danish-committee-on-adverse-drug-reactions between 1978 and 1987. *Journal of Internal Medicine 232*, 133-138. doi:DOI 10.1111/j.1365-2796.1992.tb00562.x

Fuchs, C. D. and Trauner, M. (2022). Role of bile acids and their receptors in gastrointestinal and hepatic pathophysiology. *Nat Rev Gastroenterol Hepatol 19*, 432-450. doi:10.1038/s41575-021-00566-7

Funk, C., Pantze, M., Jehle, L. et al. (2001). Troglitazone-induced intrahepatic cholestasis by an interference with the hepatobiliary export of bile acids in male and female rats. Correlation with the gender difference in troglitazone sulfate formation and the inhibition of the canalicular bile salt export pump (bsep) by troglitazone and troglitazone sulfate. *Toxicology 167*, 83-98. doi:10.1016/s0300-483x(01)00460-7

Garcia-Canaveras, J. C., Donato, M. T., Castell, J. V. et al. (2012). Targeted profiling of circulating and hepatic bile acids in human, mouse, and rat using a uplc-mrm-ms-validated method. *J Lipid Res 53*, 2231-2241. doi:10.1194/jlr.D028803

Geethalakshmi, S. and Mageshkumar, S. (2014). Benign recurrent intrahepatic cholestasis: A rare case report. *Int J Sci Study 2*, 222-224.

Ghouri, Y. A., Tahan, V. and Shen, B. (2020). Secondary causes of inflammatory bowel diseases. *World J Gastroenterol 26*, 3998-4017. doi:10.3748/wjg.v26.i28.3998

Gijbels, E., Vilas-Boas, V., Deferm, N. et al. (2019). Mechanisms and in vitro models of drug-induced cholestasis. *Arch Toxicol 93*, 1169-1186. doi:10.1007/s00204-019-02437-2

Gijbels, E. and Vinken, M. (2019). Mechanisms of drug-induced cholestasis. In (eds.), *Experimental cholestasis research*. Springer.

Graffner, H., Gillberg, P. G., Rikner, L. et al. (2016). The ileal bile acid transporter inhibitor a4250 decreases serum bile acids by interrupting the enterohepatic circulation. *Aliment Pharmacol Ther 43*, 303-310. doi:10.1111/apt.13457

Guillouzo, A., Corlu, A., Aninat, C. et al. (2007). The human hepatoma heparg cells: A highly differentiated model for studies of liver metabolism and toxicity of xenobiotics. *Chem Biol Interact 168*, 66-73. doi:10.1016/j.cbi.2006.12.003

Guo, C., Chen, W. D. and Wang, Y. D. (2016). Tgr5, not only a metabolic regulator. *Front Physiol 7*, 646. doi:10.3389/fphys.2016.00646

Guo, G. L., Lambert, G., Negishi, M. et al. (2003). Complementary roles of farnesoid x receptor, pregnane x receptor, and constitutive androstane receptor in protection against bile acid toxicity. *J Biol Chem 278*, 45062-45071. doi:10.1074/jbc.M307145200

Hengstler, J. G., Utesch, D., Steinberg, P. et al. (2000). Cryopreserved primary hepatocytes as a constantly available in vitro model for the evaluation of human and animal drug metabolism and enzyme induction. *Drug Metabolism Reviews 32*, 81-118. doi:Doi 10.1081/Dmr-100100564

Higashiyama, H., Uemura, M., Igarashi, H. et al. (2018). Anatomy and development of the extrahepatic biliary system in mouse and rat: A perspective on the evolutionary loss of the gallbladder. *J Anat 232*, 134-145. doi:10.1111/joa.12707

Hofmann, A. F. (1961). Micellar solubilization of fatty acids and monoglycerides by bile salt solutions. *Nature 190*, 1106-1107. doi:10.1038/1901106a0

Hofmann, A. F. (1994). Pharmacology of ursodeoxycholic acid, an enterohepatic drug. *Scand J Gastroenterol Suppl 204*, 1-15. doi:10.3109/00365529409103618

Hofmann, A. F. (1999). Bile acids: The good, the bad, and the ugly. *News Physiol Sci 14*, 24-29. doi:10.1152/physiologyonline.1999.14.1.24

Hofmann, A. F. (2009). The enterohepatic circulation of bile acids in mammals: Form and functions. *Front Biosci (Landmark Ed) 14*, 2584-2598. doi:10.2741/3399

Huch, M., Gehart, H., van Boxtel, R. et al. (2015). Long-term culture of genome-stable bipotent stem cells from adult human liver. *Cell 160*, 299-312. doi:10.1016/j.cell.2014.11.050

Humbert, L., Maubert, M. A., Wolf, C. et al. (2012). Bile acid profiling in human biological samples: Comparison of extraction procedures and application to normal and cholestatic patients. *J Chromatogr B Analyt Technol Biomed Life Sci 899*, 135-145. doi:10.1016/j.jchromb.2012.05.015

Hylemon, P. B., Zhou, H., Pandak, W. M. et al. (2009). Bile acids as regulatory molecules. *J Lipid Res 50*, 1509-1520. doi:10.1194/jlr.R900007-JLR200

IARC, W. G. o. t. E. o. C. R. t. H. (2014). Trichloroethylene, tetrachloroethylene, and some other chlorinated agents. *IARC monographs on the evaluation of carcinogenic risks to humans 106*, 1.

Jahn, D. and Geier, A. (2018). Bile acids in nonalcoholic steatohepatitis: Pathophysiological driving force or innocent bystanders? *Hepatology 67*, 464-466. doi:10.1002/hep.29543

Jansen, P. L., Strautnieks, S. S., Jacquemin, E. et al. (1999). Hepatocanalicular bile salt export pump deficiency in patients with progressive familial intrahepatic cholestasis. *Gastroenterology 117*, 1370-1379. doi:10.1016/s0016-5085(99)70287-8

Jansen, P. L. and Sturm, E. (2003). Genetic cholestasis, causes and consequences for hepatobiliary transport. *Liver Int 23*, 315-322. doi:10.1034/j.1478-3231.2003.00856.x

Jantti, S. E., Kivilompolo, M., Ohrnberg, L. et al. (2014). Quantitative profiling of bile acids in blood, adipose tissue, intestine, and gall bladder samples using ultra high performance liquid chromatography-tandem mass spectrometry. *Anal Bioanal Chem 406*, 7799-7815. doi:10.1007/s00216-014-8230-9

Jia, W., Xie, G. and Jia, W. (2018). Bile acid-microbiota crosstalk in gastrointestinal inflammation and carcinogenesis. *Nat Rev Gastroenterol Hepatol 15*, 111-128. doi:10.1038/nrgastro.2017.119

Jia, W., Li, Y., Cheung, K. C. P. et al. (2023). Bile acid signaling in the regulation of whole body metabolic and immunological homeostasis. *Sci China Life Sci* 1-17. doi:10.1007/s11427-023-2353-0

Jiao, N., Baker, S. S., Chapa-Rodriguez, A. et al. (2018). Suppressed hepatic bile acid signalling despite elevated production of primary and secondary bile acids in nafld. *Gut 67*, 1881-1891. doi:10.1136/gutjnl-2017-314307

Keogh, J. P. (2012). Membrane transporters in drug development. *Adv Pharmacol 63*, 1-42. doi:10.1016/B978-0-12-398339-8.00001-X

Kirkpatrick, R. B., Green, M. D., Hagey, L. R. et al. (1988). Effect of side chain length on bile acid conjugation: Glucuronidation, sulfation and coenzyme a formation of nor-bile acids and their natural c24 homologs by human and rat liver fractions. *Hepatology 8*, 353-357.

Kis, E., Ioja, E., Nagy, T. et al. (2009). Effect of membrane cholesterol on bsep/bsep activity: Species specificity studies for substrates and inhibitors. *Drug Metab Dispos 37*, 1878-1886. doi:10.1124/dmd.108.024778

Kuntz, E. and Kuntz, H. (2008). Hepatology: Textbook and atlas: History, morphology, biochemistry, diagnostics, clinic. *Therapy* 595-604.

Le Vee, M., Noel, G., Jouan, E. et al. (2013). Polarized expression of drug transporters in differentiated human hepatoma heparg cells. *Toxicol In Vitro 27*, 1979-1986. doi:10.1016/j.tiv.2013.07.003

Le Vee, M., Moreau, A., Jouan, E. et al. (2022). Inhibition of canalicular and sinusoidal taurocholate efflux by cholestatic drugs in human hepatoma heparg cells. *Biopharm Drug Dispos 43*, 265-271. doi:10.1002/bdd.2333

LeCluyse, E. L. and Alexandre, E. (2010). Isolation and culture of primary hepatocytes from resected human liver tissue. In (eds.), *Hepatocytes*. Springer.

Leist, M., Ghallab, A., Graepel, R. et al. (2017). Adverse outcome pathways: Opportunities, limitations and open questions. *Arch Toxicol 91*, 3477-3505. doi:10.1007/s00204-017-2045-3

Lennernäs, H., Palm, K., Fagerholm, U. et al. (1996). Correlation between paracellular and transcellular drug permeability in the human jejunum and caco-2 monolayers. *Int. J. Pharm 127*, 103-107.

Leschelle, X., Robert, V., Delpal, S. et al. (2002). Isolation of pig colonic crypts for cytotoxic assay of luminal compounds: Effects of hydrogen sulfide, ammonia, and deoxycholic acid. *Cell Biol Toxicol 18*, 193-203. doi:10.1023/a:1015515821390

Louisse, J., Beekmann, K. and Rietjens, I. M. C. M. (2017). Use of physiologically based kinetic modeling-based reverse dosimetry to predict in vivo toxicity from in vitro data. *Chem Res Toxicol 30*, 114-125. doi:10.1021/acs.chemrestox.6b00302

Lu, P. H., Li, C. C., Chiang, Y. W. et al. (2021). Dissecting the conformational dynamics of the bile acid transporter homologue asbt(nm). *J Mol Biol 433*, 166764. doi:10.1016/j.jmb.2020.166764
Lu, Z. N., He, H. W. and Zhang, N. (2022). Advances in understanding the regulatory mechanism of organic solute transporter alpha-beta. *Life Sci 310*, 121109. doi:10.1016/j.lfs.2022.121109
Lübberstedt, M., Müller-Vieira, U., Mayer, M. et al. (2011). Heparg human hepatic cell line utility as a surrogate for primary human hepatocytes in drug metabolism assessment in vitro. *Journal of pharmacological and toxicological methods 63*, 59-68.
Makishima, M., Lu, T. T., Xie, W. et al. (2002). Vitamin d receptor as an intestinal bile acid sensor. *Science 296*, 1313-1316. doi:10.1126/science.1070477
Maran, R. R., Thomas, A., Roth, M. et al. (2009). Farnesoid x receptor deficiency in mice leads to increased intestinal epithelial cell proliferation and tumor development. *J Pharmacol Exp Ther 328*, 469-477. doi:10.1124/jpet.108.145409
Marasco, G., Cremon, C., Barbaro, M. R. et al. (2022). Pathophysiology and clinical management of bile acid diarrhea. *J Clin Med 11*, 3102. doi:10.3390/jcm11113102
Marion, T. L., Leslie, E. M. and Brouwer, K. L. (2007). Use of sandwich-cultured hepatocytes to evaluate impaired bile acid transport as a mechanism of drug-induced hepatotoxicity. *Mol Pharm 4*, 911-918. doi:10.1021/mp0700357
Meier, P. J. and Stieger, B. (2002). Bile salt transporters. *Annu Rev Physiol 64*, 635-661. doi:10.1146/annurev.physiol.64.082201.100300
Miele, L., Valenza, V., La Torre, G. et al. (2009). Increased intestinal permeability and tight junction alterations in nonalcoholic fatty liver disease. *Hepatology 49*, 1877-1887. doi:10.1002/hep.22848
Monteiro-Cardoso, V. F., Corliano, M. and Singaraja, R. R. (2021). Bile acids: A communication channel in the gut-brain axis. *Neuromolecular Med 23*, 99-117. doi:10.1007/s12017-020-08625-z
Morgan, R. E., van Staden, C. J., Chen, Y. et al. (2013). A multifactorial approach to hepatobiliary transporter assessment enables improved therapeutic compound development. *Toxicol Sci 136*, 216-241. doi:10.1093/toxsci/kft176
Mouzaki, M., Wang, A. Y., Bandsma, R. et al. (2016). Bile acids and dysbiosis in non-alcoholic fatty liver disease. *PLoS One 11*, e0151829. doi:10.1371/journal.pone.0151829
Murali, A., Giri, V., Cameron, H. J. et al. (2021). Elucidating the relations between gut bacterial composition and the plasma and fecal metabolomes of antibiotic treated wistar rats. *Microbiology Research 12*, 82-122. doi:10.3390/microbiolres12010008
Noorlander, A., Wesseling, S., Rietjens, I. M. C. M. et al. (2021). Incorporating renal excretion via the oct2 transporter in physiologically based kinetic modelling to predict in vivo kinetics of mepiquat in rat. *Toxicol Lett 343*, 34-43. doi:10.1016/j.toxlet.2021.02.013
Notenboom, S., Weigand, K. M., Proost, J. H. et al. (2018). Development of a mechanistic biokinetic model for hepatic bile acid handling to predict possible cholestatic effects of drugs. *European Journal of Pharmaceutical Sciences 115*, 175-184.
Nozaki, Y. and Izumi, S. (2020). Recent advances in preclinical in vitro approaches towards quantitative prediction of hepatic clearance and drug-drug interactions involving organic anion transporting polypeptide (oatp) 1b transporters. *Drug Metab Pharmacokinet 35*, 56-70. doi:10.1016/j.dmpk.2019.11.004
Olander, M., Wisniewski, J. R., Matsson, P. et al. (2016). The proteome of filter-grown caco-2 cells with a focus on proteins involved in drug disposition. *J Pharm Sci 105*, 817-827. doi:10.1016/j.xphs.2015.10.030
Oorts, M., Van Brantegem, P., Deferm, N. et al. (2021). Bosentan alters endo- and exogenous bile salt disposition in sandwich-cultured human hepatocytes. *J Pharmacol Exp Ther 379*, 20-32. doi:10.1124/jpet.121.000695
Padda, M. S., Sanchez, M., Akhtar, A. J. et al. (2011). Drug-induced cholestasis. *Hepatology 53*, 1377-1387. doi:10.1002/hep.24229

Pelkonen, O. and Turpeinen, M. (2007). In vitro-in vivo extrapolation of hepatic clearance: Biological tools, scaling factors, model assumptions and correct concentrations. *Xenobiotica 37*, 1066-1089. doi:10.1080/00498250701620726

Perez, M. J. and Briz, O. (2009). Bile-acid-induced cell injury and protection. *World J Gastroenterol 15*, 1677-1689. doi:10.3748/wjg.15.1677

Pinto, M., Robineleon, S., Appay, M. D. et al. (1983). Enterocyte-like differentiation and polarization of the human-colon carcinoma cell-line caco-2 in culture. *Biology of the Cell 47*, 323-330.

Pires, D. E., Blundell, T. L. and Ascher, D. B. (2015). Pkcsm: Predicting small-molecule pharmacokinetic and toxicity properties using graph-based signatures. *J Med Chem 58*, 4066-4072. doi:10.1021/acs.jmedchem.5b00104

Prasad, B., Achour, B., Artursson, P. et al. (2019). Toward a consensus on applying quantitative liquid chromatography-tandem mass spectrometry proteomics in translational pharmacology research: A white paper. *Clin Pharmacol Ther 106*, 525-543. doi:10.1002/cpt.1537

Puri, P., Daita, K., Joyce, A. et al. (2018). The presence and severity of nonalcoholic steatohepatitis is associated with specific changes in circulating bile acids. *Hepatology 67*, 534-548. doi:10.1002/hep.29359

Rietjens, I. M. C. M., Louisse, J. and Punt, A. (2011). Tutorial on physiologically based kinetic modeling in molecular nutrition and food research. *Mol Nutr Food Res 55*, 941-956. doi:10.1002/mnfr.201000655

Rodgers, T. and Rowland, M. (2006). Physiologically based pharmacokinetic modelling 2: Predicting the tissue distribution of acids, very weak bases, neutrals and zwitterions. *J Pharm Sci 95*, 1238-1257. doi:10.1002/jps.20502

Rodriguez-Duque, J. C., Calleja, J. L., Iruzubieta, P. et al. (2023). Increased risk of mafld and liver fibrosis in inflammatory bowel disease independent of classic metabolic risk factors. *Clin Gastroenterol Hepatol 21*, 406-414 e407. doi:10.1016/j.cgh.2022.01.039

Runge, S. W., Hill, B. J., Moran, W. M. et al. (2006). A simple classroom teaching technique to help students understand michaelis-menten kinetics. *CBE Life Sci Educ 5*, 348-352. doi:10.1187/cbe.06-04-0160

Russell, W. M. S. and Burch, R. L. (1959). *The principles of humane experimental technique*. Vol. Methuen.

ieira-Silva, S., Machiels, K. et al. (2016). Primary sclerosing cholangitis is characterised by intestinal dysbiosis independent from ibd. *Gut 65*, 1681-1689. doi:10.1136/gutjnl-2015-311004

Sachar, M., Kumar, V., Gormsen, L. C. et al. (2020). Successful prediction of positron emission tomography-imaged metformin hepatic uptake clearance in humans using the quantitative proteomics-informed relative expression factor approach. *Drug Metab Dispos 48*, 1210-1216. doi:10.1124/dmd.120.000156

Sangaraju, D., Katavolos, P., Liang, X. et al. (2022). Establishment of baseline profiles of 50 bile acids in preclinical toxicity species: A comprehensive assessment of translational differences and study design considerations for biomarker development. *Toxicol Appl Pharmacol 443*, 116008. doi:10.1016/j.taap.2022.116008

Schwarz, M. (2004). Pathways and defects of bile acid synthesis: Insights from in vitro and in vivo experimental models. *Drug Discovery Today: Disease Models 1*, 205-212.

Shah, R. and John, S. (2018). Cholestatic jaundice.

Sobczak, M., Fabisiak, A., Murawska, N. et al. (2014). Current overview of extrinsic and intrinsic factors in etiology and progression of inflammatory bowel diseases. *Pharmacol Rep 66*, 766-775. doi:10.1016/j.pharep.2014.04.005

Soroka, C. J., Ballatori, N. and Boyer, J. L. (2010). Organic solute transporter, ostα-ostβ: Its role in bile acid transport and cholestasis. Seminars in liver disease, *© Thieme Medical Publishers 30*, 178-185.

Srivastava, A. (2014). Progressive familial intrahepatic cholestasis. *J Clin Exp Hepatol 4*, 25-36. doi:10.1016/j.jceh.2013.10.005

Strautnieks, S. S., Byrne, J. A., Pawlikowska, L. et al. (2008). Severe bile salt export pump deficiency: 82 different abcb11 mutations in 109 families. *Gastroenterology 134*, 1203-1214. doi:10.1053/j.gastro.2008.01.038

Sundaram, V. and Bjornsson, E. S. (2017). Drug-induced cholestasis. *Hepatol Commun 1*, 726-735. doi:10.1002/hep4.1088

Tabas, L. B. and Dantzig, A. H. (2002). A high-throughput assay for measurement of multidrug resistance protein-mediated transport of leukotriene c4 into membrane vesicles. *Analytical biochemistry 310*, 61-66.

Tarling, E. J., de Aguiar Vallim, T. Q. and Edwards, P. A. (2013). Role of abc transporters in lipid transport and human disease. *Trends Endocrinol Metab 24*, 342-350. doi:10.1016/j.tem.2013.01.006

Ticho, A. L., Malhotra, P., Dudeja, P. K. et al. (2019). Bile acid receptors and gastrointestinal functions. *Liver Res 3*, 31-39. doi:10.1016/j.livres.2019.01.001

van der Mark, V. A., de Waart, D. R., Ho-Mok, K. S. et al. (2014). The lipid flippase heterodimer atp8b1–cdc50a is essential for surface expression of the apical sodium-dependent bile acid transporter (slc10a2/asbt) in intestinal caco-2 cells. *Biochimica et Biophysica Acta (BBA)-Molecular Basis of Disease 1842*, 2378-2386.

van Ginneken, C. A. and Russel, F. G. (1989). Saturable pharmacokinetics in the renal excretion of drugs. *Clin Pharmacokinet 16*, 38-54. doi:10.2165/00003088-198916010-00003

Vilas-Boas, V., Gijbels, E., Cooreman, A. et al. (2019). Industrial, biocide, and cosmetic chemical inducers of cholestasis. *Chem Res Toxicol 32*, 1327-1334. doi:10.1021/acs.chemrestox.9b00148

Vildhede, A., Mateus, A., Khan, E. K. et al. (2016). Mechanistic modeling of pitavastatin disposition in sandwich-cultured human hepatocytes: A proteomics-informed bottom-up approach. *Drug Metab Dispos 44*, 505-516. doi:10.1124/dmd.115.066746

Vinken, M., Landesmann, B., Goumenou, M. et al. (2013). Development of an adverse outcome pathway from drug-mediated bile salt export pump inhibition to cholestatic liver injury. *Toxicol Sci 136*, 97-106. doi:10.1093/toxsci/kft177

Visconti, A., Le Roy, C. I., Rosa, F. et al. (2019). Interplay between the human gut microbiome and host metabolism. *Nature Communications 10*, 1-10. doi:10.1038/s41467-019-12476-z

Vrieze, A., Out, C., Fuentes, S. et al. (2014). Impact of oral vancomycin on gut microbiota, bile acid metabolism, and insulin sensitivity. *J Hepatol 60*, 824-831. doi:10.1016/j.jhep.2013.11.034

Walker, D. I., Uppal, K., Zhang, L. et al. (2016). High-resolution metabolomics of occupational exposure to trichloroethylene. *Int J Epidemiol 45*, 1517-1527. doi:10.1093/ije/dyw218

Wang, J., Bakker, W., Zheng, W. et al. (2022). Exposure to the mycotoxin deoxynivalenol reduces the transport of conjugated bile acids by intestinal caco-2 cells. *Arch Toxicol 96*, 1473-1482. doi:10.1007/s00204-022-03256-8

Wigg, A. J., Roberts-Thomson, I. C., Dymock, R. B. et al. (2001). The role of small intestinal bacterial overgrowth, intestinal permeability, endotoxaemia, and tumour necrosis factor alpha in the pathogenesis of non-alcoholic steatohepatitis. *Gut 48*, 206-211. doi:10.1136/gut.48.2.206

Younossi, Z., Anstee, Q. M., Marietti, M. et al. (2018). Global burden of nafld and nash: Trends, predictions, risk factors and prevention. *Nat Rev Gastroenterol Hepatol 15*, 11-20. doi:10.1038/nrgastro.2017.109

Zhang, J., He, K., Cai, L. et al. (2016). Inhibition of bile salt transport by drugs associated with liver injury in primary hepatocytes from human, monkey, dog, rat, and mouse. *Chem Biol Interact 255*, 45-54. doi:10.1016/j.cbi.2016.03.019

Zhang, J., Lyu, A. and Wang, C. (2023). The molecular insights of bile acids homeostasis in host diseases. *Life Sciences* 121919.

Zhang, N., Wang, J., Bakker, W. et al. (2022). In vitro models to detect in vivo bile acid changes induced by antibiotics. *Arch Toxicol 96*, 3291-3303. doi:10.1007/s00204-022-03373-4

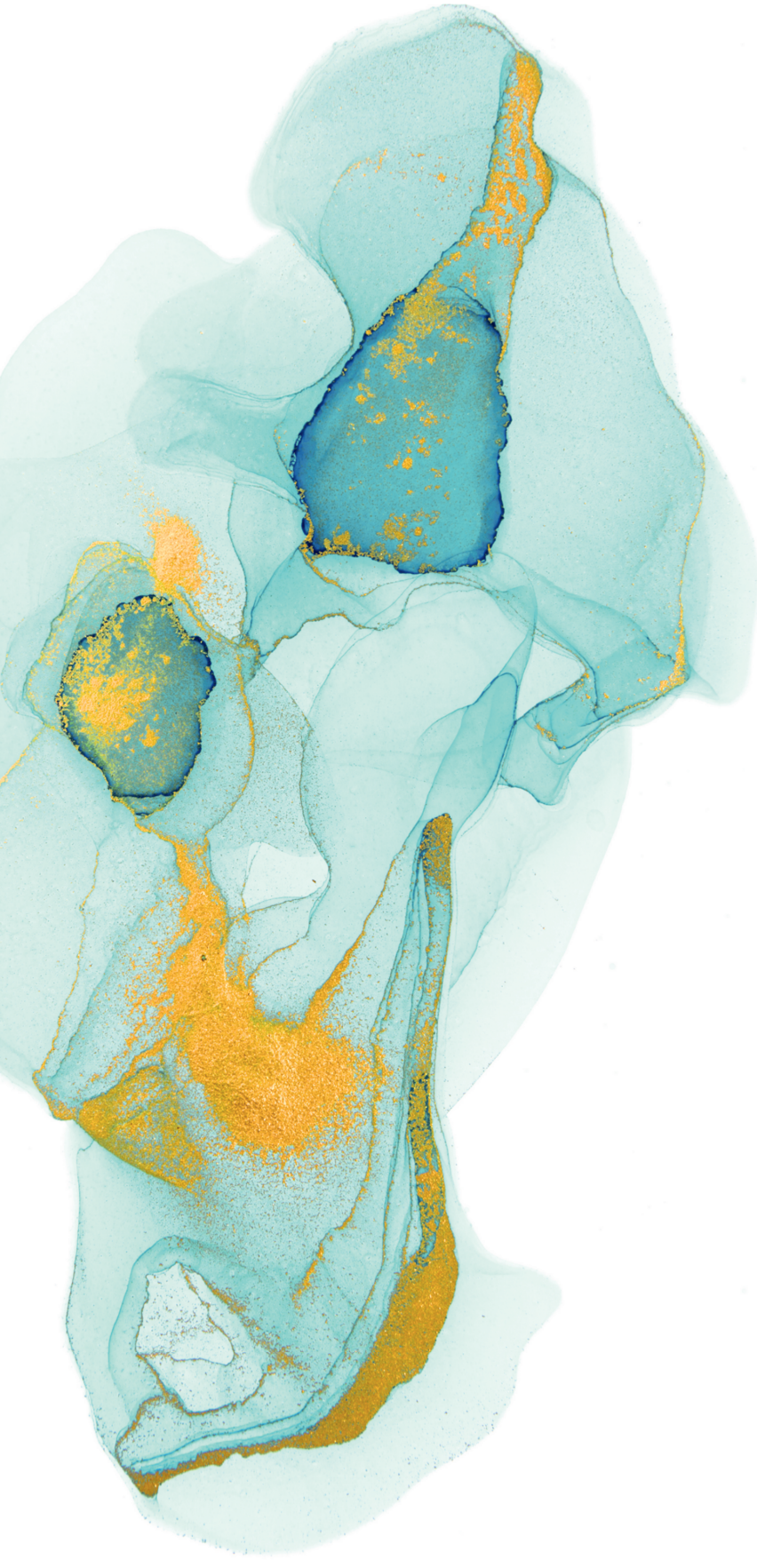

Chapter 2

Hepatic bile acid synthesis and secretion: Comparison of *in vitro* methods

Véronique M.P. de Bruijn, Zhenguo Wang, Wouter Bakker, Weijia Zheng, Bart Spee & Hans Bouwmeester
Published in Toxicology Letters (2022), 365:46-60.

Abstract

Reliable hepatic *in vitro* systems are crucial for the safety assessment of xenobiotics. Certain xenobiotics decrease the hepatic bile efflux, which can ultimately result in cholestasis. Preclinical animal models and the currently available in vitro systems poorly predict a xenobiotic's cholestatic potential. Here, we compared the phenotype and capacity of three liver derived in vitro systems to emulate human functionality to synthesize and secrete bile acids (BAs).

To this end, basal BA production of sandwich cultured human hepatocytes (SCHHs), HepaRG cells (HepaRGs) and hepatocyte-like intrahepatic cholangiocyte organoids (ICO-heps) were analyzed, and the effect of the known BSEP (Bile Salt Export Pump)-inhibitors bosentan and lopinavir on BA disposition in SCHHs and HepaRGs was quantified. RT-qPCR of selected target genes involved in maturation status, synthesis, transport and conjugation of BAs was performed to mechanistically underpin the observed differences in BA homeostasis.

ICO-heps produced a (very) low amount of BAs. SCHHs are a powerful tool in cholestasis-testing due to their high basal BA production and high transporter expression compared to the other models tested. HepaRGs were responsive to both selected BSEP-inhibitors and produced a BA profile that is most similar to the human *in vivo* situation, making them a suitable and practical candidate for cholestasis-testing.

Keywords: Bile acids and salts ● Cholestasis ● New approach methodologies

List of abbreviations: AOP, Adverse Outcome Pathway; BA, bile acid; DILI, drug-induced liver injury; ICO-heps, hepatocyte-like intrahepatic cholangiocyte organoids; KE, key event; KER, key event relationship; LOD, limit of detection, LOQ, limit of quantification; MIE, molecular initiating event; SCHH, sandwich-cultured human hepatocytes, (T/G)CA, (tauro/glyco)cholic acid; T/GCDCA, tauro/glycochenodeoxcholic acid, T/GDCA, tauro/glycodeoxycholic acid; GUDCA, glycoursodeoxycholic acid

2.1 Introduction

Drug-induced liver injury (DILI) is one of the foremost reasons for drug-withdrawal, and has thus large financial consequences for the pharmaceutical industry (van Tonder et al., 2013). Drug-induced cholestasis is a subgroup of DILI and refers to impeded bile flow leading to the accumulation of bile acids (BAs) in the liver and subsequent spillage to the systemic circulation (Noor, 2015). Not only drugs, but also the phytotoxins like pyrrolizidine alkaloids, food additives, and biocides can cause cholestasis (Lu et al., 2021; Vilas-Boas et al., 2019, 2020). Causes of cholestasis range from changes in transporters to hepatocellular or bile canalicular changes as described in an Adverse Outcome Pathway (AOP) (Gijbels et al., 2020). Currently, hepatic safety testing of drugs is performed predominantly by *in vivo* screening. However, animal studies can only predict 50% of human drug induced liver injury, including cholestasis (Olson et al., 2000). Due to the poor predictivity as well as the ethical constraints of animal testing, new approach methodologies (NAMs) to assess the cholestatic potential of xenobiotics are being developed (Deferm et al., 2019). Presently available *in vitro* models detect hardly half of the clinical DILI events (Laverty et al., 2010), hence research is ongoing to design *in vitro* models with higher predictivity. Next, the optimal *in vitro* model would be suitable for long-term culture and not require fresh liver tissue (Ramli et al., 2020; Vinken, 2018).

BAs are the major functional components of bile, and have been known to serve as emulsifiers of dietary lipids and lipid-soluble vitamins in the intestine for a long time. Additionally, BAs are increasingly recognized as important signaling molecules between the gut microbes and the host. BAs are synthesized in the liver *via* cytochrome P450 (CYP)-mediated oxidation of cholesterol. The classical pathway of BA synthesis is initiated by CYP7A1 and the alternative pathway is initiated by CYP27A1 (Axelson et al., 2000). Via various liver enzymatic reactions, ultimately the primary BAs cholic acid (CA) and chenodeoxycholic acid (CDCA) are formed in humans. In the liver, these primary BAs are conjugated with taurine or glycine, resulting in tauro- or glycocholic acid (TCA, GCA) and tauro- or glycochenodeoxycholic acid (TCDCA, GCDCA). Subsequently, BAs are secreted from the liver into the bile canaliculus *via* the canalicular bile salt export pump (BSEP, ABCB11) (Jia et al., 2018). Inhibition of BSEP is a common cause of cholestasis, although inhibition does not necessarily lead to cholestasis and *vice versa* as cholestasis is not always linked with BSEP-inhibition (Gijbels et al., 2019). Recently, an AOP network was established for human hepatotoxicity (Arnesdotter et al., 2021), connecting 14 linear AOPs related to human hepatotoxicity. This network visualizes the complex interaction between biological processes involved in hepatotoxicity and elucidates multiple molecular initiating events (MIE), which rely on a sequence of key events (KEs) linked by key event relationships (KERs), that eventually could lead to hepatotoxicity, or cholestasis more specifically. In the current work, the effect of the known BSEP-inhibitors bosentan and lopinavir on the BA homeostasis was assessed in three different *in vitro* models. Bosentan inhibits BSEP in a non-competitive nature (Fattinger et al., 2001), while lopinavir leads to transcriptional repression of BSEP *via* interaction with farnesoid X receptor (FXR) (Garzel et al., 2014).

Upon secretion to the bile duct, BAs are transported to the intestine, where the gut microbes metabolize BAs to a wide array of primary and secondary BAs (Chiang, 2017; Jia et al., 2018). The BAs are reabsorbed into enterocytes and *via* the portal vein transported back to the liver. This cyclic process of BA secretion into the intestine, reabsorption and return to the liver is called enterohepatic

recycling. Every day, around 90–95% of the intestinal BAs is recycled between the gut and the liver (Chiang, 2009; Dawson et al., 2009). Accordingly, a disturbance of the hepatic BA homeostasis will not only result in a local adverse effect on the liver, but will also distort the gut-liver axis.

Different cell-based systems emulate many liver functions involved in the development of drug-mediated hepatoxicity and are therefore potential powerful *in vitro* models to study cholestasis. Various hepatic *in vitro* systems are available, ranging from simple monolayers to more advanced 3D cultures, using immortalized, primary, or stem cell derived cell sources. Culturing cells in a 3D spheroid configuration provides several benefits over monolayers, such as improved cell viability and phenotypic stability (Bell et al., 2018). Primary human hepatocytes cultured in a spheroid configuration maintain typical hepatocyte functions such as albumin and urea production and glycogen storage over a period of at least 5 weeks (Bell et al., 2016; Messner et al., 2018), and have shown promising for detecting DILI with a predictivity of 69% (Vorrink et al., 2018).

In the current work we compare three different hepatic *in vitro* systems, *i.e.* sandwich cultured human hepatocytes (SCHHs), HepaRG cells in a monolayer configuration (HepaRGs) and hepatocyte-like intrahepatic cholangiocyte organoids in a 3D configuration (ICO-heps). Primary human hepatocytes are typically isolated from resected liver tissue with a two-step collagenase perfusion technique (Hengstler et al., 2000; LeCluyse and Alexandre, 2010). To overcome the limited availability of fresh liver tissue, cryopreserved hepatocytes are commercially available (Hengstler et al., 2000). Upon seeding, primary hepatocytes rapidly lose their typical *in vivo* morphology and differentiation status. When cultured in a sandwich configuration (sandwich cultured human hepatocytes, SCHH), *i.e.* between two layers of extracellular matrix, primary hepatocytes maintain their polarized phenotype for a longer period (Gijbels et al., 2019). The hepatic hepatoma cell line HepaRG is another commonly used *in vitro* tool to study cholestasis. HepaRG cultures consist of two cell populations, one resembling hepatocytes and one resembling cholangiocytes (Kanebratt and Andersson, 2008). Next, organoid models could provide a solution for some of the drawbacks of primary hepatocytes or hepatoma-derived cells. Here, we used intrahepatic cholangiocyte organoids (ICOs) isolated from human biopsies. These are bipotential cells able to differentiate towards the hepatic and cholangiocytic lineage (Marsee et al., 2021). ICOs can be differentiated towards hepatocyte-like cells (ICO-hep) when cultured in differentiation medium, which is deprived of inducers of proliferation such as Rspondin-1 and forskolin (Huch et al., 2015; Schneeberger et al., 2020; Verstegen et al., 2020).

The aim of the current work was to compare three hepatic *in vitro* systems for their ability to emulate human liver functionality to synthesize and secrete BAs. To this end, basal production of 18 BAs by SCHHs, HepaRGs and ICO-heps was measured using LC-MS/MS. qPCR of selected target genes involved in maturation status, BA synthesis, transport and conjugation was performed to mechanistically underpin the observed differences in BA homeostasis. We selected typical hepatocyte markers, *i.e.* albumin (*ALB*) and *CYP3A4*, to evaluate the hepatic lineage of the *in vitro* models (Marsee et al., 2021), and leucine-rich repeat-containing G-protein coupled receptor 5 (*LGR5*) as a stemness marker (Verstegen et al., 2020). The transporters selected were all part of the AOP for cholestasis, and *FXR* was included due to its central role in the regulation of BA homeostasis (Chiang and Ferrell, 2022; Gijbels et al., 2020). *CYP7A1* was selected as it is the rate limiting enzyme in the classical BA synthesis pathway, *CYP27A1* for its crucial role in the alternative BA synthesis pathway and bile acid coenzyme

A:aminoacid N-acyltransferase enzyme (*BAAT*) to explain the differences observed in the conjugation state of the BAs produced by the SCHHs, HepaRGs and ICO-heps (Axelson et al., 2000; Chiang, 2013; Russell, 2003).

2.2 Materials and methods

Chemicals

Lopinavir (CAS 192725–17–0) and bosentan hydrate (CAS 157212–55–0) were purchased from Sigma-Aldrich (Zwijndrecht, the Netherlands). These compounds were dissolved in dimethyl sulfoxide (DMSO) (CAS 67–68–5). DMSO was purchased from Acros Organics (Geel, Belgium). For all cell cultures, we used HBSS, purchased from Gibco (Thermo Fisher Scientific, Paisley, UK) and trypsin-EDTA (trypsin 0.025%/EDTA 0.01%), purchased from Invitrogen (Thermo Fisher Scientific, Breda, the Netherlands).

Cell culture

Cryopreserved primary human hepatocytes (4 × lot HU8317 from one donor, 1 × lot HPP2380204 pooled from 5 donors), plating and cell maintenance supplement pack, FCS were purchased from Thermo Fisher Scientific (Landsmeer, the Netherlands). The plating and maintenance media were prepared in William's E culture medium (Thermo Fisher Scientific). Human hepatocyte thawing medium was obtained from Sigma-Aldrich. Lot HU8317 was obtained from a Caucasian 59-year old male, HPP2380204 contains hepatocytes from 4 females and 1 male, aged 52–69, all Caucasians. Primary human hepatocytes were thawed and plated according to the supplier's protocol. The seeding density was 400,000 cells per well in a 24-wells plate. The hepatocytes were allowed to form a monolayer for 6 h, and then the hepatocytes were overlayed with Matrigel (Corning, New York, NY, USA). The Matrigel was allowed to settle overnight. Hereafter, the cells were washed twice with HBSS and the medium was replaced with hepatocyte maintenance medium containing a solvent control, 50 µM bosentan or 50 µM lopinavir (final DMSO concentration, 0.5% (v/v)). Previous research showed that 24 h exposure to 50 µM of bosentan and lopinavir did not reduce cell viability but decreased endogenous BA accumulation in HepaRGs and sandwich cultured rat hepatocytes, respectively (Burbank et al., 2017; Griffin et al., 2013). 50 µM bosentan did not result in cytotoxicity in sandwich cultured rat hepatocytes (Susukida et al., 2015). We performed a resazurin assay confirming that 24 h exposure to 50 µM lopinavir did not affect HepaRG cell viability, see supplementary material for experimental details and results. The HepaRG cell line was purchased from Biopredic International (Rennes, France). Passages 17–20 were used. The growth medium (GM) was composed of 500 mL William's E culture medium, completed with 5 mL penicillin-streptomycin solution (P/S) and 5 mL L-glutamine, all were purchased from Thermo Fisher Scientific, 0.25 mL 0.05% human insulin (5 µg/mL), 50 mL 10% fetal calf serum (FCS) and 5 mL hydrocortisone-21-hemisuccinate (HCC) (10 mg/mL) were purchased from Sigma-Aldrich. The differentiation medium (DM) was composed of GM with 1.7% (v/v) DMSO. Undifferentiated HepaRG cells were seeded at a density of 200,000 cells per well in a 6-wells plate and differentiated according to the supplier's protocol. Following the differentiation, medium was replaced by serum free medium, to deplete the cells from bovine BAs present in FCS. After 24 h, the cells were washed twice with HBSS and the medium was replaced with serum free medium

containing a solvent control, 50 µM bosentan or 50 µM lopinavir (final DMSO concentration, 0.5% (v/v)). For the establishment of intrahepatic cholangiocytes organoids (ICOs), human liver biopsies were acquired from transplantation residual tissues that were used to ascertain if the liver tissue was healthy prior to transplantation at the Erasmus Medical Center Rotterdam approved by the Medical Ethical Council (MEC 2014–060). Establishment of ICO cultures was performed as follows: Liver biopsies were cut into small pieces and enzymatic dissociation was performed by incubation with type II collagenase (0.125 mg/mL; Gibco, Thermo Fisher Scientific, Waltham, MA, USA) and dispase (0.125 mg/mL; Gibco) in DMEM GlutaMAX (Gibco) containing 0.1 mg/mL DNase I (Roche, Basel, Switzerland), 1% (v/v) FCS (Gibco) and 1% (v/v) P/S (Gibco) at 37 ℃ in a water bath incubator. The supernatant of digested liver biopsies was collected and replaced with fresh enzyme-supplemented medium. Collection of supernatant and replacement with fresh medium was repeated three times. Single cells were collected and washed in cold DMEM GlutaMAX medium containing 1% (v/v) FCS and 1% (v/v) P/S and centrifuged at 400 g for 5 min. The single cells were mixed with cold Matrigel (Corning) and seeded in droplets (50 µL) in a 24 well plate. After Matrigel gelation, expansion medium (EM) was added and cells were incubated at 37 ℃ with 5% CO2 (v/v). The expansion medium was Advanced DMEM/F12 medium (Gibco) supplemented with 1% (v/v) HEPES (10 mM; Gibco), 1% (v/v) P/S, 1% (v/v) GlutaMax (Gibco), 10% (v/v) Rspondin-1 conditioned medium (the Rspon1-Fc-expressing cell line was a kind gift from Calvin J. Kuo), 2% (v/v) B27 supplement without vitamin A (Invitrogen, Carlsbad, CA, USA), 1% (v/v) N2 supplement (Invitrogen), Nicotinamide (10 mM; Sigma-Aldrich, St. Louis, MO, USA), N-acetylcysteine (1.25 mM; Sigma-Aldrich), fibroblast growth factor 10 (100 ng/mL; FGF10; Peprotech, Rocky Hill, NJ, USA), recombinant human (Leu15)-gastrin I (10 nM; GAS; Tocris Bioscience, Bristol, UK), 10 µM forskolin (Tocris Bioscience), epidermal growth factor (50 ng/mL; EGF; Peprotech), hepatocyte growth factor (25 ng/ mL; HGF; Peprotech) and A8301 (5 µM; transforming growth factor b inhibitor; Tocris Bioscience). Organoids were passaged every 7–10 days at ratio of 1:3–1:4 and medium was refreshed every 2–3 days. For the differentiation of ICOs to hepatocyte-like cells (ICO-heps), the BMP7 (25 ng/mL; Peprotech) was added in EM to prime differentiation for 3 days prior to shifting the cells to differentiation medium (DM). The DM was based on Advanced DMEM/F12 containing 1% (v/v) HEPES, 1% (v/v) P/S, 1% (v/v) GlutaMAX, 2% (v/v) B27 supplement without vitamin A, 1% (v/v) N2 supplement, 1.25 mM N-acetylcysteine, 10 nM GAS, 50 ng/mL EGF, 25 ng/mL HGF, 500 nM A8301, fibroblast growth factor 19 (100 ng/mL; FGF19; Peprotech), BMP-7 (25 ng/mL; Peprotech), dexamethasone (30 µM; Sigma-Aldrich) and DAPT (10 µM; Selleckchem, Houston, TX, USA). Organoids were kept in DM for 7 days and medium was refreshed every 2–3 days.

Time-dependent BA synthesis and secretion

Medium and cells were collected to quantify BA content in the different *in vitro* models at different time points. The cost-effectiveness of HepaRGs allowed us to test more different timepoints (0, 4, 24, 48 and 72 h) than was possible for the SCHHs or ICO-heps (0, 24, 48 h). No fresh medium was supplied between the time points in order to avoid a disturbance of the effect of BAs on their own synthesis and secretion. To sample the cells for subsequent analysis, trypsin was used to detach the cells from the plates. Firstly, cells were counted to be used for the normalization of the BA synthesis rate. Next, the cell suspensions were centrifuged for 5 min at 100 g at 4 °C, the supernatant was discarded and

MilliQ was added to lyse the cells in order to measure intracellular BA content. Cell and medium samples were kept for at least 15 min at 4°C and subsequently transferred to -80 °C. If all BA concentrations in the cell or medium samples were below the Limit of Detection (LOD), the samples were lyophilized in a Christ Alpha 1–2 LD plus freeze-dryer and redissolved in methanol. If BA concentrations were sufficiently high and no lyophilization was needed, the samples were mixed with ACN (50:50 v/v). Samples were centrifuged for 15 min at 15,000*g* and the supernatant was transferred to LC-MS/MS vials with inserts, and the BA content in the samples was analysed using LC-MS/MS. For HepaRGs and SCHHs, triplicate measurements were performed in 3 independent experiments. For the SCHHs, we used 2 × one donor and 1 × 5 pooled donors. All 3 measurements were given the same weight in the data analysis, as we did not observe prominent interdonor differences based on the two batches of cells used in the analysis (Supplementary Fig. S2). For the ICO-heps duplicate measurements were performed for 4 different donors.

Bile acid profiling by LC-MS/MS

BA analysis was performed on a triple quadrupole LC-MS/MS system, model LCMS-8050 (Shimadzu Corporation, Japan), which was able to measure 18 BAs: UDCA, HDCA, CDCA, DCA, HCA, CA, GLCA, GUDCA, GDCA, GCDCA, GCA, TUDCA, THDCA, TCDCA, TDCA, TCA, TLCA and LCA. BAs in samples and standards were separated on an Kinetex C18 column (1.7 µm × 100 A × 50 mm × 2.1 mm, Phenomenex 00B-4475AN) using an ultra-high performance liquid chromatography (UHPLC) system (Shimadzu) with gradient elution using MilliQ water (0.01% formic acid) and methanol/acetonitrile (50%v/50%v) as mobile phase A and B, respectively. In order to enhance chromatographic performance, a C18 2.1 mm security guard (Phenomenex AJ0–8782) precolumn was used. Samples were injected (2 µL) onto the column equilibrated in 30% B at a flow rate of 0.4 mL/min. Initially, the mobile phase composition was 30% of B, followed by a linear ramp to 70% of B until 10.0 min. A linear change to 98% of B was executed until 11.0 min, which was held for another 7 min before returning to 30% of B at 19.0 min and remained until 25 min. The column temperature was set at 40 ℃ and the sample tray temperature was set at 4 ℃. The mass spectrometer (MS) used electrospray ionization (ESI) in negative ion mode. The ESI parameters were as below: Nebulizing gas flow, 3 L/minutes; drying gas flow and heating gas flow, 10 L/minutes; Interface temperature, 300 ℃; Desolvation temperature, 526 ℃; heat block temperature, 400 ℃. Selective ion monitoring (SIM) and multiple reaction monitoring (MRM) were used for the detection of the BAs. The LOD was determined as the lowest measurable concentration with a signal-to-noise-ratio larger than 3; limit of quantification (LOQ) was set at the lowest measurable concentration with a signal-to-noise-ratio largen than 10. LODs and LOQs were determined in methanol. Any BA concentration below the LOQ was set to 0 for further analysis. As we observed a matrix effect on the sensitivity of our analytical method, standards for the calibration curve were prepared in the same matrix as the samples. Data were collected and processed using the LabSolutions software (Shimadzu). The MS parameters, LODs, LOQs and an exemplary chromatogram are provided in Supplementary Table S1 and Fig. S1.

RT-qPCR

RNA from HepaRGs, SCHHs and ICOs was isolated, in addition RNA was isolated from three liver biopsies from healthy tissues. The RNA from the three liver biopsies was pooled and used as a reference. RNA from the HepaRGs and ICOs was isolated both after expansion and differentiation. HepaRG RNA was isolated after 14 days of maintenance in GM (HepaRG-GM), and after 14 days maintenance in GM followed by 14 days of differentiation in DM (HepaRG-DM). For the organoids, RNA was isolated after a period of growth in EM (ICOs), and after 7 days of differentiation in DM (ICO-heps). SCHHs RNA was isolated 30–32 h after the Matrigel overlay. RNA was isolated using RNeasy Mini Kit (Qiagen; Hilden, Germany) following the manufacturer's instructions. cDNA synthesis was performed using the iScriptTM cDNA synthesis kit according to the manufacturer's instructions (Bio-Rad, Veenendaal, the Netherlands). RT-qPCR was used to measure the relative gene expression using validated primers (Table B.2) following the SYBR method (Bio-Rad). Normalization was done using the reference genes hypoxanthine-guanine phosphoribosyltransferase 1 (HPRT1), hydroxymethylbilane synthase (HMBS) and ribosomal protein L19 (RPL19). Lastly, relative mRNA levels were calculated and the levels in liver tissue were set to 1. For the organoids, samples from 5 donors were analysed, for HepaRG, 3 independent experiments were performed the cells originate from 1 donor, for SCHH we performed 4 independent experiments (1 donor HU8317).

Data analysis

The R package tidyverse version 1.3 was used for data exploration and visualization (Wickham, 2019). Statistical significance was determined by a one-way ANOVA with a Dunnett/Bonferroni correction for multiple tests. Results were considered statistically significant when $p < .05$. Hierarchical clustering analysis was done in R using the heatmap.2 function from the R package gplots. Ward's clustering method with Euclidean as distance measure was used to compute the dendrograms. All analyses were performed in R version 4.0.2 (R Core Team, 2020). For all in vitro models de novo BA synthesis rate was calculated as $(BA_{medium,t48}+BA_{cells,t48}-BA_{medium,t0}-BA_{cells,t0})/48$. BA synthesis rate was expressed in pmoles/10^6 hepatocytes/h. For the HepaRGs, it was assumed that 50% of the cell population consisted of hepatocytes and 50% of cholangiocytes (Cerec et al., 2007). As a reference, the daily BA synthesis rate of a human liver was calculated based on a synthesis rate of 0.35 mg/g liver/day (Ellis et al., 1998), a hepatocellularity of 139×10^6 hepatocytes/g liver (Sohlenius-Sternbeck, 2006) and 1500 g of liver (Barter et al., 2007). This corresponds to about 240 pmoles/10^6 hepatocytes/h.

2.3 Results

HepaRG cells secrete conjugated primary bile acids

HepaRGs secreted the conjugated primary BAs GCA, TCA, GCDCA and TCDCA (Fig. 1A). The concentrations of the remaining 14 BAs were below the LOQ (See Supplementary Table B.1 for the LOQs of all individual BAs). CDCA conjugates were more abundantly secreted than CA conjugates, with GCDCA being the most abundant BA in the cell culture medium. No unconjugated or secondary BAs were detected in the cells or medium. The amount of intracellular BAs did not change significantly over time, while the total BA pool (cells with medium) significantly increased after 72 h indicating de novo BA synthesis (Fig. 1B). Upon 4 h or 24 h treatment with 50 µM lopinavir or 50 µM bosentan, no

statistically significant alterations were observed in the medium or total BA pool, although a slight but not significant decrease in the medium BA content was observed after 24 h of treatment. The total intracellular BA content, as well as intracellular GCDCA and TCDCA specifically, decreased significantly upon 24 h treatment with bosentan or lopinavir compared to the control (Fig. 2). After both 4 h and 24 h treatment with lopinavir, but not in the control or bosentan-treated cells, a small amount of CDCA was detected in both cells and the medium, however, the respective amount could not be quantified (below LOQ, data not shown).

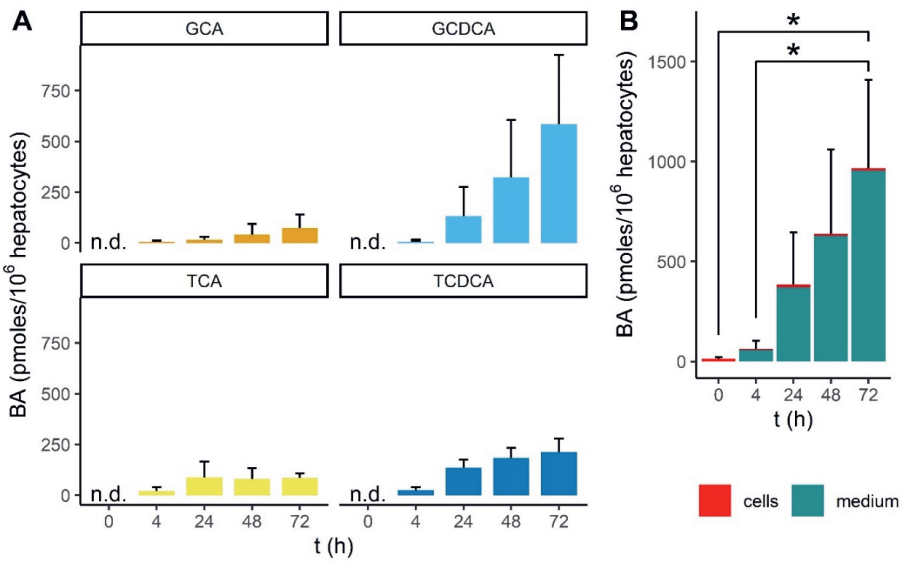

Figure 1 Bile acid content upon incubation of differentiated HepaRG cells in serum-free cell culture medium between 0 and 72h without medium renewal. A) Medium B) Intracellular and medium. Values represent the mean+SD of triplicate measurements in 3 independent experiments. Significance was assessed with a one way ANOVA followed by post hoc tests using Bonferroni's correction. Statistically significant altered bile acid contents are indicated with *. n.d. = not detected (< LOD). T/GCA=tauro/glycocholic acid, T/GCDCA=tauro/glycochenodeoxcholic acid

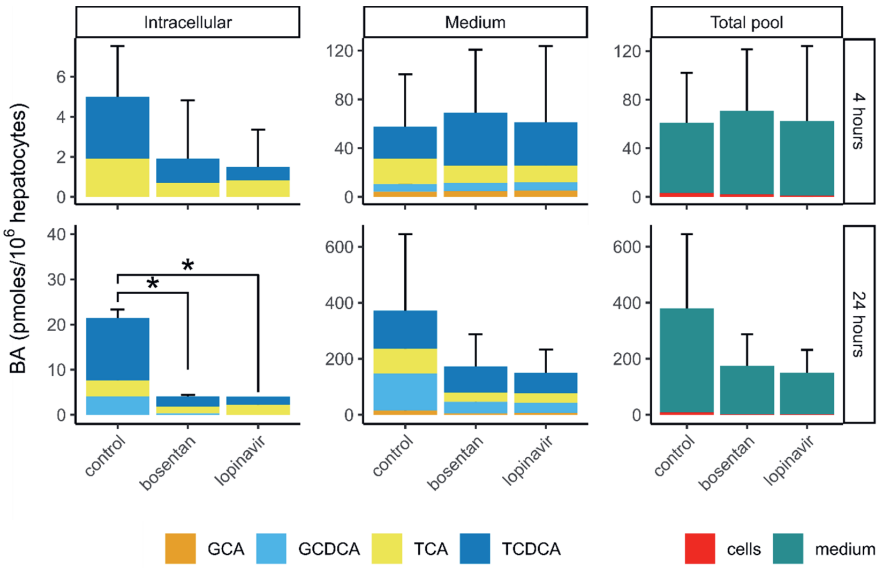

Figure 2 Bile acid content of differentiated HepaRG cells incubated in serum-free cell culture medium upon incubation with a solvent control, 50 µM bosentan or 50 µM lopinavir for 4 or 24 hours. Values represent the mean+SD of triplicate measurements in 3 independent experiments. Significance was assessed with a one way ANOVA followed by post hoc tests using Dunnett's correction.
Statistically significant altered bile acid contents are indicated with *. T/GCA=tauro/glycocholic acid, T/GCDCA=tauro/glycochenodeoxcholic acid.

SCHHs secrete mainly glycine conjugated primary bile acids

Sandwich cultured human hepatocytes (SCHHs) secreted all four conjugated primary BAs known to be present in humans. Glycineconjugates were secreted more abundantly to the medium than taurine-conjugates, with GCA being the most abundant BA in the medium (Fig. 3A). Intracellular BAs did not change over time, but the total BA pool significantly increased after 48 h compared to t = 0 h (Fig. 3B). The bosentan or lopinavir treatment did not induce any significant changes in the total or intracellular BA pool, however, the GCDCA content in the medium was significantly decreased upon lopinavir treatment and TCDCA was detected in the cells in the control, but not after lopinavir or bosentan treatment (Fig. 4). Small amounts of GDCA, TDCA and TCA were detected in the medium after bosentan and lopinavir treatment, however, these amounts could not be quantified (<LOQ, data not shown). TDCA and GDCA were not detected in the control medium (<LOD, data not shown).

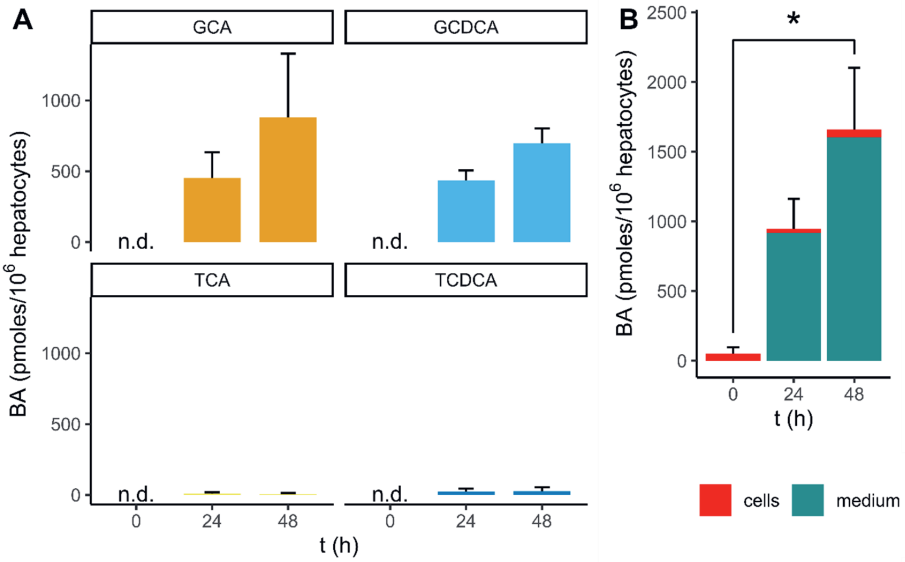

Figure 3 Bile acid content upon incubation of sandwich cultured human hepatocytes in serum-free cell culture medium between 0 and 48h without medium renewal. A) Medium B) Intracellular and medium. Values represent the mean+SD of triplicate measurements in 3 independent experiments. In total 6 different donors were assessed (2x one donor, 1x pooled 5 donors). Significance was assessed with a one way ANOVA followed by post hoc tests using Dunnett's correction. Statistically significant altered bile acid contents are indicated with *. T/GCA=tauro/glycocholic acid, T/GCDCA=tauro/glycochenodeoxcholic acid. n.d. = not detected (< LOD)

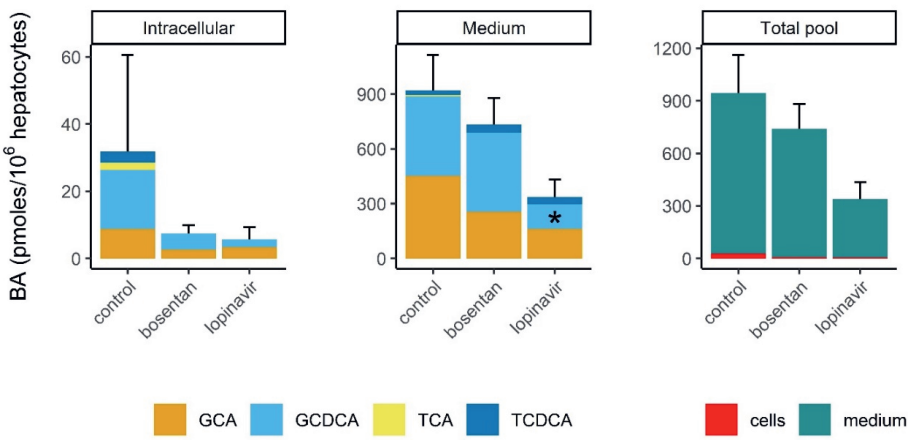

Figure 4 Bile acid content of sandwich cultured human hepatocytes upon 24h incubation with a solvent control, 50 µM bosentan or 50 µM lopinavir. Values represent the mean+SD of triplicate measurements in 3 independent experiments. In total 6 different donors were assessed (2x one donor, 1x pooled 5 donors). Significance was assessed with a one way ANOVA followed by post hoc tests using Dunnett's correction. Statistically significant altered bile acid contents are indicated with *. T/CA=tauro/glycocholic acid, T/GCDCA=tauro/glycochenodeoxcholic acid.

ICO-heps produce a limited amount of bile acids

ICO-heps synthesized and secreted (very) low amounts of BAs. Up until 48 h after medium renewal, all BAs in the medium of ICO-heps were below the LOD (data not shown). After 48 h of incubation, CA and GCA comprised the majority of the secreted BAs. Four different liver biopsy donors were tested, and this resulted in similar BA secretion profiles after 48 h (no statistical differences in the levels of individual BAs between the different donors), see Fig. 5A. Therefore, the results from these different donors were averaged and compared with the other hepatic in vitro systems. Intracellular BA content was below the LOD at all of the tested time points (data not shown).

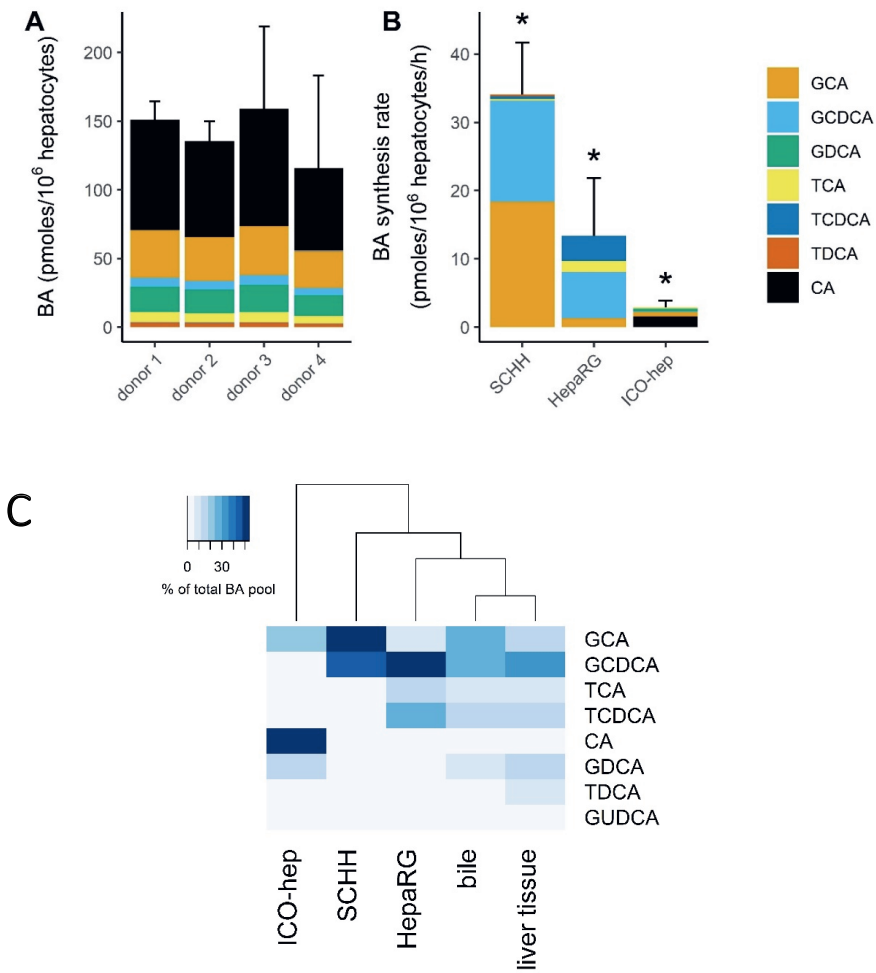

Figure 5 [see next page for caption]

Figure 5A Bile acid secretion to serum-free cell culture medium by hepatocyte-like intrahepatic cholangiocyte organoids (ICO-hep) after 48h without medium renewal. Values represent the mean+SD of duplicate measurements of 4 different donors. B) Comparison of bile acid synthesis rates of sandwich cultured human hepatocytes (SCHH), HepaRGs and ICO-heps. Data presented come from cells originating from 6, 1 and 4 different donors, respectively. Synthesis rates were corrected for intracellular bile acids present at t=0h, see Material & Methods. Significance was assessed with a one way ANOVA followed by post hoc tests using Bonferroni's correction. Statistically significant alterations are indicated with *. C) Hierarchical clustering analysis of bile acid profiles of ICO-heps, SCHH, HepaRG, bile or liver tissue. For the *in vitro* models (ICO-heps, SCHH, HepaRG) bile acid content was quantified in the medium. Bile acid content in bile and liver tissue were derived from literature, as reviewed by Rodrigues (2014). Bile acids were calculated as percentage of the entire pool in the respective tissue/fluid. Only bile acids that were >1% of the total pool were included. (T/G)CA=(tauro/glyco)cholic acid, T/GCDCA=tauro/glycochenodeoxcholic acid, T/GDCA=tauro/glycodeoxycholic acid, GUDCA=glycoursodeoxycholic acid

Comparison of bile acid profiles and synthesis rates

The *de novo* synthesis rate was the highest in SCHHs, followed by HepaRGs and lastly ICO-heps (Fig. 5B). As the BA levels produced by ICO-heps were so low, bosentan's and lopinavir's effect on the BA pool were not assessed. Next, the BA profile secreted by the different hepatic in vitro systems were visualized and compared with human *in vivo* BA profiles in liver tissue and bile using hierarchical clustering analysis (HCA) (Fig. 5C). The human *in vivo* data were obtained from literature (Rodrigues et al., 2014). The HCA revealed a large similarity between the BA profile in bile and liver tissue *in vivo*. The HepaRGs clustered more closely with the *in vivo* bile and liver data than SCHHs and ICO-heps.

Expression of BA transporters is the highest in SCHHs

Differential gene expression of the non-treated *in vitro* models was analyzed by RT-qPCR of samples from organoids, HepaRG and SCHHs. Organoids and HepaRG were analyzed under expansion/growth conditions (ICOs, HepaRG-GM) and differentiation conditions (ICO-heps, HepaRG-DM). The analysis revealed many differences in mRNA levels between the cell types. mRNA levels of enzymes responsible for BA synthesis (CYP7A1 and CYP27A1) were comparable across ICO-heps, HepaRGs and SCHHs. Bile acid-CoA:amino acid N-acyltransferase (BAAT) mRNA levels were the highest in SCHHs followed by HepaRGs. ICOs and ICO-heps showed the lowest BAAT mRNA levels of the models studied (Fig. 6A). Interestingly, mRNA levels of most BA transporters were significantly higher in the SCHHs than in the differentiated HepaRGs and ICOheps, *i.e.* mRNA levels of ATP-binding cassette, sub-family B member 11 (ABCB11, Bile Salt Export Pump (BSEP)), ATP binding cassette subfamily C member 2 (ABCC2, multidrug resistance-associated protein 2 (MRP2)), solute carrier family 10 member 1 (SLC10A1, Na+-taurocholate cotransporting polypeptide (NTCP)), solute carrier organic anion transporter family member 1B1 (SLCO1B1, organic anion transporting polypeptide 1B1 (OATP1B1)) and solute carrier family 51 subunit alpha (SLC51A, organic solute transporter α (OSTα), but not its subunit OSTβ (SLC51B) (Fig. 6B). Stemness of the ICOs before differentiation was indicated by the presence of LGR5. Hepatic markers ALB and CYP3A4 were slightly increased after differentiation (ICO-hep), indicating differentiation towards the hepatocyte lineage (Fig. 6C).

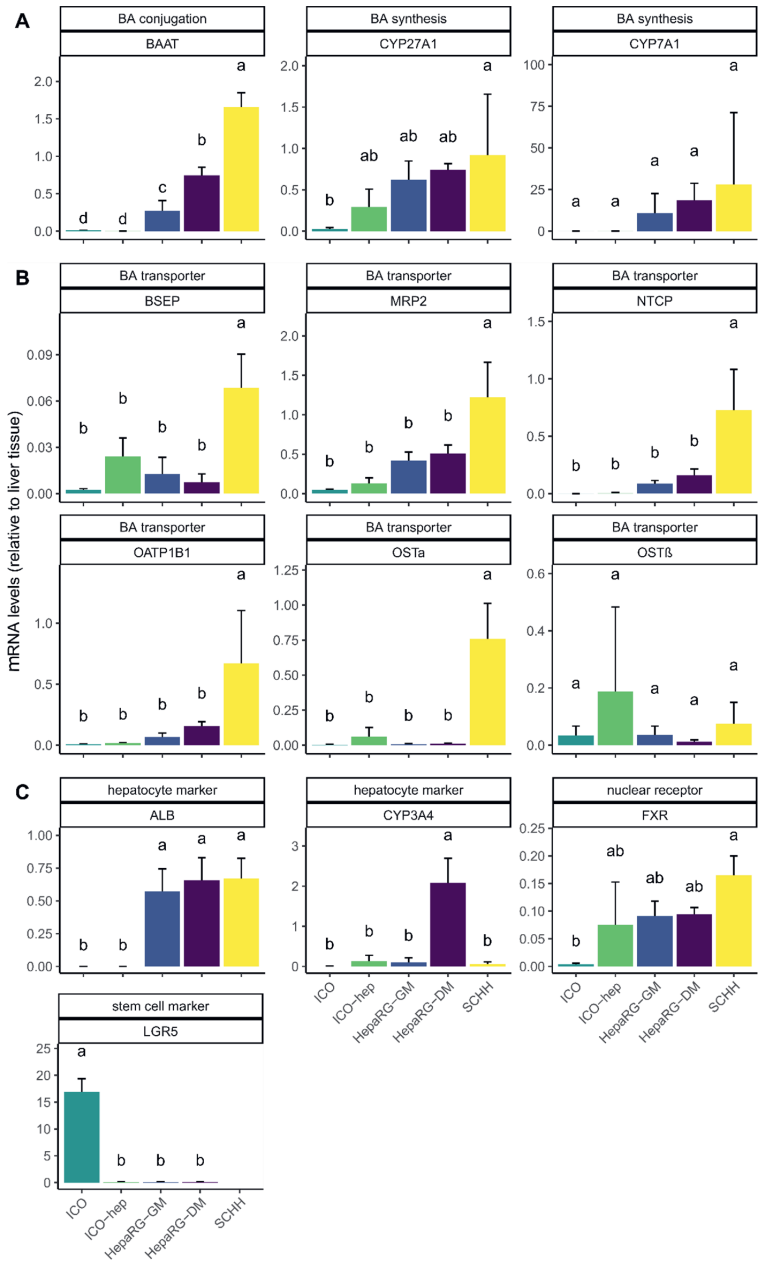

Figure 6 mRNA levels of target genes in organoids under expansion or differentiation conditions (ICO, ICO-hep), HepaRGs under growth or differentiation conditions (HepaRG-GM, HepaRG-DM) and sandwich cultured human hepatocytes (SCHH). mRNA levels in a pooled liver biopsy sample were set to 1 (n=1) as a reference. Data represent mean+SD. Organoids: 5 donors, HepaRG: 3 independent experiments, SCHH: 4 independent experiments, donor HU8317. For details about the target genes, see Table B.1. Groups that share the same letter (a or b) are not statistically significantly different. Significance was assessed with a one way ANOVA followed by post hoc tests using Bonferroni correction. A) enzymes involved in BA synthesis and conjugation, B) BA transporters, C) stem cell/hepatocyte markers

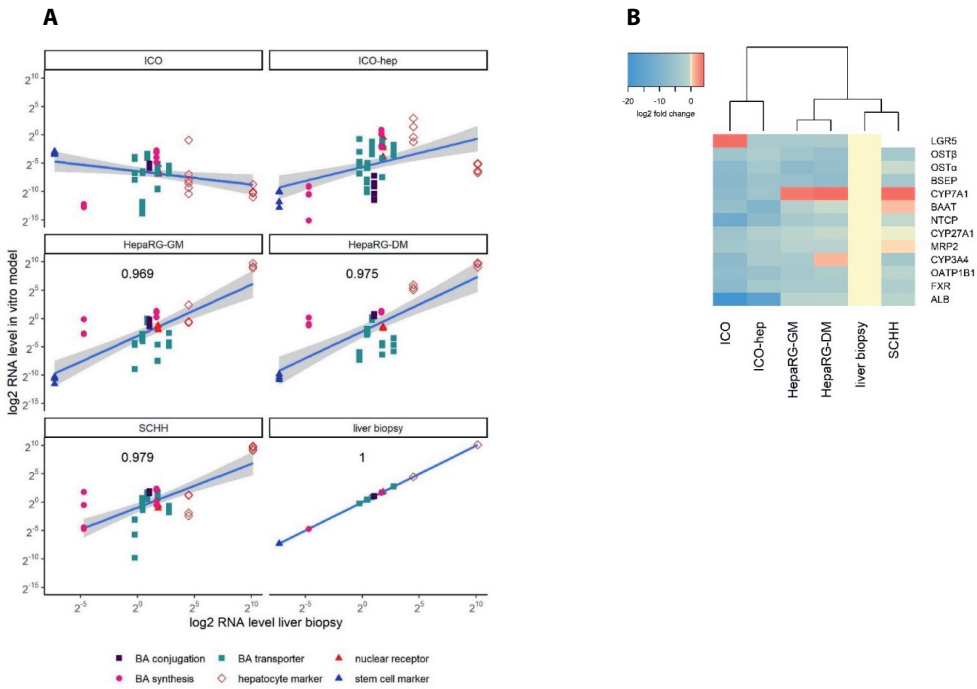

Figure 7 Correlation of mRNA levels of selected target genes between organoids under expansion or differentiation conditions (ICO, ICO-hep), HepaRGs under growth or differentiation conditions (HepaRG-GM, HepaRG-DM) and sandwich cultured human hepatocytes (SCHH). Organoids: 5 donors, HepaRG: 3 independent experiments, SCHH: 4 independent experiments, donor HU8317. For details about the target genes, see Table S1. A) Linear correlation between the in vitro models and liver biopsy. Pearson's correlation coefficient was calculated and shown in the plot if significantly different from 0. B) Hierarchical clustering analysis. Values were normalized to a pooled liver biopsy sample. Missing values are colored white.

The mRNA profiles of SCHHs and HepaRGs are the most similar to a liver biopsy

HepaRG and SCHH mRNA levels show a strong correlation with those obtained for a liver biopsy (Pearson's $r > 0.96$), while there was no statistically significant correlation found between the mRNA levels of the selected target genes in ICOs/ICO-heps and the liver biopsy (Fig. 7A). HCA shows that SCHHs cluster the closest with the liver biopsy, followed by HepaRG-GM/HepaRG-DM, and in line with the correlation analysis, the ICOs/ICO-heps mRNA levels are the most distinctive from the liver biopsy (Fig. 7B).

Table 1 Practical considerations and applicability domain of explored *in vitro* models

	Cell type of origin	Intended cell type(s) after differentiation	Pros	Cons
HepaRG cells	Hepatocellular carcinoma	Hepatocytes and cholangiocytes (~ 50/50)	• Easy *in vitro* proliferation, maintenance and storage • Suitable for long term exposure • Reproducible • Robust	• Tumorigenic phenotype
Hepatocyte-like intrahepatic cholangiocyte organoids (ICO-hep)	Intrahepatic cholangiocyte	Hepatocytes	• Unlimited availability and indefinite proliferation • Allows to study differences between donors	• Low isolation and purification rate
Sandwich cultured human hepatocytes (SCHH)	Hepatocyte	-	• Golden standard • Allows to study differences between donors	• Donor material needed for every experiment

2.4 Discussion

The current study compares the capacity of three different hepatic *in vitro* systems to emulate human liver functionality to synthesize and secrete BAs. BA synthesis rates and profiles, responsiveness to selected BSEP-inhibitors and selected target genes were analysed for: hepatocyte-like intrahepatic cholangiocyte organoids (ICO-heps), sandwich cultured human hepatocytes (SCHH) and HepaRG cells (HepaRGs). The data reveal that differentiated HepaRGs and SCHHs correlate the closest to human liver *in vivo* data at the selected endpoints.

In the current study, we employed organoids derived from biopsies of healthy human liver, and uniquely studied the BA synthesis and secretion capacity. Intrahepatic cholangiocyte organoids were isolated from liver biopsies and differentiated towards hepatocyte-like cells (ICO-heps) (Huch et al., 2015; Schneeberger et al., 2020). An advantage of tissue derived organoids, compared to induced pluripotent stem cells (iPSCs), is that they display high levels of genetic stability and are devoted to their tissue of origin (Prior et al., 2019). As the liver consists of multiple cell types, we evaluated the hepatocyte fate and maturation of the ICO-heps by assessing mRNA levels of stem cell and hepatocyte markers. Significant downregulation of the stem cell marker *LGR5* and increased hepatocyte markers upon differentiation suggests that the ICO-heps were differentiated towards the hepatic lineage. Typical liver functionalities, such as BA synthesis, glycogen storage, phase I and phase II drug metabolism and ammonia detoxification, have previously been identified in ICO-heps (Huch et al., 2015). However, single cell analysis of the human liver revealed a large diversity in cell (sub)types in the biliary tract, including cholangiocytes that express hepatocyte markers, such as *ALB, SERPINA1* and *CYP3A4* (Aizarani et al., 2019). Hence, it remains to be determined whether the ICO-heps used in the

current study had truly differentiated towards a hepatocyte-phenotype, or whether they were cholangiocytes that upregulated some hepatocyte markers and perform BA synthesis.

A major advantage of ICO-heps over HepaRGs is their non-cancerous nature, and ICO-heps require drastically less fresh liver tissue than SCHHs because of their indefinite proliferation capacity *in vitro* (Table 1). Currently, ICOs are explored to be used for mechanistic disease modeling (Nguyen et al., 2021), personalized medicine and drug screening (Broutier et al., 2017), and tissue transplantation (Huch et al., 2015; Reza et al., 2021).

From the three hepatic *in vitro* models tested, the *de novo* BA synthesis rate was the highest in SCHHs (31 ± 7 pmoles/106 hepatocytes/ h), which is higher than the range reported in literature (7–19 pmoles/ 106 hepatocytes/h (Ellis et al., 1998; Sharanek et al., 2015)), but still 7-fold lower than the *in vivo de novo* synthesis rate by the human liver (Ellis et al., 1998; Sohlenius-Sternbeck, 2006). The BA *de novo* synthesis rate and BA profile produced by HepaRGs are consistent with literature (Sharanek et al., 2015). Both HepaRGs and SCHHs secrete, in line with previous reported data, conjugated primary BAs (Behr et al., 2020; Ellis et al., 1998; Sharanek et al., 2015). The most striking difference between the HepaRGs and SCHHs is the predominance of glycine-conjugated BAs secreted by SCHHs (96%), whereas HepaRGs also secrete a substantial amount of tauro-conjugates (42%). This discrepancy between these two models has been previously attributed to the tumour origin of HepaRGs (Sharanek et al., 2015). Compared to the *in vivo* situation the formation of tauro-conjugates by HepaRGs results in a BA profile more similar to the profile in liver and bile than the SCHHs, given that ~30% of BAs in human bile are tauro-conjugates (Rodrigues et al., 2014). The conjugation state of a BA depends on the substrate availability (glycine or L-cysteine, taurine's precursor) (Starokozhko et al., 2017). HepaRGs and SCHHs were both cultivated in William's E medium, hence differences in substrate availability cannot explain this differences in BA composition. The ICO-heps showed the lowest BA synthesis rate and the most distinct BA profile compared to human bile and liver tissue profiles. mRNA levels of *CYP7A1*, the rate limiting enzyme in BA synthesis, were comparable across all three *in vitro* models, but the *BAAT* mRNA levels were significantly lower in the ICO-heps. This provides a plausible explanation for the incomplete BA conjugation by ICO-heps and the subsequent abundancy of CA. We found high *CYP3A4* levels and similar *ALB* and *FXR* levels in HepaRGs compared to SCHHs. Similar results were reported in literature for HepaRGs compared to primary human hepatocytes cultured in suspension (Kanebratt and Andersson, 2008). *CYP3A4* and *BSEP* mRNA levels were low in SCHHs compared to the pooled liver sample (fold change <0.1). A recent study showed that mRNA levels of a number of key hepatocyte genes, including *CYP3A4* and *BSEP*, were drastically reduced in SCHHs on day 2 of culture due to dedifferentiation. The SCHHs can redifferentiate after prolonged culturing (Yang and Li, 2021). Our analysis was performed on day 1, but dedifferentiation provides a plausible explanation for the low *CYP3A4* and *BSEP* RNA levels in the SCHHs compared to the pooled liver sample. mRNA levels of *ALB, CYP7A1 and CYP27A1, BAAT* and the remaining BA transporters, except *OSTβ*, had a fold expression of > 0.5 compared to the pooled liver sample, indicating that the SCHHs had not fully dedifferentiated. Even though *BSEP* mRNA levels were low in SCHHs, we found that mRNA levels of all selected BA transporters, but not *OSTβ*, were significantly lower in HepaRGs than in SCHHs, which is in line with previous results (Susukida, Sekine et al., 2016). Irrespective of the low mRNA levels it has been shown that both HepaRGs and SCHHs have functional BA transporters and are

suitable for BA transport studies (Bachour-El Azzi, Sharanek et al., 2015; De Bruyn et al., 2013; Guguen-Guillouzo and Guillouzo, 2019; Sharanek et al., 2015).

We next studied the responsiveness of the cell systems to a FXR-mediated transcriptional repression of BSEP by lopinavir (Garzel et al., 2014) and direct BSEP inhibition by bosentan (Fattinger et al., 2001) on the BA content in medium and cells. Bosentan exposure did not affect the amount of BAs secreted to the medium by HepaRGs, but resulted in a decrease of intracellular BA content in HepaRGs, confirming previous results (Burbank et al., 2017). The results point towards the presence of a compensatory mechanism to counteract or prevent intrahepatic BA accumulation. This adaptive response is visualized and described in the AOP for cholestasis, and indicates that through activation of the nuclear receptors Farnesoid X receptor (FXR), Pregnane X receptor (PXR) and constitutive androstane receptor (CAR), sinusoidal BA efflux is increased by the upregulation of several ABC-transporters, such as *ABBC3* (MRP3) and *ABCC2* (MRP2), and hepatic BA influx is reduced by a downregulation of *SLC10A1* (NTCP). These mechanisms have been verified for HepaRGs treated with bosentan using qPCR for various BA transporters and immunolabeling of MRP3 (Burbank et al., 2017). Lopinavir treatment resulted in similar changes in BA disposition in HepaRGs as bosentan. Lopinavir's agonistic effect on FXR-activation is expected to repress not only BSEP transcription, but also increase the sinusoidal BA efflux and reduce BA uptake. The observed similar alterations in the BA pool upon exposure of HepaRGs to lopinavir and bosentan, *i.e*. an intracellular BA reduction but no effects on BA secretion to the medium, suggest an at least partially shared mechanism of action between lopinavir and bosentan treatment. In the SCHHs, we have found a decrease in GCDCA medium content upon lopinavir-treatment, which was also found in a study with primary rat hepatocytes (Griffin et al., 2013). Previously, a decrease in GCA and GCDCA content in the cell lysate, and a decrease GCA in the culture medium, have been reported upon 24 h bosentan-treatment with concentrations ranging from 10 to 100 µM in SCHHs (Lepist et al., 2014; Oorts, Van Brantegem et al., 2021), but we could not confirm this. No adverse effect of 24 h treatment with 50 µM bosentan (Burbank et al., 2017) or lopinavir on HepaRG cell viability was observed (current study). An 192 h (8 day) exposure to 50 µM bosentan reduced the viability of spheroid cultures primary human hepatocytes (Hendriks et al., 2016), while 24 h exposure to 50 µM lopinavir or bosentan did not affect the cell viability of sandwich-cultured primary rat hepatocytes (Griffin et al., 2013; Susukida et al., 2015). Therefore, a reduction of cell viability of the human SCHHs following bosentan or lopinavir treatment cannot be fully excluded as a possible explanation for the observed differences in BA disposition in the SCHHs. As ICO-heps showed a low BA production, the applicability of this model to predict the effects of reduced BSEP activity was not assessed.

Collectively, the data reveal important differences in phenotype and BA homeostasis between the three human hepatic *in vitro* systems tested. The BA synthesis rate of SCHHs and HepaRGs is (still) superior to ICO-heps, and also their BA profiles and the mRNA levels of the selected target genes cluster closer together with the human *in vivo* situation than the ICO-heps. While SCHHs have the highest BA synthesis rate and BA transporter expression from the models tested, HepaRGs showed the most *in vivo* like BA profile and responsiveness to the selected BSEP-inhibitory or repressing compounds. By that, HepaRGs provide a powerful and practical *in vitro* model for cholestasis testing.

Funding information Z. Wang and W. Zheng were supported by a scholarship for PhD candidates from the China Scholarship Council (No. 201808620130, No. 202003250128). The authors declare no conflict of interest.

Declaration of Competing Interest The authors declare the following financial interests/personal relationships which may be considered as potential competing interests. Weijia Zheng reports financial support was provided by China Scholarship Council. Zhenguo Wang reports financial support was provided by China Scholarship Council.

Acknowledgements We would like to thank prof.dr.ir. I.M.C.M Rietjens for carefully proof-reading the manuscript. We thank L.H.J. de Haan for her skillful assistance in setting up the cell cultures.

References

Aizarani, N., Saviano, A., Mailly, L., Durand, S., Herman, J.S., Pessaux, P., Grün, D., 2019. A human liver cell atlas reveals heterogeneity and epithelial progenitors. Nature 572 (7768), 199–204.

Arnesdotter, E., Spinu, N., Firman, J., Ebbrell, D., Cronin, M.T., Vanhaecke, T., Vinken, M., 2021. Derivation, characterisation and analysis of an adverse outcome pathway network for human hepatotoxicity. Toxicology 459, 152856.

Axelson, M., Ellis, E., M¨ork, B., Garmark, K., Abrahamsson, A., Bj¨orkhem, I., Einarsson, C., 2000. Bile acid synthesis in cultured human hepatocytes: support for an alternative biosynthetic pathway to cholic acid. Hepatology 31 (6), 1305–1312.

Bachour-El Azzi, P., Sharanek, A., Burban, A., Li, R., Gu´evel, R.L., Abdel-Razzak, Z., Guillouzo, A., 2015. Comparative localization and functional activity of the main hepatobiliary transporters in HepaRG cells and primary human hepatocytes. Toxicol. Sci. 145 (1), 157–168.

Barter, Z.E., Bayliss, M.K., Beaune, P.H., Boobis, A.R., Carlile, D.J., Edwards, R.J., Pelkonen, O.R., 2007. Scaling factors for the extrapolation of in vivo metabolic drug clearance from in vitro data: reaching a consensus on values of human micro-somal protein and hepatocellularity per gram of liver. Curr. Drug Metab. 8 (1), 33–45.

Behr, A.-C., Kwiatkowski, A., Ståhlman, M., Schmidt, F.F., Luckert, C., Braeuning, A., Buhrke, T., 2020. Impairment of bile acid metabolism by perfluorooctanoic acid (PFOA) and perfluorooctanesulfonic acid (PFOS) in human HepaRG hepatoma cells. Arch. Toxicol. 94 (5), 1673–1686. https://doi.org/10.1007/s00204-020-02732-3.

Bell, C.C., Dankers, A.C., Lauschke, V.M., Sison-Young, R., Jenkins, R., Rowe, C., Walker, T., 2018. Comparison of hepatic 2D sandwich cultures and 3D spheroids for long-term toxicity applications: a multicenter study. Toxicol. Sci. 162 (2), 655–666. Retrieved from: 〈https://www.ncbi.nlm.nih.gov/pmc/articles/PMC5888952 /pdf/kfx289.pdf〉

Bell, C.C., Hendriks, D.F., Moro, S.M., Ellis, E., Walsh, J., Renblom, A., Snoeys, J., 2016. Characterization of primary human hepatocyte spheroids as a model system for drug-induced liver injury, liver function and disease. Sci. Rep. 6 (1), 1–13.

Broutier, L., Mastrogiovanni, G., Verstegen, M.M., Francies, H.E., Gavarr´o, L.M., Bradshaw, C.R., Gaspersz, M.P., 2017. Human primary liver cancer–derived organoid cultures for disease modeling and drug screening. Nat. Med. 23 (12), 1424–1435. Retrieved from. 〈 https://www.ncbi.nlm.nih.gov/pmc/articles/PM C5722201/pdf/emss-74480.pdf〉

Burbank, M.G., Sharanek, A., Burban, A., Mialanne, H., Aerts, H., Guguen-Guillouzo, C., Guillouzo, A., 2017. Mechanistic insights in cytotoxic and cholestatic potential of the endothelial receptor antagonists using heparg cells. Toxicol. Sci. 157 (2), 451–464. Retrieved from. 〈https://hal-univ-rennes1.archives-ouvertes.fr/hal-01558815/document〉 .

Cerec, V., Glaise, D., Garnier, D., Morosan, S., Turlin, B., Drenou, B., Corlu, A., 2007. Transdifferentiation of hepatocyte-like cells from the human hepatoma HepaRG cell line through bipotent progenitor. Hepatology 45 (4), 957–967.

Chiang, J., 2013. Bile acid metabolism and signaling. Compr. Physiol. 3, 1191–1212 (Link). 〈https://goo.gl/dC6DBB〉.

Chiang, J.Y., 2009. Bile acids: regulation of synthesis. J. lipidres. 50 (10).

Chiang, J.Y., 2017. Bile acid metabolism and signaling in liver disease and therapy. Liver Res. 1 (1), 3–9. Retrieved from. 〈https://www.ncbi.nlm.nih.gov/pmc/articles/PMC5663306/pdf/nihms881361.pdf〉.

Chiang, J.Y., Ferrell, J.M., 2022. Discovery of farnesoid X receptor and its role in bile acid metabolism. Mol. Cell. Endocrinol., 111618

Dawson, P.A., Lan, T., Rao, A., 2009. Bile acid transporters. J. Lipid Res. 50 (12), 2340–2357.

De Bruyn, T., Chatterjee, S., Fattah, S., Keemink, J., Nicolaï, J., Augustijns, P., Annaert, P., 2013. Sandwich-cultured hepatocytes: utility for in vitro exploration of hepatobiliary drug disposition and drug-induced hepatotoxicity. Expert Opin. Drug Metab. Toxicol. 9 (5), 589–616.

Deferm, N., De Vocht, T., Qi, B., Van Brantegem, P., Gijbels, E., Vinken, M., Annaert, P., 2019. Current insights in the complexities underlying drug-induced cholestasis. Crit. Rev. Toxicol. 49 (6), 520–548. 〈https://www.tandfonline.com/doi/full/10.1080/10 408444.2019.1635081〉.

Ellis, E., Goodwin, B., Abrahamsson, A., Liddle, C., Mode, A., Rudling, M., Einarsson, C., 1998. Bile acid synthesis in primary cultures of rat and human hepatocytes. Hepatology 27 (2), 615–620. https://doi.org/10.1002/hep.510270241.

Fattinger, K., Funk, C., Pantze, M., Weber, C., Reichen, J., Stieger, B., Meier, P.J., 2001. The endothelin antagonist bosentan inhibits the canalicular bile salt export pump: a potential mechanism for hepatic adverse reactions. Clin. Pharmacol. Ther. 69 (4), 223–231. https://doi.org/10.1067/mcp.2001.114667.

Garzel, B., Yang, H., Zhang, L., Huang, S.-M., Polli, J.E., Wang, H., 2014. The role of bile salt export pump gene repression in drug-induced cholestatic liver toxicity. Drug Metab. Dispos. 42 (3), 318–322. 〈https://www.ncbi.nlm.nih.gov/pmc/articles/PMC3935137/pdf/dmd.113.054189.pdf〉.

Gijbels, E., Vilas-Boas, V., Deferm, N., Devisscher, L., Jaeschke, H., Annaert, P., Vinken, M., 2019. Mechanisms and in vitro models of drug-induced cholestasis. Arch. Toxicol. 93 (5), 1169–1186. https://doi.org/10.1007/s00204-019-02437-2.

Gijbels, E., Vilas-Boas, V., Annaert, P., Vanhaecke, T., Devisscher, L., Vinken, M., 2020. Robustness testing and optimization of an adverse outcome pathway on cholestatic liver injury. Arch. Toxicol. 1–22.

Griffin, L.M., Watkins, P.B., Perry St., C.H., Claire, R.L., Brouwer, K.L.R., 2013. Combination lopinavir and ritonavir alter exogenous and endogenous bile acid disposition in sandwich-cultured rat hepatocytes. Drug Metab. Dispos. 41 (1), 188. https://doi.org/10.1124/dmd.112.047225.

Guguen-Guillouzo, C., Guillouzo, A., 2019. Setup and use of HepaRG cells in cholestasis research. In: Vinken, M. (Ed.), Experimental Cholestasis Research. Springer New York, New York, NY, pp. 291–312.

Hendriks, D.F., Fredriksson Puigvert, L., Messner, S., Mortiz, W., Ingelman-Sundberg, M., 2016. Hepatic 3D spheroid models for the detection and study of compounds with cholestatic liability. Sci. Rep. 6, 35434. https://doi.org/10.1038/srep35434.

Hengstler, J.G., Utesch, D., Steinberg, P., Platt, K., Diener, B., Ringel, M., Gerl, M., 2000. Cryopreserved primary hepatocytes as a constantly available in vitro model for the evaluation of human and animal drug metabolism and enzyme induction. Drug Metab. Rev. 32 (1), 81–118.

Huch, M., Gehart, H., Van Boxtel, R., Hamer, K., Blokzijl, F., Verstegen, M.M., de Ligt, J., 2015. Long-term culture of genome-stable bipotent stem cells from adult human liver. Cell 160 (1–2), 299–312. Retrieved from.

Jia, W., Xie, G., Jia, W., 2018. Bile acid-microbiota crosstalk in gastrointestinal inflammation and carcinogenesis. Nat. Rev. Gastroenterol. Hepatol. 15 (2), 111–128. https://doi.org/10.1038/nrgastro.2017.119.

Kanebratt, K.P., Andersson, T.B., 2008. Evaluation of HepaRG cells as an in vitro model for human drug metabolism studies. Drug Metab. Dispos. 36 (7), 1444–1452. 〈https ://dmd.aspetjournals.org/content/36/7/1444.long〉.

Laverty, H.G., Antoine, D.J., Benson, C., Chaponda, M., Williams, D., Park, B.K., 2010. The potential of cytokines as safety biomarkers for drug-induced liver injury. Eur. J. Clin. Pharmacol. 66 (10), 961–976.

LeCluyse, E.L., Alexandre, E., 2010. Isolation and culture of primary hepatocytes from resected human liver tissue. Hepatocytes. Springer,, pp. 57–82.

Lepist, E.-I., Gillies, H., Smith, W., Hao, J., Hubert St., C., Claire III, R.L., Ray, A.S., 2014. Evaluation of the endothelin receptor antagonists ambrisentan, bosentan, macitentan, and sitaxsentan as hepatobiliary transporter inhibitors and substrates in sandwich-cultured human hepatocytes. PLOS ONE 9 (1), e87548. Retrieved from. 〈 https://www.ncbi.nlm.nih.gov/pmc/articles/PMC3907537/pdf/pone.0087548.pdf 〉.

Lu, S., Zhang, J., Lin, S., Zheng, D., Shen, Y., Qin, J., Wang, S., 2021. Recent advances in the development of in vitro liver models for hepatotoxicity testing. Bio-Des. Manuf. 4 (4), 717–734.

Marsee, A., Roos, F.J., Verstegen, M.M., Roos, F., Verstegen, M., Clevers, H., Peng, W.C., 2021. Building consensus on definition and nomenclature of hepatic, pancreatic, and biliary organoids. Cell Stem Cell 28 (5), 816–832.

Messner, S., Fredriksson, L., Lauschke, V.M., Roessger, K., Escher, C., Bober, M., Moritz, W., 2018. Transcriptomic, proteomic, and functional long-term characterization of multicellular three-dimensional human liver microtissues. Appl. Vitr. Toxicol. 4 (1), 1–12.

Nguyen, L., Jager, M., Lieshout, R., de Ruiter, P.E., Locati, M.D., Besselink, N., de Jonge, J., 2021. Precancerous liver diseases do not cause increased mutagenesis in liver stem cells. Commun. Biol. 4 (1), 1–9.

Noor, F., 2015. A shift in paradigm towards human biology-based systems for cholestaticliver diseases. J. Physiol. 593 (23), 5043–5055. https://doi.org/10.1113/JP271124.

Olson, H., Betton, G., Robinson, D., Thomas, K., Monro, A., Kolaja, G., Bracken, W., 2000. Concordance of the toxicity of pharmaceuticals in humans and in animals. Regul. Toxicol. Pharmacol. 32 (1), 56–67.

Oorts, M., Van Brantegem, P., Deferm, N., Chatterjee, S., Dreesen, E., Cooreman, A., Annaert, P., 2021. Bosentan alters endo-and exogenous bile salt disposition in sandwich-cultured human hepatocytes. J. Pharmacol. Exp. Ther. 379 (1), 20–32.

Prior, N., Inacio, P., Huch, M., 2019. Liver organoids: from basic research to therapeutic applications. Gut 68 (12), 2228–2237. Retrieved from. 〈https://gut.bmj.com/cont ent/gutjnl/68/12/2228.full.pdf〉.

R Core Team , 2020. R: A language and environment for statistical computing. Vienna, Austria: R Foundation for Statistical Computing. Retrieved from 〈https://www. R-project.org/〉.

Ramli, M.N.B., Lim, Y.S., Koe, C.T., Demircioglu, D., Tng, W., Gonzales, K.A.U., Soe, E.L., 2020. Human pluripotent stem cell-derived organoids as models of liver disease. Gastroenterology 159 (4), 1471–1486 e1412. 〈https://www.gastrojournal. org/article/S0016-5085(20)34762-4/pdf〉.

Reza, H.A., Okabe, R., Takebe, T., 2021. Organoid transplant approaches for the liver. Transpl. Int. 34 (11), 2031–2045.

Rodrigues, Lai, Y., Cvijic, M.E., Elkin, L.L., Zvyaga, T., Soars, M.G., 2014. Drug-induced perturbations of the bile acid pool, cholestasis, and hepatotoxicity: mechanistic considerations beyond the direct inhibition of the bile salt export pump. Drug Metab. Dispos. 42 (4), 566. https://doi.org/10.1124/dmd.113.054205.

Russell, D.W., 2003. The enzymes, regulation, and genetics of bile acid synthesis. Annu. Rev. Biochem. 72 (1), 137–174.
Schneeberger, K., S´anchez-Romero, N., Ye, S., van Steenbeek, F.G., Oosterhoff, L.A., Pla Palacin, I., Spee, B., 2020. Large-scale production of LGR5-positive bipotential human liver stem cells. Hepatology. https://doi.org/10.1002/hep.31037.
Sharanek, A., Burban, A., Humbert, L., Bachour-El Azzi, P., Felix-Gomes, N., Rainteau, D., Guillouzo, A., 2015. Cellular accumulation and toxic effects of bile acids in cyclosporine a-treated hepaRG hepatocytes. Toxicol. Sci. 147 (2), 573–587. https://doi.org/10.1093/toxsci/kfv155. Sohlenius-Sternbeck, A.-K., 2006. Determination of the hepatocellularity number for human, dog, rabbit, rat and mouse livers from protein concentration measurements. Toxicol. Vitr. 20 (8), 1582–1586.
Starokozhko, V., Greupink, R., van de Broek, P., Soliman, N., Ghimire, S., de Graaf, I.A. M., Groothuis, G.M.M., 2017. Rat precision-cut liver slices predict drug-induced cholestatic injury. Arch. Toxicol. 91 (10), 3403–3413. https://doi.org/10.1007/ s00204-017-1960-7.
Susukida, T., Sekine, S., Nozaki, M., Tokizono, M., Ito, K., 2015. Prediction of the clinical risk of drug-induced cholestatic liver injury using an in vitro sandwich cultured hepatocyte assay. Drug Metab. Dispos. 43 (11), 1760–1768. Retrieved from. 〈https: //dmd.aspetjournals.org/content/43/11/1760.long.
Susukida, T., Sekine, S., Nozaki, M., Tokizono, M., Oizumi, K., Horie, T., Ito, K., 2016. Establishment of a drug-induced, bile acid–dependent hepatotoxicity model using HepaRG cells. J. Pharm. Sci. 105 (4), 1550–1560. Retrieved from. 〈https://www.sci encedirect.com/science/article/pii/S0022354916003099?via%3Dihub〉.
van Tonder, J.J., Steenkamp, V., Gulumian, M., 2013. Pre-clinical assessment of the potential intrinsic hepatotoxicity of candidate drugs. New Insights into Toxicity and Drug Testing. IntechOpen.
Verstegen, M.M., Roos, F.J., Burka, K., Gehart, H., Jager, M., de Wolf, M., van Huizen, N. A., 2020. Human extrahepatic and intrahepatic cholangiocyte organoids show region-specific differentiation potential and model cystic fibrosis-related bile duct disease. Sci. Rep. 10 (1), 1–16.
Vilas-Boas, V., Gijbels, E., Cooreman, A., Van Campenhout, R., Gustafson, E., Leroy, K., Vinken, M., 2019. Industrial, biocide, and cosmetic chemical inducers of cholestasis. Chem. Res. Toxicol. 32 (7), 1327–1334. Retrieved from. 〈https://www.ncbi.nlm.nih. gov/pmc/articles/PMC7176485/pdf/EMS86148.pdf〉.
Vilas-Boas, V., Gijbels, E., Jonckheer, J., De Waele, E., Vinken, M., 2020. Cholestatic liver injury induced by food additives, dietary supplements and parenteral nutrition. Environ. Int. 136, 105422 https://doi.org/10.1016/j.envint.2019.105422.
Vinken, M., 2018. In vitro prediction of drug-induced cholestatic liver injury: a challenge for the toxicologist. Arch. Toxicol. 92 (5), 1909–1912.
Vorrink, S.U., Zhou, Y., Ingelman-Sundberg, M., Lauschke, V.M., 2018. Prediction of drug-induced hepatotoxicity using long-term stable primary hepatic 3D spheroid cultures in chemically defined conditions. Toxicol. Sci. 163 (2), 655–665.
Wickham, R., 2019. tidyverse: Easily Install and Load the 'Tidyverse'. R package (Version version 1.3.0). Retrieved from 〈https://CRAN.R-project.org/package=tidyverse〉.
Yang, Q., Li, A.P., 2021. Messenger RNA expression of albumin, transferrin, transthyretin, asialoglycoprotein receptor, cytochrome P450 isoform, uptake transporter, and efflux transporter genes as a function of culture duration in prolonged cultured cryopreserved human hepatocytes as collagen-matrigel sandwich cultures: evidence for redifferentiation upon prolonged culturing. Drug Metab. Dispos. 49 (9), 790–802.

2.5 Supplementary information

Cell viability The effect of lopinavir on the cell viability of the HepaRG cells was determined *via* the Resazurin assay. Resazurin sodium salt (CAS 62758–13–8) was purchased from Merck (Darmstadt, Germany). 560 µM resazurin was dissolved in PBS, sterilized and stored in the dark at 4 °C. 96 wells plates with fully differentiated HepaRGs were exposed to 0–150 µM lopinavir for 24 h. Next, 10% v/v resazurin was added to the HepaRG cells. The plates were incubated at 37 °C for 4 h, protected from direct light. Fluorescence was measured using the SpectraMax® iD3 from Molecular Devices. The excitation wavelength was set on 560 nm and the emission wavelength on 590 nm.

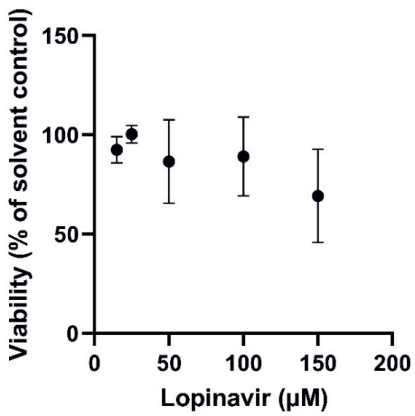

Fig. S1. Cell viability of HepaRGs upon 24 h treatment with different concentrations of lopinavir assessed using the resazurin assay. Values represent the mean±SD of triplicate measurements in 3 independent experiments.

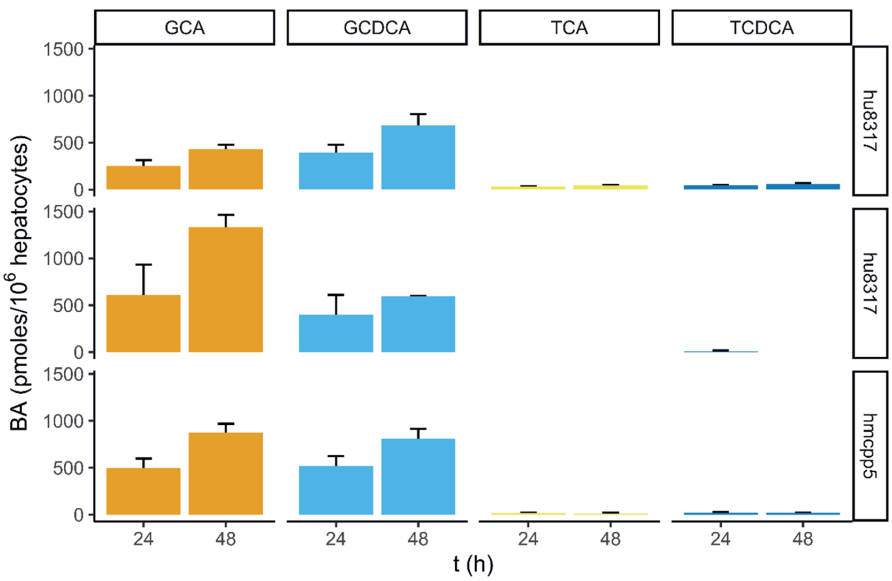

Figure S2 Bile acid content upon incubation of sandwich cultured human hepatocytes in serum-free cell culture medium between 0 and 48h without medium renewal. Each row represents the mean+sd of one biological replicate, measured in triplicate.

Table S1 MS parameters, limit of detection (LOD) and limit of quantification (LOQ) of the BAs studied.

	Mode	Q1	Q3	Retention time (min)	LOD (nM) in MeOH	LOQ (nM) in MeOH
Lithocholic acid (LCA)	SIM		375.3	12.75	10	20
Ursodeoxycholic acid (UDCA)	SIM		391.3	8.398	40	50
Hyodeoxycholic acid (HDCA)	SIM		391.3	8.889	40	50
Chenodeoxycholic acid (CDCA)	SIM		391.3	10.81	30	50
Deoxycholic acid (DCA)	SIM		391.3	11.07	5	10
Hyocholic acid (HCA)	SIM		407.3	8.145	20	30
Cholic acid (CA)	SIM		407.3	8.942	5	10
Glycolithocholic acid (GLCA)	MRM	432.3	74	11.09	5	5
Glycoursodeoxycholic acid (GUDCA)	MRM	448.3	74	6.590	5	5
Glycochenodeoxycholic acid (GCDCA)	MRM	448.3	74	9.051	5	5
Glycodeoxycholic acid (GDCA)	MRM	448.3	74	9.452	10	20
Glycocholic acid (GCA)	MRM	464.3	74	7.310	5	5
Taurolithocholic acid (TLCA)	SIM		482.3	11.08	5	10
Tauroursodeoxycholic acid (TUDCA)	SIM		498.4	6.189	5	10
Taurohyodeoxycholic acid (THDCA)	SIM		498.4	6.530	5	10
Taurochenodeoxycholic acid (TCDCA)	SIM		498.4	8.825	5	10
Taurodeoxycholic acid (TDCA)	SIM		498.4	9.283	10	20
Taurocholic acid (TCA)	SIM		514.4	7.001	5	5

SIM: Single Ion Monitoring; MRM: Multiple Reaction Monitoring; Q1: first stage MS, Q3: second stage MS; LOD: limit of detection; LOQ: limit of quantification

Table S2 List of Primers used in RT-qPCR analysis

Protein name	Symbol	Gene symbol	Forward primer	Reverse primer
Bile Salt Export Pump	BSEP	*ABCB11*	GTCATCTTGTGCTTCTTCCC	TCATTTGTAATCTGTCCCACCA
Multidrug Resistance-associated Protein 2	MRP2	*ABCC2*	GCCAACTTGTGGCTGTGATAGG	ATCCAGGACTGCTGTGGGACAT
Albumin	ALB	*ALB*	GTTCGTTACACCAAGAAAGTACC	GACCACGGATAGATAGTCTTCTG
Bile acid-CoA:amino acid N-acyltransferase	BAAT	*BAAT*	GAGGCTGCCAACTTTCTCCT	AGTACCGTGGCTGTGACTTG
Cytochrome P450 27A1	CYP27A1	*CYP27A1*	AGGCCAAGTACGGTCCAATG	GTACCAGTGGTGTCCTTCCG
Cytochrome P450 3A4	CYP3A4	*CYP3A4*	TTTTGTCCTACCATAAGGGCTTT	CACAGGCTGTTGACCATCAT
Cytochrome P450 7A1	CYP7A1	*CYP7A1*	TAAGGTGTTGTGCCACGGAA	TCCATCCATCGGGTCAATGC
Hydroxymethylbilane synthase	HMBS	*HMBS*	GGCAATGCGGCTGCAA	GGGTACCCACGCGAATCAC
Hypoxanthine phosphoribosyltransferase 1	HPRT1	*HPRT1*	TATTGTAATGACCAGTCAACAG	GGTCCTTTTCACCAGCAAG
Leucine rich repeat containing G protein-coupled receptor 5	LGR5	*LGR5*	GCAGTGTTCACCTTCCC	GGTCCACACTCCAATTCTG
Farnesoid X receptor	FXR	*NR1H4*	AGGTAGCAGAGATGCCTGTAACAA	CACAGCTCATCCCCTTTGATC
Ribosomal protein L19	RPL19	*RPL19*	ATGAGTATGCTCAGGCTTCAG	GATCAGCCCATCTTTGATGAG
Na+-taurocholate cotransporting polypeptide	NTCP	*SLC10A1*	GATATCACTGGTGGTTCTC	ATCATCCCTCCCTTGATGAC
Organic solute transporter-α subunit	OSTα	*SLC51A*	TTGTTCGCCTCCCTATTCC	TTGTGGTCTTTCCTTCGGT
Organic solute transporter-β subunit	OSTβ	*SLC51B*	TGTGGTGGTCATTATAAGCATGG	TCTTAGGTTGTTTAGGCTGTTGTG
Organic anion transporting polypeptide 1B1	OATP1B1	*SLCO1B1*	GAGCAACAGTATGGTCAGCCT	GGCAATTCCAACGGTGTTCA

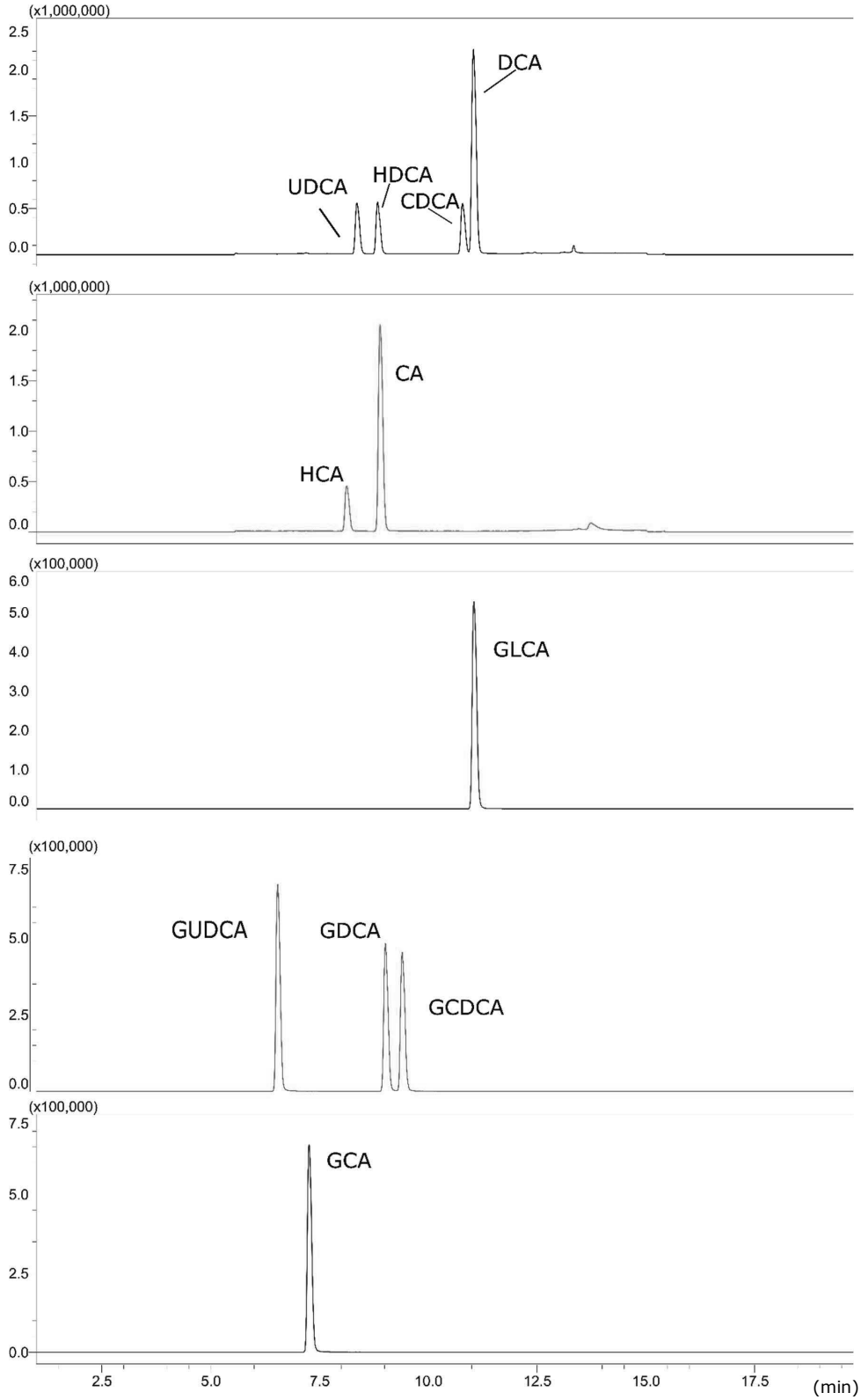
(x1,000,000)
2.5
2.0
1.5
1.0
0.5
0.0
DCA
UDCA
HDCA
CDCA
(x1,000,000)
2.0
1.5
1.0
0.5
0.0
CA
HCA
(x100,000)
6.0
5.0
4.0
3.0
2.0
1.0
0.0
GLCA
(x100,000)
7.5
5.0
2.5
0.0
GUDCA
GDCA
GCDCA
(x100,000)
7.5
5.0
2.5
0.0
GCA
2.5
5.0
7.5
10.0
12.5
15.0
17.5
(min)

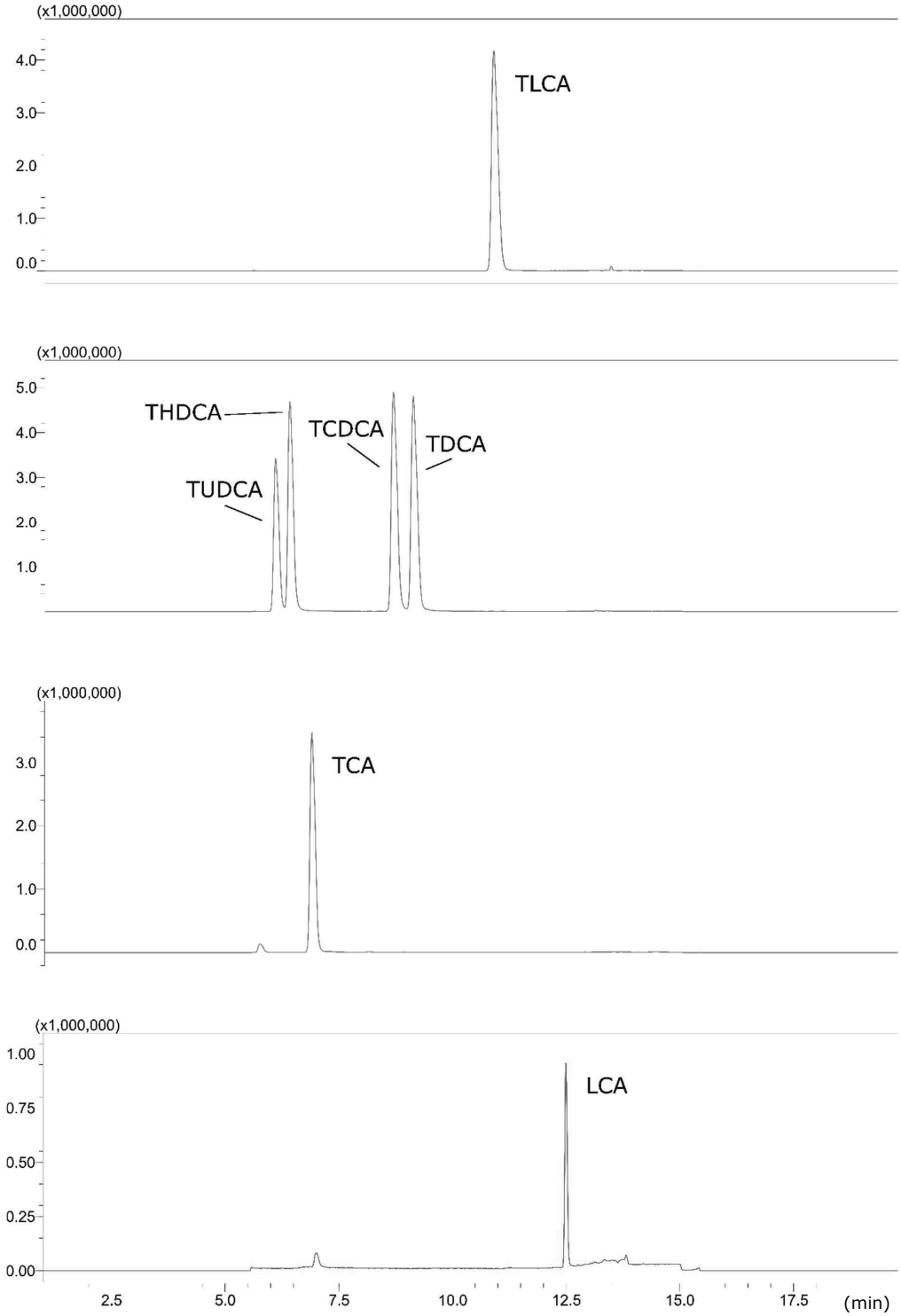

Fig. S3 Chromatograms of LC-MS/MS run. 1 µM of a mixture of 18 BAs in MeOH. Abbreviations, MS parameters and LOD are present

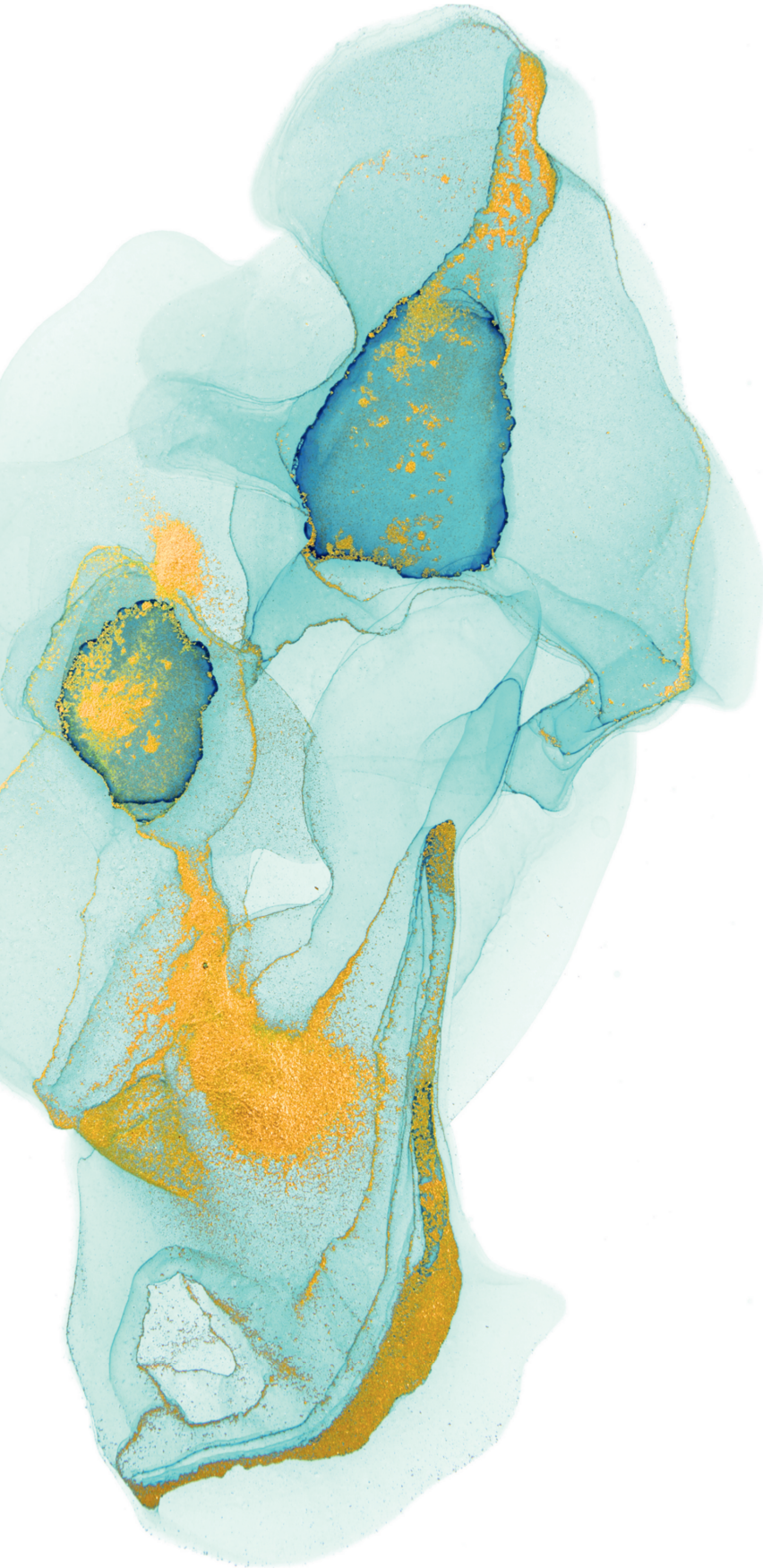

Chapter 3

Population pharmacokinetic model to generate mechanistic insights in bile acid homeostasis and drug-induced cholestasis

Véronique M. P. de Bruijn, Ivonne M. C. M. Rietjens & Hans Bouwmeester
Published in Archives of Toxicology (2022) 96(10): 2717-2730.

Abstract

Bile acids (BA) fulfill a wide range of physiological functions, but are also involved in pathologies, such as cholestasis. Cholestasis is characterized by an intrahepatic accumulation of BAs and subsequent spillage to the systemic circulation. The aim of the present study was to develop physiologically based kinetic (PBK) models that would provide a tool to predict dose-dependent BA accumulation in humans upon treatment with a Bile Salt Export Pump (BSEP) inhibitor. We developed a PBK model describing the BA homeostasis using glycochenodeoxycholic acid as an exemplary BA. Population wide distributions of BSEP abundances were incorporated in the PBK model using Markov Chain Monte Carlo simulations, and alternatively the total amount of BAs was scaled empirically to describe interindividual diferences in plasma BA levels. Next, the effects of the BSEP inhibitor bosentan on the BA levels were simulated. The PBK model developed adequately predicted the in vivo BA dynamics. Both the Markov Chain Monte Carlo simulations based on a distribution of BSEP abundances and empirical scaling of the total BA pool readily described the variations within and between data in human volunteers. Bosentan treatment disproportionally increased the maximum BA concentration in individuals with a large total BA pool or low BSEP abundance. Especially individuals having a large total BA pool size and a low BSEP abundance were predicted to be at risk for rapid saturation of BSEP and subsequent intrahepatic BA accumulation. This model provides a first estimate of personalized safe therapeutic external dose levels of compounds with BSEP-inhibitory properties.

Keywords: Bile acids and salts ● Cholestasis ● New approach methodologies

List of abbreviations: AOP, Adverse Outcome Pathway; BA, bile acid; BSEP, bile salt export pump, C_{max}, maximum concentration in plasma; DILI, drug-induced liver injury; GCDCA, glycochenodeoxycholic acid; Hct, hematocrit; IQR, interquartile range; KE, key event; PBK, physiologically-based kinetic modeling, MRP2/3/4, multidrug resistance protein 2/3/4; MIE, molecular initiating event; OSTα/β, organic solute transporter alpha/beta

3.1 Introduction

The main physiological role of bile acids (BAs) has long been recognized to be the emulsification of dietary lipids and lipid-soluble vitamins. Additionally, BAs are important signaling molecules between the gut microbes and the host and can regulate lipid, glucose and energy metabolism (Hylemon et al. 2009). Primary BAs are de novo synthesized in the liver via cytochrome P450 (CYP)-mediated oxidation of cholesterol. Subsequently, they are conjugated with taurine or glycine and either secreted into the common bile duct or into the liver sinusoids. The latter transport processes are mediated by several transporters in the liver, e.g., bile salt export pump (BSEP) and multidrug resistance protein 2 (MRP2) for BA secretion to the bile canaliculi and MRP3/4 for transport to the liver sinusoids. Via the bile, BAs are subsequently transported to the intestinal lumen, where secondary BAs are formed by microbial conversions. About 95% of the intestinal BAs are reabsorbed into the portal circulation and transported to the liver. This recycling process is called enterohepatic circulation (Farooqui and Elhence 2021; Jia et al. 2018). A disturbance in the BA homeostasis can distort the gut–liver axis and is associated with various pathologies, such as cholestasis. Cholestasis refers to a disrupted bile flow leading to the accumulation of BAs in the liver and subsequent spillage to the systemic circulation (Noor 2015). Cholestasis is among the most commonly observed adverse reactions in patients suffering from drug-induced liver injury (DILI) (Nunes et al. 2021). Currently available preclinical in vivo and in vitro screening methods are insufficiently able to predict DILI, or cholestasis more specifically (Olson et al. 2000; Vinken 2018; Xu et al. 2008). Previously, inhibition of the hepatic BSEP has been identified as a risk factor involved in the development of cholestasis (Morgan et al. 2013). The importance of hepatic BSEP inhibition for cholestasis development is underlined by its recognition as a molecular initiation event (MIE) in the Cholestasis Adverse Outcome Pathway (AOP) (Vinken et al. 2013). Recently, an AOP network was established, visualizing the complexity of biological processes involved in the onset and development of human hepatotoxicity (Arnesdotter et al. 2021). The AOP network shows that BSEP inhibition is related to the key event (KE) bile acid accumulation, which in turn causes the release of pro-inflammatory mediators, activation of nuclear receptors/transcriptional change, and/or increased reactive oxygen species production. These KEs can lead directly or via multiple KEs to cholestasis. There are several compensatory mechanisms in the human liver to counteract hepatic BA accumulation involving the upregulation of other efflux transporters, e.g., OSTα/β and MRP3/4 (Gijbels et al. 2020; Jackson et al. 2016). Even though BSEP inhibition does not necessarily lead to cholestasis, it has been shown that integrating an export assay that measures the inhibition of BA export improves hepatotoxicity predictions compared to a cytotoxicity test in primary hepatocytes alone (Brecklinghaus et al. 2022). Given the number of physiological processes involved in BA homeostasis, obtaining mechanistic insights in the synthesis, circulation and excretion of BAs is relevant to understand and predict BA-associated diseases, such as cholestasis. Computational physiologically based kinetic (PBK) modeling can be used to translate in vitro data to in vivo data (Louisse et al. 2017) and it provides a tool that can contribute to a mechanistic understanding of a xenobiotic's distribution within the human body (Jones et al. 2015). In the current work we employ PBK modeling to elucidate interindividual differences that might determine susceptibility towards BSEP inhibition-mediated cholestasis. Bosentan, a drug used to treat pulmonary artery hypertension, has been shown to inhibit BSEP in a non-competitive nature in vitro and to cause DILI in 2–18% of the

patients (Fattinger et al. 2001; Mano et al. 2007). Given the potential of BSEP inhibitors to cause cholestasis and DILI, the aim of the present study was to develop a physiologically based kinetic (PBK) modeling facilitated approach linked with Markov Chain Monte Carlo simulations, that would provide a tool to predict dose-dependent BA accumulation in humans upon treatment with a BSEP inhibitor. A first proof-of-principle was developed using bosentan as the model BSEP inhibitor and glycochenodeoxycholic acid (GCDCA) as an exemplary BA.

3.2 Methods

Conceptual model

Three PBK submodels were constructed: (A) a bile acid (BA) model, (B) a model to describe the kinetics of the active bosentan metabolite RO 47-8634 responsible for inhibition of BSEP and (C) a bosentan model (Fig. 1). Submodel A describes the synthesis, circulation and excretion of an exemplary BA, GCDCA, in a healthy reference individual. Submodels B and C were used to predict the free intrahepatic concentrations of bosentan and its active metabolite RO 47-8634. The intrahepatic concentrations were next used to predict the bosentan-induced inhibitory effects on BSEP-mediated efflux of BAs. For modeling purposes, a lumped BA pool consisting of only GCDCA was assumed, supported by the fact that GCDCA is the most abundant BA in human serum (Bathena et al. 2013). Using a grouped BA pool enables us to keep the model complexity to a minimum, making the model easier to interpret and minimizing the risk of overfitting. The model consisted of separate compartments for liver, gall bladder, intestine, blood, rapidly perfused tissue, slowly perfused tissue and adipose tissue. The enterohepatic circulation was included by a circulation of GCDCA between the liver, gall bladder and intestine. GCDCA was de novo synthesized in the liver and excreted via the feces. The major metabolite of bosentan, RO 48-5033, is formed by hydroxylation at the t-butyl group of bosentan. Moreover, RO 47-8634 is generated by O-demethylation of the phenolic methyl ester of bosentan, and RO 64-1056 is generated by, respectively, O-demethylation and hydroxylation of the two mentioned bosentan metabolites, see Fig. 2. The major pathway of elimination of bosentan and its metabolites is hepatic metabolism followed by biliary excretion (Weber et al. 1999). Both bosentan and RO 47-8634 are able to inhibit BSEP-mediated transport of taurocholic acid in a non-competitive manner, while RO 48-5033 and RO 64-1056 had only limited effects on BSEP transport and are therefore not explicitly considered in a separate submodel (Fattinger et al. 2001). The PBK models for bosentan and RO 47-8634 consisted out of separate compartments for blood, rapidly perfused tissue, slowly perfused tissue, adipose tissue and liver.

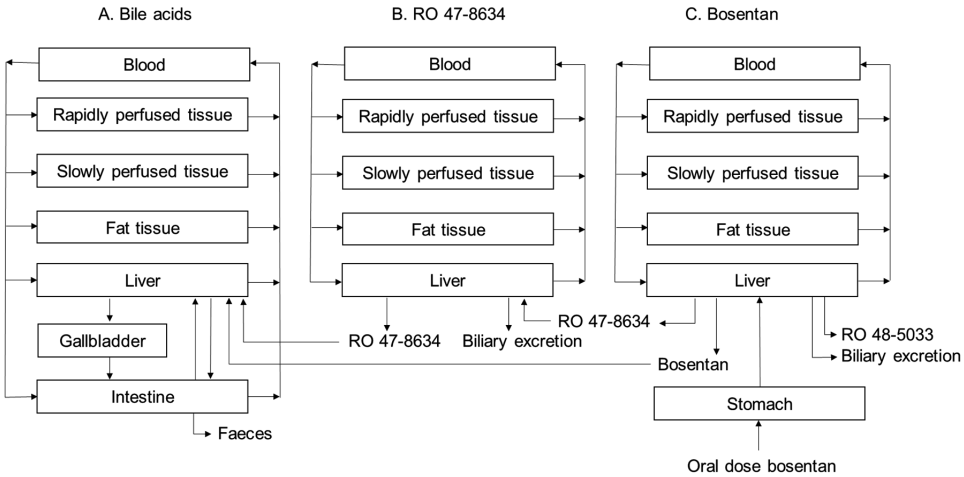

Figure 1 Schematic diagram of the PBK model for bile acids, bosentan and its active metabolite RO 47-8634. Submodels B and C were used to predict the intrahepatic free concentrations of bosentan and RO 47-8634 upon oral bosentan administration; these concentrations were subsequently used to predict the bosentan-induced effect on the bile acid concentrations using submodel A.

Physiologically based kinetic model of bile acid metabolism

Partition coefficients are important input parameters for PBK models and describe the relative distribution of a chemical between tissues and plasma at equilibrium within the organism. Tissue:plasma partition coefficients for GCDCA were calculated by a quantitative property–property relationship method described in literature (Rodgers and Rowland 2006) and obtained via the QIVIVE toolbox (Punt et al. 2020). The input parameters are summarized in Table 1. The total BA pool size in the reference individual was 3079 µmol. De novo synthesis in the liver was set to 46.8 µmol/h (Kullak-Ublick et al. 2004). To maintain the mass balance, fecal excretion of GCDCA was set equal to its de novo synthesis. GCDCA was actively transported from the liver to the common bile duct by BSEP following Michaelis–Menten kinetics. The BSEP-mediated efflux of GCDCA was described by the following equation (Eq. 1):

$$E = \frac{V_{max,BSEP} \times [CVL]}{K_{m,BSEP} + [CVL]} \qquad \text{Eq. 1}$$

where E is the BSEP-mediated efflux in µmol/h, V_{max} is the maximum efflux rate of GCDCA in blood in µmol/entire liver/hour, [CVL] the free concentration of BAs in µmol/L and $_{Km,BSEP}$ the Michaelis–Menten constant in µmol/L for BSEP-mediated BA efflux.

The V_{max} and K_m for BSEP-mediated transport of GCDCA were obtained from a vesicular transport assay in a baculovirus-infected Sf9 system (Kis et al. 2009). The authors showed that the V_{max} values in the vesicular transport assay increased upon the addition of physiological levels of cholesterol, hence, these values were used in the current PBK model. The values were reported in µmol/min/mg BSEP. In order to scale the experimental value for V_{max} expressed in in µmol/min/mg

BSEP to a value for the entire liver, an in vitro-in vivo extrapolation method was used based on absolute BSEP abundances. To this end, a scaling factor was calculated, as described in Eq. 2.

$$SF = aBSEP \times MWBSEP \times Hep \times WL \times 60 \times 10^{-9} \quad \text{Eq. 2}$$

where SF is the scaling factor in mg BSEP/entire liver, aBSEP is the BSEP abundance in pmol per 10^6 hepatocytes, MWBSEP is the molecular weight of BSEP in g/mol, Hep is the hepatocellularity in 10^6 cells/g liver, WL is the weight of liver in g, 60 is the number of minutes in an hour and 10^{-9} is used to convert pg to mg. As BSEP is a 140 kDa protein, a molecular weight of 140,000 g/mol was used.

It was assumed that half of the BAs in the common bile duct was secreted into the intestinal lumen, and the remaining half was stored in the gall bladder (Hofmann 1999). Gall bladder contractions were simulated three times per day, i.e., at 8:00, 12:00 and 16:00, assuming a meal consumption every four hours during daytime. Upon a gall bladder contraction, the entire gall bladder content was emptied in the intestinal lumen. GCDCA absorption from the intestine was assumed to follow first-order kinetics. The k_a value was obtained by fitting to in vivo data attained from Hepner and Demers (1977) and Ponz de Leon et al. (1978), which were scaled as described previously (Baier et al. 2019). Briefly, a percentage scaling factor was calculated from literature for scaling all datasets to the fraction of summed conjugated cholic, chenodeoxycholic and deoxycholic acid. Subsequently, the experimental data were multiplied by this scaling factor. Both datasets described plasma postprandial BA levels upon three subsequent meals in healthy subjects (in total 11 males and 3 females). Since the PBK model predicts whole blood concentrations and the in vivo data present plasma concentrations, the predicted whole blood concentrations were converted to plasma concentrations by dividing them by the blood:plasma ratio. The blood:plasma ratio of GCDCA was assumed to be 0.55 (1-hematocrit), which is a common assumption for acidic compounds when experimental data are lacking (Cubitt et al. 2009; Table 1). The fasting level of BAs in plasma was set to 2.4 µM (García-Cañaveras et al. 2012).

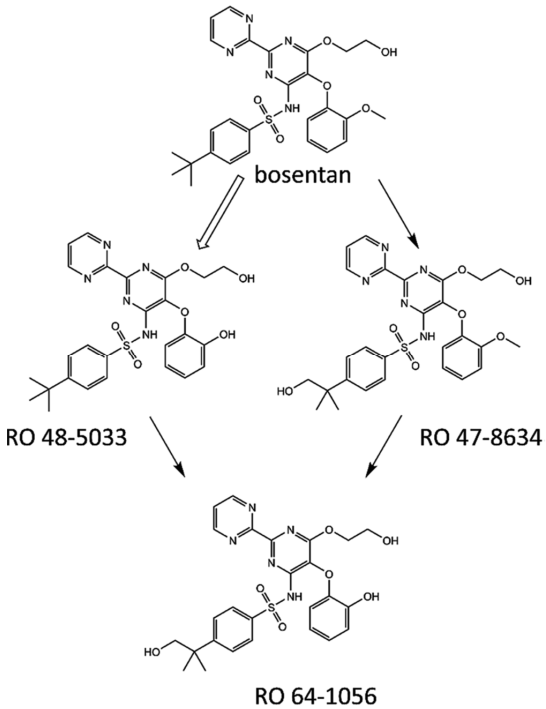

Figure 2 Metabolism of bosentan

Table 1 Physicochemical properties used to calculate the blood:tissue partition coefficients

GCDCA		Reference
p*Ka*	3.77	Law et al. (2014)
log*P*	2.12	Roda et al. (1990)
MW	449.62	
Fraction unbound	0.01	Roda et al. (1982)
Blood:plasma ratio	0.55	Assumption (1-Hct), Cubitt et al. (2009)
Bosentan		
p*Ka*	5.46	EMA (2004), Meyer (1996)
log*P*	3.1	EMA (2004), Meyer (1996)
MW	551.6	EMA (2004), Meyer (1996)
Fraction unbound	0.02	EMA (2004), Meyer (1996)
Blood:plasma ratio	0.6	EMA (2004), Meyer (1996)
RO 47-8634		
p*Ka*	5.46	ALOGPS toolbox (Tetko et al. 2005)
log*P*	3.1	ALOGPS toolbox (Tetko et al. 2005)
MW	551.6	
Fraction unbound	0.02	Calculated, Lobell and Sivarajah (2003)
Blood:plasma ratio	0.55	Assumption (1-Hct), Cubitt et al. (2009)

Sensitivity analysis

To assess the influence of the parameters on the model outcome, a sensitivity analysis was performed for the C_{max} of BAs, bosentan and RO 47-8634. The BA submodel was assessed independently from the submodels for bosentan and metabolite RO 47-8634. Based on the method reported by Evans and Andersen (2000), the sensitivity coefficients (SCs) for the model parameters were calculated as follows:

$$SC = \frac{C' - C}{P' - P} \times P/C \qquad \text{Eq. 3}$$

where *C* indicates the initial value of the model output, *C'* indicates the modified value of the model output resulting from an increase in the parameter value. *P* indicates the initial parameter value and *P'* indicates the modified parameter value after a 5% increase of its value, keeping all other parameters at their original value.

Two approaches towards describing interindividual differences in the BA pool

Two scenarios were applied to describe the variability in the systemic BA plasma levels in the reported in vivo data. In the first approach, the sensitivity analysis was used to identify parameters that have a strong influence on the C_{max} BA values and these parameters were multiplied with an empirical scaling factor "sens". The identified parameters included parameters describing the total amount of BAs present, i.e., the amount of BA in a full gall bladder and the systemic fasting BA concentration in plasma. Therefore, we empirically scaled all the parameters contributing to the total BA pool size, i.e., dose in a full gall bladder, fasting concentration and de novo synthesis. As the fecal excretion was assumed to equal de novo synthesis to maintain the mass balance, this parameter was altered accordingly. In the second approach, the variation that could occur in hepatic BSEP abundance in a Caucasian population was simulated using Markov Chain Monte Carlo simulations. Differences in BSEP abundance will result in an altered scaling factor (Eq. 2) and subsequently an altered $V_{max,\ BSEP}$. For the Markov Chain Monte Carlo simulations, a total of 10,000 simulations were performed, where in each simulation BSEP abundance was randomly taken from a log-normal distribution derived from a meta-analysis of transporter abundances in liver tissue of healthy Caucasians (Burt et al. 2016). The distribution was truncated at ± 3 SD (Punt et al. 2016), excluding individuals with BSEP abundances three times higher or lower than the geometric mean. The mean, μ_w and standard deviation, σ_w describing the log-normal distribution of BSEP abundance were derived using Eqs. 4 and 5 (Ning et al. 2019; Zhang et al. 2007).

$$\mu_w = \ln \frac{\mu_x}{\sqrt{1 + CV_x^2}} \qquad \text{Eq. 4}$$

$$\sigma_w^2 = \ln (1 + CV_x^2) \qquad \text{Eq. 5}$$

where μ_x is the mean BSEP abundance and CV_x is the coefficient of variation of BSEP abundance.

Experimental data for postprandial bile acid levels

The maximum postprandial systemic BA values were compared with values reported in literature (see for relevant references Table 2). All studies included postprandial plasma BA levels in healthy adult subjects. The reported studies measured different BA conjugates; hence, data were normalized with a percentage scaling factor as described previously (Baier et al. 2019). If necessary, data were extracted from graphs using TechDig version 2.0. The study subjects received multiple meals, and each peak in postprandial BAs was assigned to a meal when possible.

Table 2 Details of experimental studies used for model validation

Gender	Age	Reference
5 females	24-53	Angelin and Bjorkhem (1977)
8 males, 6 females	22-56	Galeazzi et al. (1980)
3 males, 2 females	25-58	Galman et al. (2005)
5 males, 3 females	24 ± 5 (mean ± SD)	Hepner and Demers (1977)
7 males, 4 males	27-61	Salemans et al. (1993)
6 males	24-39	Ponz de Leon et al. (1978)

Physiologically based kinetic model of bosentan and RO 47-8634

PBK submodels B and C were constructed to derive the intrahepatic concentrations of bosentan and its active metabolite RO 47-8634. Eventually, these concentrations were used to simulate their inhibitory effect on BSEP-mediated efflux of BAs from the liver to the common bile duct. Both submodels B and C consisted of separate compartments for blood, rapidly perfused tissue, slowly perfused tissue, fat and liver, as shown in Fig. 2. A dosing regimen of 500 mg bosentan administered orally twice a day was selected, in line with available studies from which we extracted systemic in vivo plasma levels of bosentan and its active metabolite (Weber et al. 1999). Furthermore, systemic BA levels from volunteers following this dosing regimen were available (Fattinger et al. 2001). Bosentan administration was simulated at 8:00 and 20:00. The kinetic parameters for absorption of bosentan and biliary excretion of bosentan and RO 47-8634 were obtained by fitting to experimental plasma data obtained from Weber et al. (1999). The physicochemical properties of bosentan and RO 47-8634 were used to calculate partition coefficients using the QIVIVE toolbox (Punt et al. 2020). As experimental data were lacking for the pKa and logP for RO 47-8634 these were predicted using the ALOGPS toolbox (Tetko et al. 2005). The fraction unbound of RO 47-8634 in plasma was calculated via the method described by Lobell and Sivarajah (2003) and obtained via the QIVIVE toolbox. The blood:plasma ratio of RO 47-8634 was assumed to be 0.55 (1-Hct) (Cubitt et al. 2009). The physicochemical properties of GCDCA, bosentan and RO 47-8634 are shown in Table 1.

The kinetic parameters for the metabolism of bosentan were obtained from a study with human liver microsome incubations (Sato et al. 2018). The metabolism consisted of apart following Michaelis–Menten kinetics and non-saturable metabolic clearance, as described in Eq. 6.

$$v = V_{max} \times \frac{[CVL_{bosentan}]}{Km + [CVL_{bosentan}]} + CL \times [CVL_{bosentan}] \qquad \text{Eq. 6}$$

where *v* is the velocity of metabolism in µmol/h, V_{max} is the maximum velocity of metabolism in µmol/h, $[CVL_{bosentan}]$ is the free concentration of bosentan in liver in µmol/L, K_m is the Michaelis–Menten constant of metabolism in µmol/L and CL is the non-saturable metabolic clearance in L/h per 106 cells. The reported kinetic parameters were expressed per mg microsomal protein and scaled to g liver, assuming 32 mg microsomal protein/g liver (Barter et al. 2007). The clearance was scaled from L/h per 106 cells to L/h per g liver using a hepatocellularity of 99 × 106 cells/g liver (Barter et al. 2007). To scale from g liver to entire liver, the kinetic parameters were multiplied by the liver weight. A liver weight of 20 × BW was used, i.e., 1400 g of liver for a 70 kg individual (Soars et al. 2002).

Inhibition

Bosentan and RO 47-8634 inhibit BSEP-mediated BA efflux in a non-competitive nature (Fattinger et al. 2001). Hence, the Michaelis–Menten equation in the model that represents BSEP-mediated BA efflux from the liver was modified to include the non-competitive type of inhibition by the introduction of a modulation factor $(1 + [CVL_{bosentan}]/K_{i,bosentan} + [CVL_{RO\ 47\text{-}8634}]/K_{i,RO\ 47\text{-}8634})$. The resulting equation for BSEP-mediated BA efflux is then as follows:

$$E = V_{max,BSEP}/(1 + [CVL_{bosentan}]/K_{i,bosentan} + [CVL_{RO\ 47-8634}]/K_{i,RO\ 47-8634}) \times [CVL]/(Km_{BSEP} + [CVL]) \quad \text{Eq. 7}$$

where *E* is the BSEP-mediated efflux of BAs from the liver (µmol), $V_{max,BSEP}$ is the maximum rate of BSEP-mediated BA efflux from the liver in µmol/h, $[CVL_{bosentan}]$ is the free concentration of bosentan in µmol/L in the liver, $K_{i,bosentan}$ is the inhibition constant for inhibition of the BSEP-mediated BA efflux by bosentan in µmol/L, $[CVL_{Ro\ 47\text{-}8634}]$ the free concentration of RO 47-8634 in µmol/L in the liver, $K_{i,RO\ 47–8634}$ is the inhibition constant for inhibition of the BSEP-mediated BA efflux by RO 47-8634 in µmol/L, [CVL] the free concentration of BAs in µmol/L in the liver and $K_{m,BSEP}$ is the Michaelis–Menten constant of BSEP-mediated BA efflux in µmol/L in the liver. Bosentan and RO 47-8634 inhibited BSEP-mediated transport of taurocholic acid with K_i values of 12 and 8.5 µmol/L, respectively (Fattinger et al. 2001). In the absence of data, it was assumed that the K_i values for the competition with GCDCA equalled those for taurocholic acid. The differential model equations were encoded and solved using Berkeley Madonna 10.2.8 (UC Berkeley, CA, USA) using the auto-step size algorithm. The full model code is presented in Supplementary file II. Pre- and post-treatment BA levels were compared with a Wilcoxon signed-rank test using R version 4.0.2 (R Core Team 2020). A *p* value < 0.05 was considered statistically significant.

3.3 Results

A computational model describing the synthesis, circulation and excretion of bile acids (BAs) was developed for a healthy reference individual (Fig. 3). In the simulations subjects fasted overnight and meals were simulated at 8:00, 12:00 and 16:00. Upon meal ingestion, the gall bladder was contracted, resulting in a peak in the systemic BA levels. The prediction was compared with two experimental data sets available in the literature showing postprandial BA levels (Hepner and Demers 1977; Ponz de Leon et al. 1978) (Fig. 3). The predicted systemic maximum BA concentration in plasma (C_{max}) value was 4.4

µM, which is in line with the *in vivo* data reported by Hepner and Demers (1977). The C_{max} reported by Ponz de Leon et al. (1978) is more than twofold higher (Fig. 3). The established PBK model was utilized to explore mechanistic explanations for these differences in the in vivo data. For this, a sensitivity analysis was performed to identify parameters that have a strong influence on the model outcome, i.e., the systemic plasma BA concentration. The sensitivity analysis (Fig. 4) revealed that parameters determining the amount of BA present in the body at the start of the simulations, i.e., the amount of BAs in a full gall bladder (Gdose) and systemic fasting concentration (CBfs) showed a strong positive influence on the model outcome (C_{max}). Parameters determining the scaled maximum rate of BSEP-mediated BA efflux had a strong negative influence on the C_{max}.

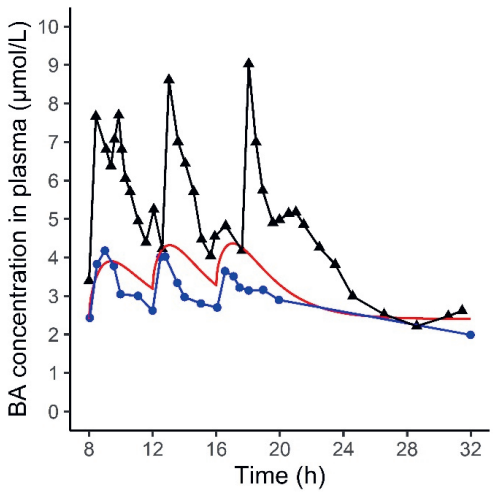

Figure 3 Predicted and observed plasma BA levels in human subjects. Subjects fasted overnight and meals were simulated at 8:00, 12:00 and 16:00. In vivo data were retrieved from Hepner and Demers (1977) (blue circles) and Ponz de Leon et al. (1978) (black triangles). The simulation is visualized in red.

Markov Chain Monte Carlo simulations for BSEP abundances

To describe the interindividual variability in the systemic BA levels observed in vivo, we employed two scenarios. In the first approach, the BSEP abundances were randomly drawn from a log-normal distribution to simulate its variability in a virtual population using Markov Chain Monte Carlo simulations. In the second scenario, we scaled the total BA pool size with an empirical scaling factor informed by the results from the sensitivity analysis (Fig. 4). To study the effect of interindividual differences in absolute BSEP abundances on the BA homeostasis, a set of 10,000 Markov Chain Monte Carlo simulations were performed. In these simulations, BSEP abundances were randomly sampled from a log-normal distribution and used for *in-vitro*-to-*in-vivo* scaling of the experimentally obtained V_{max} for BSEP-mediated efflux of BAs. The predicted C_{max} values were compared with observed C_{max} values (Fig. 5a). The predicted and observed data for healthy individuals gave comparable median values. Figure 5b displays that individuals with a low BSEP abundance have very high C_{max} values, while the probability of an individual having such a low BSEP abundance is simulated to be small (Fig. 5c).

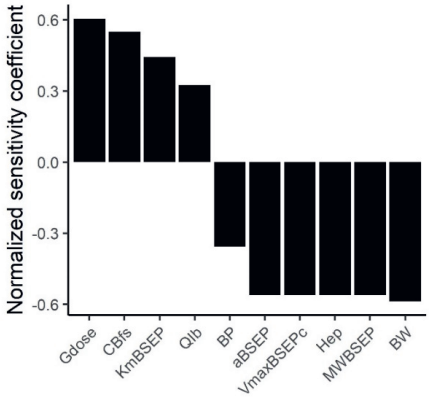

Figure 4 Sensitivity analysis of the influence of the PBK model parameters on the predicted maximal systemic BA concentration in plasma. Only parameters with an absolute normalized sensitivity coefficient > 0.1 are shown. Gdose = dose in a full gallbladder, CBfs = systemic plasma concentration in fasting state, KmBSEP = Michaelis–Menten constant for BSEP-mediated BA efflux from the liver, Qlb = fraction of bile flow transported directly from liver to intestinal lumen via common bile duct reference, BP = blood:plasma ratio, aBSEP = BSEP protein abundance, VmaxBSEPc = maximal BSEPmediated BA efflux rate, Hep = hepatocellularity, MWBSEP = molecular weight of BSEP, BW = body weight

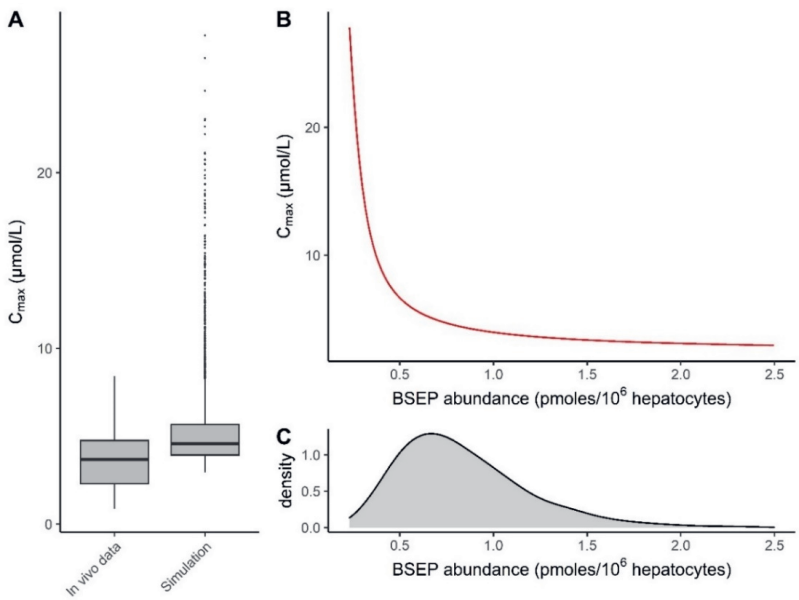

Figure 5 a Predicted and observed BA concentrations in plasma. BSEP abundances were drawn randomly from a log-normal distribution using Markov Chain Monte Carlo simulations. The details for the distribution were obtained from Burt et al. (2016). 10,000 iterations were performed, 18 iterations were excluded because BSEP abundances exceeded ± 3 SD. For details about the in vivo data set, see "Methods". **b** Relationship between simulated C_{max} and BSEP abundance. **c** Density plot of BSEP abundances used for the Markov Chain Monte Carlo simulations

Empirical scaling of the total bile acid pool size

The sensitivity analysis revealed that the amount of BAs in a full gall bladder (Gdose) and the systemic fasting concentration (CBfs) had a large influence on the systemic BA peak concentrations. Therefore, we altered the total BA pool size with an empirical scaling factor "sens" (sensitivity). The total BA pool size is governed by the amount of BAs in a full gall bladder, the systemic fasting concentration and the de novo synthesis. These parameters were multiplied with a certain value sens (0.5, 1 or 1.5). As the fecal excretion was assumed to equal de novo synthesis in order to maintain the mass balance, this parameter was altered accordingly. The total BA pool size in the reference individual was 3079 µmol. Using the respective empirical scaling factors sens this value amounted to 1540, 3079 and 4619 µmol. In Fig. 6, the effect of the empirical scaling factor sens on the systemic plasma BA concentrations is visualized and compared with available in vivo data for the C_{max} after each meal. Each of the factors for sens resulted in predictions within the boundaries of the reported in vivo data. A sens value of 1 gives a prediction within the interquartile range (IQR) of the in vivo data; a sens values of 1.5 provides a prediction above the IQR; a sens value of 0.5 predicted systemic BA plasma concentrations below the IQR after meal 1 and at the lower end of the IQR after meal 2 and 3. Furthermore, the increases in the amount of BAs in each of the organs upon introduction of the empirical scaling factors were evaluated (Table 3). With a sens value of 1.5, the intrahepatic BAs showed the largest increase relative to the reference individual (sens value 1) compared to the other organs.

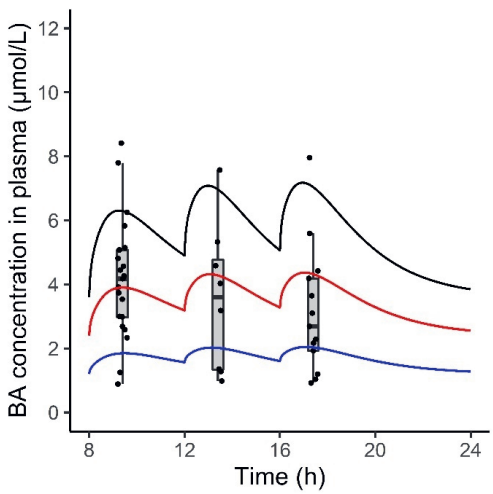

Figure 6 The effect of the empirical scaling factor sens on predicted plasma BA levels in human subjects. Subjects fasted overnight and meals were simulated at 8:00, 12:00 and 16:00. The dose in a full gall bladder, the systemic fasting concentration, the de novo synthesis and the fecal excretion were multiplied with a certain sens value (0.5, 1 or 1.5) to model the effects of different total BA pool size. The total pool size in the reference individual (sens value = 1) was 3079 µmol. The boxplots and points represent observed peak plasma BA concentrations after three meals reported in literature (see "Methods"). Blue = sens value 0.5, red = sens value 1, black = sens value 1.5

Table 3 Fold change in the amount of BAs in compartments of the PBK model upon empirical scaling of the total BA pool relative to a reference individual (sens value = 1). The total amount of BAs was multiplied with a factor 0.5 or 1.5 (sens value = 0.5 or 1.5, respectively)

	Fold change	
	Sens value 0.5	Sens value 1.5
Adipose tissue	0.4	1.8
Blood	0.4	1.8
Gall bladder	0.5	1.5
Intestinal lumen	0.5	1.5
Intestinal tissue	0.4	1.8
Liver	0.4	2.1
Rapidly perfused tissue	0.4	1.8
Slowly perfused tissue	0.4	1.8

Submodels bosentan and metabolite RO 47-8634

After the establishment of the PBK model for BAs, the submodels describing the distribution of the cholestatic drug bosentan and its metabolite RO 47-8634 upon oral administration of 500 mg were developed. The results of the simulation for the systemic levels (solid lines) and the experimental data (dots and triangles) (Weber et al. 1999) are displayed in Fig. 7. The experimental plasma data were 1.7-fold higher than the simulations for both bosentan and RO 47-8634. These PBK submodels were used to predict the free intrahepatic concentrations of bosentan and RO 47-8634 (dashed lines), and subsequently used to predict the inhibitory effect on BSEP-mediated BA efflux from the liver. The sensitivity analysis revealed that the fraction absorbed (Fa) and oral dose of bosentan (ODOSEmg) had the strongest positive influence on the C_{max}. The strongest negative influence on the model outcome was observed for the fraction of liver tissue (VLc). The normalized sensitivity coefficients are displayed in Supplementary Figure S1.

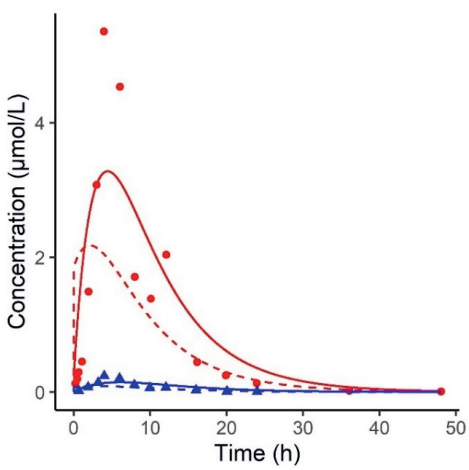

Figure 7 Predicted and observed concentrations of bosentan and RO 47-8634 upon oral administration of 500 mg bosentan. Circles and triangles represent experimental data in plasma obtained from Weber et al. (1999), the solid lines represent the predictions in plasma and the dashed lines the prediction of free concentration in the liver. Red = bosentan, blue = RO 47-8634

The effect of repeated bosentan administration on systemic BA levels was simulated for a reference individual, as well as for a virtual population using the Markov Chain Monte Carlo simulations for BSEP abundances (Fig. 8) and with the empirical scaling factor sens (Fig. 9). Fattinger et al. (2001) reported the highest DILI incidence upon a dosing regimen of 500 mg bosentan twice per day, thus the same dosing regimen was used in the simulations. Bosentan was simulated to be administered orally at 8:00 and 20:00, the first dose being administered along with breakfast. The model predicted that the systemic C_{max} values of bosentan and RO 47-8634 reached stable levels after three days of repeated bosentan dosing, respectively. Therefore, postprandial kinetics of BA levels during three days of oral bosentan administration appeared sufficient to obtain insight in the effect of repeated bosentan dosing on BA kinetics. Figure 8 shows the simulated and observed effect of bosentan treatment on the BA plasma concentrations in a virtual population with different BSEP transporter abundances, and a population of healthy individuals who developed liver injury during the clinical trial using bosentan (18% of the participants) (Fattinger et al. 2001), respectively. The pre- and posttreatment BA levels were reported in the clinical trial; likewise, we report healthy controls and post-treatment levels. Both the observed and simulated data displayed a significant increase in systemic BA concentrations upon repeated bosentan administration. Bosentan treatment increased the maximum postprandial BA level for the reference individual, as well as for the simulations with sens values of 0.5 and 1.5 (Fig. 9). The largest increase was observed with a sens value of 1.5. Maximum concentrations of BA in the liver are reported in Table 4; the largest increase was observed with a sens value of 1.5.

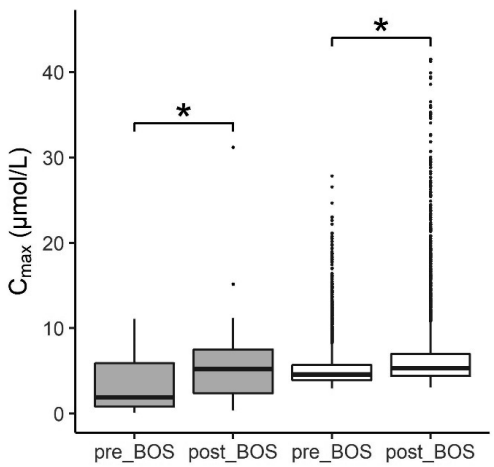

Figure 8 Predicted and observed BA concentrations in the plasma of controls and individuals administered with bosentan 500 mg twice a day. BSEP abundances were drawn randomly from a log-normal distribution using Markov Chain Monte Carlo simulations. 18 and 15 simulations were discarded because BSEP abundances exceeded ± 3 SD for controls and bosentan-treated individuals, respectively. Gray fill: in vivo data and statistical results retrieved from Fattinger et al. (2001); white fill: simulated data

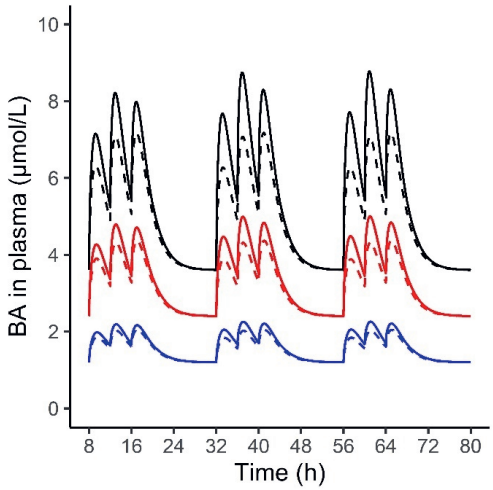

Figure 9 The effects of oral bosentan administration (500 mg twice per day) on systemic BA plasma values. Subjects fasted overnight and meals were simulated at 8:00, 12:00 and 16:00. The dose in a full gall bladder, the systemic fasting concentration, the de novo synthesis and the fecal excretion were multiplied with a certain sens value (0.5, 1 or 1.5) to model the effects of different total BA pool size. The total pool size in the reference individual (sens value = 1) was 3079 µmol. Dashed line = no bosentan; solid line = bosentan administration. Blue = sens value 0.5, red = sens value 1, black = sens value 1.5

Table 4 Maximal simulated hepatic BA concentrations in healthy controls and bosentan-administered Individuals (500 mg twice per day)

Sens value	Maximal hepatic BA concentration (nmoles/g tissue)		
	0.5	1	1.5
Control	0.2	0.5	1.1
Bosentan	0.3	0.8	1.8

3.4 Discussion

The current study presents a PBK model describing the synthesis, circulation and excretion of bile acids (BAs), using GCDCA as the model BA, in healthy and bosentan-treated individuals. Bosentan is known to inhibit the efflux of BAs from the liver to the common bile duct by noncompetitive inhibition of the hepatic BSEP transporter, which can lead to intrahepatic accumulation of BAs and their subsequent spillage to the systemic circulation (Fattinger et al. 2001; Mano et al. 2007). The current study showed that especially a large total BA pool size and a low BSEP abundance increase an individual's susceptibility towards BSEP inhibition-mediated toxicity.

Postprandial plasma BA levels were simulated and compared with in vivo data reported in literature. The reported in vivo data show a ninefold variation between individuals (Angelin and Björkhem 1977; Galeazzi et al. 1980; Gälman et al. 2005; Hepner and Demers 1977; Ponz de Leon et al. 1978; Salemans et al. 1993). Our simulations predicted BA levels that were well within the reported range and followed a similar peak pattern as reported in literature (Hepner and Demers 1977; Ponz de Leon et al. 1978). Next, we employed two scenarios to identify plausible causes of the interindividual

differences, and identify risk factors for the development of cholestasis. In the first approach, we incorporated physiologically relevant BSEP abundances in our PBK model for quantitative *in vitro*-to-*in-vivo* extrapolations of $V_{max,BSEP}$. The abundances were randomly drawn from a log-normal distribution (Burt et al. 2016) using Markov Chain Monte Carlo simulations. Our results revealed that the BA C_{max} values in the plasma of individuals with low BSEP abundances reach very high levels (Fig. 5b); 0.9% of our simulated population has abnormal systemic BA values of over 15 µM. As we identified low BSEP abundances as a risk factor for the development of cholestasis, it is important for future safety assessments of BSEP-inhibitory pharmaceuticals to get an accurate estimate of the prevalence of low abundances. Not only low transporter abundance, but also low transporter functionality as a result of inborn mutations should be considered as a cause for increased hepatic BA concentrations and susceptibility towards BSEP inhibition-mediated toxicity. Carriers of progressive familial intrahepatic cholestasis 2 (PFIC2) or benign recurrent intrahepatic cholestasis 2 (BRIC2) have a higher risk of developing cholestasis during their lifetime. Both PFIC2 and BRIC2 are caused by polymorphisms of the BSEP-coding gene which leads to a dysfunctional BSEP protein. PFIC2 and BRIC2 are estimated to occur in about 1 per 50,000 to 1 per 100,000 childbirths (Geethalakshmi and Mageshkumar 2014). In BRIC2 carriers, usually, a basal functionality of BSEP remains, while PFIC2 is more severe and patients ultimately need liver transplantation as they develop cholestasis, progressive liver fibrosis, cirrhosis and end-stage liver disease (Srivastava 2014). With accurate kinetic data for the BA transport remaining in BRIC2 or PFIC2 carriers, the current model could be used to set safe external dose levels of xenobiotics for these individuals.

The sensitivity analysis revealed that the BA levels in a full gall bladder and the fasting concentration of BAs contributed strongly to the predicted systemic BA levels, and thus could be a major determinant of the interindividual variability. Based on these results, we introduced an empirical scaling factor that modified the total amount of predicted BAs present in the body. We found that relatively small factors of 0.5 and 1.5 could predict the lower and upper range of the reported in vivo data. Our reference individual has a total BA pool of 3079 µmol; which is slightly below reported values (3672–9374 µmol (Beuers et al. 1992; Koopman et al. 1988), see supplementary file I Table S1 for the conversion to model units). This discrepancy can be explained because the BA concentration in the liver, intestine, fat, slowly and rapidly perfused tissue were set to 0 at the beginning of the simulations, while in vivo BAs circulate through these tissues. This could be overcome by carefully defining the initial state in the relevant organs, although this is challenging as experimental data are sparse for some compartments of the human body that are inaccessible. The empirical scaling factor 1.5 resulted in a total pool size well within the physiological range, while the maximal hepatic BA levels were below the physiological range (16–67 nmoles/g tissue (Aranha et al. 2008; García-Cañaveras et al. 2012)). This indicates that in our predictions a (too) large fraction was secreted from the liver or a (too) small fraction of the Bas was absorbed from the intestinal lumen, causing low predictions hepatic BA levels. Refining the PBK model with more mechanistic insights in intestinal and hepatic BA uptake might improve the predictions for intrahepatic BA levels. Interestingly, a 1.5-fold increase in the amount of BAs present in the body led to a 2.1-fold and 1.8-fold increase in the hepatic and systemic blood BA concentrations, respectively (Table 3). Along with the relatively small increase in BA levels observed in the intestinal lumen, this indicates saturation of

the BSEP-mediated efflux of BAs from the liver to the common bile duct. Via diffusion the BAs deposit from the liver to the remaining organs and the systemic circulation, resulting in elevated systemic concentrations. Hence, a large BA pool can lead to saturation of BSEP and is thereby a risk factor for the development of drug-induced cholestasis.

The next step in our study was to establish a PBK model for bosentan and its metabolite RO 47-8634 to estimate their intrahepatic concentrations, and subsequently their inhibitory effect on BSEP-mediated BA transport. Our PBK model gave a good prediction of the bosentan and RO 47–8634 concentrations in plasma (Fig. 7), given that the simulated C_{max} was within the twofold cut-off value that is commonly requested within a regulatory context (Peters and Dolgos 2019). Therefore, the bosentan model was considered fit for purpose to predict to intrahepatic bosentan and RO 47-8634 levels and use these as input in the BA PBK model. Upon the introduction of bosentan's inhibitory effect on BSEP-mediated transport in the BA model, the systemic BA levels increased, as was also reported in vivo (Fattinger et al. 2001). It should be noted that the in vivo study only measured pre- and post-treatment BA levels in individuals who developed DILI, whereas the simulated population was a healthy population. However, as the experimental and simulated pre-treatment BA levels were comparable, we assume that the individuals who developed liver injury throughout the bosentan treatment did not have a specific predisposition towards developing DILI. In line with the in vivo data, very high BA levels of up to 42 μM were observed in the simulations upon bosentan treatment. Interestingly, the simulations with the empirical scaling factor of 1.5 showed a larger increase in systemic BA levels than what was predicted for the reference individual upon bosentan treatment (Fig. 9). This larger increase further supports that BSEP-mediated BA efflux is more rapidly saturated in the individuals with a 1.5-fold scaled and thus higher total BA pool. Furthermore, plasma C_{max} values were strongly increased in individuals with low BSEP abundances. Hence, either a large total BA pool size or a low BSEP abundance can result in an overloaded BSEP transport, which in turn results in excessively high hepatic and potentially toxic BA levels, especially when a BSEP-inhibiting drug is administered.

The current PBK model condensed a complex biological system to a relatively simple set of equations, with proved to adequately predict physiological responses. The BA pool was considered as a lumped pool, with GCDCA as an exemplary BA, although in vivo the BA pool consists of various BAs, with each different kinetics and physicochemical properties. Computational models describing different BA species in the human body have been established recently (Sips et al. 2018; Voronova et al. 2020). However in contrast to these studies, in the current PBK model all but one parameters were derived experimentally. We consider this as a major strength of the current model which could only be accomplished by reducing the model complexity. We limited the number of BAs included in the model, as experimental kinetic data are simply not available for all BAs. The current model can be easily extended towards individual BAs as soon as relevant kinetic data become available. Furthermore, in the current approach basolateral transport was assumed to be completely diffusion-mediated and active transport of BAs by MRP3, MRP4 or OSTα/β was not yet considered. The expression of these transporters is low under normal conditions (Beaudoin et al. 2020; Vinken et al. 2013), and hence, incorporation of these transporters is expected to not have a substantial effect on the intrahepatic or systemic BA levels of healthy individuals. Nevertheless, under cholestatic conditions, MRP3/4 and OSTα/β are upregulated (Gijbels et al. 2020; Vinken et al. 2013), by that counteracting the intrahepatic

accumulation of BAs. Experimental data regarding basolateral transporter affinity and regulation of its expression are lacking to date, but would improve the accuracy of the simulations of cholestatic individuals.

In conclusion, the current PBK model provided novel mechanistic insight into BA homeostasis and the consequences of BSEP inhibition and helps to, *e.g.*, identify rate-limiting processes or risk factors towards developing BA related liver disease. With this, the PBK modeling approach serves as a vigorous instrument to understand the BA homeostasis without the need for animal testing. We identified that individuals with low functional BSEP abundances or a large BA pool are susceptible to BSEP-mediated cholestasis. In these individuals, BSEP-mediated hepatic BA efflux is rapidly saturated upon BSEP inhibition, causing elevated and potentially hepatotoxic BA concentrations. Since the current PBK model is data-driven (*i.e.*, most input parameters are derived experimentally), it is suitable to extrapolate to other situations or individuals. A powerful application of the coupled bosentan–BA model is the potential to predict dose-relationships for specific individuals, *e.g.*, PFIC2 or BRIC2 carriers, or to estimate safe therapeutic doses for an entire population, including the most sensitive individuals. The approach developed can easily be extended to other pharmaceuticals, for which the needed model input parameters are typically known.

Author contribution: Conceptualization I.R., H.B. and V.B., modeling: V.B., writing: V.B., review and editing: H.B. and I.R. All authors read and approved the final manuscript.
Funding: All funding was received from the Division of Toxicology (WUR).

References

Angelin B, Björkhem I (1977) Postprandial serum bile acids in healthy man. Evidence for differences in absorptive pattern between individual bile acids. Gut 18(8):606–609

Aranha MM, Cortez-Pinto H, Costa A, da Silva IBM, Camilo ME, de Moura MC, Rodrigues CM (2008) Bile acid levels are increased in the liver of patients with steatohepatitis. Eur J Gastroenterol Hepatol 20(6):519–525

Arnesdotter E, Spinu N, Firman J, Ebbrell D, Cronin MT, Vanhaecke T, Vinken M (2021) Derivation, characterisation and analysis of an adverse outcome pathway network for human hepatotoxicity. Toxicology 459:152856

Baier V, Cordes H, Thiel C, Castell JV, Neumann UP, Blank LM, Kuepfer L (2019) A physiology-based model of human bile acid metabolism for predicting bile acid tissue levels after drug administration in healthy subjects and BRIC type 2 patients. Front Physiol 10:1192. https://doi.org/10.3389/fphys. 2019.01192

Barter ZE, Bayliss MK, Beaune PH, Boobis AR, Carlile DJ, Edwards RJ, Brian Houston J, Lake BG, Lipscomb JC, Pelkonen OR, Tucke GT (2007) Scaling factors for the extrapolation of in vivo metabolic drug clearance from in vitro data: reaching a consensus on values of human micro-somal protein and hepatocellularity per gram of liver. Curr Drug Metab 8(1):33–45

Bathena SPR, Mukherjee S, Olivera M, Alnouti Y (2013) The profile of bile acids and their sulfate metabolites in human urine and serum. J Chromatogr B 942:53–62

Beaudoin JJ, Brouwer KL, Malinen MM (2020) Novel insights into the organic solute transporter alpha/beta, OSTα/β: from the bench to the bedside. Pharmacol Ther 211:107542

Beuers U, Spengler U, Zwiebel FM, Pauletzki J, Fischer S, Paumgartner G (1992) Effect of ursodeoxycholic acid on the kinetics of the major hydrophobic bile acids in health and in chronic cholestatic liver disease. Hepatology 15(4):603–608

Brecklinghaus T, Albrecht W, Kappenberg F, Duda J, Vartak N, Edlund K, Marchan R, Ghallab A, Cadenas C, Günther G, Leist M (2022) The hepatocyte export carrier inhibition assay improves the separation of hepatotoxic from non-hepatotoxic compounds. Chem Biol Interact 351:109728

Burt HJ, Riedmaier AE, Harwood MD, Crewe HK, Gill KL, Neuhoff S (2016) Abundance of hepatic transporters in Caucasians: a metaanalysis. Drug Metab Dispos 44(10):1550–1561. https:// doi. org/10. 1124/ dmd. 116. 071183

Cubitt HE, Houston JB, Galetin A (2009) Relative importance of intestinal and hepatic lucuronidation—impact on the prediction of drug clearance. Pharm Res 26(5):1073–1083

EMA (2004) Scientific discussion. Retrieved from https:// www.ema.europa.eu/en/documents/ scientific-discussion tracleer-epar-scientific- discussion_en.pdf

Evans MV, Andersen ME (2000) Sensitivity analysis of a physiological model for 2, 3, 7, 8-tetrachlorodibenzo-p-dioxin (TCDD): assessing the impact of specific model parameters on sequestration in liver and fat in the rat. Toxicol Sci 54(1):71–80

Farooqui N, Elhence A (2021) A current understanding of bile acids in chronic liver disease. J Clin Exp Hepatol

Fattinger K, Funk C, Pantze M, Weber C, Reichen J, Stieger B, Meier PJ (2001) The endothelin antagonist bosentan inhibits the canalicular bile salt export pump: a potential mechanism for hepatic adverse reactions. Clin Pharmacol Ther 69(4):223–231. https://doi. org/ 10. 1067/ mcp. 2001. 114667

Galeazzi R, Lorenzini I, Orlandi F (1980) Rifampicin-induced elevation of serum bile acids in man. Dig Dis Sci 25(2):108–112

Gälman C, Angelin B, Rudling M (2005) Bile acid synthesis in humans has a rapid diurnal variation that is asynchronous with cholesterol synthesis. Gastroenterology 129(5):1445–1453

García-Cañaveras JC, Donato MT, Castell JV, Lahoz A (2012) Targeted profiling of circulating and hepatic bile acids in human, mouse and rat using an UPLC-MRM-MS-validated method. J Lipid Res 53:2231–2241

Geethalakshmi S, Mageshkumar S (2014) Benign recurrent intrahepatic cholestasis: a rare case report. Int J Sci Study 2:222–224

Gijbels E, Vilas-Boas V, Annaert P, Vanhaecke T, Devisscher L, Vinken M (2020) Robustness testing and optimization of an adverse outcome pathway on cholestatic liver injury. Arch Toxicol 94:1–22

Hepner GW, Demers LM (1977) Dynamics of the enterohepatic circulation of the glycine conjugates of cholic, chenodeoxycholic, deoxycholic, and sulfolithocholic acid in man. Gastroenterology 72(3):499–501

Hofmann AF (1999) Bile acids: the good, the bad, and the ugly. Physiology 14(1):24–29. https:// doi. org/ 10. 1152/ physi ology online. 1999. 14.1. 24

Hylemon PB, Zhou H, Pandak WM, Ren S, Gil G, Dent P (2009) Bile acids as regulatory molecules. J Lipid Res 50(8):1509–1520. https:// doi. org/ 10. 1194/ jlr. R9000 07- JLR200

Jackson JP, Freeman KM, Friley WW, St. Claire III RL, Black C, Brouwer KR (2016) Basolateral efflux transporters: a potentially important pathway for the prevention of cholestatic hepatotoxicity. Appl in Vitro Toxicol 2(4):207–216

Jia W, Xie G, Jia W (2018) Bile acid-microbiota crosstalk in gastrointestinal inflammation and carcinogenesis. Nat Rev Gastroenterol Hepatol 15(2):111–128. https:// doi. org/ 10. 1038/ nrgas tro. 2017. 119

Jones H, Chen Y, Gibson C, Heimbach T, Parrott N, Peters S, Snoeys J, Upreti VV, Zheng M, Hall SD (2015) Physiologically based pharmacokinetic modeling in drug discovery and development: a pharmaceutical industry perspective. Clin Pharmacol Ther 97(3):247–262

Kis E, Ioja E, Nagy T, Szente L, Heredi-Szabo K, Krajcsi P (2009) Effect of membrane cholesterol on BSEP/Bsep activity: species specificity studies for substrates and inhibitors. Drug Metab Dispos 37(9):1878–1886

Koopman B, Kuipers F, Bijleveld C, Van Der Molen J, Nagel G, Vonk R, Wolthers B (1988) Determination of cholic acid and chenodeoxycholic acid pool sizes and fractional turnover rates by means of stable isotope dilution technique, making use of deuterated cholic acid and chenodeoxycholic acid. Clin Chim Acta 175(2):143–155

Kullak-Ublick GA, Stieger B, Meier PJ (2004) Enterohepatic bile salt transporters in normal physiology and liver disease. Gastroenterology 126(1):322–342. https:// doi. org/ 10. 1053/j. gastro.2003. 06. 005

Law V, Knox C, Djoumbou Y, Jewison T, Guo AC, Liu Y, Maciejewski A, Arndt D, Wilson M, Neveu V, Tang A (2014) DrugBank 4.0: shedding new light on drug metabolism. Nucleic Acids Res 42(D1):D1091–D1097

Lobell M, Sivarajah V (2003) In silico prediction of aqueous solubility, human plasma protein binding and volume of distribution of compounds from calculated pK a and AlogP98 values. Mol Diversity 7(1):69–87

Louisse J, Beekmann K, Rietjens IMCM (2017) Use of physiologically based kinetic modeling-based reverse dosimetry to predict in vivo toxicity from in vitro data. Chem Res Toxicol 30(1):114–125

Mano Y, Usui T, Kamimura H (2007) Effects of bosentan, an endothelin receptor antagonist, on bile salt export pump and multidrug resistance–associated protein 2. Biopharm Drug Dispos 28(1):13–18

Meyer RJ (1996) In vitro binding of the endothelin receptor antagonist ro 47-0203 to plasma proteins in man and animals, and red blood cell/plasma partitioning. Hoffmann-La Roche Ltd, Basel F

Morgan RE, van Staden CJ, Chen Y, Kalyanaraman N, Kalanzi J, Dunn RT, Afshari CA, Hamadeh HK (2013) A multifactorial approach to hepatobiliary transporter assessment enables improved therapeutic compound development. Toxicol Sci 136(1):216–241

Ning J, Rietjens IMCM, Strikwold M (2019) Integrating physiologically based kinetic (PBK) and Monte Carlo modelling to predict interindividual and inter-ethnic variation in bioactivation and liver toxicity of lasiocarpine. Arch Toxicol 93(10):2943–2960

Noor F (2015) A shift in paradigm towards human biology-based systems for cholestatic-liver diseases. J Physiol 593(23):5043–5055. https:// doi. org/ 10. 1113/ JP271 124

Nunes DRCMA, Breton MC, Monteiro CSJ, Dos Santos JL (2021) Drug induced liver injury: perspective of the adverse drug reaction reports to the Portuguese pharmacovigilance system from 2010 to 2019. Paper presented at the Healthcare

Olson H, Betton G, Robinson D, Thomas K, Monro A, Kolaja G, Lilly P, Sanders J, Sipes G, Bracken W, Dorato M (2000) Concordance of the toxicity of pharmaceuticals in humans and in animals. Regul Toxicol Pharmacol 32(1):56–67

Peters SA, Dolgos H (2019) Requirements to establishing confidence in physiologically based pharmacokinetic (PBPK) models and overcoming some of the challenges to meeting them. Clin Pharmacokinet 58(11):1355–1371

Ponz de Leon M, Murphy G, Dowling RH (1978) Physiological factors influencing serum bile acid levels. Gut 19(1):32–39

Punt A, Paini A, Spenkelink A, Scholz G, Schilter B, Van Bladeren PJ, Rietjens IMCM (2016) Evaluation of interindividual human variation in bioactivation and DNA adduct formation of estragole in liver predicted by physiologically based kinetic/dynamic and Monte Carlo modeling. Chem Res Toxicol 29(4):659–668

Punt A, Pinckaers N, Peijnenburg A, Louisse J (2020) Development of a web-based toolbox to support quantitative in-vitro-to-in-vivo extrapolations (QIVIVE) within nonanimal testing strategies. Chem Res Toxicol 34:460–472

R Core Team (2020) R: a language and environment for statistical computing. R Foundation for Statistical Computing, Vienna

Roda A, Cappelleri G, Aldini R, Roda E, Barbara L (1982) Quantitative aspects of the interaction of bile acids with human serum albumin. J Lipid Res 23(3):490–495

Roda A, Minutello A, Angellotti M, Fini A (1990) Bile acid structureactivity relationship: evaluation of bile acid lipophilicity using 1-octanol/water partition coefficient and reverse phase HPLC. J Lipid Res 31(8):1433–1443

Rodgers T, Rowland M (2006) Physiologically based pharmacokinetic modelling 2: predicting the tissue distribution of acids, very weak bases, neutrals and zwitterions. J Pharm Sci 95(6):1238–1257

Salemans J, Nagengast F, Tangerman A, Schaik AV, De Haan A, Jansen J (1993) Postprandial conjugated and unconjugated serum bile acid levels after proctocolectomy with ileal pouch-anal anastomosis. Scand J Gastroenterol 28(9):786–790

Sato M, Toshimoto K, Tomaru A, Yoshikado T, Tanaka Y, Hisaka A, Lee W, Sugiyama Y (2018) Physiologically based pharmacokinetic modeling of bosentan identifies the saturable hepatic uptake as a major contributor to its nonlinear pharmacokinetics. Drug Metab Dispos 46(5):740–748

Sips FLP, Eggink HM, Hilbers PAJ, Soeters MR, Groen AK, van Riel NAW (2018) In silico analysis identifies intestinal transit as a key determinant of systemic bile acid metabolism. Front Physiol 9:631. https:// doi. org/ 10. 3389/ fphys. 2018. 00631

Soars M, Burchell B, Riley R (2002) In vitro analysis of human drug glucuronidation and prediction of in vivo metabolic clearance. J Pharmacol Exp Ther 301(1):382–390

Srivastava A (2014) Progressive familial intrahepatic cholestasis. J Clin Exp Hepatol 4(1):25–36

Tetko IV, Gasteiger J, Todeschini R, Mauri A, Livingstone D, Ertl P, Palyulin VA, Radchenko EV, Zefirov NS, Makarenko AS, Tanchuk VY (2005) Virtual computational chemistry laboratory– design and description. J Comput Aided Mol Des 19(6):453–463

Vinken M (2018) In vitro prediction of drug-induced cholestatic liver injury: a challenge for the toxicologist. Arch Toxicol 92(5):1909–1912. https:// doi. org/ 10. 1007/ s00204- 018- 2201-4. pdf

Vinken M, Landesmann B, Goumenou M, Vinken S, Shah I, Jaeschke H, Willett C, Whelan M, Rogiers V (2013) Development of an adverse outcome pathway from drug-mediated bile salt export pump inhibition to cholestatic liver injury. Toxicol Sci 136(1):97–106

Voronova V, Sokolov V, Al-Khaifi A, Straniero S, Kumar C, Peskov K, Helmlinger G, Rudling M, Angelin B (2020) A physiology-based model of bile acid distribution and metabolism under healthy and pathologic conditions in human beings. Cell Mol Gastroenterol Hepatol 10(1):149–170. https:// doi. org/ 10. 1016/j. jcmgh. 2020. 02. 005

Weber C, Gasser R, Hopfgartner G (1999) Absorption, excretion, and metabolism of the endothelin receptor antagonist bosentan in healthy male subjects. Drug Metab Dispos 27(7):810–815

Xu JJ, Henstock PV, Dunn MC, Smith AR, Chabot JR, de Graaf D (2008) Cellular imaging predictions of clinical drug-induced liver injury. Toxicol Sci 105(1):97–105. https:// doi. org/ 10. 1093/ toxsci/ kfn109

Zhang X, Tsang AM, Okino MS, Power FW, Knaak JB, Harrison LS, Dary CC (2007) A physiologically based pharmacokinetic/ pharmacodynamic model for carbofuran in Sprague-Dawley rats using the exposure-related dose estimating model. Toxicol Sci 100(2):345–359

3.5 Supplementary file I

Table S1 Total BA pool sizes; scaled to presence of conjugates of CA, CDCA and DCA and to a 70 kg individual.

Koopman, 1988

CA (µmol/kg bw)	CDCA (µmol/kg bw)	total (µmol/kg bw)	total (µmol/70 kg)	scaled (µmol/70 kg)
11.1	19.8	30.9	2163	4023
18.4	9.8	28.2	1974	3672
36.5	35.5	72	5040	9374
42.5	25.1	67.6	4732	8802
19.2	20.5	39.7	2779	5169
14.3	24.9	39.2	2744	5104
26.8	25.7	52.5	3675	6836

Beuers, 1992

DCA (µmol/kg bw)	CDCA (µmol/kg bw)	total (µmol/kg bw)	total (µmol/70 kg)	scaled (µmol/70 kg)
16.3	22.4	38.7	2709	3684
42.1	18.9	61	4270	5807
30.2	13.6	43.8	3066	4170
42.2	24.9	67.1	4697	6388

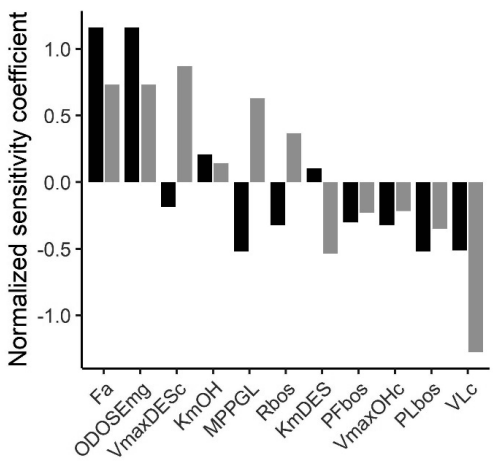

Figure S1 Sensitivity analysis of the PBK-model parameters on the predicted maximal bosentan and RO 47-8634 plasma concentrations. Black bars indicate bosentan, grey bars RO 47-8634. Only parameters with an absolute normalized sensitivity coefficient > 0.1 are shown. Fa= fraction absorbed, ODOSEmg= oral administered dose, VmaxDESc= maximal rate of RO 47-8634 formation, KmOH=Michaelis Menten constant of RO 48-5033 formation, MPPGL= microsomal protein per gram of liver, Rbos=blood:plasma ratio bosentan, KmDES=Michaelis Menten constant of RO 47-8634 formation, PFbos=fat/blood partition coefficent of bosentan, VmaxOHc=maximal rate of 48-5033 formation, PLbos= liver/blood partition coefficient of bosentan, VLc=fraction of liver tissue.

3.6 Supplementary file II PBK model code

```
; Date: June 2022
; Purpose: General PBK Model GCDCA, built with in vitro and in silico derived parameter values
; Species: Human
; Compiled by: Véronique de Bruijn
; Organisation: Wageningen University
;================================================================
;Physiological parameters
;================================================================
; tissue volumes
BW = 70 {Kg}      ; body weight human (variable, dependent on study)
VFc = 0.214       ; fraction of fat tissue                    reference: Brown et al. (1997)
VLc = 0.026       ; fraction of liver tissue                  reference: Brown et al. (1997)
VRc = 0.054       ; fraction of richly perfused tissue        reference: Brown et al. (1997)
VSc= 0.6033       ; fraction of slowly perfused tissue        reference: Brown et al. (1997)
VBc = 0.079       ; fraction of blood                         reference: Brown et al. (1997)
VIc = 0.009       ; fraction of intestinal tissue             reference: Brown et al. (1997)
VGc= 0.0007       ; fraction of gallbladder tissue            reference: Van Erpecum et al. (1992)
VLuc=0.014        ; fraction of intestinal lumen              reference: Brown et al. (1997)

VF = VFc*BW               {L or Kg} ; volume of fat tissue (calculated)
VL = VLc*BW               {L or Kg} ; volume of liver tissue (calculated)
VR = VRc* BW              {L or Kg} ; volume of  richly perfused tissue (calculated)
VS = VSc*BW               {L or Kg} ; volume of  slowly perfused tissue (calculated)
VB = VBc* BW              {L or Kg} ; volume of  blood (calculated)
VI = VIc*BW               {L or Kg} ; volume of intestinal tissue (calculated)
VG= VGc*BW                {L or Kg} ; volume of gall bladder tissue (calculated)
VLu=VLuc*BW               {L or Kg} ; volume of intestinal lumen (calculated)
;----------------------------------------------------------------------------------------------------------------
;blood flow rates
QC = 15*BW^0.74           {L/hr}    ; cardiac output   reference: Brown et al. (1997)
QFc = 0.052       ; fraction of blood flow to fat tissue              reference: Brown et al. (1997)
QLc = 0.046       ; fraction of blood flow to liver (excluding portal vein) reference: Brown et al. (1997)
QSc = 0.248       ; fraction of blood flow to slowly perfused tissue  reference: Brown et al. (1997)
QRc=0.473         ; fraction of blood flow to richly perfused tissue  reference: Brown et al. (1997)
QIc = 0.181       ; fraction of blood flow to intestines              reference: Brown et al. (1997)

QF = QFc*QC               {L/hr}    ; blood flow to fat tissue (calculated)
QL = QLc*QC               {L/hr}    ; blood flow to liver tissue (calculated)
QS = QSc*QC               {L/hr}    ; blood flow to  slowly perfused tissue (calculated)
QR = QRc*QC               {L/hr}    ; blood flow to richly perfused tissue (calculated)
QI = QIc*QC               {L/hr}    ; blood flow to intestines (calculated)
;================================================================
;Physicochemical parameters
;================================================================
```

```
;partition coefficients
logP =2.21                  ; Roda 1990
RGCDCA=0.55; blood:plasma ratio, 1-Hct, assumption
PF =0.05/RGCDCA             ; fat/blood partition coefficient       calculated using QPPR of Rodgers & Rowland
2006
PL = 0.09/RGCDCA; liver/blood partition coefficient     calculated using QPPR of Rodgers & Rowland 2006
PR = 0.125/RGCDCA           ; richly perfused tissue/blood partition coefficient       calculated using QPPR Rodgers
& Rowland 2006
PS = 0.19/RGCDCA            ; richly perfused tissue/blood partition coefficient       calculated using QPPR Rodgers
& Rowland 2006
PG=0.16/RGCDCA              ; gut/blood partition coefficient                  calculated using QPPR of Rodgers &
Rowland 2006

;================================================================
;Kinetic parameters
;================================================================
ka =1.047 {/hr}             ;absorption rate constant from intestinal lumen to liver, fitted to experimental data
Hepner (1977) and De Leon (1978)

;de novo synthesis in liver.
Ks=0.78*60*sens {umol/h/entire organ}       ; reference: Kullak-Ublick (2004)

;Faecal excretion
Kf=Ks {umol/h}                                      ; Faecal excretion equals the de novo synthesis

;biliary excretion from liver to bile canaliculi
VmaxBSEPc=5.848{umol/min/mg BSEP}                   ; reference: GCDCA from Kis (2009)
KmBSEP = 4.3 {umol/L}                               ; reference: Kis (2009)

MC=1                                    ; switch for Monte Carlo
aBSEPc=IF MC =1 THEN init(exp(NORMAL(-0.26, 0.403))) ELSE 0.839; BSEP protein abundance in pmoles/10^6
hepatocytes, reference Burt (2016)
aBSEP= IF aBSEPc  > 0.23 AND aBSEPc < 2.58  THEN aBSEPc ELSE 0.00000001

MWBSEP=140000                                       ; BSEP is a 140 kDa protein, 140 000 g/mol
Hep=99          {10^6 hepatocytes/g liver} ; reference Barter (2007)
WL=20*BW        {g}                                 ; reference Soars (2002)
SF=aBSEP*MWBSEP*Hep*WL*60*10^-9 {mg BSEP/entire lever}; scaling factor, calculated
VmaxBSEP=VmaxBSEPc*SF{umol/h/entire liver}

;uncompetitive BSEP inhibition by bosentan and its metabolite desmethyl bosentan (RO 47-8634)
Kibos=12 {umol/L}                       ; reference: Fattinger (2001)
KiDES=8.5 {umol/L}                      ; reference: Fattinger (2001)
VmaxBSEPapp=VmaxBSEP/(1+CVLbos/Kibos+CVLDES/KiDES)
```

```
;distribution of bile flow excreted from liver in the bile canaliculae
QIb = 0.5                              ; fraction of bile flow transported directly from liver to intestinal lumen via
common bile duct reference:  Molino (1986)
QGb = 1- QIb                           ; fraction of bile flow from liver stored in gall bladder, calculated

;systemic plasma concentration in fasting state
CBfs=2.4*sens {umol/L}     ; reference: García-Cañaveras (2001)

;sensitivity individual
sens=1
;===============================================================
;Run settings
;===============================================================
Gdose =3020*sens{umol}  ; dose in full gallbladder, Sips (2018)

dosingperiod =if time < 20 OR time > 32 AND time <44  OR time >56 AND time <68 THEN  1 else 0 ; stop
gallbladder contractions during the night

;time
Starttime =8 ; in hr
Stoptime = 80; in hr
DTMIN=1E-6
DTMAX=1E-4
DTOUT=0.01
TOLERANCE=1E-12
Method Auto
;===============================================================
;Model calculations
;===============================================================
; gall bladder compartment
;AG = amount in the gallbladder, umol
;AG' = Change in amount in the gallbladder, umol/hr
AG'=-pulse(AG,0, 4)*dosingperiod + VmaxBSEPapp*CVL/(KmBSEP+ CVL)*QGb
Init AG = Gdose
;-----------------------------------------------------------------------------------------------
; liver compartment
;AL = Amount in liver tissue, umol
;AL' = Change in amount in liver tissue in time,  umol/hr
AL' =QL*(CB-CVL)-VmaxBSEPapp*CVL/(KmBSEP+ CVL) + Ks + ka*ALu
            CL = AL/VL
            CVL = CL/PL
          Init AL=0
;-----------------------------------------------------------------------------------------------
; intestine compartment
;ALu= amount in intestinal lumen, umol
```

```
ALu'=pulse(AG,0, 4)*dosingperiod+VmaxBSEPapp*CVL/(KmBSEP+ CVL)*Qlb-Kf-ka*ALu
CLu=ALu/VLu
Init ALu=0

;AI' = amount GCDCA in the intestinal tissue remaining, umol
        AI' = QI*(CB-CVI)
        Init AI = 0
        CI=AI/VI
        CVI=CI/PG
;---------------------------------------------------------------------------------------------------------------
;fat compartment
;AF = Amount GCDCA in fat tissue, umol
          AF' = QF*(CB-CVF)
        Init AF = 0
        CF = AF/VF
          CVF = CF/PF
;---------------------------------------------------------------------------------------------------------------
;tissue compartment richly perfused tissue
;AR = Amount GCDCA in richly perfused tissue, umol
    AR' = QR*(CB-CVR)
    Init AR = 0
    CR = AR/VR
    CVR = CR/PR
;---------------------------------------------------------------------------------------------------------------
;tissue compartment slowly perfused tissue
;AS = Amount GCDCA in slowly perfused tissue, umol
    AS' = QS*(CB-CVS)
    Init AS = 0
    CS = AS/VS
    CVS = CS/PS
;---------------------------------------------------------------------------------------------------------------
; blood compartment

;AB = Amount GCDCA in blood (umol)
   AB' = QF*CVF + QL*CVL + QS*CVS + QR*CVR +QI*CVI - (QF+QL+QS+QR+QI)*CB
   Init AB =0
   CB = AB/VB
   CBtot=CB/RGCDCA+CBfs          ; concentration GCDCA in plasma, umol/L
;---------------------------------------------------------------------------------------------------------------
; Mass balance calculations
Total =Gdose+Ks
Calculated = AL+ AS+ AR + AB + AG + AF + AI +Kf + ALu

ERROR=((Total-Calculated)/Total+1E-30)*100
MASSBBAL=Total-Calculated + 1
```

```
;Submodel bosentan and its metabolite desmethyl bosentan (RO 47-8634)
;=====================================================================
;Physiological parameters
;=====================================================================
VRcbos =(VRc+VIc)                    ; fraction of richly perfused tissue
VScbos=(VSc+VGc+VLuc)    ; fraction of slowly perfused tissue

VRbos=VRcbos*BW                      ; volume of  richly perfused tissue (calculated)
VSbos=VScbos*BW                      ; volume of  slowly perfused tissue (calculated)
;---------------------------------------------------------------------------------------------------------------------
;blood flow rates
QRcbos = (QRc+QIc)                   ; fraction of blood flow to richly perfused tissue
QRbos=(QRcbos*QC) {L/hr}             ; blood flow to richly perfused tissue (calculated)

;=====================================================================
;Physicochemical parameters
;=====================================================================
;partition coefficients

;bosentan
Rbos= 0.6                    ; blood:plasma ratio (EMA 2004, Meyer 1996)
PFbos = 0.05/Rbos            ; fat/blood partition coefficient                    calculated using QPPR of Rodgers &
Rowland 2006
PLbos = 0.11/Rbos            ; liver/blood partition coefficient                  calculated using QPPR of Rodgers &
Rowland 2006
PRbos = 0.14/Rbos            ; richly perfused tissue/blood partition coefficient      calculated using QPPR Rodgers
& Rowland 2006
PSbos = 0.21/Rbos                    ; richly perfused tissue/blood partition coefficient      calculated using QPPR
Rodgers & Rowland 2006

;metabolite RO 47-8634 (desmethyl bosentan)
RDES=0.55                    ; blood:plasma ratio, assumption (1-Hct)
PFDES= 0.06/RDES             ; fat/blood partition coefficient                    calculated using QPPR of Rodgers &
Rowland 2006
PLDES= 0.15/RDES             ; liver/blood partition coefficient                  calculated using QPPR of Rodgers &
Rowland 2006
PRDES = 0.18       /RDES     ; rapidly perfused/blood partition coefficient calculated using QPPR of Rodgers &
Rowland 2006
PSDES = 0.30 /RDES           ; slowly perfused/blood partition coefficient   calculated using QPPR of Rodgers &
Rowland 2006

;=====================================================================
;Kinetic parameters
;=====================================================================
```

```
;Absorption from GI-tract to liver
kabos  =0.130                ; absorption {/hr}, fitted to in vivo data (Weber, 1999)
kbilebos= 23.660  ; biliary excretion bosentan {/hr}, fitted to in vivo data (Weber, 1999)
kbileDES=133.924             ; biliary excretion desmethyl bosentan {/hr}, fitted to in vivo data (Weber, 1999)
Fa=0.5                       ; fraction absorbed, reference: Weber (1996)
;-----------------------------------------------------------------------------------------------------------------
;Metabolism liver
MPPGL = 32 {mg/g}            ; microsomal protein per gram of liver, Barter (2007)

;based on metabolite formation of bosentan, scaled maximum rate of metapulism
;VmaxOH=maximum rate of hydroxyl bosentan formation
VmaxOHc = 16.4 {pmol/min/mg microsomal protein}          ; reference Sato (2008)
VmaxOH=VmaxOHc*MPPGL*WL*60*10^-6 {umol/h/entire liver}   ; calculated

; maximum rate of desmethyl bosentan formation
VmaxDESc= 7.53{pmol/min/mg microsomal protein}           ; reference Sato (2008)
VmaxDES=VmaxDESc*MPPGL*WL*60*10^-6 {umol/h/entire liver} ; calculated

;metabolites of bosentan, affinity constants (umol/L)
KmOH= 6.4{umol/L}                                        ; reference Sato (2008)
KmDES=4.8  {umol/L}                                      ; reference Sato (2008)

;non-saturable clearance
CLOHc = 0.158 {uL/min/mg microsomal protein}             ; reference Sato (2018)
CLDESc = 0.273 {uL/min/mg microsomal protein}            ; reference Sato (2018)
CLOH=CLOHc*MPPGL*WL*60*10^-6 {L/h/entire liver}          ; calculated
CLDES=CLDESc* MPPGL*WL*60*10^-6 {L/h/entire liver}       ; calculated

;====================================================================
;Run settings
;====================================================================

;Molecular weight
MWbos = 551.6   ; Molecular weight bosentan
MWDES=543.6     ; Molecular weight desmethyl bosentan

;oral dose of bosentan
ODOSEmg =500 {mg }                                       ; given oral dose in mg
ODOSEumol = ODOSEmg*1E-3/MWbos*1E6  {umol}               ; given oral dose recalculated to umol

;====================================================================
;Model calculations
;====================================================================
; stomach compartment
;Ast = Amount bosentan remaining in stomach, umol
```

```
Ast'=pulse(ODOSEumol*Fa,-4,12)-kabos*Ast
Init Ast=0

;Ast'=-kabos*Ast
;Init Ast=ODOSEumol*Fa

;-----------------------------------------------------------------------------------------------------------------
;liver compartment
;ALbos = Amount bosentan  in liver tissue, umol
        ALbos' =  kabos*Ast + QL*(CBbos - CVLbos)-AMOH'-AMDES'-Abilebos'
        Init ALbos = 0
        CLbos = ALbos/VL
        CVLbos = CLbos/PLbos

;AMOH= amount metabolized to metabolite RO48-5033 (hydroxyl bosentan), umol
        AMOH'= VmaxOH*CVLbos/(KmOH + CVLbos) + CLOH*CVLbos
        Init AMOH=0

;AMDES = amount metabolized to metabolite RO 47-8634 (desmethyl bosentan), umol
          AMDES' = VmaxDES*CVLbos/(KmDES + CVLbos)+CLDES*CVLbos
          init AMDES = 0

;Abilebos= biliary excretion of bosentan
        Abilebos' = kbilebos*ALbos
        Init Abilebos=0

;-----------------------------------------------------------------------------------------------------------------
;fat compartment

;AFbos = Amount bosentan in fat tissue (umol)
    AFbos' = QF*(CBbos-CVFbos)
    Init AFbos = 0
    CFbos = AFbos/VF
    CVFbos = CFbos/PFbos

;-----------------------------------------------------------------------------------------------------------------
;tissue compartment richly perfused tissue

;ARbos = Amount bosentan in richly perfused tissue (umol)
    ARbos' = QRbos*(CBbos-CVRbos)
    Init ARbos = 0
    CRbos = ARbos/VRbos
    CVRbos = CRbos/PRbos

;-----------------------------------------------------------------------------------------------------------------
```

```
;tissue compartment slowly perfused tissue

;ASbos = Amount bosentan in slowly perfused tissue (umol)
      ASbos' = QS*(CBbos-CVSbos)
      Init ASbos = 0
      CSbos = ASbos/VSbos
      CVSbos = CSbos/PSbos

;----------------------------------------------------------------------------------------------------------
; blood compartment

;ABbos = Amount bosentan in blood (umol)
     ABbos' = QL*CVLbos + QF*CVFbos+ QS*CVSbos + QRbos*CVRbos - (QL+QF+QS+QRbos)*CBbos
     Init ABbos = 0
     CBbos = ABbos/VB
     AUCbos' = CBbos
     Init AUCbos = 0

CBbosp_umol=CBbos/Rbos {umol/L}                    ; concentration bosentan in plasma, umol/L
CBbosp_ug=CBbosp_umol*MWbos {ug/L}          ; concentration bosentan in plasma, ug/L
;=====================================================================
;Mass balance calculations
;=====================================================================
Totalbos' = pulse(ODOSEumol *Fa, -4, 12)
Init Totalbos = 1E-50
Calculatedbos = Ast + AFbos + ASbos + ARbos  + ABbos + ALbos +AMOH + AMDES+Abilebos

ERRORbos=((Totalbos-Calculatedbos)/Totalbos+1E-30)*100
MASSBBALbos=Totalbos-Calculatedbos + 1
;=====================================================================
;desmethyl bosentan (RO 47-8634)
;=====================================================================
;ALDES = amount remaining in liver of metabolite RO 47-8634 (desmethyl bosentan) (umol)
        ALDES'=QL*(CBDES-CVLDES)+AMDES'-AbileDES'
        Init ALDES=0
        CLDES=ALDES/VL
        CVLDES=CLDES/PLDES

;AbileDES=amount desmethyl bosentan excrted via bile, umol
        AbileDES'=kbileDES*ALDES
        Init AbileDES=0
;----------------------------------------------------------------------------------------------------------
;fat compartment

;AFDES = Amount Desmethyl bosentan in fat tissue (umol)
```

```
    AFDES' = QF*(CBDES-CVFDES)
    Init AFDES = 0
    CFDES = AFDES/VF
    CVFDES = CFDES/PFDES

;-----------------------------------------------------------------------------------------------------------------
;tissue compartment richly perfused tissue

;ARDES = Amount Desmethyl bosentan in richly perfused tissue (umol)
    ARDES' = QRbos*(CBDES-CVRDES)
    Init ARDES = 0
    CRDES = ARDES/VRbos
    CVRDES = CRDES/PRDES

;-----------------------------------------------------------------------------------------------------------------
;tissue compartment slowly perfused tissue

;ASDES = Amount Desmethyl bosentan in slowly perfused tissue (umol)
    ASDES' = QS*(CBDES-CVSDES)
    Init ASDES = 0
    CSDES = ASDES/VSbos
    CVSDES = CSDES/PSDES

;-----------------------------------------------------------------------------------------------------------------
; blood compartment

;ABDES = Amount Desmethyl bosentan in blood (umol)
ABDES' = QL*CVLDES + QF*CVFDES+ QS*CVSDES + QRbos*CVRDES - (QL+QF+QS+QRbos)*CBDES
        Init ABDES = 0
        CBDES = ABDES/VB
        AUCDES' = CBDES
        Init AUCDES = 0

CBDESp_umol=CBDES/RDES {umol/L}                    ; concentration  desmethyl  bosentan in plasma, umol/L
CBDESp_ug=CBDESp_umol*MWDES {ug/L}   ; concentration  desmethyl bosentan in plasma, ug/L

;=====================================================================
;Mass balance calculations
;=====================================================================
TotalDES'=AMDES'
Init TotalDES=1e-50
CalculatedDES=AFDES+ARDES+ABDES+ALDES+ASDES+AbileDES

ERRORDES=((TotalDES-CalculatedDES)/TotalDES+1E-30)*100
MASSBBALDES=TotalDES-CalculatedDES + 1
```

References

Barter, Z. E., Bayliss, M. K., Beaune, P. H., Boobis, A. R., Carlile, D. J., Edwards, R. J., ... & Rostami-Hodjegan, A. (2007). Scaling factors for the extrapolation of in vivo metabolic drug clearance from in vitro data: reaching a consensus on values of human micro-somal protein and hepatocellularity per gram of liver. *Current drug metabolism*, *8*(1), 33-45.

Brown RP, Delp MD, Lindstedt SL, Rhomberg LR, Beliles RP (1997) Physiological parameter values for physiologically based pharmacokinetic models. Toxicol Ind Health 13(4):407-84

Burt, H. J., Riedmaier, A. E., Harwood, M. D., Crewe, H. K., Gill, K. L., & Neuhoff, S. (2016). Abundance of hepatic transporters in Caucasians: a meta-analysis. Drug Metabolism and Disposition, 44(10), 1550-1561.

De Leon, M. P., Murphy, G. M., & Dowling, R. H. (1978). Physiological factors influencing serum bile acid levels. *Gut*, *19*(1), 32-39.

EMA (2004). Scientific discussion. Retrieved from: https://www.ema.europa.eu/en/documents/scientific-discussion/tracleer-epar-scientific-discussion_en.pdf

Fattinger, K., Funk, C., Pantze, M., Weber, C., Reichen, J., Stieger, B., & Meier, P. J. (2001). The endothelin antagonist bosentan inhibits the canalicular bile salt export pump: a potential mechanism for hepatic adverse reactions. Clinical Pharmacology & Therapeutics, 69(4), 223-231.

García-Cañaveras, J. C., Donato, M. T., Castell, J. V., & Lahoz, A. (2012). Targeted profiling of circulating and hepatic bile acids in human, mouse, and rat using a UPLC-MRM-MS-validated method. *Journal of lipid research*, *53*(10), 2231-2241.

Hepner, G. W., & Demers, L. M. (1977). Dynamics of the enterohepatic circulation of the glycine conjugates of cholic, chenodeoxycholic, deoxycholic, and sulfolithocholic acid in man. *Gastroenterology*, *72*(3), 499-501.

Hofmann, A. F. (1999). Bile acids: the good, the bad, and the ugly. *Physiology*, *14*(1), 24-29.

Hofmann, A. F., Molino, G., Milanese, M., & Belforte, G. (1983). Description and simulation of a physiological pharmacokinetic model for the metabolism and enterohepatic circulation of bile acids in man. Cholic acid in healthy man. *The Journal of clinical investigation*, 71(4), 1003-1022.

Kis, E., Ioja, E., Nagy, T., Szente, L., Heredi-Szabo, K., & Krajcsi, P. (2009). Effect of membrane cholesterol on BSEP/Bsep activity: species specificity studies for substrates and inhibitors. *Drug metabolism and disposition*, 37(9), 1878-1886.

Kullak-Ublick, G. A., Stieger, B., & Meier, P. J. (2004). Enterohepatic bile salt transporters in normal physiology and liver disease. *Gastroenterology*, *126*(1), 322-342.

Meyer, R., J. . (1996). In vitro binding of the endothelin receptor antagonist ro 47-0203 to plasma proteins in man and animals, and red blood cell/plasma partitioning. *Basel F: Hoffmann-La Roche Ltd*.

Roda, A., Minutello, A., Angellotti, M. A., & Fini, A. (1990). Bile acid structure-activity relationship: evaluation of bile acid lipophilicity using 1-octanol/water partition coefficient and reverse phase HPLC. *Journal of lipid research*, *31*(8), 1433-1443.

Rodgers, T., & Rowland, M. (2006). Physiologically based pharmacokinetic modelling 2: predicting the tissue distribution of acids, very weak bases, neutrals and zwitterions. Journal of pharmaceutical sciences, 95(6), 1238-1257.

Sato, M., Toshimoto, K., Tomaru, A., Yoshikado, T., Tanaka, Y., Hisaka, A., ... & Sugiyama, Y. (2018). Physiologically based pharmacokinetic modeling of bosentan identifies the saturable hepatic uptake as a major contributor to its nonlinear pharmacokinetics. Drug Metabolism and Disposition, 46(5), 740-748.

Sips, F. L., Eggink, H. M., Hilbers, P. A., Soeters, M. R., Groen, A. K., & Van Riel, N. A. (2018). In silico analysis identifies intestinal transit as a key determinant of systemic bile acid metabolism. Frontiers in physiology, 9, 631.

Soars, M. G., Burchell, B., & Riley, R. J. (2002). In vitro analysis of human drug glucuronidation and prediction of in vivo metabolic clearance. *Journal of Pharmacology and Experimental Therapeutics*, *301*(1), 382-390.

Van Erpecum, K. J., Henegouwen, G. P. V. B., Stolk, M. F., Hopman, W. P., Jansen, J. B., & Lamers, C. B. (1992). Fasting gallbladder volume, postprandial emptying and cholecystokinin release in gallstone patients and normal subjects. *Journal of hepatology*, *14*(2-3), 194-202

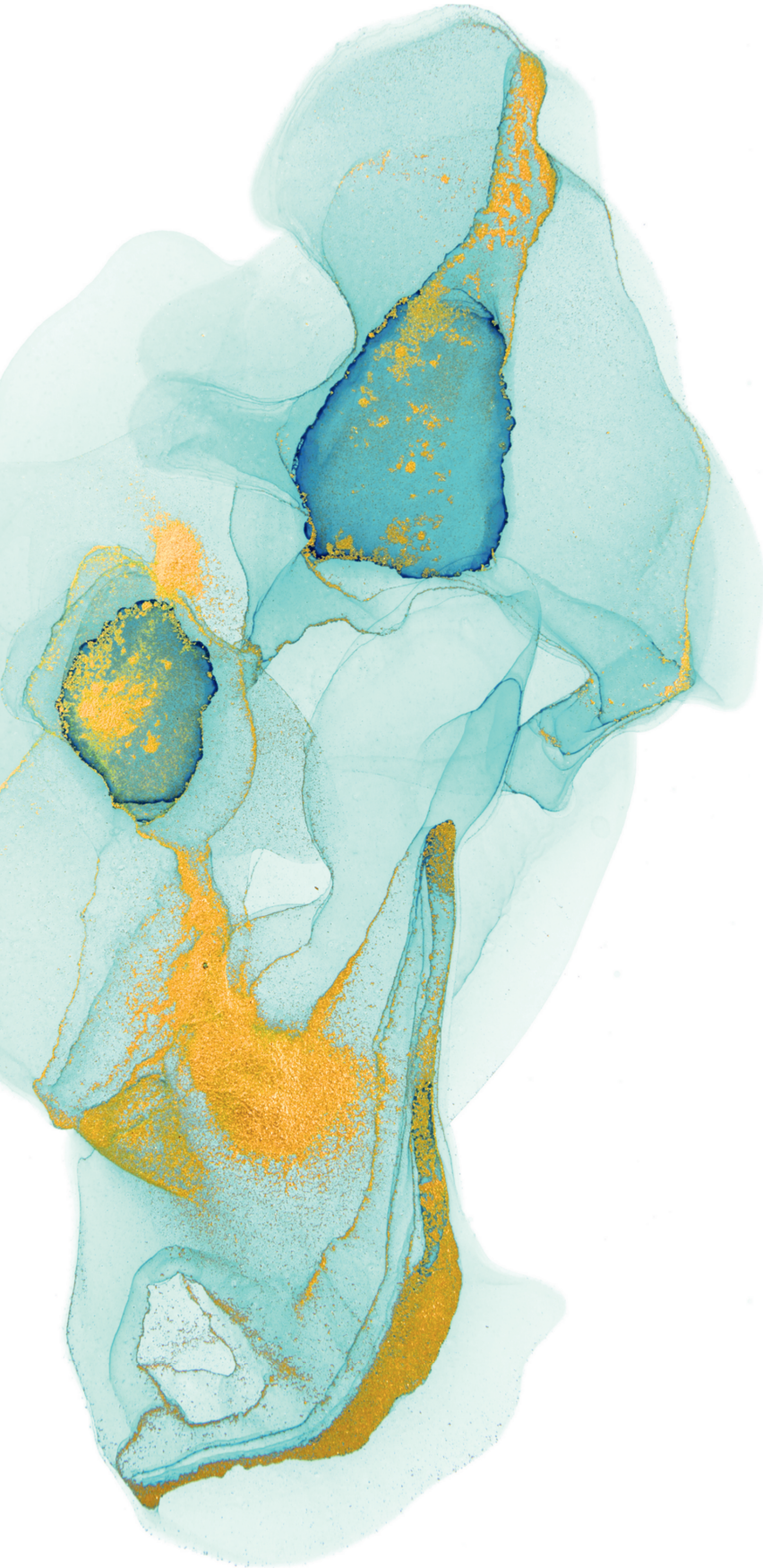

Chapter 4

Intestinal *in vitro* transport assay combined with physiologically based kinetic modeling as a tool to predict bile acid levels *in vivo*

Véronique M.P. de Bruijn, Willem te Kronnie, Ivonne M.C.M. Rietjens & H. Bouwmeester
Published in ALTEX-Alternatives to animal experimentation (2023) 40(4)

Abstract

Purpose · Bile acid homeostasis is vital for numerous metabolic and immune functions in humans. The enterohepatic circulation of bile acids is extremely efficient, with ~95% of the intestinal bile acids being reabsorbed. Disturbing intestinal bile acid uptake is expected to substantially affect intestinal and systemic bile acid levels. Here, we aimed to predict the effects of apical sodium-dependent bile acid transporter (ASBT)-inhibition on systemic plasma levels. For this, we combined the *in vitro* Caco-2 cell transport assays with physiologically based (PBK) modeling. For this proof-of-principle study we used the selective ASBT-inhibitor odevixibat (ODE) as a model compound.
Approach · Caco-2 cells grown on culture inserts were used to obtain transport kinetic parameters of glycocholic acid (GCA). The apparent Michaelis Menten constant ($K_{m,app}$), apparent maximal intestinal transport rate ($V_{max,app}$) and ODE's inhibitory constant (K_i) were determined for GCA. These kinetic parameters were incorporated in a PBK model and used to predict the ASBT inhibition effects on plasma bile acid levels.
Main findings · GCA is transported over Caco-2 cells in an active and sodium-dependent manner, indicating the presence of functional ASBT. ODE inhibited GCA transport dose-dependently. The PBK model predicted that oral doses of ODE reduced conjugated bile acid levels in plasma. Our simulations match *in vivo* data and provide a first proof-of-principle for the incorporation of active intestinal bile acid uptake in a bile acid PBK model. This approach could in future be of use to predict the effects of other ASBT-inhibitors on plasma and intestinal bile acid levels.

Key words: Bile Acids and Salts ● Caco-2 ● Apical sodium dependent bile acid transporter (ASBT) ● Odevixibat ● quantitative-*in-vitro*-to-*in-vivo* extrapolation (QIVIVE)

List of abbreviations: AOP, adverse outcome pathway; ASBT, apical sodium-dependent bile acid transporter; ABL, aqueous boundary layer; BA, bile acid; BABP, bile acid binding protein; BSEP, bile salt export pump; C_{max}, maximal concentration in plasma; DCA, deoxycholic acid; GCA, glycocholic acid; GCDCA, glycochenodeoxycholic acid; GDCA, glycodeoxycholic acid; LOD, limit of detection; LOQ, limit of quantification; NAFLD, non-alcoholic fatty liver disease; NTCP, Na^+-taurocholate cotransporting polypeptide; OATP: organic anion transporting polypeptide; ODE: odevixibat; OST α/β, organic solute transporter α/β; PBK, physiologically based kinetic; TEER, transepithelial electrical resistance; TCA, taurocholic acid; T_{max}, time it takes to reach C_{max}; uBA, unconjugated bile acid

4.1 Introduction

Bile acids (BAs) have emerged as critical signalling molecules for energy, glucose and lipid metabolism, cell proliferation as well as regulation of the immune system (Jia et al., 2018; Fuchs and Trauner, 2022). BA homeostasis is primarily regulated by the gut-liver axis, where primary BAs are produced in the liver, metabolized to more hydrophobic secondary BAs by the intestinal microbiome and taken up via the intestinal epithelium into the portal vein to be recirculated to the liver. The BA pool shapes the microbiome community by acting on bacterial cell membranes, but also reduces intestinal membrane integrity by affecting the epithelial cells (Begley et al., 2005). High amounts of the secondary BA deoxycholic acid (DCA) reduced intestinal integrity in pig colonic crypts (Leschelle et al., 2002) and in rabbit small intestine (Fasano et al., 1990). Reduced intestinal integrity is related to diarrhoea, bacterial overgrowth and inflammatory bowel disease (Marasco et al., 2022; Miele et al., 2009). Furthermore, bacterial products are more likely to translocate to the liver and trigger an inflammatory response in case of reduced membrane integrity. Intestinal inflammation may then translocate to the liver, ultimately resulting in liver inflammation and stress responses (Duan et al., 2022; Sabino et al., 2016). Disturbances of the BA pool predisposes an individual to the development of liver disease, *e.g.* cholestasis (Gijbels and Vinken, 2019), Non-Alcoholic Fatty Liver Disease (NAFLD) (Mouzaki et al., 2016) and gastrointestinal carcinogenesis (Li et al., 2022). It has been shown that fecal concentrations of DCA and its conjugates increased with disease activity and fibrosis stage, an important hallmark of NAFLD (Smirnova et al., 2022). Hence, a well-balanced BA pool is essential for gut-liver axis homeostasis and human health.

BAs are *de novo* synthesized in the liver from cholesterol. Upon conjugation with glycine or taurine, BAs are actively secreted via the Bile Salt Export Pump (BSEP) to the bile canaliculi (Lin et al., 2023). Via the bile canaliculi, the conjugated BAs enter the intestinal lumen where they can be deconjugated and where ~95% of intestinal BAs is reabsorbed via both active and passive processes (Kullak-Ublick et al., 2004). Unconjugated BAs are passively absorbed along the whole length of the small intestine, while the majority of both conjugated and unconjugated BAs is actively reabsorbed from the ileum (Martinez-Augustin and Sanchez de Medina, 2008; Krag and Phillips, 1974; Li et al., 2018). The most effective reabsorption of BAs takes place in the terminal ileum and is mediated by the apical sodium-dependent bile acid transporter (ASBT), a member of the solute carrier (SLC) super-family encoded by the *SLC10A2* gene (Dawson, 2011; Lin et al., 2023). Via ASBT, BAs are taken up in the enterocytes where they bind to the Bile Acid Binding Protein (BABP) and are excreted to the basolateral side in the portal blood via the organic solute transporter (OST) α/β (Lu et al., 2022). Via the portal vein the BAs are transported to the liver where they are taken up by Na^+-taurocholate cotransporting polypeptide (NTCP) and transporters from the organic anion transporting polypeptide (OATP) family (Chiang and Ferrell, 2022). BAs that escape ileal reabsorption are metabolized by the gut microbiome into a wide array of secondary BAs, followed by either absorption from the colon or fecal excretion (Jia et al., 2018). The remarkably efficient uptake of BAs from the intestinal lumen implies that this process is of crucial importance for BA homeostasis, and alterations in intestinal BA uptake potentially affect the onset and development of different types of liver disease (Duan et al., 2022; Yang et al., 2020). Consequently, ASBT has been an attractive target for drug development since its discovery. For instance, odevixibat (ODE) has recently been approved for the treatment of progressive familial intrahepatic cholestasis, and trials for the treatment of other cholestatic diseases are still ongoing (Deeks, 2021). ODE is a selective and reversible ASBT-inhibitor, and the drug reduces the BA levels in plasma/serum by reducing the reuptake of BAs in the ileum, while the fecal BA levels are increased (Graffner et al., 2016). Individuals with progressive familial intrahepatic cholestasis typically

have increased plasma BA levels, and a reduction is considered beneficial in these specific cases. Reduced bile acid absorption was observed in preclinical and clinical studies of inflammatory bowel disease, and was typically accompanied by decreased ASBT levels (Fitzpatrick and Jenabzadeh, 2020). This indicates that even though a reduction of ASBT-mediated BA absorption is beneficial for individuals suffering from cholestatic diseases, it might have an adverse effect on otherwise healthy individuals. Several xenobiotics, *e.g.* the mycotoxin deoxynivalenol and the antibiotic tobramycin, are known to reduce intestinal BA uptake *in vitro* (Wang et al., 2022; Zhang et al., 2022). For an accurate human hazard assessment of chemicals it is crucial to understand how xenobiotics alter BA homeostasis and could potentially affect host health.

Quantitative knowledge of the synthesis, absorption, distribution, metabolism and excretion of BAs is paramount for understanding BA-associated pathologies. Here, physiologically based kinetic (PBK) modeling provides a powerful tool to integrate physicochemical and biological properties of BAs, and to predict the effects of drug interventions or xenobiotic exposure without the need for animal derived data. PBK modeling contributes thus to the 3R principle (Replacement, Reduction and Refinement) in chemical risk assessment. Several kinetic models describing the processes involved in BA homeostasis have been developed previously. Early work describes the metabolism and circulation of several major BAs in the gastrointestinal tract and circulatory system (Hofmann et al., 1983; Molino et al., 1986). Active transport processes are increasingly being recognized as important modulators in the BA homeostasis, but they were not included in this early work. For example, inhibition of BSEP can lead to a toxic BA accumulation inside hepatocytes and cause cholestasis. The relevance of hepatic BSEP inhibition for cholestasis development has been recognized in the Cholestasis Adverse Outcome Pathway (AOP) (Vinken et al., 2013). Active transport processes were included in more recent modeling work (Sips et al., 2018; Voronova et al., 2020; Baier et al., 2019). Advancements in computational power and biological understanding of the processes involved in BA homeostasis allowed for the development of more complex and dynamic models. The work of Voronova et al (2020), for example, described the autoregulation of BA synthesis by farnesoid receptor X (FXR) (Voronova et al., 2020), and Sips et al. (2018) modelled the intestinal transit of BAs in detail (Sips et al., 2018). Increased complexity of mathematical models typically comes with an increased number of required input parameters – parameters that cannot always be derived experimentally and pose the risk of overfitting. Therefore, we previously developed a data-driven PBK model describing BA homeostasis, *i.e.* a PBK model with the vast majority of parameters derived experimentally. The model included active BSEP-mediated hepatic canalicular BA efflux (de Bruijn et al., 2022a), but did not yet include transporter-mediated hepatic sinusoidal BA uptake or ASBT-mediated ileal BA absorption. In the present study we aim to extend the PBK model to also include ASBT-mediated ileal BA absorption and NTCP-mediated hepatic uptake and predict the effects of ASBT-inhibition on systemic plasma levels. This provides mechanistic insights in the effects of ASBT and its inhibition on whole-body BA homeostasis, with a focus on the gut-liver axis. To this end, we employed PBK modeling and we evaluated the effect of ODE-mediated ASBT-inhibition on plasma BA levels. The required kinetic parameters for ileal absorption were derived from human Caco-2 cells grown in culture inserts. We focused on the glycine-conjugated forms of three major bile acids, *i.e.* glycocholic (GCA), glycochenodeoxycholic (GCDCA) and glycodeoxycholic acid (GDCA) and a generic unconjugated BA (uBA). The taurine-conjugates were not explicitly considered, as the BA pool in human serum consists of only ~15% taurine-conjugates, compared to ~45% glycine-conjugates and ~40% unconjugated BAs (Bathena et al., 2013). GCA and GDCA were selected, because their abundance in plasma showed the steepest decrease upon 7-day ODE-treatment in healthy individuals. GCDCA is the most abundant BA

in human plasma and was therefore also included. The model developed may serve as a quantitative tool to evaluate various potential mode-of-actions in the framework of BA-associated diseases upon exposure to xenobiotics.

4.2 Material & Methods

Cell culture

Human colon carcinoma Caco-2 cells were purchased from the American Type Culture Collection (Rockville, MD, USA. The Caco-2 cells (passage number 15–28) were grown at 37 °C with 5% CO_2 in Modified Eagle's Medium (MEM) GlutaMax™ supplemented with 20% (v/v) fetal calf serum, 0.86% (v/v) 50 mg/mL L-glutamine-Penicillin-Streptomycin solution and 0.86% (v/v) 100 mM pyruvate as culture medium (CM), all purchased at Gibco BRL (Breda, The Netherlands). Cells were subcultured twice a week at 50-60% confluence using 0.05% trypsin-EDTA (Gibco BRL).

Cell viability assessment

Caco-2 cells were seeded at 40 000 cells/well in a 96-well plate, and allowed to attach to the plate for 24 h. The effect of odevixibat (ODE) (99.85%, MedChemExpress, Monmoth Junction, NJ, USA) on the viability of Caco-2 cells 24h post-seeding was evaluated by using the WST-1 assay. Briefly, Caco-2 cells were exposed to 0–500 µM ODE for 24 h. ODE was dissolved in dimethylsulfoxide (DMSO) (Merck KGaA, Darmstadt, Germany) and 200× diluted in CM. 0.5 µM potassium dichromate was used as a positive control. Subsequently, the cells were incubated with WST-1 reagent 2-(2-methoxy-4-nitrophenyl)-3-(4-nitrophenyl)-5-(2,4-disulfophenyl)-2H-tetrazolium (Sigma-Aldrich, St. Louis, MO, USA) at 37°C. For this, WST-1 was added at 5% of the medium volume and the absorbance was measured at 440 nm and 620 nm with a SpectraMax iD3 multi-mode microplate reader (Molecular Devices; San Jose, CA, USA) after 60 min. Data were obtained by subtracting the 620 nm signal from the 440 nm signal. The cell viability was expressed as percentage of the solvent control group.

Intestinal Caco-2 monolayer barrier integrity assessment

Caco-2 cells were seeded at 180 000 cells/cm^2 in 24-well polycarbonate membrane inserts with 0.4 µm pore size (Corning Costar, Schnelldorf, Germany) and maintained in culture for 19-21 days. The integrity of Caco-2 cells was assessed using transepithelial electrical resistance (TEER) and/or the lucifer yellow assay. The TEER was measured with MilliCell® ERS-2 Epithelial Volt-Ohm Meter (Millipore, Amsterdam, The Netherlands). The TEER was measured prior to and post transport experiments, and data obtained from inserts with TEER values > 300 Ω × cm^2 were considered acceptable. For the lucifer yellow assay, the exposure medium was removed by rinsing the monolayers with Hank's balanced salt solution (Gibco BRL) supplemented with 10 mM HEPES (transport buffer), at pH 7.4. After that 50 µM lucifer yellow (Sigma-Aldrich) in DMSO (0.5% v/v) in transport buffer was added to the apical side of the culture insert. After 60 min, samples were taken basolaterally and the fluorescence was measured at 485/535 nm excitation/emission with a SpectraMax iD3 multi-mode microplate reader (Molecular Devices). Apparent permeability values (P_{app}) were calculated according to the following equation:

$$P_{app} = \frac{dQ}{dt} \times \frac{1}{A \times C_0} \quad \text{Eq. 1}$$

Where P_{app} is expressed in cm/s, dQ/dt is the change in the basolateral lucifer yellow concentration (nmole/s), A is the surface of the culture insert (cm^2) and C_0 is the initial apical lucifer yellow

concentration (nmole/cm^3). Lucifer yellow P_{app} values <0.4 × 10^{-6} cm/s were considered acceptable (Wang et al., 2008).

Transport assays

For the transport assays, Caco-2 monolayers grown in culture inserts for 19-21 days were used. CM was removed and replaced with transport buffer. The cells were allowed to equilibrate for 30 mins. Next, transport buffer was removed, the test solution was added apically and samples were taken at the basolateral side after 0-180 min of incubation. The test solutions contained 0.5% DMSO (v/v). In the first set of experiments, the cells were incubated with 5 µM glycocholic acid hydrate (GCA) (Sigma-Aldrich, ≥97%), deoxycholic acid (Sigma-Aldrich, ≥99%), glycochenodeoxycholic acid or glycodeoxcycholic acid (Avanti, Birmingham, AL, USA, ≥99%) and samples were taken after 0, 30, 60, 90, 120, 150 and 180 min of incubation. These experiments were performed at 4°C and 37°C to distinguish between active and passive transport processes. After 180 minutes, samples were taken from the apical and basolateral chamber, and after washing twice with ice-cold PBS, the membrane was cut out of the culture insert and transferred to an Eppendorf tube containing 65% (v/v) MeOH in MilliQ. The samples were ultrasonicated for 15 mins (Bandelin Sonorex rk100), centrifuged for 15 mins at 15,000*g* and the supernatant was transferred to LC-MS/MS vials and stored at -20°C until analysis by LC-MS/MS. The amounts detected in the cells, apical and basolateral chamber were summed up to calculate the mass balance. Mass balances were considered acceptable when >80% of the initially added amount was recovered.

In further experiments, GCA was used as model BA. Due to the similar physicochemical properties of the tested BAs, it was assumed that the inhibitor constant (K_i) was independent of the substrate used. As described in section 2.8, literature was used to translate the experimentally obtained kinetic parameters for GCA to kinetic parameters for GCDCA and GDCA. Cells were incubated at 37°C with 5 µM GCA and an ODE concentration range (0.0005 – 5 nM) to determine the half inhibitory concentration (IC_{50}) of ODE on GCA transport. Next, the cells were incubated under time-optimised conditions with a concentration range of GCA to determine its kinetic parameters ($V_{max,app}$ and $K_{m,app}$). As sodium-binding drives the conformational changes in ASBT required for transport of its substrates (Al-Hilal et al., 2014), we performed transport assays in transport buffer without sodium to confirm the sodium-dependency of the transport and quantify the passive transport rate at different GCA concentrations. The active transport rate was determined by subtracting the passive transport rate from the total transport rate. The K_i was determined by incubating the cells with a concentration range of GCA in the presence of an ODE concentration close to the IC_{50}. Albeit it is unlikely that ODE affected passive sodium-independent transport, this was not experimentally confirmed in the current work. We assumed that the passive transport rate was not altered by addition of ODE. All transport assays were performed in triplicate.

Reusing culture inserts

To overcome the limited availability of culture inserts, they were reused up to one time based on the protocol by Kato et al. (2021). Briefly, the cells were removed from the culture inserts after performing a transport assay with 0.25% (v/v) trypsin-EDTA and kept sterile. Firstly, culture inserts were incubated with trypsin-EDTA for 1 h at 37°C. Trypsin-EDTA was aspirated and replaced with fresh trypsin-EDTA solution, both apical and basolateral. After 24 h, all trypsin-EDTA was removed and the culture inserts were washed twice with PBS, followed by two washes with sterile MilliQ water. Culture inserts were left to airdry and stored at 4°C until further use. We did not observe any significant

differences in TEER values between new and recycled culture inserts. WST-1 showed similar cell viability (Supplementary Material I Figure S1), and we did not detect any BAs in the basolateral chamber when we performed a blank transport assay without BAs added (Sharanek et al., 2015).

Bile acid profiling using LC-MS/MS

BA analysis was performed on a triple quadrupole LC-MS/MS system, model LCMS-8045 (Shimadzu Corporation, Japan) and based on our previous work (de Bruijn et al., 2022b; Zhang et al., 2022; Wang et al., 2022). GCA/GCDCA/GDCA/DCA were quantified. BAs in samples and standards were separated on a Kinetex C18 column (1.7 µm × 100 A × 50 mm × 2.1 mm, Phenomenex 00B-4475-AN, Utrecht, the Netherlands) using an ultra-high performance liquid chromatography (UHPLC) system (Shimadzu) with gradient elution using MilliQ water (0.01% formic acid) and methanol/acetonitrile (50% v/v) as mobile phase A and B, respectively. In order to enhance chromatographic performance, a C18 2.1 mm security guard (Phenomenex AJ0-8782) precolumn was used.

Samples were injected (2 µL) onto the column equilibrated in 30% B at a flow rate of 0.4 mL/min. Initially, the mobile phase composition was 30% B, followed by a linear ramp to 70% B until 10.0 min. A linear change to 98% B was executed until 11.0 min, which was held for another 7 min before returning to 30% B at 19.0 min and remained until 25 min. The column temperature was set at 40℃ and the sample tray temperature was set at 4 ℃.

The mass spectrometer (MS) used electrospray ionization (ESI) in negative ion mode. The ESI parameters were as follows: Nebulizing gas flow, 3L/minutes; drying gas flow and heating gas flow, 10 L/minute; Interface temperature, 300 ℃; Desolvation temperature, 526 ℃; heat block temperature, 400 ℃. Selective ion monitoring (SIM) and multiple reaction monitoring (MRM) were used for the detection of the bile acids.

Limit of Detection (LOD) and Limit of Quantification (LOQ) of BA concentration in transport buffer were based on the signal-to-noise ratio. Signal-to-noise ratios of 3:1 and 10:1 were used as these are generally accepted for estimating LOD and LOQ, respectively (Shrivastava and Gupta, 2011). Here, LOD and LOQ were set to BA concentrations in transport buffer that resulted in a signal-to-noise ratio of at least 3:1 or 10:1, respectively. For subsequent calculations concentrations <LOD were set to 0 and concentrations ≥LOD and <LOQ were set to 0.5 × LOQ. As we observed a matrix effect on the sensitivity of our analytical method, standards for the calibration curve were prepared in transport buffer. Data were collected and processed using the LabSolutions software (Shimadzu). The MS parameters, LODs and LOQs are provided in Supplementary material I Table S1.

Data analysis

R version 4.1.0. was used for all data analysis and simulations (R Core Team, 2022). The R package tidyverse version 1.3.1 was used for data exploration and visualization (Wickham, 2019). Statistical significance was determined by a one-way ANOVA followed by Bonferroni's correction for multiple tests. Results were considered statistically significant when $p<0.05$. The appropriate model to estimate the IC_{50} of ODE-mediated inhibition of GCA transport was selected by minimizing the logLikelihood. The best fit was achieved by the three-parameter log-logistic function using the package 'drc' version 3.0.1 (Ritz et al., 2015). The lower and upper limit were constrained to 0 and 100 (%), respectively, and the Hill slope was variable. From the Lineweaver-Burk plot (Lineweaver and Burk, 1934), we derived that ODE inhibited GCA transport in a competitive nature. Previous research showed that *in vitro* permeability is affected by unstirred water layers in the vicinity of the culture insert and the culture insert itself, which is jointly referred to as the aqueous boundary layer (ABL). The ABL acts as a

permeability barrier in transport experiments and was previously shown to bias kinetic estimates (Balakrishnan et al., 2007). Therefore, taking into account the aqueous boundary layer (ABL) resistance, the transport rate could be described as (Balakrishnan et al., 2007) (Eq. 2):

$$V_{app} = \frac{P_{ABL} \times \frac{V_{max,app}}{K_{m,app}\left(1 + \frac{[\mathrm{ODE}] \times F_{ub}}{K_i}\right) + [GCA] \times F_{ub}}}{P_{ABL} + \frac{V_{max,app}}{K_{m,app}\left(1 + \frac{[\mathrm{ODE}] \times F_{ub}}{K_i}\right) + [GCA] \times F_{ub}}} \times [\mathrm{GCA}] \times F_{ub} \quad \text{Eq. 2}$$

Where V_{app} is the active apparent GCA transport rate from the apical to basolateral chamber in nmoles $min^{-1} cm^{-2}$, P_{ABL} the permeability across the ABL in cm/min, $V_{max,app}$ the maximal apparent active GCA transport rate nmoles $min^{-1} cm^{-2}$, [GCA] the concentration of GCA in nmoles cm^{-3}, F_{ub} the fraction unbound *in vitro,* $K_{m,app}$ the apparent Michaelis-Menten constant in nmoles cm^{-3}, [ODE] the concentration of ODE in nmole/L and K_i the inhibitor constant in nmole/L. P_{ABL} was set to 4.2×10^{-3} cm min^{-1} (Balakrishnan et al., 2007). Fraction unbound *in vitro* was set to 1, *i.e.* the nominal concentration equalled the free concentration. This was justified as the transport buffer did not contain any protein (Gilbert-Sandoval et al., 2020). The parameters were optimized using the 'nls' function in R (R Core Team, 2022).

Physiologically based kinetic (PBK) model

To describe the synthesis, absorption, distribution, metabolism and excretion of BAs, four physiologically based kinetic (PBK) submodels were constructed; a glyochenodeoxycholic acid (GCDCA), a glycocholic acid (GCA), a glycodeoxycholic acid (GDCA) and an unconjugated BA (uBA) model. Combined these BAs represent ~85% of the BA pool in human serum (Bathena et al., 2013). The PBK submodels were based on our previous work (de Bruijn et al., 2022a). Modifications were made to expand the model to four BAs instead of one lumped BA pool, to describe intestinal transit and absorption in more detail and the liver as a permeability-limited model. Briefly, each submodel consisted of separate compartments representing gall bladder, intestine, blood, rapidly perfused tissue, slowly perfused tissue, adipose tissue and extra- and intracellular water in liver. Figure 1 displays the conceptual model. In PBK models, organs are typically described using perfusion-limited models. This modeling approach assumes that compounds diffuse passively into the organ's water and are instantly homogenously distributed throughout the organ (Rietjens et al., 2011). For transporter-mediated uptake, however, permeability and not perfusion is the rate-limiting step. Therefore, perfusion-limited models cannot be used and a permeability-limited model should be used to simulate transporter-mediated uptake (Jamei et al., 2014). In these models, the respective organ is divided in an extracellular water and intracellular water compartment. In the present BA model the liver compartment was modelled in this way to enable description of the NTCP-mediated active transport from the extracellular to the intracellular liver water compartment and of the BSEP-mediated active transport from the intracellular water compartment to the bile. The extracellular water compartment is in instantaneous equilibrium with the blood in the vascular space and serves as a barrier compartment for entry into the intracellular tissue compartment. As sinusoidal efflux is low under normal physiological conditions (Dawson et al., 2009), this process was not included to limit model complexity. The extracellular water:plasma partition coefficients were calculated by a quantitative property-property relationship (Peyret et al., 2010). The BA fraction available for transport and metabolism in intracellular and extracellular water was set to 1, since transcellular trafficking of BAs is

highly efficient and effectively mediated by bile acid-binding proteins (BABPs) (Toke, 2022). Tissue:plasma partition coefficients for the BAs were calculated by a method described in literature (Rodgers and Rowland, 2006) and obtained via the QIVIVE toolbox (Punt et al., 2020). Recent work showed that the method of Lobell and Sivarajah (2003) to describe the fraction unbound resulted in the most accurate model predictions (Punt et al., 2022), hence this method was used here. As deoxycholic acid (DCA) is the most abundant uBA in human serum, DCA's physicochemical properties were selected to describe uBAs. The physicochemical properties of the BAs used to calculate the tissue:plasma partition coefficients are described in Table 1.

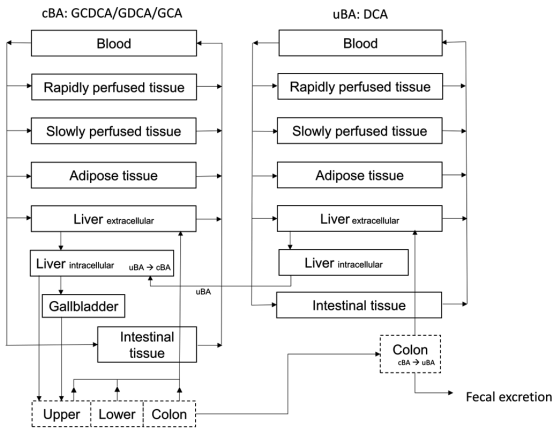

Figure 1 Conceptual model. cBA=conjugated BA, uBA=unconjugated BA, GCA=glycocholic acid, GCDCA=glycochenodeoxycholic acid, GDCA=glycodeoxcycholic acid, DCA=deoxycholic acid

Table 1 Physicochemical properties of the model BAs used to calculated the blood:tissue partition coefficients

	GCDCA	GCA	GDCA	DCA	Ref.
pKa	3.77	3.77	4.6	4.65	(Law et al., 2014), (Schwarz et al., 1996)
logP	2.12	1.65	2.25	3.5	(Roda et al., 1990)
MW	449.62	465.6	449.62	392.57	
Fraction unbound	0.061	0.088	0.055	0.02	Calculated, (Lobell and Sivarajah, 2003)

The enterohepatic circulation was included by a circulation of BA between the liver, gall bladder and intestine. BAs were *de novo* synthesized in the liver and excreted via the intestinal compartments into the feces. Hepatic BA efflux was simulated to be actively transported from the liver directly into the intestine or to the gallbladder by BSEP following Michaelis-Menten kinetics. The BSEP-mediated effluxes of BAs were described by the following equation (Eq. 3):

$$V_{BSEP} = \frac{V_{max,BSEP} \times [CVL]}{K_{m,BSEP} + [CVL]} \quad \text{Eq.3}$$

Where V_{BSEP} is the BSEP-mediated efflux of BAs from the liver in µmole/h, $V_{max,BSEP}$ is the maximum rate of BSEP-mediated BA efflux from the liver µmole/entire liver/hour, [CVL] the free

concentration of BAs in the liver in µmole/L and $K_{m,BSEP}$ the Michaelis-Menten constant in µmole/L for BSEP-mediated BA efflux.

The $V_{max,app}$ and $K_{m,app}$ for BSEP-mediated transport of GCDCA and GCA were taken from literature as obtained in a vesicular transport assay in a baculovirus-infected Sf9 system (Kis et al., 2009) and scaled to the *in vivo* situation as described previously (de Bruijn et al., 2022a). The authors showed that the $V_{max,app}$ values in the vesicular transport assay increased upon the addition of physiological levels of cholesterol, hence, these values were used in the current PBK model. The literature study investigated GCA and GCDCA, but not GDCA (Kis et al., 2009). Therefore, the kinetic data for BSEP-mediated GDCA transport were extracted from a study with transfected HEK293 cells reported by Notenboom et al. (2018). The $V_{max,app}$ of BSEP-mediated transport as obtained by Notenboom et al. (2018) was initially measured in pmole/min/mg protein. To make the measurements consistent with GCA and GCDCA, the $V_{max,app}$ values for GDCA were converted to µmole/min/mg BSEP using GCDCA mediated transport, which was measured in both the study by Notenboom et al. (2018) and Kis et al. (2009), as a reference. Consequently, the GDCA simulations were performed with $V_{max,app,GDCA} = V_{max,app,GCDCA[Sf9\ vesicles]} / V_{max,app,GCDCA[HEK293\ vesicles]} \times V_{max,app,GDCA[HEK293\ vesicles]}$=8.4 µmole/min/mg BSEP.

The intestine was divided in three compartments: 1) the upper intestines (duodenum + jejunum), where BAs are passively absorbed, 2) the lower intestine (ileum), where BAs are absorbed through an carrier-mediated process, and 3) the colon, where BAs are rapidly deconjugated and subsequently passively absorbed. Transit times were taken from the modified GI transit absorption (GITA) model introduced by Kimura and Higaki (2002), different transit times were used during fasting (17:30 – 8:00) and fed state. During day time, three meals and gall bladder contractions were simulated, *i.e.* at 8:00, 12:00 and 16:00. The parameters describing passive uptake were derived from perfusion studies (Krag and Phillips, 1974), and were assumed to be the same for jejunum and colon.

Kinetic parameters for active GCA transport were derived from our Caco-2 study. For scaling to the *in vivo* situation, the experimentally derived $V_{max,app}$ was multiplied by the total surface of the ileum and an empirical scalar, which was calculated as follows (Eq. 4):

$$SF = \pi d \times l \times ES \qquad \text{Eq. 4}$$

Where S is the ileal surface in cm^2, d is the diameter of the ileum (cm), l is the length of the ileum (cm) and p represent the mathematical constant of 3.14. A diameter and length of 5 and 300 cm were taken, respectively (Kararli, 1995). ES is an empirical scalar to better approximate the *in vivo* situation and was set to 2.8. ES accounts for inherent differences between Caco-2 cells and the human entire ileum, such as variations in ASBT expression or activity, tissue complexity and cellular interactions.

Subsequently, the calculated GCA $V_{max,\ in\ vivo}$ was used to scale the relative $V_{max,\ invitro}$ of GCDCA and GDCA obtained from literature to the *in vivo* situation. These values were retrieved from an ASBT-Madin-Darby canine kidney (MDCK) monolayer assay (Balakrishnan et al., 2006). The authors reported a large variation in ASBT expression levels between studies, therefore, they measured taurocholic acid flux to serve as a normalizing approach. In this way they obtained a V_{max} relative to the TCA V_{max} for 15 different BAs. We used the following equation to scale the relative V_{max} ($V_{max,BA,rel}$) to the *in vivo* V_{max} ($V_{max,BA,\ in\ vivo}$):

$$V_{max,BA,in\ vivo} = V_{max,BA,rel} \times \frac{V_{max,GCA,in\ vivo}}{V_{max,GCA,rel}} \qquad \text{Eq. 5}$$

Where $V_{max,BA,\ in\ vivo}$ is the *in vivo* maximal ASBT-mediated transport rate for the BA of interest, $V_{max,BA,rel}$ the maximal ASBT-mediated transport rate for the BA of interest relative to TCA, $V_{max,GCA,invivo}$ the maximal ASBT-mediated GCA transport rate obtained from our *in vitro* studies and scaled to the *in vivo* situation (Eq. 4) and $V_{max,GCA,rel}$ the maximal ASBT-mediated transport rate of GCA relative to TCA. For GDCA and GCDCA $K_{m,app}$ values from Balakrishnan et al. (2006) were incorporated in the PBK model without any further scaling. For GCA, we averaged our experimentally derived $K_{m,app}$ and the $K_{m,app}$ values from Balakrishnan et al. (2006). The effects of the different values for $K_{m,app}$ on the outcomes of the model calculations were also analyzed.

BAs escaping ileal absorption enter the colon, where they are rapidly and instantly deconjugated by the gut microbiome (Zhang et al., 2022). Upon reabsorption and entering the liver, these uBAs are rapidly and instantly conjugated (Falany et al., 1994). This is supported by the fact that only 0.3% of hepatic BAs exist in its unconjugated form (Garcia-Canaveras et al., 2012). Consequently, the intestinal deconjugation and hepatic conjugation rates were set to 1000 hr^{-1}.

Hepatic uptake of conjugated BAs from the extracellular water into the intracellular water was simulated as a permeability limited NTCP-mediated process. uBAs are taken up via passive diffusion (Notenboom et al., 2018). In this study, it was assumed that the diffusion of uBAs from the extracellular water to the intracellular water occurs at a rate equivalent to the hepatic blood flow. The $K_{m,app,}$ $V_{max,app}$ and scaling factor for *vitro-in vivo* scaling for the NTCP-mediated transport were obtained from a study with NTCP-transfected HEK293 cells (Notenboom et al., 2018). These authors determined the scaling factor by comparing the NTCP abundance in NTCP-transfected HEK293 cells and human liver tissue. The hepatic BA uptake rate was described by the following equation (Eq. 6):

$$\frac{d}{dt}AL_{IW,upt} = \frac{V_{max,NTCP} \times [CVL_{EW}]}{K_{m,\mathrm{NTCP}} + [\mathrm{CVL}_{EW}]} \qquad \text{Eq.6}$$

Where d/dt $AL_{iw,upt}$ is the BA uptake rate into the intracellular water in µmole/entire liver/hour, CVL_{EW} the effluent concentration of the extracellular water, $V_{max,NTCP}$ is the maximal NTCP-mediated uptake rate in µmole/entire liver/hour, and $K_{m,NTCP}$ the Michaelis-Menten constant in µmole/L for NTCP-mediated uptake. The $V_{max,NTCP}$ in pmoles min^{-1} 10^{-6} hepatocytes was extrapolated to units appropriate for the PBK model, *i.e.* µmoles $hour^{-1}$ entire $liver^{-1}$, by multiplying the $V_{max,NTCP,}$ with the hepatocellularity (10^6 hepatocytes/g liver) (Barter et al., 2007), weight of the liver (g) (Soars et al., 2002), 60 to convert minutes to hours and 10^{-6} to convert pmoles to µmoles. OATP-transporters were not explicitly considered, because rat Ntcp was proven to be responsible for more than 80% of conjugated bile acids (TCA) uptake (Kouzuki et al., 1998) and we assumed a comparable ratio in human hepatocytes. Instead, $V_{max,NTCP}$ was divided by 0.8 to account for the additional effects of OATP-mediated transport. As an up to 18-fold difference in GCDCA affinity for NTCP was reported in literature (Notenboom et al., 2018; Jani et al., 2018), GCDCA simulations were ran with the K_m as reported by Notenboom et al., a 18-fold reduced K_m and the average of these two values.

Lastly, given that the inhibition of ASBT by ODE was shown to be competitive in nature, the effects of ODE on the plasma BA concentrations was simulated by adjusting the K_m of ASBT-mediated uptake with a modulation factor of $1 + \frac{[\mathrm{ODE}] \times \mathrm{F}_{ub}}{Ki}$ as described in Eq. 2. Where ODE is the total concentration of ODE in the ileum, F_{ub} is the fraction unbound in the ileum *in vivo* and K_i the inhibitory constant as derived from our experiments. As ODE is poorly absorbed, no absorption was simulated and the full dose was assumed to be equally distributed over 9 L of gastrointestinal fluid (Deeks, 2021; Hendriksen et al., 2003). F_{ub} in the ileum was set equal to the F_{ub} in plasma, *i.e.* 0.3% (EMA, 2021).

The differential model equations were encoded and solved using the package 'RxODE' version 1.1.5 (Fidler M, 2022). The model code and input parameters are available in the 4.6 Supplementary Material II.

Sensitivity analysis

To assess the influence of the parameters on the model outcome, a local sensitivity analysis was performed for the C_{max} of BAs using the package 'FME' version 1.3.6.2 (Soetaert and Petzoldt, 2010). The sensitivity analysis for T_{max} was performed manually. Based on the method reported by Evans and Andersen (2000), the sensitivity coefficients (SCs) for the model parameters were calculated as follows:

$$SC = \frac{C' - C}{P' - P} \times P/C \qquad \text{Eq. 7}$$

where C indicates the initial value of the model output, C′ indicates the modified value of the model output resulting from an increase in the parameter value. P indicates the initial parameter value and P′ indicates the modified parameter value after a 5% increase of its value, keeping all other parameters at their original value.

4.3 Results

Bile acids cross Caco-2 monolayers via passive and active transport

19-21 day old Caco-2 monolayers grown in culture inserts were apically exposed to 500 pmoles of four BAs to optimize the incubation time for obtaining kinetic parameters and study the mode of transport. We observed apical-to-basolateral transport of glyochenodeoxycholic acid (GCDCA), glycocholic acid (GCA), glycodeoxycholic acid (GDCA) and deoxycholic acid (DCA). Transport of GCA was observed exclusively at 37°C (>300 pmoles), no transport was detected at 4°C. Comparable amounts GCDCA and GDCA were transported at 37°C, while for these two conjugated BAs limited transport at 4°C was observed especially at 180 min, albeit so low that it could not be quantified (<LOQ) (Figure 2). DCA transport was observed at both 4°C and 37°C without a significant effect of temperature on the total amount transported after 180 mins. For all four BAs a linear relationship between time and the amount of BAs transported was observed at 37°C (Pearson's correlation coefficient 0.79-0.94, p<0.05).

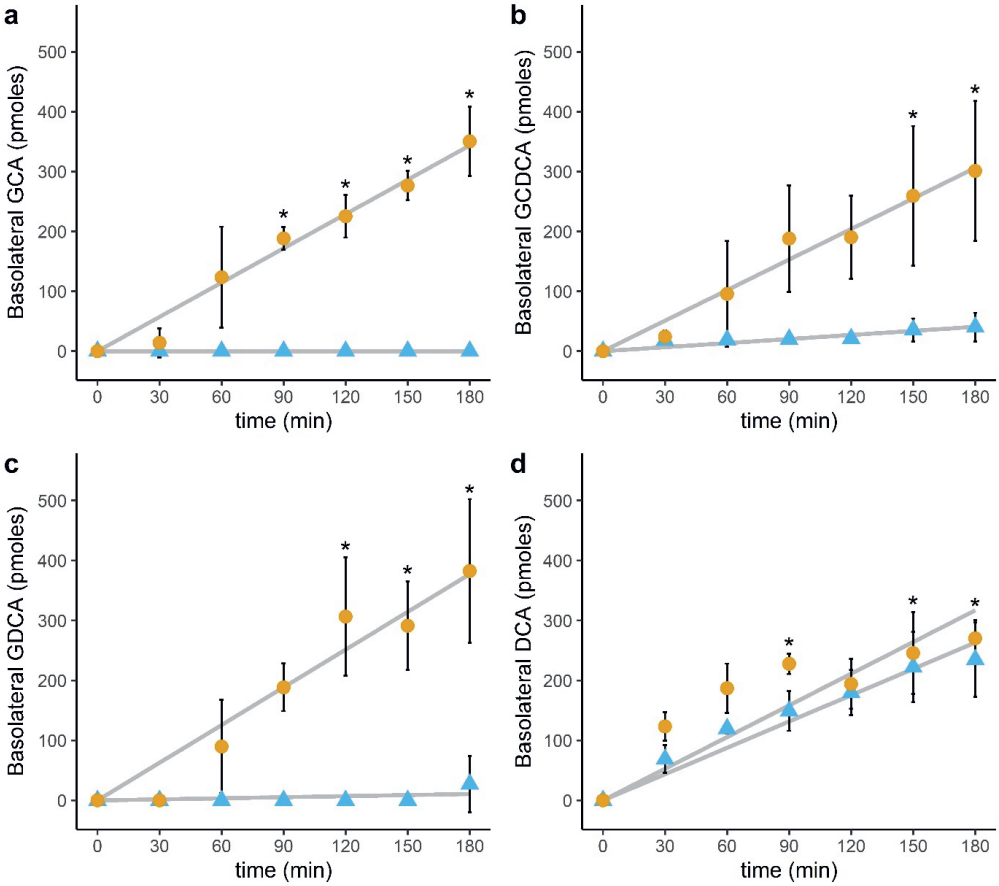

Figure 2 Bile acid transport across a Caco-2 monolayer measured during 180 min at 37°C (orange circles) or 4°C (blue triangles). 500 pmoles of GCA/GCDCA/GDCA/DCA were added to the apical chamber at t=0, and samples were taken from the basolateral chamber at different timepoints. Data are expressed as mean ± SD, N=3. LOD/LOQ are reported in Supplementary Material I Table SI. GCA=glycocholic acid, GCDCA=glycochenodeoxycholic acid, GDCA=glycodeoxcycholic acid, DCA=deoxycholic acid. Significance compared to t=0 min was assessed with a one way ANOVA followed by post hoc tests using Bonferroni's correction. Statistically significant differences in basolateral amount of bile acids compared to t=0 are indicated with *.

ODE inhibits GCA transport dose-dependently

To assess the effect of the known ASBT-inhibitor ODE on the GCA apical-to-basolateral transport over Caco-2 cells, 500 pmoles of GCA and a concentration range of ODE were added to the apical chamber of a culture insert with a confluent monolayer of Caco-2 cells and the basolateral GCA was measured. The results from the WST-1 assay confirmed that ODE concentrations up to 500 µM did not affect cell viability (4.5 Supplementary material I Figure S2A). Combined exposure to the increasing concentrations of ODE and 500 pmoles GCA did not have statistically significant effects on TEER values (4.5 Supplementary material I Figure S2B). We observed that ODE inhibited GCA apical-to-basolateral transport in a dose-dependent manner (Figure 3), and the IC_{50} value was estimated to be 0.04 nM ODE.

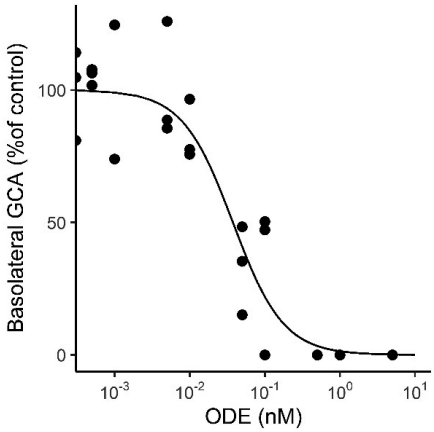

Figure 3 Odevixibat(ODE)-dependent inhibition of glycocholic acid (GCA) transport across Caco-2 monolayers. Values are normalized to the control. N=3.

ODE inhibits GCA transport in a competitive manner

Finally, the Caco-2 transport assay was used to obtain kinetic parameters for the PBK model. Our results showed that the GCA transport rate saturated with increasing GCA concentrations. A relatively small amount of GCA (<16% of the total GCA transport) was transported in the absence of sodium, *i.e.* via passive processes. The active transport rate was determined by subtracting the passive transport rate from the total transport rate (Figure 4a). The nature of ODE inhibition of GCA transport was evaluated using a Lineweaver-Burk plot (Figure 4b). For this the reciprocal of the GCA concentration (1/GCA) was plotted versus the reciprocal of the reaction speed (1/V), either with or without 0.08nM ODE. ANOVA demonstrated that the slope, but not the intercept, was significantly different between the two curves. Hence, incubation with ODE increased the $K_{m,app,}$ but did not affect $V_{max,app}$, indicating that ODE inhibits GCA transport in a competitive manner. Consequently, the following parameters were obtained for active GCA transport from Eq. 2: $V_{max,app}$=71.5 pmoles min^{-1} cm^{-2}, $K_{m,app}$=22.5 µM, K_i=0.02 nM.

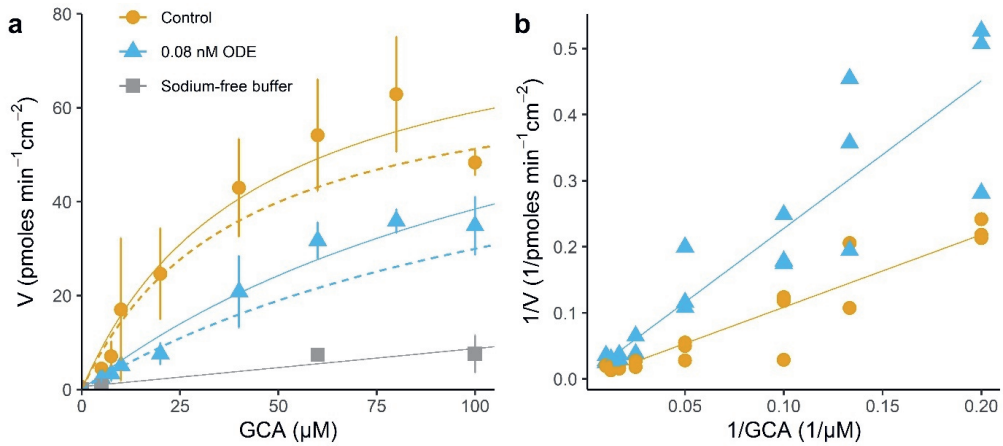

Figure 4 Concentration-dependent transport of glycocholic acid (GCA) across Caco-2 monolayers and inhibition by odevixibat (ODE) a) GCA transport rate after incubation with control buffer in the presence or absence of 0.08 nM ODE or with sodium-free buffer. The solid lines indicate the total transport; the dashed lines indicate active transport only, and were calculated by subtracting the transport rate in absence of sodium from the total transport rate. Values represent the mean ± SD, N=3. b) Lineweaver-Burk plot. Lines with and without ODE share the same intercept, but not slope (ANOVA).

Postprandial bile acid kinetics are readily described by the PBK model

The parameters for active GCA transport obtained using the Caco-2 transport assay were incorporated in the PBK model using the total ileal surface and an empirical scalar for *in vitro-in vivo* scaling, as described in Eq. 4. The PBK model describes the synthesis, absorption, distribution, metabolism and excretion of BAs for a healthy individual. For the first set of predictions, meals were simulated at 8:00, 12:00 and 16:00. This meal regimen was in accordance with the regimen used in the study of Hepner and Demers (1977) of which the data were used to validate our predictions. A second *in vivo* dataset available for model evaluation describes the postprandial BA kinetics for 8 hours after one meal (Lamaziere et al., 2020). The observed and predicted plasma BA-time profiles are displayed in Figure 5. GCA and uBA postprandial kinetics were predicted within 2-fold of both *in vivo* data sets, GDCA was predicted within 2-fold of the data obtained by Hepner and Demers (1977), but the model overpredicted the other *in vivo* data set with 25-fold (Lamaziere et al, 2020), which also underlines the interstudy and/or interindividual differences. Three scenarios with different K_m values for NTCP-mediated GCDCA transport were simulated (Figure 6). K_m values of 10, 0.6 and 5.3 μM, derived from Notenboom et al. (2018), Jani et al. (2018) and the average of these two studies, respectively, were used to run the simulations. The GCDCA C_{max} decreased with a decreasing K_m. The lowest K_m value resulted in only a minor increase in plasma GCDCA levels compared to the fasting state. The best fit to the *in vivo* data was obtained when the K_m values of the two studies were averaged. For further simulations, the averaged K_m value reported was used for GCDCA, given its better fit to the *in vivo* data. We used the average of our experimentally derived ABL-corrected $K_{m,app}$ and the $K_{m,app}$ reported in literature for ASBT-mediated GCA transport. The influence of different K_m values on the postprandial GCA kinetics are depicted in 4.5 Supplementary Material I Figure S3.

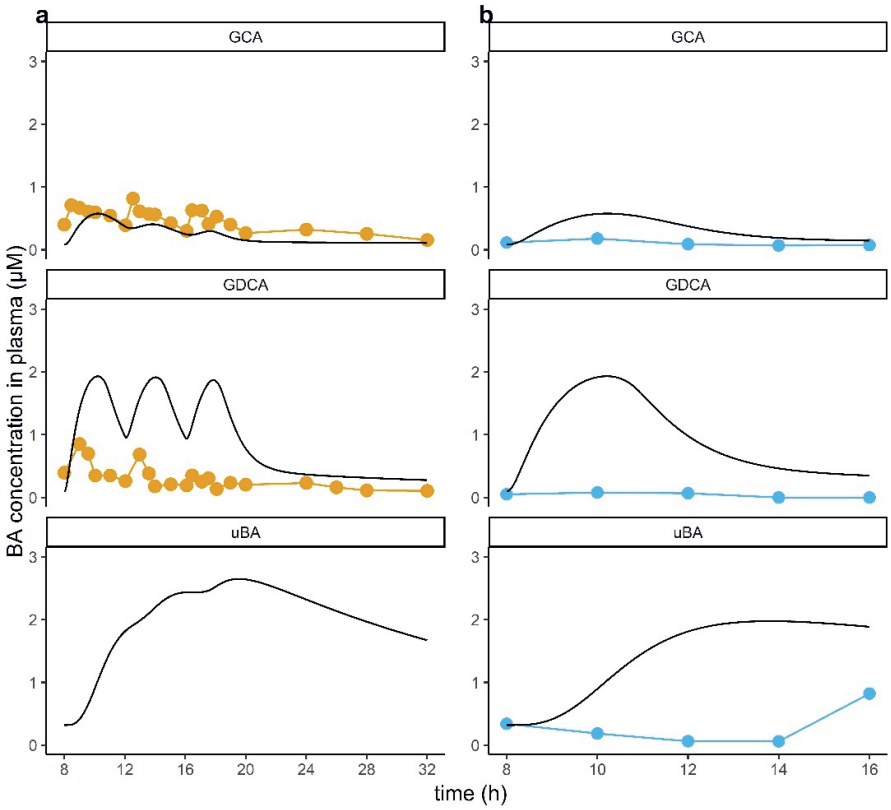

Figure 5 Observed and predicted postprandial bile acid kinetics. Black solid line=prediction**.** a) Meals were simulated at 8:00, 12:00 and 16:00. Orange circles=in vivo data obtained from Hepner and Demers (1977). b) A single meal was simulated at 8:00. Blue circles= in vivo data obtained from Lamaziere (2020). GCA=glycocholic acid, GDCA=glycodeoxycholic acid; uBA=unconjugated bile acids

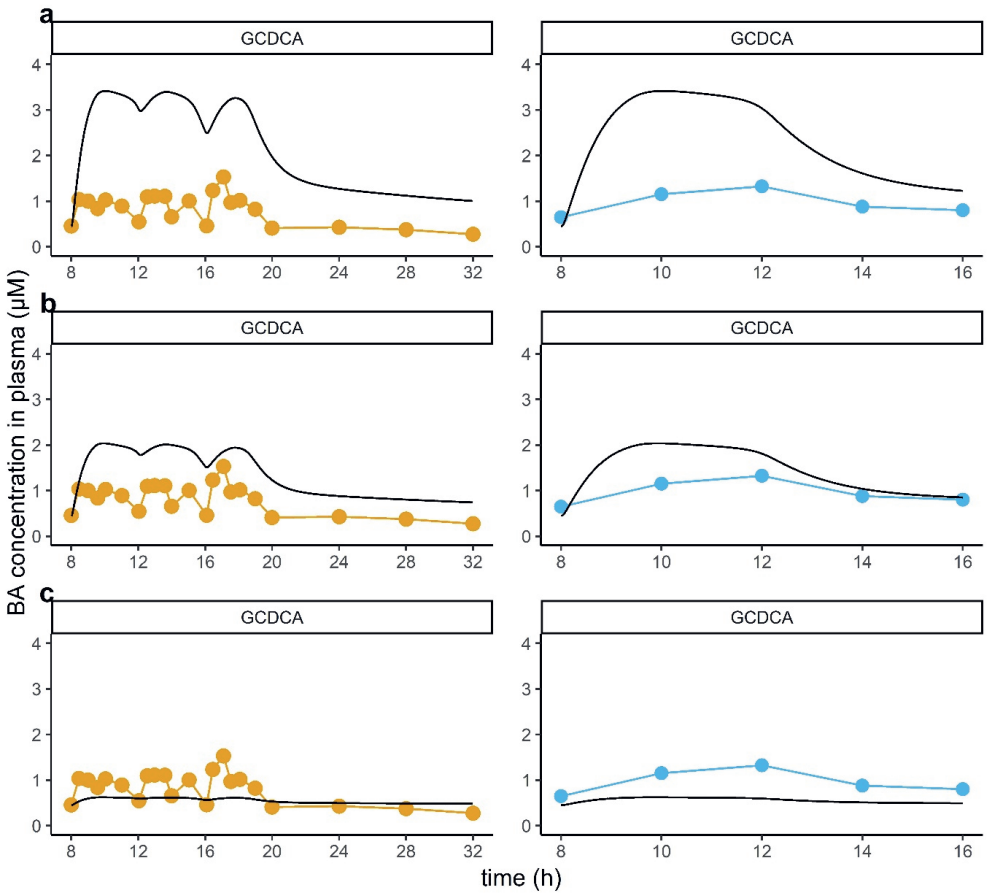

Figure 6 Observed and predicted postprandial GCDCA kinetics using different kinetic parameters for NTCP affinity. Black solid line=prediction**.** Left column: Meals were simulated at 8:00, 12:00 and 16:00. Orange circles=in vivo data obtained from Hepner and Demers (1977). Right column: Meal was simulated at 8:00. Blue circles= in vivo data obtained from Lamaziere (2020). a) K_m=10 µM (Notenboom et al. (2018), b) K_m=5.3 µM (average Notenboom et al. (2018) and Jani et al. (2018) c) K_m=0.568 µM (Jani et al. (2018)). GCDCA=glycochenodeoxycholic acid

ODE lowers the simulated plasma levels of conjugated bile acids

The effects of ODE-administration on the plasma and colonic BA levels were simulated using the perfusion-limited liver model and the two different sets of kinetic parameters to describe BSEP-mediated hepatic GDCA efflux. The simulated change in total plasma BAs was within the 95% confidence interval (CI) observed in a previous phase I clinical trial (Graffner et al., 2016). The current PBK model only simulated the concentrations of GCA, GCDCA, GDCA and uBA, while tauro-conjugates also circulate through the human body. Tauro-conjugates represent ~15% of the BAs in human plasma and to correct for the presence of tauro-conjugates, the predicted BA concentrations in Figure 7a/c were divided by 0.85 (black dashed line) to present a better estimate of the whole BA pool. The plasma levels of conjugated BAs (GCA, GCDCA and GDCA) were predicted by the PBK model to decrease ODE dose-dependently, while the uBA plasma levels showed a slight increase (Figure 7b). The uBA levels in the colon were predicted to increase with increasing ODE dosages (Figure 7c).

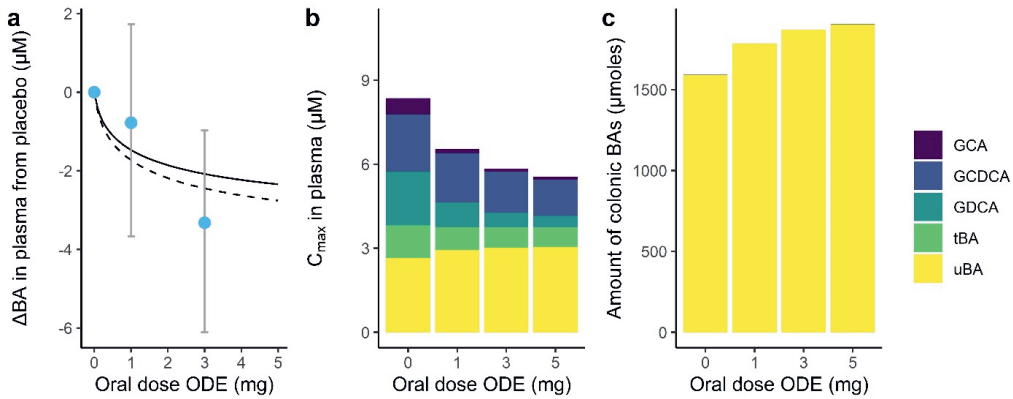

Figure 7 Bile acid levels in individuals receiving the placebo or ODE using a) Predicted versus observed change in maximal total plasma bile acids compared to the placebo on day 1 of ODE treatment. Blue circles are in vivo data retrieved from Graffner (2016)(mean± 95% CI), black solid line is the prediction for the sum of GCA, GCDCA, GDCA and uBA, black dashed line is the prediction corrected for tauroconjugates b) Predicted BA C_{max} for different BAs and c) Predicted maximal amounts of colonic BAs; note that in colon the amounts of the conjugated BAs (GCA, GCDCA and GDCA) were <0.6 μmoles. GCA=glycocholic acid, GCDCA=glycochenodeoxycholic acid; GDCA=glycodeoxycholic acid; tBA=tauroconjugated bile acids; uBA=unconjugated bile acids

Sensitivity analysis

To assess the influence of the parameters on the C_{max} and T_{max}, a local sensitivity analysis was performed. Figure 8a shows that parameters related to the active transport of GCA over the intestine and from extracellular to intracellular water and their scaling have a strong influence on the GCA C_{max} (absolute normalized sensitivity coefficient >0.5). Not only the maximal ASBT-mediated intestinal uptake rate (VmaxASBTc_GCA), but also the kinetic parameters describing NTCP-mediated hepatic uptake (VmaxNTCPc_GCA and KmNTCP_GCA) strongly influence the model outcome. ES_all and surface_all are used for the scaling of VmaxASBTc_GCA, and Hep_all_GCA is included in the scaling of VmaxNTCP_GCA, but also in the BSEP-mediated hepatic efflux. Furthermore, the ileal transit time in the fed stad (kti_fed), blood:plasma (BP_all) ratio, body weight (BW_all) and the factor used incorporate OATP-mediated transport negatively (SF_OATP) negatively impact GCA C_{max}. The portal blood flow (QPVc_all) has a positive influence on the GCA C_{max}. The sensitivity analyses for GCA, GCDCA and GDCA are roughly similar (Supplementary Material I Figure S5), while uBA and GCDCA C_{max} are not strongly influenced by transporter-mediated processes or their scaling factors when the low K_m value for NTCP-mediated transport of GCDCA of 0.568 μM is used as a baseline. Even though parameters related to BSEP-mediated active hepatic efflux do not have a strong influence on plasma BA C_{max}, they were shown to strongly influence the maximal intracellular concentrations of GCA, GCDCA and GDCA in the liver (Supplementary Material I Figure S5). Figure 8b shows that the gall bladder emptying time (get_all) and body weight (BW) have the strongest delaying influence on the GCA T_{max}, while the cardiac output (QC_all), the fraction of the arterial blood flow to the liver (QAVc_all) and ileal transit time in fed state (kti_fed) have the strongest accelerating influence on GCA T_{max}. The sensitivity analyses for the other BAs consistently identified intestinal transit time as an important parameter for T_{max} (Supplementary Material I Figure S6). It should be noted that the

normalized sensitivity coefficients for T_{max} are around one order of magnitude smaller than those for C_{max}.

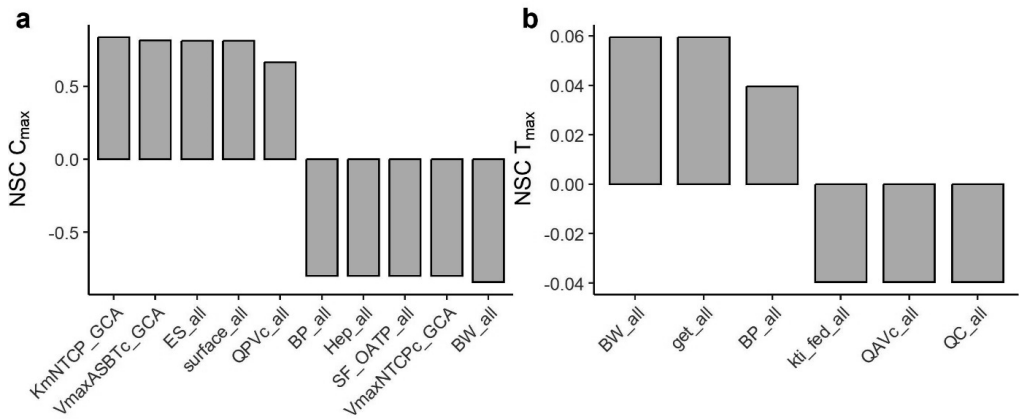

Figure 8 Sensitivity analysis of the influence of the PBK model parameters on the predicted outcomes. a) Sensitivity analysis for maximal systemic GCA concentration in plasma (C_{max}). Only parameters with an absolute normalized sensitivity coefficient (NSC) > 0.5 are shown. b) Sensitivity analysis for the time taken before reaching C_{max} (T_{max}). Only parameters with an absolute normalized sensitivity coefficient (NSC) > 0.03 are shown. KmNTCP=Michaelis–Menten constant for NTCP-mediated BA uptake in the liver, VmaxASBTc= maximal ASBT-mediated GCA absorption rate over the ileal epithelium, ES=empirical scalar for in vitro-in vivo extrapolation of Caco-2 derived kinetic parameters, surface=cylindrical surface of ileum, QPVc=fraction of blood flow through the portal vein, BP=blood:plasma ratio, Hep=hepatocellularity, SF_OATP=scaling factor to adjust hepatic uptake for OATP-mediated uptake, VmaxNTCPc= maximal NTCP-mediated GCA hepatic uptake rate, BW=body weight, get=gall bladder ejection time, kti_fed=ileal transit time in fed state, QAVc=fraction of blood flow to liver through the arterial vein. QC=cardiac output. _GCA indicates a parameter specifically for the GCA submodel, _all indicates a parameter that is shared for all BA submodels.

4.4 Discussion

For this work the aim was to predict the effects of ASBT-inhibition on systemic plasma levels and by that obtain mechanistic insights in whole-body BA homeostasis, with a focus on the gut-liver axis. To this end, we obtained kinetic parameters for the active intestinal glycocholic acid (GCA) transport across Caco-2 monolayers and incorporated these in a physiologically based kinetic (PBK) model describing the synthesis, absorption, distribution, metabolism and excretion of BAs. The current study shows that Caco-2 cells transported GCA in an active and sodium-dependent manner, indicating that apical sodium-dependent bile acid transporter (ASBT) functionality is maintained in Caco-2 cells. Subsequently, Caco-2 cells were applied to obtain kinetic parameters for ASBT-mediated GCA transport over the intestinal epithelium. These parameters were incorporated in the PBK model after *in vitro* to *in vivo* scaling. The integration of active intestinal uptake in the PBK model allowed us to incorporate dose-dependent BA transport inhibition induced by the selective and reversible ASBT inhibitor odevixibat (ODE). Our PBK model predicted that the plasma concentrations of conjugated BAs decrease upon ODE treatment, while unconjugated BA plasma concentrations are predicted to slightly increase. These predictions were in line with observations in the only available clinical phase I study reporting systemic plasma and fecal bile acids (Graffner et al., 2016). The sensitivity analysis

revealed that active transport processes strongly influence the maximal conjugated BA concentration in plasma (C_{max}). The affinity of conjugated BAs for Na^+-taurocholate cotransporting polypeptide (NTCP) as well as the maximal rate of ASBT-mediated ileal uptake (Vmax_ASBTc) and the parameters required for its scaling have a strong positive influence on the C_{max}. Our results indicate that accurate estimates for active ileal and hepatic transport processes are key for high predictive power of a PBK model describing BA homeostasis. The developed BA PBK model is to our knowledge the first PBK model that includes experimentally derived data for NTCP-mediated hepatic BA uptake, BSEP-mediated hepatic BA efflux and ASBT-mediated ileal BA uptake.

In the current study it was shown that Caco-2 cells transport BAs via active transport and passive diffusion processes. Although no differences were observed in the total transport of GCA, glyochenodeoxycholic acid (GCDCA), glycodeoxycholic acid (GDCA) and deoxycholic acid (DCA), notable differences in passive diffusion were observed between the BAs tested upon addition of 500 pmoles BA to the apical chamber, especially between the conjugated and unconjugated BAs. DCA was translocated primarily via passive diffusion, while for the conjugated BAs GCDCA and GDCA a very small amount (<LOQ) and for GCA no detectable amount was transported via passive diffusion. In line with literature, the passive BA diffusion rate followed their lipophilicity: DCA > GCDCA ≈ GDCA > GCA (Aldini et al., 1996).

Caco-2 cells are a robust intestinal cell model with apical brush borders, tight junctions and expression of several clinically relevant transporters, including transporters of the ATP binding cassette (ABC), multidrug resistance protein (MRP) and solute carrier (SLC) family (Olander et al., 2016; Antunes et al., 2013). Our results confirm that the GCA transport over Caco-2 cells is active and sodium-dependent, indicating the presence of a functional SLC-transporter. We trust that the Caco-2 cells performed ASBT-mediated BA transport, because a) GCA transport was completely inhibited upon addition of ≥0.5 nM of the selective ASBT inhibitor ODE at a low (5 µM) GCA concentration and b) our $K_{m,app}$ is within a 2-fold range of the $K_{m,app}$ value obtained from ASBT transfected MDCK cells reported in literature (Balakrishnan et al., 2006). Even though ASBT gene expression was confirmed for Caco-2 cells (Wang et al., 2022; van der Mark et al., 2014), ASBT protein expression was not conclusively demonstrated. ASBT protein expression could not be detected by LC-MS/MS (Bruck et al., 2017; Olander et al., 2016), but Western blot analysis by van der Mark et al. (2014) revealed that ASBT expression is low in Caco-2 cells compared to the human ileum. Differences in the detection limit of the analytical techniques, Caco-2 cell clones and/or culture conditions provide plausible explanations for the inconsistent results for ASBT protein expression in Caco-2 cells (Sambuy et al., 2005). We consider the sodium-dependency and ODE-mediated inhibition of GCA transport strong indicators of the presence of functional ASBT in Caco-2 monolayers. In the current study, an empirical scalar of 2.8 was employed to correct for differences between the *in vitro* and *in vivo* situation, such as differences in ASBT expression and/or activity and other chemical, physical or biological differences. However, for optimal scientific validity, a mechanistic justification for the scaling factor is desirable, enabling its application to other substances. The mechanistic justification of the scaling factor could be based on the establishment of a relative activity factor (RAF), in which transport of a probe substrate *in vitro* is compared against the *in vivo* situation. RAFs have been proven relatively successful for the prediction of metabolic conversions, but their applicability for transporter-mediated processes remains to be verified (Kumar et al., 2021).

The Caco-2 cells were cultured in medium containing fetal calf serum (FCS). FCS contains an undefined cocktail of growth factors, hormones, vitamins and is typically used to ensure growth and proliferation in cell cultures. In order to contribute to the 3R (reduce, refine, replace) principles,

increasing attention goes to the development of animal-free chemically-defined alternatives for FCS. Several synthetic supplements have been tested, but did not allow various cell types to proliferate and differentiate properly (van der Valk et al., 2018). Human platelet lysate seems a promising substitute for FCS. Caco-2 cell viability was slightly enhanced in cells grown with this lysate compared to FCS, and the cells differentiated to cells of the enterocytic lineage (Wanes et al., 2021). Yet, functional similarity to the human intestinal epithelium remains to be demonstrated.

The kinetic parameters obtained in the Caco-2 transport assay were incorporated in a PBK model describing the synthesis, distribution, metabolism and excretion of BAs. Our simulations for GCA, GDCA, and uBA accurately predicted the at least one dataset of observed BA concentrations, that is, within 2-fold. GCDCA postprandial kinetics were simulated with three different K_m values for NTCP-mediated transport, where the lowest value (0.6 µM, Jani et al., 2018) gave a close fit with the *in vivo* data, while the highest value (10 µM, Notenboom et al., 2018) resulted in a ~5-fold overprediction. The large discrepancy between the two experimental datasets can be attributed to intersystem (transfected CHO versus HEK293 cells), biological and/or chemical differences. Given its large influence on the postprandial kinetics, it is crucial to establish reliable kinetic parameters for NTCP-mediated transport and understand the reasons for these discrepancies. The predicted BA concentrations were still within the range of C_{max} values reported in literature. Up to 22-fold differences in plasma BA C_{max} between individuals have been reported, which could be due to biological interindividual differences (Baier et al., 2019; Lamaziere et al., 2020; Steiner et al., 2011; Fiamoncini et al., 2016), while interstudy differences between individuals may also be due to technical differences. Due to these differences a PBK model predicted C_{max} may be more than 2-fold different from data reported for individual volunteers in literature.

Our simulations reflect a consistently delayed time to reach C_{max} (T_{max}) compared to the *in vivo* datasets. The sensitivity analysis revealed that a prolonged gall bladder ejection time had the strongest delaying effect on T_{max}. In the current model the gall bladder ejection time was set to 90 minutes, which was derived from a study using scintigraphic measurements in healthy individuals. In this study, the volunteers were administered an isotope and the isotope amount in the gallbladder was quantified at selected timepoints using a gamma camera (Jazrawi et al., 1995). The accuracy of the predicted T_{max} might be improved by describing gall bladder motility in more detail, for example by using a normalized Rayleigh function which shows a transient increase and subsequent decrease of gall bladder emptying rate over time (Sips et al., 2018). Given that the effect of gall bladder ejection time on T_{max} was relatively small (NSC<0.1), this approach was not applied in the current work.

The data from our transport assays indicated that ODE is a competitive inhibitor of GCA transport, with an estimated IC_{50} of 0.04 nM which is about 2-fold lower than literature (0.1 nM) (EMA, 2021). We predicted a decrease in plasma BAs, and especially the conjugated BAs (GCA, GCDCA and GDCA), upon treatment with a single oral dose of ODE. The decrease in total BAs was in line with literature. *In vivo* data in healthy individuals on day 7 of treatment with ODE showed a similar change in BA profile, *i.e.* a decrease in plasma conjugated BAs and a slight increase in the unconjugated BAs DCA and CDCA (Graffner et al., 2016). The authors also observed an increase in fecal unconjugated BAs on day 7 of ODE treatment. Likewise, we simulated an increased amount of colonic unconjugated BAs, which can be directly translated into increased fecal amounts due to reduced intestinal ASBT mediated uptake of these conjugated BAs. Treatment with 3 mg ODE is shown to significantly reduce plasma fibroblast growth factor 19 (FGF-19) levels in healthy individuals. This results in a reduced inhibition of hepatic BA synthesis, which is reflected by increased plasma levels of the BA precursor C4 (Graffner et al., 2016). It is important to note that the PBK model developed included only a basic

adaptive response, which does not allow for dynamic changes in synthesis rate, microbiome's composition or intestinal membrane integrity. Therefore, we only modeled the effects of ODE upon a single administration. Quantitatively capturing dynamic changes in a computational model requires many assumptions and fitting of parameters, which has been done previously (Voronova et al., 2020). A major strength of our PBK model is that the majority of input parameters is derived experimentally, but accordingly the adaptive response was not modelled in detail. Nevertheless, the current model is proven useful for the prediction of short-term effects in healthy individuals.

In the current work, we report an apparent Michaelis Menten constant or $K_{m,app}$, because the value relates to the overall process of transport across the Caco-2 monolayer including not only apical influx, but also intracellular transport by bile acid binding protein (BABP) and basolateral efflux by organic solute transporter (OST) α/β. The $K_{m,app}$ can differ between *in vitro* and *in vivo* test systems. For example, for taurocholic acid (TCA), the typical model BA for transport experiments, $K_{m,app}$ values for intestinal uptake ranging from 4.4 to 600 µM have been reported using transfected cell lines/oocytes, human precision cut intestinal slices and a human perfusion study *in vivo* (Balakrishnan et al., 2006; Zhu et al., 2021; Li et al., 2018; Krag and Phillips, 1974). Besides biological differences in *e.g.* OSTα/β or BABP activity, the physical hydrodynamic barrier between the bulk solution and the surface with the transporter differs depending on the test system used. *In vitro* the restricted liquid flow in the vicinity of a culture insert will create a zone where the diffusional movement of molecules exceeds the convection. The formed layer is referred to as the unstirred water layer or aqueous boundary layer (ABL). Besides, the culture insert itself will affect the compound's permeability (Korjamo et al., 2009). Balakrishnan et al. (2007) studied the effect of the ABL in culture inserts and derived an equation that can be used to correct the affinity of influx transporters for the ABL. This equation was employed in this work (Eq. 2), and resulted in a $K_{m,app}$ of 23 µM, versus 39 µM when the resistance by the ABL was not considered. The intestinal peristaltic movements can be expected to drastically reduce the ABL *in vivo* resulting in lower $K_{m,app}$ values. It has been concluded previously that the ABL does not play a clinically significant role in the intestinal absorption of drugs *in vivo* and hence, $K_{m,app}$ values derived from static *in vitro* models should be corrected for the ABL before the values can be extrapolated to the *in vivo* situation (Korjamo et al., 2009). Where *in vitro* the ABL hampers a molecule's transport to a culture insert, *in vivo* a molecule first has to migrate through the mucus layer before it reaches the intestinal epithelium. Caco-2 cells represent cells of the enterocytic lineage, and do not fully represent the cell types present in the human ileal epithelium. Especially the lack of mucin-producing Goblet cells and thus a mucus layer could affect the $K_{m,app}$. The HT29-MTX cell line has emerged as a cell line that forms Goblet cells and can be used to complement Caco-2 cells. Co-culturing HT29-MTX cells with Caco-2 cells results in similar gene expression profiles to gastrointestinal tissue, and a mucus layer on top of the epithelium (Pontier et al., 2001). Yet, coculturing HT29-MTX and Caco-2 cells did not modulate permeability compared to Caco-2 cells alone, and ergo does not provide an improved $K_{m,app}$ that takes into account the mucus effects (McCright et al., 2022; Lock et al., 2018). Due to the absence of functional differences in permeability between the coculture and monoculture system, we have decided to use the well-characterized and robust Caco-2 monoculture system.

The current results underline the importance of active ileal and hepatic transport processes for accurate predictions of systemic plasma BA levels. We demonstrate that Caco-2 cells can be used to quantitatively study ODE's inhibitory effects on GCA transport. By incorporating the obtained kinetic parameters in a PBK model we were able to accurately predict the changes in plasma BA levels upon a single oral dose of ODE. The current model can serve as a quantitative tool to predict alterations in plasma BA levels upon xenobiotic-exposure.

Data availability statement

The model code can be found in supplementary material II. In *vitro* transport data are available upon request from the corresponding author.

Conflict of interest

The authors do not report a conflict of interest.

Acknowledgements

We would like to thank Wouter Bakker for his help with the LC-MS/MS measurements.

References

Al-Hilal, T. A., Chung, S. W., Alam, F. et al. (2014). Functional transformations of bile acid transporters induced by high-affinity macromolecules. *Sci Rep 4*, 4163. doi:10.1038/srep04163

Aldini, R., Roda, A., Montagnani, M. et al. (1996). Relationship between structure and intestinal absorption of bile acids with a steroid or side-chain modification. *Steroids 61*, 590-597. doi:10.1016/s0039-128x(96)00119-5

Antunes, F., Andrade, F., Araujo, F. et al. (2013). Establishment of a triple co-culture in vitro cell models to study intestinal absorption of peptide drugs. *Eur J Pharm Biopharm 83*, 427-435. doi:10.1016/j.ejpb.2012.10.003

Baier, V., Cordes, H., Thiel, C. et al. (2019). A physiology-based model of human bile acid metabolism for predicting bile acid tissue levels after drug administration in healthy subjects and bric type 2 patients. *Front Physiol 10*, 1192. doi:10.3389/fphys.2019.01192

Balakrishnan, A., Wring, S. A. and Polli, J. E. (2006). Interaction of native bile acids with human apical sodium-dependent bile acid transporter (hasbt): Influence of steroidal hydroxylation pattern and c-24 conjugation. *Pharm Res 23*, 1451-1459. doi:10.1007/s11095-006-0219-4

Balakrishnan, A., Hussainzada, N., Gonzalez, P. et al. (2007). Bias in estimation of transporter kinetic parameters from overexpression systems: Interplay of transporter expression level and substrate affinity. *J Pharmacol Exp Ther 320*, 133-144. doi:10.1124/jpet.106.107433

Barter, Z. E., Bayliss, M. K., Beaune, P. H. et al. (2007). Scaling factors for the extrapolation of in vivo metabolic drug clearance from in vitro data: Reaching a consensus on values of human micro-somal protein and hepatocellularity per gram of liver. *Current drug metabolism 8*, 33-45.

Bathena, S. P., Mukherjee, S., Olivera, M. et al. (2013). The profile of bile acids and their sulfate metabolites in human urine and serum. *J Chromatogr B Analyt Technol Biomed Life Sci 942-943*, 53-62. doi:10.1016/j.jchromb.2013.10.019

Begley, M., Gahan, C. G. M. and Hill, C. (2005). The interaction between bacteria and bile. *Fems Microbiology Reviews 29*, 625-651. doi:10.1016/j.femsre.2004.09.003

Bruck, S., Strohmeier, J., Busch, D. et al. (2017). Caco-2 cells - expression, regulation and function of drug transporters compared with human jejunal tissue. *Biopharm Drug Dispos 38*, 115-126. doi:10.1002/bdd.2025

Chiang, J. Y. L. and Ferrell, J. M. (2022). Discovery of farnesoid x receptor and its role in bile acid metabolism. *Mol Cell Endocrinol 548*, 111618. doi:10.1016/j.mce.2022.111618

Dawson, P. A., Lan, T. and Rao, A. (2009). Bile acid transporters. *J Lipid Res 50*, 2340-2357. doi:10.1194/jlr.R900012-JLR200

Dawson, P. A. (2011). Role of the intestinal bile acid transporters in bile acid and drug disposition. *Handb Exp Pharmacol* 169-203. doi:10.1007/978-3-642-14541-4_4

de Bruijn, V. M. P., Rietjens, I. M. C. M. and Bouwmeester, H. (2022a). Population pharmacokinetic model to generate mechanistic insights in bile acid homeostasis and drug-induced cholestasis. *Arch Toxicol 96*, 2717-2730. doi:10.1007/s00204-022-03345-8

de Bruijn, V. M. P., Wang, Z., Bakker, W. et al. (2022b). Hepatic bile acid synthesis and secretion: Comparison of in vitro methods. *Toxicol Lett 365*, 46-60. doi:10.1016/j.toxlet.2022.06.004

Deeks, E. D. (2021). Odevixibat: First approval. *Drugs* 1-6.

Duan, S., Li, X., Fan, G. et al. (2022). Targeting bile acid signaling for the treatment of liver diseases: From bench to bed. *Biomed Pharmacother 152*, 113154. doi:10.1016/j.biopha.2022.113154
EMA (2021). Assessment report: Bylvay.
Falany, C. N., Johnson, M. R., Barnes, S. et al. (1994). Glycine and taurine conjugation of bile acids by a single enzyme. Molecular cloning and expression of human liver bile acid coa:Amino acid n-acyltransferase. *J Biol Chem 269*, 19375-19379.
Fasano, A., Budillon, G., Guandalini, S. et al. (1990). Bile acids reversible effects on small intestinal permeability. An in vitro study in the rabbit. *Dig Dis Sci 35*, 801-808. doi:10.1007/BF01536791
Fiamoncini, J., Curi, R. and Daniel, H. (2016). Metabolism of bile acids in the post-prandial state. *Essays in biochemistry 60*, 409-418.
Fidler M, H. M., Wilkins J, Wang W (2022). Rxode: Facilities for simulating from ode-based models. _
Fitzpatrick, L. R. and Jenabzadeh, P. (2020). Ibd and bile acid absorption: Focus on pre-clinical and clinical observations. *Front Physiol 11*, 564. doi:10.3389/fphys.2020.00564
Fuchs, C. D. and Trauner, M. (2022). Role of bile acids and their receptors in gastrointestinal and hepatic pathophysiology. *Nat Rev Gastroenterol Hepatol 19*, 432-450. doi:10.1038/s41575-021-00566-7
Garcia-Canaveras, J. C., Donato, M. T., Castell, J. V. et al. (2012). Targeted profiling of circulating and hepatic bile acids in human, mouse, and rat using a uplc-mrm-ms-validated method. *J Lipid Res 53*, 2231-2241. doi:10.1194/jlr.D028803
Gijbels, E. and Vinken, M. (2019). Mechanisms of drug-induced cholestasis. In (eds.), *Experimental cholestasis research*. Springer.
Gilbert-Sandoval, I., Wesseling, S. and Rietjens, I. M. C. M. (2020). Predicting the acute liver toxicity of aflatoxin b1 in rats and humans by an in vitro-in silico testing strategy. *Mol Nutr Food Res 64*, e2000063. doi:10.1002/mnfr.202000063
Graffner, H., Gillberg, P. G., Rikner, L. et al. (2016). The ileal bile acid transporter inhibitor a4250 decreases serum bile acids by interrupting the enterohepatic circulation. *Aliment Pharmacol Ther 43*, 303-310. doi:10.1111/apt.13457
Hendriksen, B. A., Felix, M. V. and Bolger, M. B. (2003). The composite solubility versus ph profile and its role in intestinal absorption prediction. *AAPS PharmSci 5*, E4. doi:10.1208/050104
Hepner, G. W. and Demers, L. M. (1977). Dynamics of the enterohepatic circulation of the glycine conjugates of cholic, chenodeoxycholic, deoxycholic, and sulfolithocholic acid in man. *Gastroenterology 72*, 499-501.
Hofmann, A. F., Molino, G., Milanese, M. et al. (1983). Description and simulation of a physiological pharmacokinetic model for the metabolism and enterohepatic circulation of bile acids in man. Cholic acid in healthy man. *J Clin Invest 71*, 1003-1022. doi:10.1172/jci110828
Jamei, M., Bajot, F., Neuhoff, S. et al. (2014). A mechanistic framework for in vitro-in vivo extrapolation of liver membrane transporters: Prediction of drug-drug interaction between rosuvastatin and cyclosporine. *Clin Pharmacokinet 53*, 73-87. doi:10.1007/s40262-013-0097-y
Jani, M., Beéry, E., Heslop, T. et al. (2018). Kinetic characterization of bile salt transport by human ntcp (slc10a1). *Toxicology in Vitro 46*, 189-193.
Jazrawi, R. P., Pazzi, P., Petroni, M. L. et al. (1995). Postprandial gallbladder motor function: Refilling and turnover of bile in health and in cholelithiasis. *Gastroenterology 109*, 582-591.
Jia, W., Xie, G. and Jia, W. (2018). Bile acid-microbiota crosstalk in gastrointestinal inflammation and carcinogenesis. *Nat Rev Gastroenterol Hepatol 15*, 111-128. doi:10.1038/nrgastro.2017.119
Kararli, T. T. (1995). Comparison of the gastrointestinal anatomy, physiology, and biochemistry of humans and commonly used laboratory animals. *Biopharm Drug Dispos 16*, 351-380. doi:10.1002/bdd.2510160502
Kato, T., Mikami, Y., Sun, L. et al. (2021). Reuse of cell culture inserts for in vitro human primary airway epithelial cell studies. *Am J Respir Cell Mol Biol 64*, 760-764. doi:10.1165/rcmb.2021-0033LE
Kimura, T. and Higaki, K. (2002). Gastrointestinal transit and drug absorption. *Biol Pharm Bull 25*, 149-164. doi:10.1248/bpb.25.149

Kis, E., Ioja, E., Nagy, T. et al. (2009). Effect of membrane cholesterol on bsep/bsep activity: Species specificity studies for substrates and inhibitors. *Drug Metab Dispos 37*, 1878-1886. doi:10.1124/dmd.108.024778
Korjamo, T., Heikkinen, A. T. and Monkkonen, J. (2009). Analysis of unstirred water layer in in vitro permeability experiments. *J Pharm Sci 98*, 4469-4479. doi:10.1002/jps.21762
Kouzuki, H., Suzuki, H., Ito, K. et al. (1998). Contribution of sodium taurocholate co-transporting polypeptide to the uptake of its possible substrates into rat hepatocytes. *Journal of Pharmacology and Experimental Therapeutics 286*, 1043-1050.
Krag, E. and Phillips, S. F. (1974). Active and passive bile acid absorption in man. Perfusion studies of the ileum and jejunum. *J Clin Invest 53*, 1686-1694. doi:10.1172/JCI107720
Kullak-Ublick, G. A., Stieger, B. and Meier, P. J. (2004). Enterohepatic bile salt transporters in normal physiology and liver disease. *Gastroenterology 126*, 322-342. doi:10.1053/j.gastro.2003.06.005
Kumar, A. R., Prasad, B., Bhatt, D. K. et al. (2021). In vitro–to–in vivo extrapolation of transporter-mediated renal clearance: Relative expression factor versus relative activity factor approach. *Drug Metabolism and Disposition 49*, 470-478.
Lamaziere, A., Rainteau, D., Kc, P. et al. (2020). Distinct postprandial bile acids responses to a high-calorie diet in men volunteers underscore metabolically healthy and unhealthy phenotypes. *Nutrients 12*, 3545. doi:10.3390/nu12113545
Law, V., Knox, C., Djoumbou, Y. et al. (2014). Drugbank 4.0: Shedding new light on drug metabolism. *Nucleic Acids Res 42*, D1091-1097. doi:10.1093/nar/gkt1068
Leschelle, X., Robert, V., Delpal, S. et al. (2002). Isolation of pig colonic crypts for cytotoxic assay of luminal compounds: Effects of hydrogen sulfide, ammonia, and deoxycholic acid. *Cell Biol Toxicol 18*, 193-203. doi:10.1023/a:1015515821390
Li, M., Vokral, I., Evers, B. et al. (2018). Human and rat precision-cut intestinal slices as ex vivo models to study bile acid uptake by the apical sodium-dependent bile acid transporter. *Eur J Pharm Sci 121*, 65-73. doi:10.1016/j.ejps.2018.05.005
Li, S., Qu, X., Zhang, L. et al. (2022). Serum total bile acids in relation to gastrointestinal cancer risk: A retrospective study. *Front Oncol 12*, 859716. doi:10.3389/fonc.2022.859716
Lin, S., Wang, S., Wang, P. et al. (2023). Bile acids and their receptors in regulation of gut health and diseases. *Prog Lipid Res 89*, 101210. doi:10.1016/j.plipres.2022.101210
Lineweaver, H. and Burk, D. (1934). The determination of enzyme dissociation constants. *Journal of the American chemical society 56*, 658-666.
Lobell, M. and Sivarajah, V. (2003). In silico prediction of aqueous solubility, human plasma protein binding and volume of distribution of compounds from calculated pka and alogp98 values. *Mol Divers 7*, 69-87. doi:10.1023/b:modi.0000006562.93049.36
Lock, J. Y., Carlson, T. L. and Carrier, R. L. (2018). Mucus models to evaluate the diffusion of drugs and particles. *Adv Drug Deliv Rev 124*, 34-49. doi:10.1016/j.addr.2017.11.001
Lu, Z. N., He, H. W. and Zhang, N. (2022). Advances in understanding the regulatory mechanism of organic solute transporter alpha-beta. *Life Sci 310*, 121109. doi:10.1016/j.lfs.2022.121109
Marasco, G., Cremon, C., Barbaro, M. R. et al. (2022). Pathophysiology and clinical management of bile acid diarrhea. *J Clin Med 11*, 3102. doi:10.3390/jcm11113102
Martinez-Augustin, O. and Sanchez de Medina, F. (2008). Intestinal bile acid physiology and pathophysiology. *World J Gastroenterol 14*, 5630-5640. doi:10.3748/wjg.14.5630
McCright, J., Sinha, A. and Maisel, K. (2022). Generating an in vitro gut model with physiologically relevant biophysical mucus properties. *Cell Mol Bioeng 15*, 479-491. doi:10.1007/s12195-022-00740-0
Miele, L., Valenza, V., La Torre, G. et al. (2009). Increased intestinal permeability and tight junction alterations in nonalcoholic fatty liver disease. *Hepatology 49*, 1877-1887. doi:10.1002/hep.22848
Molino, G., Hofmann, A. F., Cravetto, C. et al. (1986). Simulation of the metabolism and enterohepatic circulation of endogenous chenodeoxycholic acid in man using a physiological

pharmacokinetic model. *Eur J Clin Invest 16*, 397-414. doi:10.1111/j.1365-2362.1986.tb01015.x
Mouzaki, M., Wang, A. Y., Bandsma, R. et al. (2016). Bile acids and dysbiosis in non-alcoholic fatty liver disease. *PLoS One 11*, e0151829. doi:10.1371/journal.pone.0151829
Notenboom, S., Weigand, K. M., Proost, J. H. et al. (2018). Development of a mechanistic biokinetic model for hepatic bile acid handling to predict possible cholestatic effects of drugs. *European Journal of Pharmaceutical Sciences 115*, 175-184.
Olander, M., Wisniewski, J. R., Matsson, P. et al. (2016). The proteome of filter-grown caco-2 cells with a focus on proteins involved in drug disposition. *J Pharm Sci 105*, 817-827. doi:10.1016/j.xphs.2015.10.030
Peyret, T., Poulin, P. and Krishnan, K. (2010). A unified algorithm for predicting partition coefficients for pbpk modeling of drugs and environmental chemicals. *Toxicology and applied pharmacology 249*, 197-207.
Pontier, C., Pachot, J., Botham, R. et al. (2001). Ht29-mtx and caco-2/tc7 monolayers as predictive models for human intestinal absorption: Role of the mucus layer. *Journal of Pharmaceutical Sciences 90*, 1608-1619. doi:DOI 10.1002/jps.1111
Punt, A., Pinckaers, N., Peijnenburg, A. et al. (2020). Development of a web-based toolbox to support quantitative in-vitro-to-in-vivo extrapolations (qivive) within nonanimal testing strategies. *Chemical Research in Toxicology*
Punt, A., Louisse, J., Beekmann, K. et al. (2022). Predictive performance of next generation human physiologically based kinetic (pbk) models based on in vitro and in silico input data. *ALTEX 39*, 221-234. doi:10.14573/altex.2108301
Rietjens, I. M. C. M., Louisse, J. and Punt, A. (2011). Tutorial on physiologically based kinetic modeling in molecular nutrition and food research. *Mol Nutr Food Res 55*, 941-956. doi:10.1002/mnfr.201000655
Ritz, C., Baty, F., Streibig, J. C. et al. (2015). Dose-response analysis using r. *PLoS One 10*, e0146021. doi:10.1371/journal.pone.0146021
Roda, A., Minutello, A., Angellotti, M. A. et al. (1990). Bile acid structure-activity relationship: Evaluation of bile acid lipophilicity using 1-octanol/water partition coefficient and reverse phase hplc. *J Lipid Res 31*, 1433-1443.
Rodgers, T. and Rowland, M. (2006). Physiologically based pharmacokinetic modelling 2: Predicting the tissue distribution of acids, very weak bases, neutrals and zwitterions. *J Pharm Sci 95*, 1238-1257. doi:10.1002/jps.20502
Sabino, J., Vieira-Silva, S., Machiels, K. et al. (2016). Primary sclerosing cholangitis is characterised by intestinal dysbiosis independent from ibd. *Gut 65*, 1681-1689. doi:10.1136/gutjnl-2015-311004
Sambuy, Y., Angelis, I., Ranaldi, G. et al. (2005). The caco-2 cell line as a model of the intestinal barrier: Influence of cell and culture-related factors on caco-2 cell functional characteristics. *Cell Biology and Toxicology 21*, 1-26. doi:10.1007/s10565-005-0085-6
Schwarz, M. A., Neubert, R. H. and Rüttinger, H. H. (1996). Application of capillary electrophoresis for characterizing interactions between drugs and bile salts. Part i. *Journal of Chromatography A 745*, 135-143.
Sharanek, A., Burban, A., Humbert, L. et al. (2015). Cellular accumulation and toxic effects of bile acids in cyclosporine a-treated heparg hepatocytes. *Toxicological Sciences 147*, 573-587. doi:10.1093/toxsci/kfv155
Shrivastava, A. and Gupta, V. B. (2011). Methods for the determination of limit of detection and limit of quantitation of the analytical methods. *Chron. Young Sci 2*, 21-25.
Sips, F. L. P., Eggink, H. M., Hilbers, P. A. J. et al. (2018). In silico analysis identifies intestinal transit as a key determinant of systemic bile acid metabolism. *Front Physiol 9*, 631. doi:10.3389/fphys.2018.00631

Smirnova, E., Muthiah, M. D., Narayan, N. et al. (2022). Metabolic reprogramming of the intestinal microbiome with functional bile acid changes underlie the development of nafld. *Hepatology 76*, 1811-1824. doi:10.1002/hep.32568

Soars, M., Burchell, B. and Riley, R. (2002). In vitro analysis of human drug glucuronidation and prediction of in vivo metabolic clearance. *Journal of Pharmacology and Experimental Therapeutics 301*, 382-390.

Soetaert, K. and Petzoldt, T. (2010). Inverse modelling, sensitivity and monte carlo analysis inrusing packagefme. *Journal of Statistical Software 33*, 1-28. doi:10.18637/jss.v033.i03

Steiner, C., Othman, A., Saely, C. H. et al. (2011). Bile acid metabolites in serum: Intraindividual variation and associations with coronary heart disease, metabolic syndrome and diabetes mellitus. *PLOS ONE 6*, e25006. doi:10.1371/journal.pone.0025006

Toke, O. (2022). Structural and dynamic determinants of molecular recognition in bile acid-binding proteins. *Int J Mol Sci 23*, 505. doi:10.3390/ijms23010505

van der Mark, V. A., de Waart, D. R., Ho-Mok, K. S. et al. (2014). The lipid flippase heterodimer atp8b1–cdc50a is essential for surface expression of the apical sodium-dependent bile acid transporter (slc10a2/asbt) in intestinal caco-2 cells. *Biochimica et Biophysica Acta (BBA)-Molecular Basis of Disease 1842*, 2378-2386.

van der Valk, J., Bieback, K., Buta, C. et al. (2018). Fetal bovine serum (fbs): Past - present - future. *ALTEX 35*, 99-118. doi:10.14573/altex.1705101

Vinken, M., Landesmann, B., Goumenou, M. et al. (2013). Development of an adverse outcome pathway from drug-mediated bile salt export pump inhibition to cholestatic liver injury. *Toxicol Sci 136*, 97-106. doi:10.1093/toxsci/kft177

Voronova, V., Sokolov, V., Al-Khaifi, A. et al. (2020). A physiology-based model of bile acid distribution and metabolism under healthy and pathologic conditions in human beings. *Cell Mol Gastroenterol Hepatol 10*, 149-170. doi:10.1016/j.jcmgh.2020.02.005

Wanes, D., Naim, H. Y. and Dengler, F. (2021). Proliferation and differentiation of intestinal caco-2 cells are maintained in culture with human platelet lysate instead of fetal calf serum. *Cells 10*, 3038. doi:10.3390/cells10113038

Wang, J., Bakker, W., Zheng, W. et al. (2022). Exposure to the mycotoxin deoxynivalenol reduces the transport of conjugated bile acids by intestinal caco-2 cells. *Arch Toxicol 96*, 1473-1482. doi:10.1007/s00204-022-03256-8

Wang, Q., Strab, R., Kardos, P. et al. (2008). Application and limitation of inhibitors in drug-transporter interactions studies. *Int J Pharm 356*, 12-18. doi:10.1016/j.ijpharm.2007.12.024

Yang, N., Dong, Y. Q., Jia, G. X. et al. (2020). Asbt(slc10a2): A promising target for treatment of diseases and drug discovery. *Biomed Pharmacother 132*, 110835. doi:10.1016/j.biopha.2020.110835

Zhang, N., Wang, J., Bakker, W. et al. (2022). In vitro models to detect in vivo bile acid changes induced by antibiotics. *Arch Toxicol 96*, 3291-3303. doi:10.1007/s00204-022-03373-4

Zhu, Q., Komori, H., Imamura, R. et al. (2021). A novel fluorescence-based method to evaluate ileal apical sodium-dependent bile acid transporter asbt. *J Pharm Sci 110*, 1392-1400. doi:10.1016/j.xphs.2020.11.030

4.5 Supplementary material I

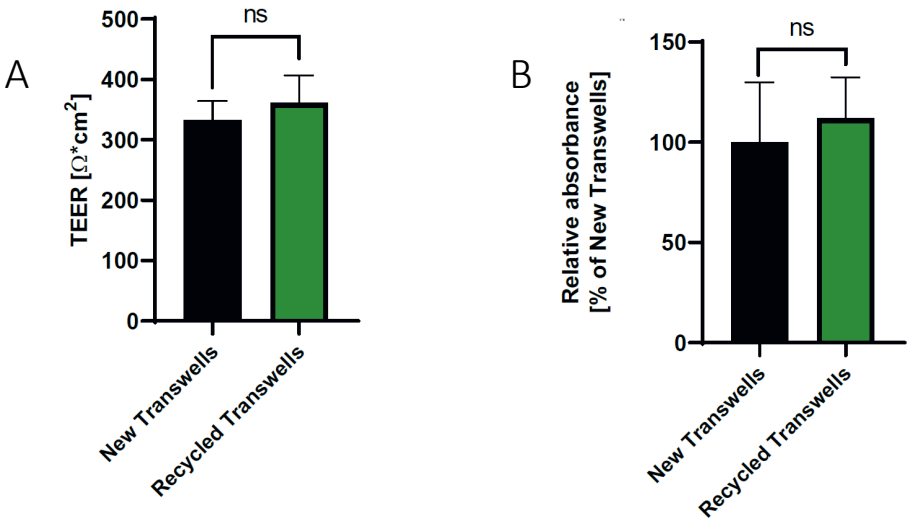

Figure S1. Membrane integrity and cell viability in new cell culture inserts (N=5) vs recycled cell culture inserts (N=50). A) Mean TEER values+SD 12 days after seeding B) WST-1 assay. Mean relative absorbances+SD 17 days after seeding. Ns=no significant differences (unpaired T-test).

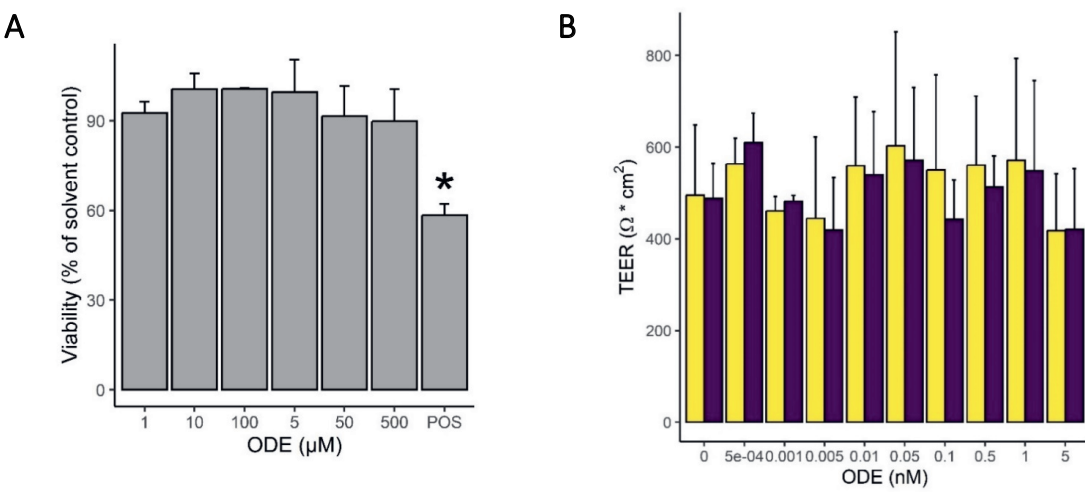

Figure S2. The effect of Odevixibat on Caco-2 cells. A) The effect of 24h exposure to Odevixibat on cell viability of undifferentiated Caco-2 cells assessed using the WST-1 assay. Absorbance is normalized to the solvent control. Values represent the mean±SD of triplicate measurements in 3 independent experiments. Significance was assessed with a one way ANOVA followed by post hoc tests using Bonferroni's correction. Statistically significant differences in cell viability are indicated with * . POS=positive control (0.5 μM potassium dichromate). B) The effects of 3h co-exposure to 5 μM of GCA and an ODE concentration range on TEER values of Caco-2 cells cultured on culture inserts on day 19-21. Values represent the mean±SD, N=3.

Table S1. MS parameters and limit of detection (LOD) and limit of quantification (LOQ) of the BAs studied

	Mode	Q1	Q3	Retention time (min)	LOD (nM)	LOQ (nM)
Deoxycholic acid (DCA)	SIM		391.3	11.073	100	150
Glycochenodeoxycholic acid (GCDCA)	MRM	448.3	74	9.051	40	60
Glycodeoxycholic acid (GDCA)	MRM	448.3	74	9.452	190	200
Glycocholic acid (GCA)	MRM	464.3	74	7.310	122	140

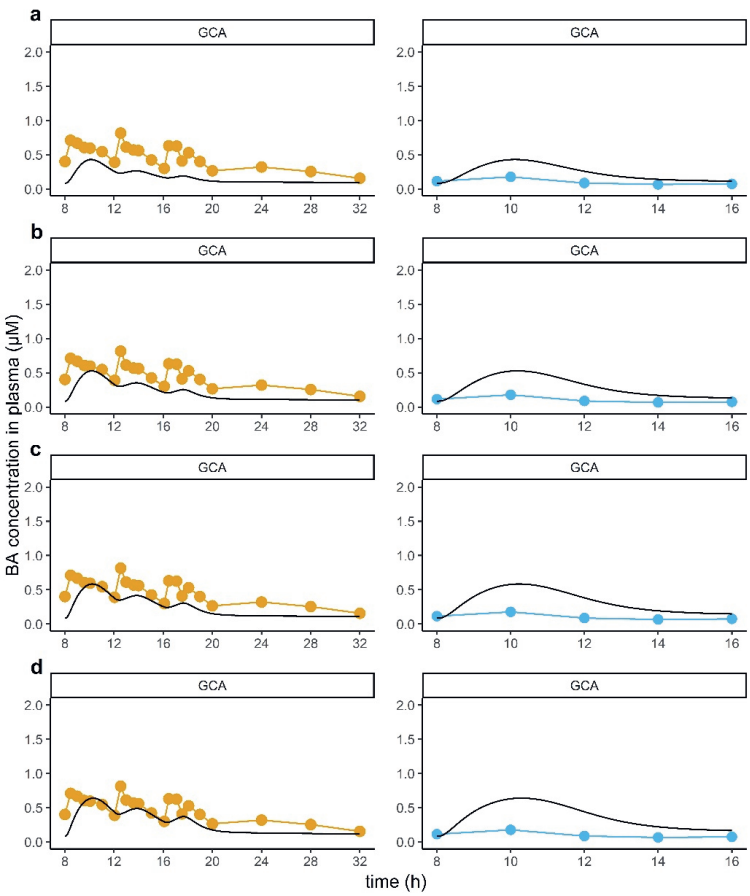

Figure S3. Observed and predicted postprandial GCA kinetics using different values for K_m-values for active intestinal uptake. Black solid line=prediction**.** Left column: Meals were simulated at 8:00, 12:00 and 16:00. Orange circles=in vivo data obtained from Hepner and Demers (1977). Right column: Meal was simulated at 8:00. Blue circles= in vivo data obtained from Lamaziere (2020). a) K_m=39 µM (experimentally derived, no correction for the aqueous boundary layer), b) K_m=22.5 µM (experimentally derived, corrected for the aqueous boundary layer), c) K_m=16.8 µM (average of experimental ABL-corrected and literature), d) K_m=11 µM (literature). GCA=glycocholic acid, GCDCA=glycochenodeoxycholic acid; GDCA=glycodeoxycholic acid; uBA=unconjugated bile acids

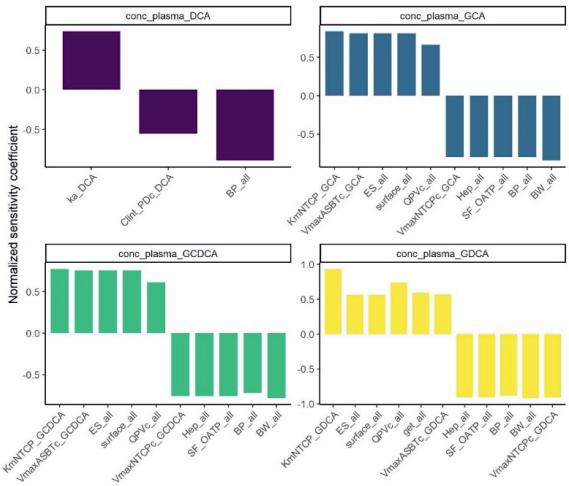

Figure S4. Sensitivity analysis of the influence of the PBK model parameters on the predicted maximal systemic BA concentration in plasma (C_{max}). Only parameters with an absolute normalized sensitivity coefficient > 0.5 are shown. ka=first order rate absorption constant, Clint_PDc=passive diffusion intrinsic clearance, BP=blood:plasma ratio, KmNTCP=Michaelis–Menten constant for NTCP-mediated hepatic uptake, VmaxASBTc= maximal ASBT-mediated GCA absorption rate over the ileal epithelium, ES=empirical scalar for in vitro-in vivo extrapolation of Caco-2 derived kinetic parameters, surface=cylindrical surface of ileum, QPVc=fraction of blood flow to liver through the portal vein, VmaxNTCPc=maximal NTCP-mediated hepatic BA uptake, Hep=hepatocellularity, SF_OATP= scaling factor to adjust hepatic uptake for OATP-mediated uptake, BW=body weight, get=gall bladder ejection time. _GCA, _GCDCA or _GDCA indicates a parameter specifically for the GCA, GCDCA or GDCA submodel, respectively, _all indicates a parameter that is shared for all BA submodels.

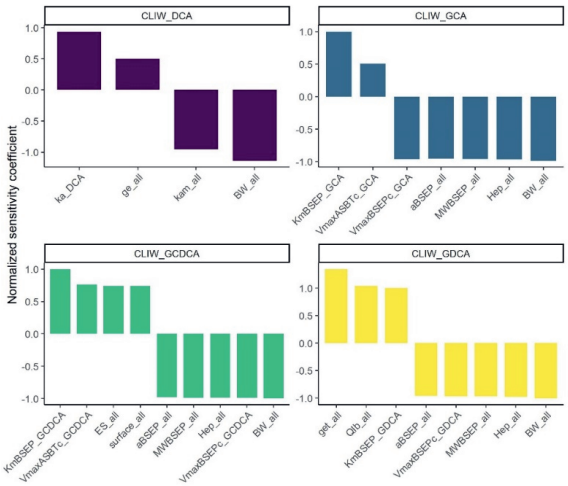

Figure S5. Sensitivity analysis of the influence of the PBK model parameters on the predicted maximal bile acid concentrations in the intracellular liver. Only parameters with an absolute normalized sensitivity coefficient > 0.5 are shown. ka= first order rate absorption constant, ge=first order rate constant for gall bladder ejection rate, kam=first order rate constant for amidation, BW=body weight, get=gall bladder emptying time, KmBSEP=Michaelis–Menten constant for BSEP-mediated BA efflux from the liver, VmaxASBTc= maximal ASBT-mediated GCA absorption rate over the ileal epithelium, , VmaxBSEPc=maximal BSEP-mediated BA efflux rate, aBSEP= BSEP protein abundance, MWBSEP=molecular weight of BSEP, Hep=hepatocellularity, ES=empirical scalar for in vitro-in vivo extrapolation of Caco-2 derived kinetic parameters, surface=ileal surface, get=gall bladder ejection time, Qlb= fraction of bile flow transported directly from liver to intestinal lumen via common bile duct. GCA, _GCDCA or _GDCA indicates a parameter specifically for the GCA, GCDCA or GDCA submodel, respectively, _all indicates a parameter that is shared for all BA submodels.

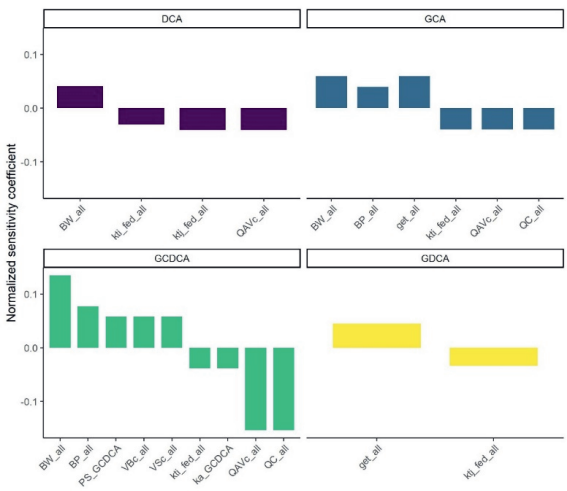

Figure S6. Sensitivity analysis of the influence of the PBK model parameters on the predicted time it takes to reach maximum plasma BA concentration (T_{max}). Only parameters with an absolute normalized sensitivity coefficient > 0.03 are shown. BW= body weight, kti_fed=ileal transit time in fed state, ktj_fed=jejunum transit time in fed state, QAVc=fraction of blood flow through the hepatic arterial vein, BP=blood:plasma ratio, get=gall bladder ejection time, QC=cardiac output, PS=slowly perfused tissue/plasma partition coefficient, VBc=fraction of blood (excluding portal vein), VSc=fraction of slowly perfused tissue, ka=first order rate constant for

absorption. GCA, _GCDCA or _GDCA indicates a parameter specifically for the GCA, GCDCA or GDCA submodel, respectively, _all indicates a parameter that is shared for all BA submodels.

4.6 Supplementary material II

```
#PBK model 4 bile acids
#GCDCA, GCA, GDCA + DCA
#species: human
#author: Véronique de Bruijn
#date: june 2023

## The input parameters, as well as their units, explanation and a reference is described in the supplementary Excel file “parms_4BA_compLiver.xlsx”. Save this file in the working directory and load it in in step 1.

#load required packages
library(RxODE)
library(tidyverse)
library(readxl)
library(data.table)
library(pmxTools)

#set working directory
setwd()

#Simulations
amount.units="umol"       #unit for the amount
time.units="h"            #unit for time
nbr.doses=1       #number of doses
time.0=8                  #time start dosing
time.end=32       #time end of simulation
time.frame=0.01           #time steps of simulation
N=1                       #Number of individuals

#########################################################
#step 1: read in parameters
parms <- read_excel("parms_4BA_compLiver.xlsx") %>%
  dplyr::select(1:6)

parms_long <- melt(setDT(parms), id.vars=1, variable.name="parm") %>%
  mutate(name=paste(parm, parm.1, sep="_"))%>% dplyr::select(3,4)%>% drop_na()

my_names <- parms_long$name
var <- parms_long$value

parameters <- setNames(var, my_names)

Gdose <- parms %>% filter(parm=="Gdose")

#########################################################
#step 2: initial values compartment
```

```
inits <- c(dose_GCDCA=Gdose$GCDCA,
        ALEW_GCDCA=0,
        ALIW_GCDCA=0,
        ALu_GCDCA=0,
        Aup_GCDCA=0,
        Alow_GCDCA=0,
        Acol_GCDCA=0,
        AI_GCDCA=0,
        AP_GCDCA=0,
        AF_GCDCA=0,
        AR_GCDCA=0,
        AS_GCDCA=0,
        AB_GCDCA=0,
        dose_GDCA=Gdose$GDCA,
        ALEW_GDCA=0,
        ALIW_GDCA=0,
        ALu_GDCA=0,
        Aup_GDCA=0,
        Alow_GDCA=0,
        Acol_GDCA=0,
        AP_GDCA=0,
        AI_GDCA=0,
        AF_GDCA=0,
        AR_GDCA=0,
        AS_GDCA=0,
        AB_GDCA=0,
        dose_GCA=Gdose$GCA,
        ALEW_GCA=0,
        ALIW_GCA=0,
        ALu_GCA=0,
        AP_GCA=0,
        AI_GCA=0,
        AF_GCA=0,
        AR_GCA=0,
        AS_GCA=0,
        AB_GCA=0,
        ALEW_DCA=0,
        ALIW_DCA=0,
        Acol_DCA=0,
        AI_DCA=0,
        AP_DCA=0,
        AF_DCA=0,
        AR_DCA=0,
        AS_DCA=0,
        AB_DCA=0)

#########################################################
#step 3: exposure
qd <- eventTable(amount.units = amount.units, time.units = time.units) %>%
  add.dosing(dose=0.00001, cmt="ALEW_GCDCA",nbr.doses = 1, do.sampling=FALSE) %>%
```

```
  et(seq(from = time.0, to = time.end, by = time.frame))

#########################################################
#step 4: differential equations
PBK <- RxODE({

  ##Physiological parameters
  #Tissue volumes
  VF = VFc_all*BW_all;                #       {L or Kg} ; volume of fat tissue (calculated)
VLIW = VLIWc_all*BW_all; #            {L or Kg} ; volume of liver intracellular water (calculated)
  VLEW = VLEWc_all*BW_all;            #       {L or Kg} ; volume of liver extracellular water (calculated)
  VL=VLEW+VLIW;
  VR = VRc_all*BW_all;                #       {L or Kg} ; volume of richly perfused tissue (calculated)
  VS = VSc_all*BW_all;                #       {L or Kg} ; volume of slowly perfused tissue (calculated)
  VB = VBc_all*BW_all;                #       {L or Kg} ; volume of blood excluding portal vein (calculated)
  VI = VIc_all*BW_all;                #       {L or Kg} ; volume of intestinal tissue (calculated)
  VG= VGc_all*BW_all;                 #       {L or Kg} ; volume of gall bladder tissue (calculated)
  VLu=VLuc_all*BW_all;                #       {L or Kg} ; volume of intestinal lumen (calculated)
  VP=VBPc_all*BW_all;       #         {L or Kg} ; volume of portal blood

  #Blood flow rates
  QF = QFc_all*QC_all;                #       {L/hr}    ; blood flow to fat tissue (calculated)
  QAV = QAVc_all*QC_all;   #          {L/hr}    ; arterial blood flow to liver tissue (calculated)
  QPV= QPVc_all*QC_all;               #       {L/hr}    ; portal blood flow to liver tissue (calculated)
  QS = QSc_all*QC_all;                #       {L/hr}    ; blood flow to slowly perfused tissue (calculated)
  QR = QRc_all*QC_all;                #       {L/hr}    ; blood flow to richly perfused tissue (calculated)
  QI = QIc_all*QC_all;                #       {L/hr}    ; blood flow to intestines (calculated)

  ## Scaling of maximal transport rate (Vmax) for BSEP, ASBT and NTCP mediated BA transport
  WL=20*BW_all; #weight of liver, g
  SF_BSEP=aBSEP_all*MWBSEP_all*Hep_all*WL*10^-9; # {mg BSEP/entire liver}; scaling factor for BSEP
mediated hepatic efflux for GCA and GCDCA
  SF_ASBT=surface_all*10^-6*SA_all; # {cm2/entire ileum}; fitted
  SF_NTCP=Hep_all*SF_OATP_all*WL*10^-6; #{10^6 hepatocytes/entire liver}; scaling factor for hepatic
transport

  VmaxBSEP_GCDCA=VmaxBSEPc_GCDCA*SF_BSEP*60; # {umol/h/entire liver} maximum speed for BSEP-
mediated GCDCA efflux (calculated)
  VmaxASBT_GCDCA=VmaxASBTc_GCDCA*SF_ASBT*60; #{umol/hr/ileum} : maximum speed for ASBT-mediated
GCDCA uptake (calculated)
  VmaxNTCP_GCDCA=VmaxNTCPc_GCDCA*SF_NTCP*60; #{umol/hr/entire liver}: maximum speed for hepatic
GCDCA uptake (calculated)

  VmaxBSEP_GCA=VmaxBSEPc_GCA*SF_BSEP*60; # {umol/h/entire liver} maximum speed for BSEP-mediated
GCA efflux (calculated)
  VmaxASBT_GCA=VmaxASBTc_GCA *SF_ASBT*60; # {umol/hr/ileum} : maximum speed for ASBT-mediated GCA
uptake (calculated)
  VmaxNTCP_GCA=VmaxNTCPc_GCA*SF_NTCP*60; #{umol/hr/entire liver}: maximum speed for hepatic GCDCA
uptake (calculated)
```

```
 VmaxBSEP_GDCA=VmaxBSEPc_GDCA*SF_BSEP*60; # {umol/h/entire liver} maximum speed for BSEP-mediated GDCA efflux (calculated).
 VmaxASBT_GDCA=VmaxASBTc_GDCA*SF_ASBT*60; #{umol/hr/ileum} : maximum speed for ASBT-mediated GDCA uptake (calculated)
 VmaxNTCP_GDCA=VmaxNTCPc_GDCA*SF_NTCP*60; #{umol/hr/entire liver}: maximum speed for hepatic GCDCA uptake (calculated)

 ## Fast/fed state
 #ge=ifelse((ctime>8 & ctime<(8+get_all)), ge_all,0); #specifying the duration of gallbladder emptying (1 meal)
 ge=ifelse(((ctime >8 & ctime<(8+get_all)) | (ctime>12 & ctime<(12+get_all)) | (ctime>16 & ctime<(16+get_all))), ge_all,0); # specifying the duration of gallbladder emptying (3 meals)
 #(umol/hr/entire liver), calculated
 ktj=ifelse(ctime>17.5 | ctime <8, ktj_fasted_all, ktj_fed_all); #specifying different jejunum transit rates for fast/fed state (1/hr)
 kti=ifelse(ctime>17.5 | ctime <8, kti_fasted_all, kti_fed_all); #specifying different ileum transit rates for fast/fed state (1/hr)

 QGb_all=1-QIb_all; #fraction of bile flow from liver stored in gall bladder, calculated

 ## Competitive inhibition by ODE on ASBT-mediated BA transport
 IDOSE=ODOSEmg_all/740.29/9*10^6*ODE_fub_all; #free ODE concentration in ileum, calculated (nM), MW=740.29, volume intestinal tract=9L
 modf_Km=1+(IDOSE/0.02); #modulation factor for Km based on competitive inhibition, Ki=0.02 nM (experimental)
 ODOSEmg_all=ODOSEmg_all;

 ## Model calculations


 ### GCDCA submodel ###
 CLEW_GCDCA=ALEW_GCDCA/VLEW; # concentration in the extracellular water (liver)
 CVLEW_GCDCA=CLEW_GCDCA/(PEWP_GCDCA*BP_all); #concentration leaving the extracellular water (liver)
 CLIW_GCDCA=ALIW_GCDCA/VLIW; # concentration in intracellular water (liver)
 CIl_GCDCA=Alow_GCDCA/VIl_all;                    # concentration in the ileum (umol/L)
 CI_GCDCA=AI_GCDCA/VI;                    # concentration in the intestinal tissue (umol/L)
 CVI_GCDCA=CI_GCDCA/(PG_GCDCA*BP_all);          # concentration in venous blood leaving the intestinal tissue(umol/L)
 CF_GCDCA=AF_GCDCA/VF;                    # concentration in the fat tissue (umol/L)
 CVF_GCDCA=CF_GCDCA/(PF_GCDCA*BP_all);          # concentration in venous blood leaving the fat tissue (umol/L)
 CR_GCDCA=AR_GCDCA/VR;                    # concentration in the rapidly perfused tissue (umol/L)
 CVR_GCDCA=CR_GCDCA/(PR_GCDCA*BP_all);          # concentration in venous blood leaving the rapidly perfused tissue (umol/L)
 CS_GCDCA=AS_GCDCA/VS;                    # concentration in the slowly perfused tissue (umol/L)
 CVS_GCDCA=CS_GCDCA/(PS_GCDCA*BP_all);          # concentration in venous blood leaving slowly perfused tissue (umol/L)
 CB_GCDCA=AB_GCDCA/VB;                    # concentration in blood excluding portal vein (umol/L)
 CP_GCDCA=AP_GCDCA/VP;                     # concentration in portal blood (umol/L)
```

```
 d/dt(dose_GCDCA) = -ge*dose_GCDCA+VmaxBSEP_GCDCA*CLIW_GCDCA/(KmBSEP_GCDCA +
CLIW_GCDCA)*QGb_all     ;                              #change in amount in the gall bladder, umol
 d/dt(ALEW_GCDCA)=QAV *(CB_GCDCA -CVLEW_GCDCA)+QPV*(CP_GCDCA-CVLEW_GCDCA) -
VmaxNTCP_GCDCA * CVLEW_GCDCA/(KmNTCP_GCDCA + CVLEW_GCDCA);                  # change in amount in
extracellular water (liver), umol
 d/dt(ALIW_GCDCA)= -VmaxBSEP_GCDCA *CLIW_GCDCA /(KmBSEP_GCDCA +
CLIW_GCDCA)+VmaxNTCP_GCDCA * CVLEW_GCDCA/(KmNTCP_GCDCA + CVLEW_GCDCA)
+kam_all*ALIW_DCA*Gdosel_GCDCA+Acol_DCA*0.05*Gdosel_GCDCA ; # change in amount in intracellular
water (liver), umol
 d/dt(Aup_GCDCA)= ge*dose_GCDCA +VmaxBSEP_GCDCA *CLIW_GCDCA /(KmBSEP_GCDCA +
CLIW_GCDCA)*Qlb_all-ka_GCDCA*Aup_GCDCA-ktj*Aup_GCDCA; # change in amount in upper intestinal lumen,
umol
 d/dt(Alow_GCDCA)=ktj*Aup_GCDCA-kti*Alow_GCDCA-VmaxASBT_GCDCA *Cll_GCDCA
/(KmASBT_GCDCA*modf_Km + Cll_GCDCA);            # change in amount in ileum, umol
 d/dt(Acol_GCDCA)=kti*Alow_GCDCA-ka_GCDCA*Acol_GCDCA-kdec_all*Acol_GCDCA;# change in amount in
colon, umol
 d/dt(AI_GCDCA)=QI*(CB_GCDCA -CVI_GCDCA);       # change in amount in intestinal tissue, umol
 d/dt(AP_GCDCA)=ka_GCDCA*Aup_GCDCA+VmaxASBT_GCDCA *Cll_GCDCA /(KmASBT_GCDCA*modf_Km +
Cll_GCDCA)+ka_GCDCA*Acol_GCDCA - QPV*CP_GCDCA; #amount in portal blood, umol
 d/dt(AF_GCDCA)=QF*(CB_GCDCA -CVF_GCDCA) ;     # change in amount in fat tissue, umol
 d/dt(AR_GCDCA)=QR*(CB_GCDCA -CVR_GCDCA) ;     # change in amount in rapidly perfused tissue, umol
 d/dt(AS_GCDCA)= QS*(CB_GCDCA -CVS_GCDCA);     # change in amount in slowly perfused tissue, umol
 d/dt(AB_GCDCA)=QF*CVF_GCDCA + (QAV+QPV)*CVLEW_GCDCA + QS*CVS_GCDCA + QR *CVR_GCDCA +QI
*CVI_GCDCA -(QF+QAV+QS+QR+QI) *CB_GCDCA;      # change in amount in blood, umol

 conc_plasma_GCDCA=(CB_GCDCA/BP_all)+CBfs_GCDCA; #concentration in **plasma**, umol

 ### GCA submodel ###
 CLEW_GCA=ALEW_GCA/VLEW;     # concentration in the extracellular water (liver)
CVLEW_GCA=CLEW_GCA/(PEWP_GCA*BP_all); #concentration in venous blood leaving the
extracellular water (liver)
 CLIW_GCA=ALIW_GCA/VLIW;                  # concentration in intracellular water (liver)
 Cll_GCA=Alow_GCA/Vll_all;                # concentration in the ileum (umol/L)
 CI_GCA=AI_GCA/VI;                  # concentration in the intestinal tissue (umol/L)
 CVI_GCA=CI_GCA/(PG_GCA*BP_all);          # concentration in venous blood leaving the intestinal
tissue(umol/L)
 CF_GCA=AF_GCA/VF;                        # concentration in the fat tissue (umol/L)
 CVF_GCA=CF_GCA/(PF_GCA*BP_all);          # concentration in venous blood leaving the fat tissue (umol/L)
 CR_GCA=AR_GCA/VR;                        # concentration in the rapidly perfused tissue (umol/L)
 CVR_GCA=CR_GCA/(PR_GCA*BP_all);          # concentration in venous blood leaving the rapidly perfused tissue
(umol/L)
 CS_GCA=AS_GCA/VS;                        # concentration in the slowly perfused tissue (umol/L)
 CVS_GCA=CS_GCA/(PS_GCA*BP_all);  # concentration in venous blood leaving slowly perfused tissue (umol/L)
 CB_GCA=AB_GCA/VB;                        # concentration in blood excluding portal vein (umol/L)
 CP_GCA=AP_GCA/VP;                  # concentration in portal blood (umol/L)

 d/dt(dose_GCA) = -ge*dose_GCA+VmaxBSEP_GCA*CLIW_GCA/(KmBSEP_GCA + CLIW_GCA)*QGb_all        ; #
change in amount in the gall bladder, umol
 d/dt(ALEW_GCA)=QAV *(CB_GCA -CVLEW_GCA)+QPV*(CP_GCA-CVLEW_GCA) -VmaxNTCP_GCA *
CVLEW_GCA/(KmNTCP_GCA + CVLEW_GCA); # change in amount in extracellular water (liver), umol
```

```
 d/dt(ALIW_GCA)= -VmaxBSEP_GCA *CLIW_GCA /(KmBSEP_GCA + CLIW_GCA)+VmaxNTCP_GCA *
CVLEW_GCA/(KmNTCP_GCA + CVLEW_GCA) +kam_all*ALIW_DCA *Gdosel_GCA+ Acol_DCA*0.05*Gdosel_GCA ;
# change in amount in intracellular water (liver), umol
 d/dt(Aup_GCA)= ge*dose_GCA +VmaxBSEP_GCA *CLIW_GCA /(KmBSEP_GCA + CLIW_GCA)*QIb_all-
ka_GCA*Aup_GCA-ktj*Aup_GCA; # change in amount in upper intestinal lumen, umol
 d/dt(Alow_GCA)=ktj*Aup_GCA-kti*Alow_GCA-VmaxASBT_GCA *CII_GCA /(KmASBT_GCA*modf_Km + CII_GCA);
# change in amount in ileum, umol
 d/dt(Acol_GCA)=kti*Alow_GCA-ka_GCA*Acol_GCA-kdec_all*Acol_GCA;# change in amount in colon, umol
 d/dt(AI_GCA)=QI*(CB_GCA -CVI_GCA);       # change in amount in intestinal tissue, umol
 d/dt(AP_GCA)=ka_GCA*Aup_GCA+VmaxASBT_GCA *CII_GCA /(KmASBT_GCA*modf_Km +
CII_GCA)+ka_GCA*Acol_GCA - QPV*CP_GCA;            #amount in portal blood, umol
 d/dt(AF_GCA)=QF*(CB_GCA -CVF_GCA) ;    # change in amount in fat tissue, umol
 d/dt(AR_GCA)=QR*(CB_GCA -CVR_GCA) ;    # change in amount in rapidly perfused tissue, umol
 d/dt(AS_GCA)= QS*(CB_GCA -CVS_GCA);    # change in amount in slowly perfused tissue, umol
 d/dt(AB_GCA)=QF*CVF_GCA + (QAV+QPV)*CVLEW_GCA + QS*CVS_GCA + QR *CVR_GCA +QI *CVI_GCA -
(QF+QAV+QS+QR+QI) *CB_GCA;     # change in amount in blood, umol

 conc_plasma_GCA=(CB_GCA/BP_all)+CBfs_GCA; #concentration in **plasma**, umol

 ### GDCA submodel ###
 CLEW_GDCA=ALEW_GDCA/VLEW;            # concentration in the extracellular water (liver), (umol/L)
 CVLEW_GDCA=CLEW_GDCA/(PEWP_GDCA*BP_all); #concentration in venous blood leaving the extracellular
water (liver) (umol/)
 CLIW_GDCA=ALIW_GDCA/VLIW;            # concentration in intracellular water (liver)
 CII_GDCA=Alow_GDCA/VII_all;          # concentration in the ileum (umol/L)
 CI_GDCA=AI_GDCA/VI;                          # concentration in the intestinal tissue (umol/L)
 CVI_GDCA=CI_GDCA/(PG_GDCA*BP_all);   # concentration in venous blood leaving the intestinal
tissue(umol/L)
 CF_GDCA=AF_GDCA/VF;                          # concentration in the fat tissue (umol/L)
 CVF_GDCA=CF_GDCA/(PF_GDCA*BP_all);   # concentration in venous blood leaving the fat tissue (umol/L)
 CR_GDCA=AR_GDCA/VR;                          # concentration in the rapidly perfused tissue (umol/L)
CVR_GDCA=CR_GDCA/(PR_GDCA*BP_all);    # concentration in venous blood leaving the rapidly perfused tissue
(umol/L)
 CS_GDCA=AS_GDCA/VS;                          # concentration in the slowly perfused tissue (umol/L)
 CVS_GDCA=CS_GDCA/(PS_GDCA*BP_all);   # concentration in venous blood leaving slowly perfused tissue
(umol/L)
CB_GDCA=AB_GDCA/VB;           # concentration in blood excluding portal vein (umol/L)
 CP_GDCA=AP_GDCA/VP;                   # concentration in portal blood (umol/L)

 d/dt(dose_GDCA) = -ge*dose_GDCA+VmaxBSEP_GDCA*CLIW_GDCA/(KmBSEP_GDCA + CLIW_GDCA)*QGb_all
                  ; # change in amount in the gall bladder, umol
 d/dt(ALEW_GDCA)=QAV *(CB_GDCA -CVLEW_GDCA)+QPV*(CP_GDCA-CVLEW_GDCA) -VmaxNTCP_GDCA *
CVLEW_GDCA/(KmNTCP_GDCA + CVLEW_GDCA); #change in amount in extracellular liver compartiment, umol
 d/dt(ALIW_GDCA)= -VmaxBSEP_GDCA *CLIW_GDCA /(KmBSEP_GDCA + CLIW_GDCA)+VmaxNTCP_GDCA *
CVLEW_GDCA/(KmNTCP_GDCA +
CVLEW_GDCA)+kam_all*ALIW_DCA*Gdosel_GDCA+Acol_DCA*0.05*Gdosel_GDCA ; #change in amount in
intracellular liver compartiment, umol
 d/dt(Aup_GDCA)= ge*dose_GDCA +VmaxBSEP_GDCA *CLIW_GDCA /(KmBSEP_GDCA + CLIW_GDCA)*QIb_all-
ka_GDCA*Aup_GDCA-ktj*Aup_GDCA; # change in amount in upper intestinal lumen, umol
```

```
 d/dt(Alow_GDCA)=ktj*Aup_GDCA-kti*Alow_GDCA-VmaxASBT_GDCA *CIl_GDCA /(KmASBT_GDCA*modf_Km +
CIl_GDCA); # change in amount in ileum, umol
 d/dt(Acol_GDCA)=kti*Alow_GDCA-ka_GDCA*Acol_GDCA-kdec_all*Acol_GDCA;# amount in colon, umol
 d/dt(AI_GDCA)=QI*(CB_GDCA -CVI_GDCA);              # change in amount in intestinal tissue, umol
 d/dt(AP_GDCA)=ka_GDCA*Aup_GDCA+VmaxASBT_GDCA *CIl_GDCA /(KmASBT_GDCA*modf_Km +
CIl_GDCA)+ka_GDCA*Acol_GDCA - QPV*CP_GDCA; #amount in portal blood, umol
 d/dt(AF_GDCA)=QF*(CB_GDCA -CVF_GDCA) ;          # change in amount in fat tissue, umol
 d/dt(AR_GDCA)=QR*(CB_GDCA -CVR_GDCA) ;          # change in amount in rapidly perfused tissue, umol
 d/dt(AS_GDCA)= QS*(CB_GDCA -CVS_GDCA);          # change in amount in slowly perfused tissue, umol
 d/dt(AB_GDCA)=QF*CVF_GDCA + (QAV+QPV)*CVLEW_GDCA + QS*CVS_GDCA + QR *CVR_GDCA +QI
*CVI_GDCA -(QF+QAV+QS+QR+QI) *CB_GDCA;          # change in amount in blood, umol

 conc_plasma_GDCA=(CB_GDCA/BP_all)+CBfs_GDCA;            #concentration in **plasma**, umol

 ### DCA submodel ###
 CLEW_DCA=ALEW_DCA/VLEW;                                  # concentration in the liver (umol/L)
 CVLEW_DCA=CLEW_DCA/(PEWP_DCA*BP_all);       # concentration in venous blood leaving the liver (umol/L)
 CLIW_DCA=ALIW_DCA/VLIW;                                  # concentration in intracellular water (liver)
 CI_DCA=AI_DCA/VI;        # concentration in the intestinal tissue (umol/L)
 CVI_DCA=CI_DCA/(PG_DCA*BP_all);          # concentration in venous blood leaving the intestinal
tissue(umol/L)
 CF_DCA=AF_DCA/VF;                                        # concentration in the fat tissue (umol/L)
 CVF_DCA=CF_DCA/(PF_DCA*BP_all);         # concentration in venous blood leaving the fat tissue (umol/L)
 CR_DCA=AR_DCA/VR;                # concentration in the rapidly perfused tissue (umol/L)
 CVR_DCA=CR_DCA/(PR_DCA*BP_all);         # concentration in venous blood leaving the rapidly perfused tissue
(umol/L)
CS_DCA=AS_DCA/VS;        # concentration in the slowly perfused tissue (umol/L)
 CVS_DCA=CS_DCA/(PS_DCA*BP_all);          # concentration in venous blood leaving slowly perfused tissue
(umol/L)
 CB_DCA=AB_DCA/VB;                # concentration in blood excluding portal vein (umol/L)
 CP_DCA=AP_DCA/VP;                                        # concentration in portal vein (umol/L)

 d/dt(ALEW_DCA)=QAV*(CB_DCA -CVLEW_DCA)+QPV*(CP_DCA-CVLEW_DCA)-Clint_PD_DCA*CVLEW_DCA; #
change in amount in extracellular water liver, umol/hr
 d/dt(ALIW_DCA)=Clint_PD_DCA*CVLEW_DCA-kam_all*ALIW_DCA; # change in amount in intracellular water
liver, umol/hr
 d/dt(Acol_DCA)=kdec_all*(Acol_GCDCA+Acol_GCA+Acol_GDCA)-ka_DCA*Acol_DCA-0.05*Acol_DCA; # change
in amount in colon, umol/hr
 d/dt(AI_DCA)=QI*(CB_DCA-CVI_DCA);           # change in amount in intestinal tissue, umol/hr
 d/dt(AP_DCA)=ka_DCA*Acol_DCA - QPV*CP_DCA; # change in amount in portal vein tissue, umol/hr
 d/dt(AF_DCA)=QF*(CB_DCA -CVF_DCA) ;        # change in amount in fat tissue, umol/hr
 d/dt(AR_DCA)=QR*(CB_DCA -CVR_DCA) ;        # change in amount in rapidly perfused tissue, umol/hr
 d/dt(AS_DCA)= QS*(CB_DCA -CVS_DCA);     # change in amount in slowly perfused tissue, umol/hr
 d/dt(AB_DCA)=QF*CVF_DCA + (QAV+QPV)*CVLEW_DCA + QS*CVS_DCA + QR *CVR_DCA +QI *CVI_DCA -
(QF+QS+QR+QI+QAV) *CB_DCA;        # change in amount in blood, umol/hr

 conc_plasma_DCA=(CB_DCA/BP_all)+CBfs_DCA;#concentration in **plasma**, umol
})

##########################################################
```

```
##Step 5: Solve the model
qd$ctime <- qd$time
print(PBK)

solve.pbk<- as_tibble(solve(PBK, params=parameters, events = qd, inits=inits, cores=4,
covs_interpolation="nocb"))

## Mass balance calculations
solve.pbk %>%
mutate(OUT=dose_GCDCA+ALEW_GCDCA+ALIW_GCDCA+Aup_GCDCA+Alow_GCDCA+Acol_GCDCA+AI_GCDCA+
AP_GCDCA+AF_GCDCA+AR_GCDCA+AS_GCDCA+AB_GCDCA+ALEW_DCA+ALIW_DCA+Acol_DCA+AI_DCA+AP_DC
A+ AF_DCA+AR_DCA+AS_DCA+AB_DCA+dose_GCA+ALEW_GCA+ALIW_GCA+Aup_GCA+Alow_GCA +Acol_GCA+
AP_GCA +AI_GCA+AF_GCA +AR_GCA+AS_GCA+AB_GCA+
dose_GDCA+ALEW_GDCA+ALIW_GDCA+Aup_GDCA+Alow_GDCA+ Acol_GDCA+AI_GDCA+AP_GDCA +
AF_GDCA+AR_GDCA+AS_GDCA+AB_GDCA,
            MB=Gdose$GCDCA+Gdose$GDCA+Gdose$GCA-OUT)
```

Table S1 Input parameters similar for all bile acid submodels, or for respectively GCDCA, GCA, GDCA or DCA (model bile acid for uBA)

parm	all	GCDCA	GCA	GDCA	DCA	description	unit	ref
BW	70					body weight	kg	Brown (1997)
VFc	0.214					fraction of fat tissue		Brown (1997)
VLc	0.026					fraction of liver tissue		Brown (1997)
VLIWc	0.02171					fraction of liver intracellular water		Brown (1997)
VLEWc	0.00429					fraction of liver extracellular water		Brown (1997)
VRc	0.054					fraction of rapidly perfused tissue		Brown (1997)
VSc	0.6033					fraction of slowly perfused tissue		Brown (1997)
VBc	0.0726					fraction of blood (excluding portal vein)		Brown (1997)
VBPc	0.0064					fraction of portal blood		Brown (1997)
VIc	0.009					fraction of intestinal tissue		Hofman (1983)
VGc	0.0007					fraction of gall bladder tissue		Van Eprecum (1992)
VLuc	0.014					fraction of intestinal lumen		Brown (1997)
QC	347.9075					cardiac output	L/hr	Brown (1997)
QFc	0.052					fraction of blood flow to fat tissue		Brown (1997)
QAVc	0.046					fraction of blood flow to liver via arterial vein		Brown (1997)
QPVc	0.181					fraction of blood flow to liver via portal vein		Brown (1997)
QSc	0.248					fraction of blood flow to slowly perfused tissue		Brown (1997)
QRc	0.292					fraction of blood flow to rapidly perfused tissue		Brown (1997)
QIc	0.181					fraction of blood flow to intestinal tissue		Brown (1997)
PF		0.05	0.06	0.05	0.05	fat/plasma partition coefficient		Brown (1997)
PL		0.1	0.13	0.12	0.1	liver/plasma partition coefficient		calculated using QPPR of Rodgers & Rowland 2006
PR		0.136	0.172	0.156	0.13	richly perfused tissue/plasma partition coefficient		calculated using QPPR of Rodgers & Rowland 2006
PS		0.19	0.22	0.21	0.2	slowly perfused tissue/plasma partition coefficient		calculated using QPPR of Rodgers & Rowland 2006
PG		0.18	0.21	0.19	0.17	gut/plasma partitioncoefficient		calculated using QPPR of Rodgers & Rowland 2006
PEWP		0.31	0.31	0.31	0.31	extracellular water/plasma partition coefficient		calculated using QPPR of Peyret (2010)
PCEW		1	1	1	1	cell/extracellular water partition coefficient		calculated using QPPR of Peyret (2010)
BP	0.55	0.55	0.55	0.55	0.55	blood:plasma ratio		1-HCt, assumption
ka		0.09	0	0.09	0.01	absorption rate constant in upper intestines and colon, fitted to experimental data	/hr	Krag (1974), Voronova (2020)
aBSEP	0.839					BSEP protein abudance	pmoles/10^6 hepatocytes	Burt (2016)
MWBSEP	140000					molecular weight BSEP	g/mole	
Hep	99					hepatocellularity	10^6 hepatocytes per g liver	Barter (2007)
VmaxNTCPc		510	561	600		maximal rate of bile acid uptake into HepaRG cells, unscaled	pmoles/10^6 hepatocytes/min	Notenboom (2018)
KmNTCP		5.284	9.2	8.4		maximal rate of bile acid uptake into HepaRG cells, unscaled	µM	GCDCA: average of Notenboom (2018) and Jani (2018), GCA + GDCA: Notenboom (2018)
SF_OATP	1.25					NTCP-mediated transport is only 80% of transport; correction factor to correct for total hepatic transport		
Clint_PDc		0	0	0	78.975	passive diffusion	L/hr	For DCA: set equal to blood flow to liver
VmaxBSEPc		5.8	7	8.4		maximal rate of BSEP-mediated transport, unscaled	umole/min/mg BSEP	Kis (2009), Notenboom (2018)
KmBSEP		4.3	25.9	19		Michaelis-Menten constant for BSEP-mediated transport	umole/L	Kis (2009), Notenboom (2018)
ktj_fasted	2.44					upper intestine transit rate in fasted state	/hr	Kimura (2002)
ktj_fed	2.155					upper intestine transit rate in fed state	/hr	Kimura (2002)
kti_fasted	2.76					ileum transit rate in fasted state	/hr	Kimura (2002)
kti_fed	1.2					ileum transit rate in fed state	/hr	Kimura (2002)
VmaxASBTc		203.2	71.5	211.2072		maximal rate of ASBT-mediated transport, unscaled	pmoles/min/cm2	GCA experimental, GCDCA and GDCA from Balakrishnan (2006)

[Table continues on next page]

surface	4712					cylindrical surface of ileum	cm2	calculated from radius and length, input from Kararli (1995)
ES	2.8					empirical scalar for in vitro-in vivo extrapolation VmaxASBTc		empirical
KmASBT		0.662	16.8	1.1		Michaelis-Menten constant for ASBT-mediated transport	umol/L	Balakrishnan (2006)
Qlb	0.5					fraction of bile flow transported directly from liver to intestinal lumen via common bile duct		Molino (1986)
CBfs		0.45	0.085	0.1	0.32	systemic plasma concentration in fasting state	umol/L	García-Cañaveras (2001)
Gdosel		0.518	0.238	0.244		fraction of each BA produced in liver from DCA		Rodrigues (2014)
Gdose	3020	1564.36	810.3385	419.7553		dose of BA produced in liver from DCA	umol	Sips 2018
Vll	5.9					volume ileum	L	calculated from radius and length, input from Kararli (1995)
kam	1000					amidation rate constant	/hr	assumption: immediate conjugation in liver
kdec	1000					deconjugation constant	/hr	assumption: immediate deconjugation in colon
ge	1.2					gallbladder emptying rate	/hr	Molino (1986)
get	1.5					gallbladder ejection time	hr	Jazrawi (1995)
ODOSEmg	0					dose of ODE	mg	
ODE_fub	0.003					plasma		plasma equals Fub in caecum

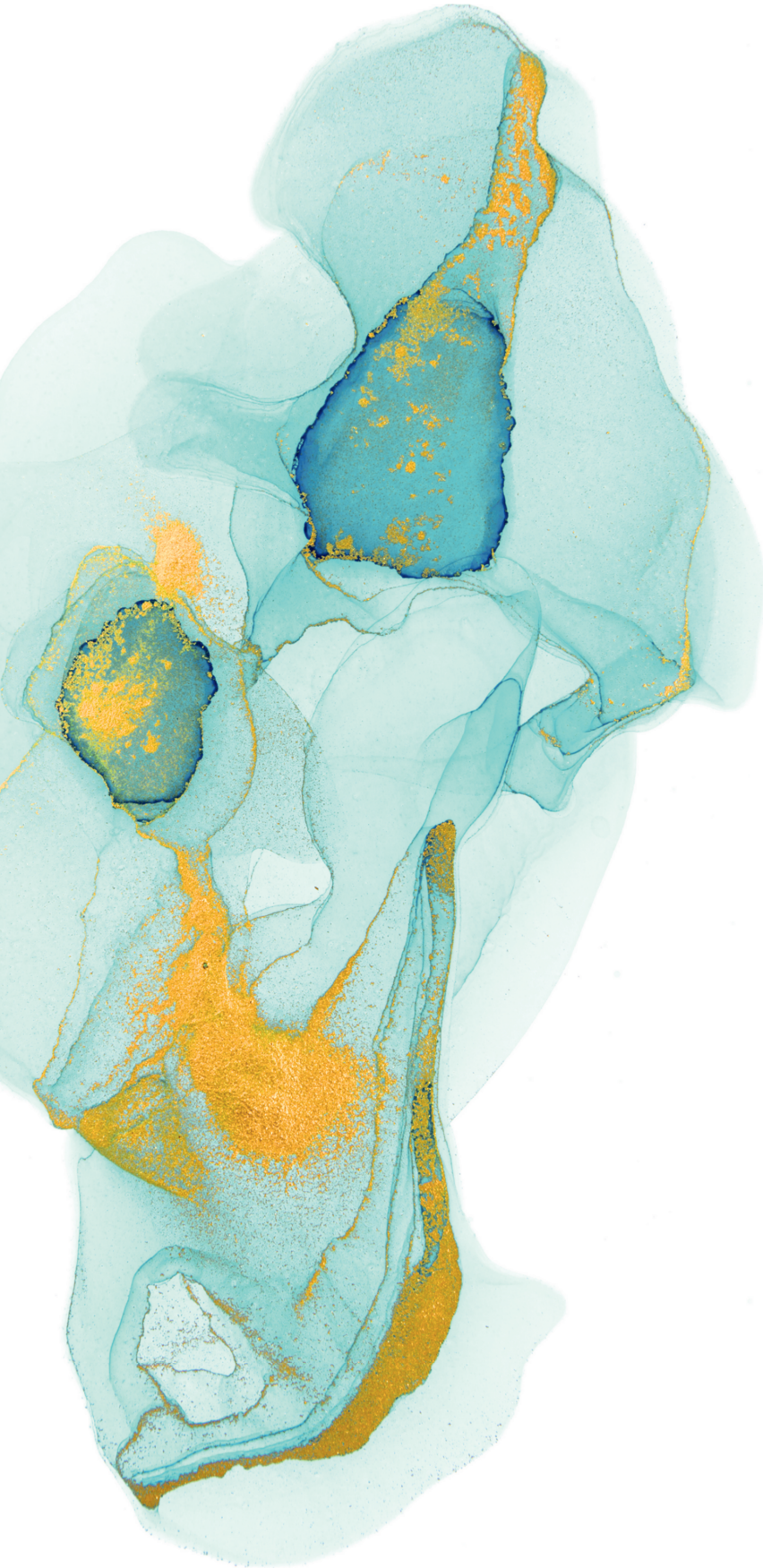

Chapter 5

Application of physiologically based (PBK) modelling to quantify the effect of the antibiotic tobramycin on bile acid levels in human plasma

Nina Zhang, Ivonne M.C.M. Rietjens & Véronique M.P. de Bruijn

Submitted

Abstract

Systemic bile acid homeostasis plays an important role in human health. In this study, a physiologically based kinetic (PBK) model that includes microbial bile acid deconjugation and intestinal reuptake via the apical sodium dependent bile acid transporter (ASBT) was applied to predict the systemic plasma bile acid concentrations in human upon oral treatment with the antibiotic tobramycin. Tobramycin was previously shown to inhibit intestinal deconjugation and reuptake of bile acids and to affect bile acid homeostasis upon oral exposure of rats. Kinetic parameters to define the effects of tobramycin on intestinal bile acid transport were determined *in vitro* using a Caco-2 cell layer transwell model for studying the intestinal translocation of 4 model bile acids including glycochenodeoxycholic acid (GCDCA), glycocholic acid (GCA), glycodeoxycholic acid (GDCA) and deoxycholic acid (DCA) the latter as a model for unconjugated bile acids (uBA). Kinetic constants for the effect of tobramycin on intestinal microbial deconjugation were taken from previous *in vitro* studies using anaerobic fecal incubations. The PBK model simulations predicted that exposure to tobramycin at the dose level also used in the previous 28 day rat study would reduce human plasma C_{max} levels of GCA, GCDCA, GDCA and uBA by 42.4%, 27.7%, 16.9% and 75.8%. The reduction of conjugated bile acids is governed especially via an effect on ASBT mediated intestinal uptake, and not via the effect of tobramycin on intestinal deconjugation, likely because deconjugation happens to a large extent in the colon which has limited subsequent bile acid reuptake. The results reflect that oral exposure to xenobiotics that are not or poorly bioavailable can affect systemic bile acid homeostasis. Altogether, the PBK model appears to provide a 3R compliant tool to evaluate the effect of oral exposure to xenobiotics on host bile acid homeostasis via effects on intestinal bile acid deconjugation and reuptake.

Key words: Bile acids ● Caco-2 cells ● apical sodium dependent bile acid transporter (ASBT) ●Physiologically based kinetic (PBK) model ● tobramycin

List of abbreviations: ASBT, apical sodium-dependent bile acid transporter; BSEP, bile salt export pump, BSH, bile salt hydrolase, CA, cholic acid; CDCA, chenodeoxycholic acid; C_{max}, maximal concentration in plasma; DCA, deoxycholic acid; GCA, glycocholic acid; GCDCA, glycochenodeoxycholic acid; GDCA, glycodeoxycholic acid; NTCP, Na^+-taurocholate cotransporting polypeptide; PBK, physiologically based kinetic; TEER, transepithelial electrical resistance; uBA, unconjugated bile acid

5.1 Introduction

Cholesterol conversion to bile acids is an important metabolic pathway in humans (Di Ciaula et al., 2018; Hofmann, 1999a). Bile acids play a key role in inducing bile flow and biliary lipid secretion, assimilating the dietary fat and lipid-soluble vitamins in the intestinal tract (Chiang, 1998). Two major primary bile acids are cholic acid (CA) and chenodeoxycholic acid (CDCA) which are synthetized from cholesterol in the liver (Russell and Setchell, 1992). Before secretion from liver into bile canaliculi, CA and CDCA are conjugated with taurine or glycine to form the corresponding taurine and glycine conjugated bile acid (Bahar and Stolz, 1999; Vlahcevic et al., 1999). Upon bile acid secretion through the bile duct into the gastrointestinal tract, about 95% of the bile acids are reabsorbed from ileum and colon via the portal vein back to the liver, with only a minor amount being excreted into feces (Hofmann, 1999b; Dowling, 1972; Dawson, 2018). This so-called enterohepatic circulation is a highly efficient process sustaining bile acid homeostasis.

Many transporters participate in this enterohepatic circulation including the Na^+ taurocholate co-transporting polypeptide (NTCP) and the bile salt export pump (BSEP) in the liver, and the apical sodium-dependent bile acid transporter (ASBT) and the organic solute transporter OST α/β in the intestine (Halilbasic et al., 2013; Stieger et al., 2007; Balakrishnan and Polli, 2006; Dawson et al., 2005). These bile acid transporters facilitate bile acid absorption and excretion within the body, and contribute to bile acid homeostasis under physiological conditions. Gut microbiota also participates in the bile acid metabolism. In the colon, efficient deconjugation of conjugated primary bile acids is catalyzed by bile salt hydrolases (BSH) present in a variety of gut microbiota such as *Clostridium*, *Bacteroides*, *Lactobacillus* and *Enterococcus* and others (Begley et al., 2005; Ridlon et al., 2006; Jones et al., 2008).

Recently we developed a physiologically based kinetic (PBK) model to describe bile acid metabolism in humans (de Bruijn et al. 2022). This model included the activity of the bile salt export pump (BSEP) in the liver enabling modeling of the effect of the BSEP inhibitor bosentan on bile acid profiles in human plasma. In a subsequent study also the activity of the ASBT responsible for intestinal reuptake of bile acids was included in the PBK model enabling characterization of the effect of the ASBT inhibitor Odevixibat on human bile acid plasma levels (de Bruijn et al., 2023). The aim of the present study was to apply the model to investigate the effect of the antibiotic tobramycin on bile acid homeostasis. Tobramycin is an aminoglycoside antibiotic known to affect protein synthesis in bacterial as well as human cells thus leading to a reduction in normal functional protein formation (Wangen and Green, 2020; Neu, 1976). A previous 28 day study in young adult Wistar rats reported that oral exposure to tobramycin at dose levels affecting the intestinal microbiota but not causing systemic toxicity, substantially affected bile acid levels in host feces and plasma samples (Murali et al., 2023). Previous studies in an *in vitro* transwell intestinal transport model with Caco-2 cell layers revealed that pre-exposure of the Caco-2 cells to tobramycin significantly reduced the transport of taurochenodeoxycholic acid (TCDCA) and glycochenodeoxycholic acid (GCDCA) across the Caco-2 cell layer (Zhang et al., 2023). Given that both *in vivo* but also in Caco-2 cells the ASBT is responsible for the transport of conjugated bile acids across the intestinal cell layer (Balakrishnan and Polli, 2006; Balakrishnan et al., 2006; Dawson, 2011; Chen et al., 2012; Xiao and Pan, 2017), this effect of tobramycin is likely mediated via an effect on the expression level of ASBT. To predict the

consequences of this effect of tobramycin for bile acid plasma levels in human, the previously developed PBK model was used to predict the effects of tobramycin on plasma levels of three model conjugated bile acids including glycocholic acid (GCA), glycochenodeoxycholic acid (GCDCA), and glycodeoxycholic acid (GDCA). Effects on deoxycholic acid (DCA) were also characterized, because DCA is known to be the most abundant unconjugated bile acid (uBA) in human plasma (Rodrigues et al., 2014) and thus representative for the behavior of unconjugated bile acids (uBAs). To define the PBK model parameters, transport of a mixture of these bile acids across Caco-2 cell layers upon pre-exposure and co-exposure of the Caco-2 cells with tobramycin was quantified. Kinetic data for the effect of tobramycin on deconjugation of conjugated bile acids were taken from a previous study with human fecal incubations (Zhang et al., 2023). Thus, data generated *in vitro* were used as input in the PBK model to predict the effects of tobramycin on *in vivo* plasma bile acid levels in humans.

5.2 Materials and methods

Chemicals and reagents

Tobramycin was obtained from Sigma-Aldrich (Schnelldorf, Germany). Glycocholic acid (GCA), glycochenodeoxycholic acid (GCDCA), glycodeoxycholic acid (GDCA) and deoxycholic acid (DCA) were purchased from Sigma-Aldrich (Schnelldorf, Germany). Phosphate buffered saline (PBS) was purchased from Gibco (Paisley, UK). Fetal Bovine Serum (FBS) was obtained from GE Healthcare Life Sciences Hyclone Laboratories (Logan, Utah, USA). 0.05% Trypsin-EDTA, minimum essential medium (MEM), penicillin-streptomycin-glutamine solution (PSG), sodium pyruvate, Hank's balanced salt solution (HBSS) and HEPES buffer solution were purchased from Gibco (Paisley, UK). Corning Costar 24 well transwell plates were purchased from Corning Life Sciences (Schnelldorf, Germany). Acetonitrile (ACN) and methanol were obtained from Biosolve BV (Valkenswaard, Netherlands). Dimethyl sulfoxide (DMSO) was purchased from Sigma-Aldrich (Darmstadt, Germany).

Cell culture

The human epithelial Caco-2 cell line (used in passage number 15-22) was purchased from the American Type Culture Collection (Rockville, MD, USA). Cells were cultivated in MEM with 20% FBS, 1% sodium pyruvate and 1% PSG. The cells were grown in 75 cm^2 flasks in an incubator at 37 ℃, 5% CO_2 and 100% humidity. Cells were subcultured when reaching 50%-60% confluence with 0.05% trypsin-EDTA.

In vitro bile acid transport

For the transport assay, 1.8×10^5 Caco-2 cells/cm^2 in 100 µL medium were seeded at the apical side of the wells of a Corning 24 well transwell plate and 600 µL MEM medium was added to the basolateral side. Cells were cultivated for 18 days to form intestinal cell layers, with fresh medium provided every other day. In order to exclude effects of other antibiotics than tobramycin, MEM medium without PSG was used when cells were cultured in the 24 well transwell plates. Caco-2 cells were exposed to 45 mM tobramycin or solvent control for 48 h after 18 days cultivation in the transwell plate. The concentration of tobramycin was based on the dose level that was shown in a reported *in vivo* rat bioassay to affect bile acid homeostasis (Murali et al., 2023), converting the dose of 1000 mg/kg

bw/day to a concentration of 45 mM as reported previously (Zhang et al., 2022). Integrity of the cell layers in the wells was checked by measurement of the transepithelial electrical resistance (TEER) values, before and after the pre-exposure or co-exposure of the cells to tobramycin or control in transport buffer, as well as at the end of the transport experiment. The TEER value was measured with a Millicell® ERS-2 Volt-Ohm Meter (Millipore, Amsterdam, Netherlands) and expressed Ω×cm^2 and only cell layers with a TEER value above 500 Ω×cm^2 were used for transport experiments.

After pre-exposure with tobramycin or solvent control, the exposure medium was removed and the cell layers were cultured in transport medium (HBSS supplemented with 10 mM HEPES, pH 7.4) for 30 min. Following this 30 min incubation in transport medium, 5 µM GCA, 5 µM GCDCA, 5 µM GDCA and 5 µM DCA as a mixture dissolved in transport medium, were added to the apical part of the transwell plate, and incubation was continued. Samples of 50 µL were taken and replenished from the basolateral compartment at 1h, 2h and 3h, following addition of the bile acid mixture, and analyzed by LC-MS/MS for bile acid levels. Co-exposure of the cells to a mixture of GCA, GCDCA, GDCA and DCA each at 5 µM and 45 mM tobramycin was performed in a similar way starting at day 20 of culture.

Bile acid profiling by LC-MS/MS

Bile acid profiling was performed using a triple quadrupole LCMS-8045 instrument (Shimadzu Corporation, Japan). The method applied was able to measure 20 different bile acids which were separated on a Kinetex C18 column (1.7 µm × 100 A × 50 mm × 2.1 mm, Phenomenex 00B-4475-AN). For the LC-MS/MS runs, mobile phase A (MilliQ water containing 0.01% formic acid) and mobile phase B (50% acetonitrile/ 50% methanol) were used. The injection volume was 1 µL and the flow rate 0.4 mL/min. The gradient applied was as follows: 0-10 min 30-70% B, kept at 70% B for 1 min, changed from 70-98% B from 11-19 min, kept at 98% B for 1 min; and then changed from 98 to 30% B from 20-25 min followed by 10 min equilibration at 30% B before the next injection. Electrospray ionization (ESI) was used in a negative ion mode within the mass spectrometer. The ESI parameters included Nebulizing gas flow 3 L/min; drying gas flow and heating gas flow 10 L/min; interface voltage 3 kV; interface current 0.9 uA; interface temperature 300 ℃; Desolvation temperature 526 ℃; DL temperature 250 ℃; heat block temperature 400 ℃; Conversion Dynode Voltage 10 kV; detector voltage 2.16 kV; IG Vacuum 1.8e-03 Pa; PG Vacuum 9.4e+01 Pa; CID Gas 230 kPa. Both selective ion monitoring (SIM) and multiple reaction monitoring (MRM) were used for the bile acid detection in order to obtain optimal sensitivity for each bile acid. Detailed bile acid identification and quantification was achieved using the characteristics previously described (Zhang et al., 2023; Zhang et al., 2022).

Physiologically based kinetic (PBK) model of bile acid homeostasis

PBK modeling was used to predict *in vivo* human plasma concentrations of GCA, GCDCA, GDCA and uBA with or without tobramycin treatment, using the PBK model previously described (de Bruijn et al., 2023). uBA represents a lumped pool of unconjugated bile acids, including DCA, but also lithocholic, cholic and chenodeoxycholic acid. The unconjugated bile acids were lumped to reduce model complexity. DCA was used as a model bile acid to obtain kinetic rate constants and tissue:partition coefficients for the uBAs, because it is the most abundant secondary uBA in human serum (Rodrigues et al., 2014). GCA, GCDCA and GDCA deconjugation in the intestine to their corresponding uBAs was

assumed to be rapid and complete by setting the deconjugation rate to 1000 hr^{-1}. After hepatic reuptake, uBAs were rapidly conjugated with a rate constant of 1000 hr^{-1}. The fraction of GCA, GDCA and GCDCA formed in the liver was derived from the fraction of these bile acids present in human liver biopsies (Rodrigues et al., 2014). The Michaelis-Menten equation in the PBK model that represents ASBT-mediated bile acid transport across the intestine is as follows:

Equation 1: $$v = \frac{Vmax,ASBT \times [S]}{Km,ASBT+S}$$

Where v is the velocity of transport in µmol/h, $V_{max,ASBT}$ is the maximum velocity of transport in µmol/h, $K_{m,ASBT}$ is the Michaelis-Menten constant of transport in µmol/L and S is the concentration of the respective bile acid expressed in µmol/L. Tobramycin pre-exposure of the Caco-2 cells inhibited bile acid transport most likely by downregulating the protein expression of the bile acid transporter ASBT. Co-exposure of the cells to tobramycin and the bile acids inhibited bile acid transport by direct interactions. The inhibition of the ASBT mediated transport was modelled by reducing the V_{max} to include the effect of pre-exposure and by reducing the absorption rate constant k_a to include the effect of co-exposure, with the level of reduction being derived from the data obtained in the *in vitro* Caco-2 model system to set the% of reduction of the V_{max} or k_a respectively. The model code is the same as the code applied in Chapter 4 and can be found in section 4.5 supplementary material II.

Data analysis and Statistics

Bile acid profile data were analyzed using the Labsolutions software within the LC-MS/MS system. Graphical figures were drawn by using Graphpad Prism 5 (San Diego, USA) and R version 4.1.0. Statistical analysis was performed by Student's t test. The effects were considered significant when $P<0.05$. All the data are presented as mean ± SD from at least three independent measurements.

5.3 Results

Caco-2 cell layer integrity

TEER values were detected before, during and after the bile acid transport assays in order to ensure that the barrier integrity of the cell layers was not affected by the pre-exposure with tobramycin or the co-exposure with tobramycin during the transport experiment. The TEER values of the cell layers confirmed that these cell layers were not affected by the pre-exposure and co-exposure for both control and tobramycin treatment conditions (supplementary information Figure S1 and S2). Also the presence of the bile acids did not affect the TEER value (supplementary information Figure S1 and S2).

Transport of a mixture of bile acids across Caco-2 cell layers pre-exposed to tobramycin

Figure 1 presents the time dependent transport of a mixture of the 4 bile acids (GCA, GCDCA, GDCA, and DCA as the model compound for the uBAs) across the Caco-2 cell layers without or with pre-exposure of the cell layers to tobramycin. Table 2 presents the apparent permeability coefficients (P_{app} values) (expressed in cm/s) derived from the data at 1h incubation. Pre-exposure of the cells with tobramycin reduced the transport of GCA and GCDCA to a significant extent while reduction of the transport of GDCA was not significant and there was no effect on DCA transport. The data also reveal that transport of GCDCA, GDCA and DCA was comparable and at least 2-fold higher than that of GCA.

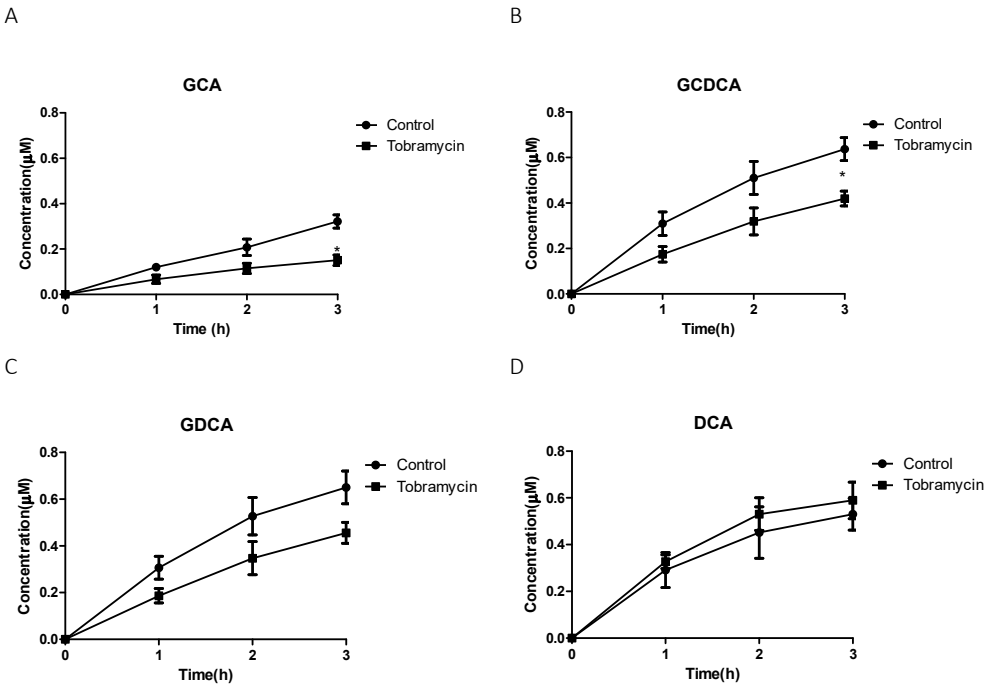

Figure 1 Time dependent transport of a mixture of bile acids (GCA, GCDCA, GDCA and DCA) across the Caco-2 cell layers upon **pre-exposure** of the cell layers without (control) or with 45 mM tobramycin (**P*< 0.05). Results are expressed as mean ± SD, n=3.

Table 1 Permeability constants (P_{app} values) for the transport of a mixture of bile acids (GCA, GCDCA, GDCA and DCA) across Caco-2 cell layers upon **pre-exposure** of the cell layers without (control) or with 45 mM tobramycin (**P*< 0.05). Results are expressed as mean ± SD, n=3.

Bile acid	P_{app} (in 10^{-5} cm/s)		Residual transport activity (% of control)
	Control	Tobramycin	
GCA	1.0±0.1	0.5±0.1*	50.0
GCDCA	2.1±0.2	1.4±0.1*	66.7
GDCA	2.2±0.1	1.8±0.3	82.0
DCA	2.9±0.7	3.3±0.3	113.8

From the results presented in table 1, it follows that the effect of pre-exposure of the Caco-2 cells to tobramycin on bile acid transport is due to an effect on active transport. This follows from the observation that the transport of DCA which is known to be predominantly transported via passive diffusion (Dietschy, 1968) is not inhibited, while that of GCA, a bile acid that predominantly crosses the intestinal barrier via ASBT mediated active transport (Dawson et al., 2009) is inhibited to the largest extent. The residual transport activity followed the same order as the lipophilicity (DCA > GDCA ≈ GCDCA > GCA), indicating that active transport is reduced and passive transport contributes to a variable extent to the remaining transport, depending on the lipophilicity (Aldini et al., 1996; Roda et al., 1982).

Based on these considerations the consequences of the effect of tobramycin on bile acid transport via an effect on the ASBT transporter expression levels was investigated by reducing the V_{max} for ASBT mediated transport in the PBK model to reflect the% residual transport activity presented in table 1.

Transport of a mixture of bile acids across the Caco-2 cell layers upon co-exposure with tobramycin

Since tobramycin appeared also able to disturb bile acid transport via direct effects, bile acid transport upon co-exposure of a mixture of bile acids with tobramycin across the Caco-2 cell layers was quantified. Figure 2 and table 2 present the results obtained and demonstrate that tobramycin co-exposure reduced the transport of GCDCA and DCA significantly, while it did not affect the transport of GCA, and the reduction in transport of GDCA was not significant. The P_{app} values for DCA, GCDCA, GDCA were again at least 2-fold higher than that of GCA.

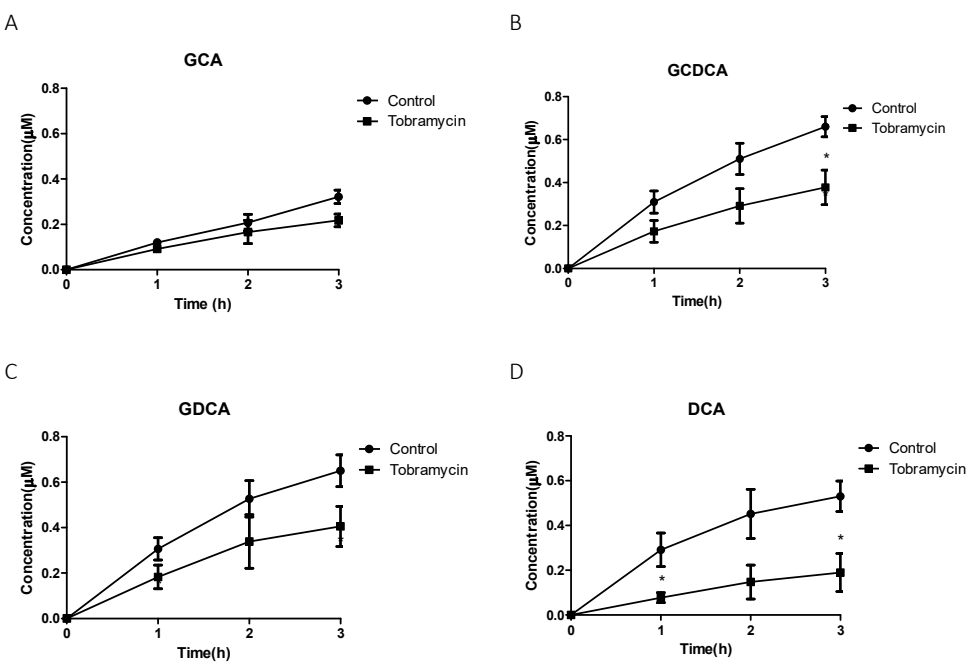

Figure 2 [see next page for caption]

Figure 2 Time dependent transport of a mixture of bile acids (GCA, GCDCA, GDCA and DCA) across the Caco-2 cell layers upon **co-exposure** without (control) or with 45 mM tobramycin (*P< 0.05). Results are expressed as mean ± SD, n=3.

Table 2 Permeability constants (P_{app} values) for the transport of a mixture of bile acids (GCA, GCDCA, GDCA and DCA) across Caco-2 cell layers upon **co-exposure** without (control) or with 45 mM tobramycin (*P< 0.05). Results are expressed as mean ± SD, n=3.

Bile acid	P_{app} (in 10^{-5} cm/s)		Residual transport activity (% of control)
	Control	Tobramycin	
GCA	1.0±0.1	0.9±0.1	90.0
GCDCA	2.2±0.2	1.3±0.1*	59.0
GDCA	2.1±0.1	1.7±0.3	81.0
DCA	3.0±0.6	0.8±0.1*	27.0

The P_{app} values in table 2 reveal that inhibition of bile acid transport upon co-exposure of the Caco-2 cells to tobramycin and the bile acids most likely results from an effect on passive diffusion and not from an effect on the ASBT transporter. This follows from the fact that the reduction is most substantial for DCA, the most lipophilic bile acid, which is transported mainly by passive diffusion. The residual transport activity increased with decreasing lipophilicity. In line with this finding, the smallest effect was observed for GCA, which is the least lipophilic bile acid and is predominantly transported by active ASBT mediated transport. Thus, to investigate the consequences of this effect of tobramycin for the plasma bile acid levels, the absorption rate constants for intestinal uptake (k_a) in the PBK model were reduced to reflect the% residual transport activity presented in table 2.

Prediction of the consequences of inhibition of bile acid reuptake by tobramycin for the *in vivo* plasma bile acid concentrations

Figure 3 presents the PBK model simulations for *in vivo* plasma GCA, GCDCA, GDCA and uBA concentrations with and without tobramycin treatment. The curves reflect the consequences of 3 meals a day at 8:00, 12:00 and 16:00 respectively and are based on V_{max} and k_a values that are adapted in line with the results from table 1 and 2. The results obtained reveal that, in line with the *in vitro* bile acid transport results, systemic plasma levels of especially the 3 conjugated bile acids are reduced by effects of tobramycin on ASBT expression levels while plasma uBA levels are especially sensitive to effects of the co-exposure on passive diffusion and not affected by the effects on ASBT expression levels. Given that upon *in vivo* exposure to tobramycin both effects of pre- and co-exposure are likely to occur simultaneously, the purple lines in Figure 3 present the PBK model predictions where both the effect on V_{max} and k_a were taken into account.

These data reveal that for all four bile acids tobramycin exposure at an oral dose level similar to what was applied in the 28 day rats studies is predicted to result in a substantial reduction of the plasma C_{max} concentrations by 42.4%, 27.7%, 16.9% and 75.8% of the concentrations without tobramycin for GCA, GCDCA, GDCA and uBA respectively.

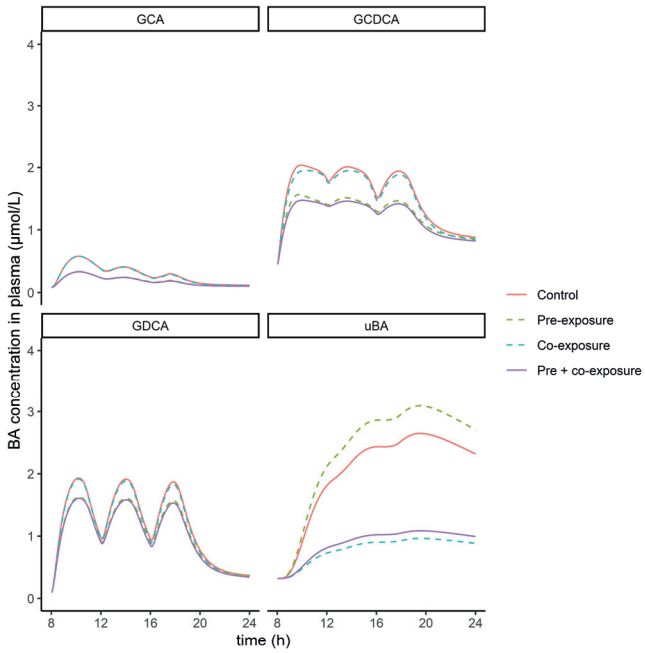

Figure 3 PBK model based predictions for the effects of an oral dose of 1000 mg/kg bw tobramycin on the systemic plasma levels of the bile acids (GCA, GCDCA, GDCA and uBA). The curves present simulations assuming 3 meals (at 8:00, 12:00 and 16:00) per day. The curves present the predicted plasma levels without tobramycin (control; red solid lines), with the effect of tobramycin on ASBT expression levels (based on pre-exposure to tobramycin) (green dotted lines), with the direct effect on bile acid absorption (based on co-exposure to tobramycin) (blue dotted lines) and with taking both effects of tobramycin into account (based on pre-exposure and co-exposure to tobramycin) (purple solid lines).

Prediction of the consequences of the effect of tobramycin on intestinal bile acid deconjugation for the *in vivo* plasma bile acid concentrations

Previously tobramycin was also shown to inhibit intestinal bile acid deconjugation by the microbiota(Zhang et al., 2023). To further elucidate the consequences of this effect of tobramycin on bile acid metabolism further PBK modeling was performed. *In vitro* anaerobic incubations with human fecal slurry and a mixture of bile acids demonstrated that tobramycin inhibited deconjugation of GCA and GCDCA resulting in 28.1% and 47.2% residual activity (Zhang et al., 2023). To include this effect in the PBK modeling the deconjugation constant for the model that predicted the effect of tobramycin treatment was assumed to decrease from 1000 hr^{-1} to 281 hr^{-1} for GCA and 472 hr^{-1} for GCDCA. This change appeared to influence the PBK model predictions for the plasma levels of uBA (Table 3), which residual C_{max} reduced from 41.5% to 24.2% when considering intestinal microbial deconjugation. This outcome is in line with the *in vitro* anaerobic incubation results that revealed that tobramycin inhibited deconjugation of conjugated bile acids resulting in reduced uBA accumulation (Zhang et al., 2023).

Table 3 PBK model based predicted residual C_{max} of the bile acids (GCA, GCDCA, GDCA and uBA) in human plasma when simulated without and with the effects of tobramycin on intestinal microbial deconjugation while also including the effects of tobramycin on intestinal reuptake of the bile acids compared to control (without tobramycin).

	Residual C_{max} (%)			
	GCA	GCDCA	GDCA	uBA
Without intestinal deconjugation	57.6	72.3	83.1	41.5
With intestinal deconjugation	57.6	72.3	83.1	24.2

Interindividual variation in bile acid pool size

The total bile acid pool size is determined by the amount of bile acids in the gallbladder, the systemic fasting concentrations and the *de novo* synthesis. Previous PBK modeling results revealed that the amount of bile acids in a full bladder (Gdose) and systemic fasting concentrations (CBfs) have the largest impact on the systemic maximal bile acid concentrations C_{max} (de Bruijn et al., 2022). To reflect differences in this total bile acid pool known to exist between individuals, the total bile acid pool size in the model can be adapted by the scaling factor sensitivity (sens). Setting the sens value at 0.5, 1 and 1.5, results in PBK models that reflect individuals with different total bile acid pools. Figure 4 shows the effects of this change in the total bile acid pool on the consequences for the effect of tobramycin on the systemic bile acid concentrations. From this it follows that the effect of tobramycin on C_{max} levels for each bile acid is predicted to be similar for all sens values, amounting to 56-59% residual C_{max} for GCA, to 70-74% residual C_{max} for GCDCA, to 82-87% residual C_{max} for GDCA, and to 24-26% residual C_{max} for uBA.

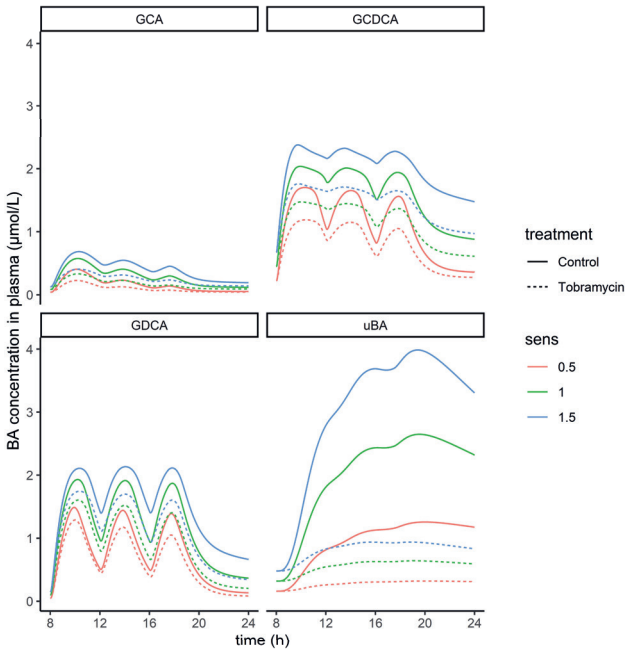

Figure 4 PBK model based predictions for the effect of tobramycin on the systemic plasma levels of the bile acids (GCA, GCDCA, GDCA, uBA) for individuals with different total bile acid pools. The curves present simulations assuming 3 meals (at 8:00, 12:00 and 16:00) per day. The curves present the plasma levels without tobramycin (control: solid lines) and with tobramycin (dotted lines) including both an effect on the V_{max} for ASBT mediated transport (based on pre-exposure caco-2 cell experiments), and a direct effect on k_a for intestinal reuptake (based on co-exposure Caco-2 cell experiments). The total bile acid pool size in the model was multiplied with a certain sens value (0.5, 1 or 1.5). Red=sens value 0.5, green=sens value 1, and blue=sens value 1.5.

5.4 Discussion

The antibiotic tobramycin was shown to inhibit intestinal deconjugation and reuptake of bile acids in previous studies (Zhang et al., 2022; Zhang et al., 2023). These *in vitro* results were in line with the observation of increased fecal bile acid levels and reduced plasma levels in an *in vivo* 28 day rat study (Murali et al., 2023). In the present study we used the PBK model previously developed to predict the effects on the systemic plasma bile acid levels in human induced by the ASBT inhibitor Odevixibat to study the effects of exposure to tobramycin on human plasma bile acid levels (de Bruijn et al., 2023). In previous *in vitro* studies using the Caco-2 cell layer transwell model, it was shown that the transport of the bile acids was mediated by active transport via the ASBT since the transport was substantially lower at 4°C as compared to 37°C (Zhang et al. submitted) and also in the absence of sodium (de Bruijn et al., 2023). In the present study, a PBK model that included microbial deconjugation and intestinal reuptake via the ASBT was applied to predict the systemic plasma bile acid concentrations in human upon treatment with the antibiotic tobramycin. Results obtained can be compared to results from the 28 day rat study showing effects of tobramycin on bile acid homeostasis (Murali et al., 2023) and results from a study in which the effects of the approved ASBT inhibitor drug Odevixibat on plasma and fecal bile acid levels in human volunteers were reported (Graffner et al., 2016). The

predicted plasma concentrations of conjugated bile acids (GCA, GCDCA, GDCA) decreased while that of the unconjugated bile acid (DCA) was not significantly increased upon Odevixibat treatment (de Bruijn et al., 2023). This is in line with the effects of Odevixibat on systemic plasma data in human reported in the literature (Graffner et al., 2016). Also, the relative amount of glycine conjugated bile acids in human serum was reported to be about 45% of the total bile acid pool, for unconjugated bile acids this values amounted to about 40% and for taurine conjugated bile acids it was about 15% (Bathena et al., 2013). Therefore, these bile acids were considered as the target bile acids in the PBK model.

To obtain kinetic parameters to define the effects of tobramycin on intestinal bile acid transport, *in vitro* Caco-2 cell layer transwell experiments were performed to quantify the effect of tobramycin on the intestinal translocation of 4 model bile acids. After pre-incubation and co-incubation of the Caco-2 cells to tobramycin and a mixture of GCA, GCDCA, GDCA and DCA, tobramycin was shown to inhibit the transport of these bile acids, and these effects were included in the model via reducing the V_{max} and k_a parameters. The PBK model simulated predictions for the time dependent plasma concentrations of the bile acids thus obtained show that tobramycin exposure was predicted to reduce the plasma levels of GCA, GCDCA and uBA significantly while the level of GDCA was affected to a lesser extent. The results of our PBK model predictions can also be compared to reported concentrations of GCDCA in human serum (control) which are about 5 fold higher than those of GCA (García-Cañaveras et al., 2012), while in our simulations GCDCA plasma concentrations were also predicted to be higher (2 fold) than those of GCA.

Kinetic constants for the effect of tobramycin on intestinal deconjugation were taken from previous *in vitro* studies using anaerobic fecal incubations (Zhang et al., 2022; Zhang et al., 2023). Tobramycin is an aminoglycoside antibiotic, acting against gram-negative bacteria by performing bactericidal effects (Reyhanoglu and Reddivari, 2019; Brogden et al., 1976). In our previous studies, 16S rRNA analysis revealed that tobramycin treatment changed gut microbiota composition significantly (Zhang et al., 2022; Murali et al., 2023); it also affected the deconjugation of fecal bile acids showing significant suppression of deconjugation of GCA and GCDCA in both rat and human fecal incubations (Zhang et al., 2022; Zhang et al., 2023). About 95% of bile acids are actively reabsorbed in the small intestine, while the remaining 5% of bile acids enters the colon where the majority is recaptured and only a minor amount is excreted in the feces (Chiang, 2009). The effect of tobramycin on intestinal deconjugation appeared not to affect plasma C_{max} levels likely because deconjugation mainly occurs in the colon for only a limited portion of the total bile acid pool.

The PBK model simulations of the present study revealed that oral exposure to tobramycin at the high dose level tested before in the 28 day rat study of 1000 mg/kg bw (Murali et al., 2023) is predicted to reduce human plasma C_{max} levels of GCA, GCDCA, GDCA and uBA by 42.4%, 27.7%, 16.9% and 75.8%, so levels that were predicted to amount to about 0.58, 0.72, 0.83 and 0.24 times the control values. Human data to evaluate the PBK model predictions are not available but a comparison can be made to results from the 28 days *in vivo* rat study (Murali et al 2023). In this 28 day study rats were exposed to tobramycin at a dose level that was selected to affect the intestinal microbiome without causing systemic toxicity. In the rat study tobramycin exposure also resulted in a reduction of plasma levels of GCA, GCDCA, GDCA and uBA (Murali et al., 2023). In the rat study the reductions in bile acid levels were especially seen in female rats where exposure to tobramycin resulted in plasma levels of GCA, GCDCA, GDCA and DCA (uBA) that were reduced to 0.35, 0.38, 0.04 times the control animals and below the limit of detection, respectively (Murali et al., 2023). Thus, in the *in vivo* rat study the tobramycin induced reduction of bile acid plasma levels occurred in the order: uBA > GDCA >

GCA ≥ GCDCA. For human the PBK model predicted the tobramycin induced reduction in plasma bile acids in human to vary in the order: uBA > GCA > GCDCA > GDCA. This shows that the PBK model simulations for plasma bile acid levels for uBA, GCA and GCDCA, but not GDCA, are in line with the *in vivo* rat study. The less pronounced effect for GDCA in the PBK model predictions for human than in the rat *in vivo* study, may originate from a species difference in the (inhibition of) the active transporters involved, being more pronounced in rat than in human.

It is also important to note that tobramycin is poorly absorbed from the gastrointestinal tract thus showing poor bioavailability upon orally administration (Reyhanoglu and Reddivari, 2019). This implies that the current PBK simulations reflect the effects of an orally administered xenobiotic on systemic plasma levels without a need for systemic bioavailability of the xenobiotic itself. It is also relevant to note that the effects on human plasma levels of bile acids upon oral exposure to tobramycin predicted in the present study, do not reflect effects expected upon intravenous or intramuscular exposure when using tobramycin at lower dose levels as an antibiotic drug in human. The results of the present study rather reflect that oral exposure to xenobiotics that are not or poorly bioavailable can affect systemic bile acid homeostasis.

Altogether, the PBK model appears to provide a 3R compliant tool to evaluate the effect of oral exposure to xenobiotics on host bile acid homeostasis via effects on intestinal bile acid deconjugation and reuptake.

Acknowledgements We thank the ELUMICA team for the investigation of this project, we also appreciate our collaboration teams - Department of Experimental Toxicology and Ecology of BASF SE and Toxicology group of ETH university. We acknowledge professor Bennard van Ravenzwaay for critical reading of this manuscript. This research received an external funding from the Long-range Research Initiative (LRI), which is an initiative from the European Chemical Industry Council. Our research is extensively reviewed by an External Science Advisory Panel from Cefic-LRI.

Conflict of interest The authors declare that they have no conflict of interest.

References

Aldini R, Roda A, Montagnani M, Cerre C, Pellicciari R, Roda E (1996) Relationship between structure and intestinal absorption of bile acids with a steroid or side-chain modification. Steroids 61(10):590-597

Bahar RJ, Stolz A (1999) Bile acid transport. Gastroenterology Clinics of North America 28(1):27-58

Balakrishnan A, Polli JE (2006) Apical sodium dependent bile acid transporter (ASBT, SLC10A2): a potential prodrug target. Molecular pharmaceutics 3(3):223-230

Balakrishnan A, Wring SA, Polli JE (2006) Interaction of native bile acids with human apical sodium-dependent bile acid transporter (hASBT): influence of steroidal hydroxylation pattern and C-24 conjugation. Pharmaceutical research 23(7):1451-1459

Bathena SPR, Mukherjee S, Olivera M, Alnouti Y (2013) The profile of bile acids and their sulfate metabolites in human urine and serum. Journal of Chromatography B 942:53-62

Begley M, Gahan CG, Hill C (2005) The interaction between bacteria and bile. FEMS microbiology reviews 29(4):625-651

Brogden R, Pinder R, Sawyer PR, Speight T, Avery G (1976) Tobramycin: a review of its antibacterial and pharmacokinetic properties and therapeutic use. Drugs 12:166-200

Chen L, Yao X, Young A, et al. (2012) Inhibition of apical sodium-dependent bile acid transporter as a novel treatment for diabetes. American Journal of Physiology-Endocrinology and Metabolism

Chiang J (1998) Regulation of bile acid synthesis. Frontiers in Bioscience-Landmark 3(4):176-193

Chiang JY (2009) Bile acids: regulation of synthesis: thematic review series: bile acids. Journal of lipid research 50(10):1955-1966
Dawson PA (2011) Role of the intestinal bile acid transporters in bile acid and drug disposition. Drug transporters:169-203
Dawson PA (2018) Bile formation and the enterohepatic circulation. Physiology of the gastrointestinal tract:931-956
Dawson PA, Hubbert M, Haywood J, et al. (2005) The heteromeric organic solute transporter α-β, Ostα-Ostβ, is an ileal basolateral bile acid transporter. Journal of Biological Chemistry 280(8):6960-6968
Dawson PA, Lan T, Rao A (2009) Bile acid transporters. Journal of lipid research 50(12):2340-2357
de Bruijn VM, Rietjens IM, Bouwmeester H (2022) Population pharmacokinetic model to generate mechanistic insights in bile acid homeostasis and drug-induced cholestasis. Archives of Toxicology 96(10):2717-2730
De Bruijn VM, Te Kronnie W, Rietjens IM, Bouwmeester H (2023) Intestinal in vitro transport assay combined with physiologically based kinetic modeling as a tool to predict bile acid levels in vivo. ALTEX-Alternatives to animal experimentation
Di Ciaula A, Garruti G, Baccetto RL, et al. (2018) Bile acid physiology. Annals of hepatology 16(1):4-14
Dietschy JM (1968) Mechanisms for the intestinal absorption of bile acids. Journal of lipid research 9(3):297-309
Dowling RH (1972) The enterohepatic circulation. Gastroenterology 62(1):122-140
García-Cañaveras JC, Donato MT, Castell JV, Lahoz A (2012) Targeted profiling of circulating and hepatic bile acids in human, mouse, and rat using a UPLC-MRM-MS-validated method. Journal of lipid research 53(10):2231-2241
Graffner H, Gillberg PG, Rikner L, Marschall HU (2016) The ileal bile acid transporter inhibitor A4250 decreases serum bile acids by interrupting the enterohepatic circulation. Alimentary pharmacology & therapeutics 43(2):303-310
Halilbasic E, Claudel T, Trauner M (2013) Bile acid transporters and regulatory nuclear receptors in the liver and beyond. Journal of hepatology 58(1):155-168
Hofmann AF (1999a) Bile acids: the good, the bad, and the ugly. Physiology 14(1):24-29
Hofmann AF (1999b) The continuing importance of bile acids in liver and intestinal disease. Archives of internal medicine 159(22):2647-2658
Jones BV, Begley M, Hill C, Gahan CG, Marchesi JR (2008) Functional and comparative metagenomic analysis of bile salt hydrolase activity in the human gut microbiome. Proceedings of the national academy of sciences 105(36):13580-13585
Murali A, Giri V, Zickgraf FM, et al. (2023) Connecting Gut Microbial Diversity with Plasma Metabolome and Fecal Bile Acid Changes Induced by the Antibiotics Tobramycin and Colistin Sulfate. Chemical Research in Toxicology doi:10.1021/acs.chemrestox.2c00316
Neu HC (1976) Tobramycin: an overview. The Journal of infectious diseases:S3-S19
Reyhanoglu G, Reddivari AKR (2019) Tobramycin.
Ridlon JM, Kang D-J, Hylemon PB (2006) Bile salt biotransformations by human intestinal bacteria. Journal of lipid research 47(2):241-259
Roda A, Cappelleri G, Aldini R, Roda E, Barbara L (1982) Quantitative aspects of the interaction of bile acids with human serum albumin. Journal of lipid research 23(3):490-495
Rodrigues AD, Lai Y, Cvijic ME, Elkin LL, Zvyaga T, Soars MG (2014) Drug-induced perturbations of the bile acid pool, cholestasis, and hepatotoxicity: mechanistic considerations beyond the direct inhibition of the bile salt export pump. Drug Metabolism and Disposition 42(4):566-574
Russell DW, Setchell KD (1992) Bile acid biosynthesis. Biochemistry 31(20):4737-4749
Stieger B, Meier Y, Meier PJ (2007) The bile salt export pump. Pflügers Archiv-European Journal of Physiology 453(5):611-620
Vlahcevic ZR, Pandak WM, Stravitz RT (1999) Regulation of bile acid biosynthesis. Gastroenterology Clinics 28(1):1-25

Wangen JR, Green R (2020) Stop codon context influences genome-wide stimulation of termination codon readthrough by aminoglycosides. Elife 9

Xiao L, Pan G (2017) An important intestinal transporter that regulates the enterohepatic circulation of bile acids and cholesterol homeostasis: the apical sodium-dependent bile acid transporter (SLC10A2/ASBT). Clinics and Research in Hepatology and Gastroenterology 41(5):509-515

Zhang N, Wang J, Bakker W, et al. (2022) In vitro models to detect in vivo bile acid changes induced by antibiotics. Archives of toxicology:1-13

Zhang N, Zheng W, Bakker W, van Ravenzwaay B, Rietjens IM (2023) In vitro models to measure effects on intestinal deconjugation and transport of mixtures of bile acids. Chemico-Biological Interactions:110445

5.5 Supplementary file

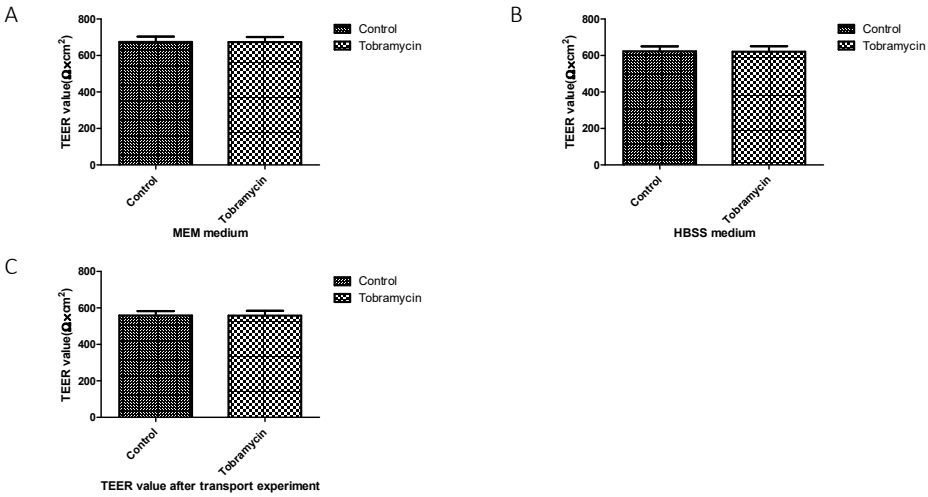

Figure S1 TEER values before (MEM medium), during (HBSS medium) and after pre-exposure a mixture of bile acids (GCA, GCDCA, GDCA and DCA) transport without (control) and with tobramycin across Caco-2 cell layers. Results are shown as mean ± SD, n=3.

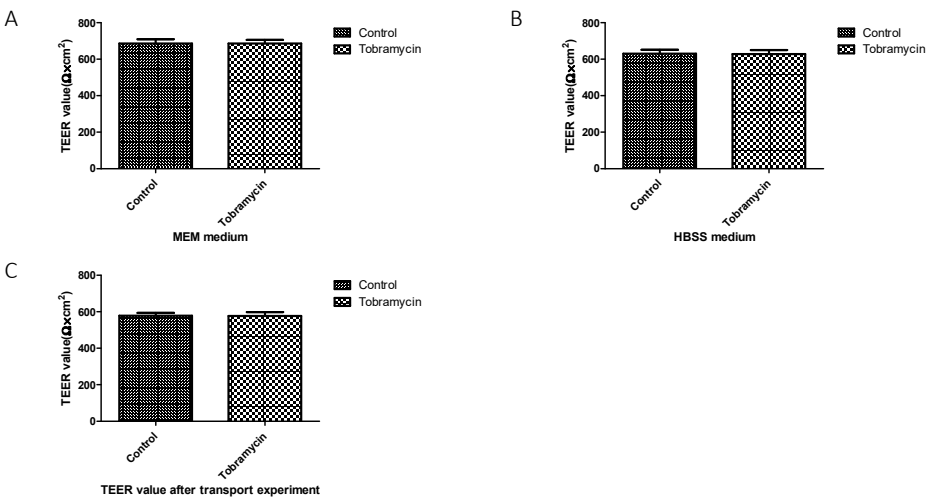

Figure S2 TEER values before (MEM medium), during (HBSS medium) and after co-exposure a mixture of bile acids (GCA, GCDCA, GDCA and DCA) transport without (control) and with tobramycin across Caco-2 cell layers. Results are shown as mean ± SD, n=3.

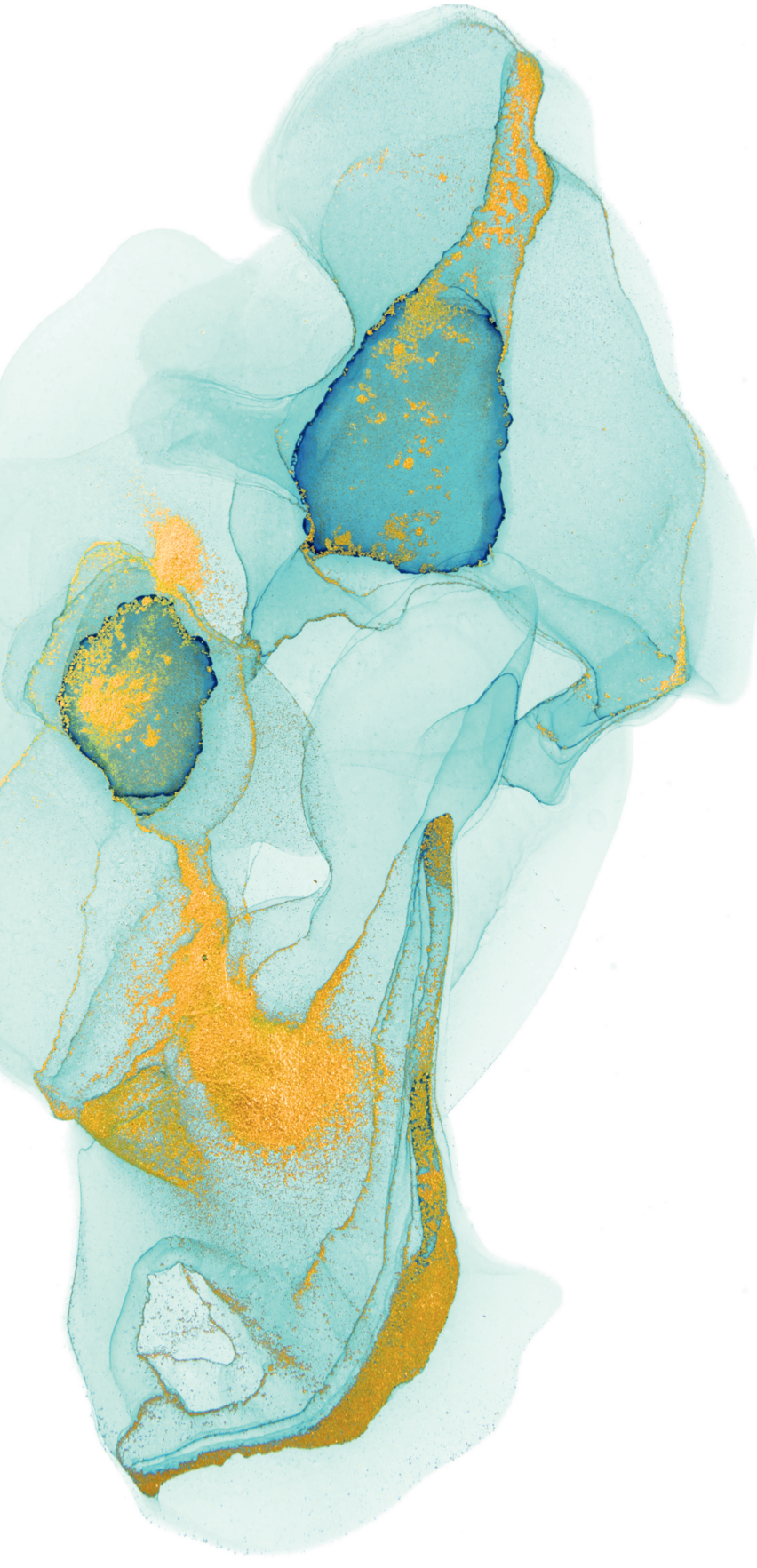

Chapter 6

From hazard to risk: a case study to predict drug-induced cholestasis using New Approach Methodologies

Véronique M.P. de Bruijn & Ivonne M.C.M. Rietjens

Submitted

Abstract

Background and Purpose: Bile acids are crucial for many metabolic and immune functions in humans and disturbance of bile acid homeostasis is known to be involved in pathologies, such as cholestasis. Drug-induced cholestasis is a sub-class of drug-induced liver injury (DILI) characterized by hepatic accumulation of bile acids and subsequent spillage to the systemic circulation. Clinical manifestation of cholestasis however only occurs in a small proportion of individuals exposed to the drug. The present study aims to develop a new approach methodology (NAM) to predict drug-induced cholestasis as a result of drug-induced hepatic bile acid efflux inhibition and the resulting bile acid accumulation.
Experimental Approach: The internal hepatic concentrations of a panel of drugs predicted by a generic physiologically based kinetic (PBK) drug model and their effects on hepatic efflux of the abundant bile acid glycochenodeoxycholic acid were incorporated in a PBK model predicting hepatic bile acid accumulation. The predicted level of accumulation was used as a measure for cholestatic potency of the drug. The selected drugs were all known to inhibit hepatic bile acid efflux in an assay with primary suspension hepatocytes and classified as common, rare or no for cholestasis incidence. Common cholestasis drugs included in the study were atorvastatin, chlorpromazine, cyclosporine, glimepiride, ketoconazole and ritonavir.
Key results: The cholestasis incidence of the drugs appeared not to be adequately predicted by their K_i for inhibition of hepatic bile acid efflux, but rather by the AUC of the PBK model predicted internal hepatic concentration of the drugs at therapeutic dose level above this K_i. People with slower clearance of the drug, a larger bile acid pool, reduced bile salt export pump (BSEP) abundance or given higher than therapeutic dose levels are predicted to be at higher risk to develop drug-induced cholestasis.
Conclusion and Implications: The results provide a proof-of-principle of using an animal-free PBK-based NAM for cholestasis risk assessment as a result of transporter inhibition. The current approach also provides mechanistic insights in risk factors towards drug-induced cholestasis.

Keywords: Bile acids and Salts ● Physiologically based kinetic (PBK) modeling ● Cholestasis ● Adverse Outcome Pathway

List of abbreviations: ADR, adverse drug reaction; AO, adverse outcome; AOP, Adverse Outcome Pathway; AUC: area under the curve, BSEP: bile salt export pump; CL_{int}, intrinsic clearance; C_{max}, maximal concentration in plasma; CYP, cytochrome P450; DILI, drug-induced liver injury
FDA, Food and Drug Administration; F_{up}, fraction unbound in plasma; GCDCA, glycochenodeoxycholic acid; MIE, Molecular Initiating Event; MRP, multidrug resistance protein; NAM, New Approach Methodology; OATP, organic anion transporter; PBK, physiologically-based kinetic; PON, paraoxonase QSAR, quantitative structure activity relationship; UGT, UDP-glucuronosyltransferases

6.1 Introduction

Drug-Induced Liver injury (DILI) is the most frequent cause for drug development discontinuation and DILI incidence is expected to increase, because of an increased dependency on drugs by the aging population (Walker et al., 2020). DILI is classified in a hepatocellular, cholestatic and a mixed type (Yu et al., 2017), where cholestatic DILI is characterized amongst others by a disrupted bile flow. While the DILI incidence is very low, with <1 in 1000 to 1 in 100 000 users (Kaplowitz, 2005; Fontana et al., 2023), the clinical outcome to the individual is devasting. Cholestatic liver injury constitutes 20-40% of DILI cases (Sundaram and Bjornsson, 2017), which underscores the critical necessity for robust tools to identify potentially cholestatic drug candidates early in the drug-discovery phase and identification of sensitive individuals. The present study aims to develop a new approach methodology (NAM) to predict drug-induced cholestasis as a result of drug-induced hepatic bile acid efflux inhibition and the resulting bile acid accumulation.

In recent years, substantial attention has been directed towards the development of Adverse Outcome Pathways (AOPs) as a conceptual framework for toxicological risk assessment. AOPs consist of a sequence that encompasses a Molecular Initiating Event (MIE), one or more Key Events (KEs), and an Adverse Outcome (AO), collectively representing responses spanning various tiers of biological complexity (Ankley et al., 2010). The fundamental principle underlying AOPs is that the MIE(s) combined with a select set of KEs can elucidate and forecast a toxicological response. Notably, these identified MIE(s) and KEs are amenable to exploration through NAMs, thereby facilitating a mechanism-centered, animal-free approach to assessing the safety of chemicals (Leist et al., 2017). Inhibition of the hepatic bile salt export pump (BSEP) is considered as MIE in the AOP of cholestasis. BSEP-inhibition leads to intrahepatic bile acid accumulation and subsequent toxicity (Vinken et al., 2013). A recent case study elucidated that two azole fungicides (propiconazole and tebuconazole) inhibited BSEP-mediated bile acid transport and affected several nuclear receptors (Knebel et al., 2022) which is in line with the AOP. Propiconazole and tebuconazole did not induce cholestasis in standard rodent *in vivo* bioassays (Heise et al., 2015; Schmidt et al., 2016; Nielsen et al., 2012), although for clinically used azole fungicides cholestasis has been reported in the European database of suspected adverse drug reaction (ADR) reports (www.adrreports.eu; accessed on the 21st of August 2023). Knebel et al. explain the discrepancy between the outcomes of their *in vitro* testing strategy and the rodent assays by the fact that the intrahepatic propiconazole and tebuconazole concentrations in the *in vivo* bioassays were too low to induce BSEP-inhibition (Schmidt et al., 2016). Hence, the *in vitro* testing strategy probably successfully revealed use of propiconazole and tebuconazole as a hazard for cholestasis, but for a risk assessment it is important to consider organ concentrations. Organ concentrations can be derived from studies with laboratory animals or in an animal-free approach using physiologically-based kinetic (PBK) modeling.

To predict drug-induced cholestasis, the drug PBK model predicted internal hepatic concentrations in humans of a series of selected drugs was incorporated in a bile acid PBK model describing the synthesis, circulation and excretion of the most abundant bile acid in human serum, glycochenodeoxycholic acid (GCDCA) (Bathena et al., 2013). Conjugated bile acids, like GCDCA, are typically transported by carrier-mediated transport, while unconjugated bile acids are mainly transported over the liver membranes via passive processes and thus unlikely to be affected by

transporter-inhibition (Notenboom et al., 2018). Simulating only one bile acid enabled us to keep the model complexity to a minimum, making the model easier to interpret and minimizing the risk of overfitting. The selected drugs are all known to inhibit hepatic bile acid efflux but are classified as common, rare or no for their incidence of inducing cholestasis. The time dependent drug-induced intrahepatic GCDCA accumulation was determined and compared to the inhibitory constant (K_i) of the drug for hepatic bile acid efflux inhibition as a measure for cholestatic potency. This newly defined approach also enabled prediction of the chances on developing cholestasis in people with slower clearance of the drug, a larger bile acid pool, reduced BSEP abundance or given higher than therapeutic dose levels. Thus, this modeling approach serves an animal-free proof-of-concept to predict drug-induced cholestasis.

6.2 Methods

Selection and classification of drugs

The criteria for the inclusion of a drug in our panel were a) causally linked to the development of DILI by the U.S. Food and Drug Administration (FDA) (Chen et al., 2016), b) oral administration in clinical practice, c) able to inhibit bile acid efflux with the half inhibitory concentration (IC_{50}) for bile acid efflux available from an assay with human suspension hepatocytes and the IC_{50} being <100 µM (Zhang et al., 2016), d) the reported DILI being not immune-mediated and e) two or more *in vivo* pharmacokinetic studies available in literature to validate the drug PBK model based predictions for plasma concentrations. The maximal concentration used for the IC_{50} determination by Zhang et al. (2016) was 100 µM. This resulted in a final inclusion of 18 drugs, *i.e.* atorvastatin, bicalutamide, bosentan, chlorpromazine, cyclosporine, deferasirox, fluoxetine, flutamide, glimepiride, haloperidol, lovastatin, ketoconazole, pioglitazone, ritonavir, rosiglitazone, saquinavir, trazodone and troglitazone. Flutamide, lovastatin and saquinavir were excluded from further simulations based on the results from the generic PBK model, as described in section 2.3. The drugs resulted in different types of DILI. The LiverTox® database classified chlorpromazine, cyclosporine and ritonavir as cholestatic DILI, the remaining drugs were classified as hepatocellular/mixed DILI (http://LiverTox.nih.gov; last accessed on the 24th of August 2023). For atorvastatin the LiverTox® database reported two cases of mixed, one of cholestatic and one of hepatocellular DILI. Glimepiride and haloperidol were not present in the LiverTox® database. The cholestasis incidence of the 15 remaining drugs was evaluated based on the European database of suspected adverse drug reaction (ADR) reports (www.adrreports.eu; last accessed on the 24th of August 2023). The following adverse reactions were considered cholestatic: cholestasis, cholestatic liver injury, cholestatic jaundice and cholestatic hepatitis. The incidence of cholestasis was classified by us, using the European ADR database as follows: common (>0.5% of ADR cholestatic), rare (0.3-0.5% of ADR cholestatic), and no (<0.3% of ADR cholestatic). The threshold for common incidence was set to 0.5% of ADR to ensure that the drugs chlorpromazine, cyclosporine and ritonavir, which were identified as cholestatic in the LiverTox® database, and were classified as common causes of cholestasis. The 0.3% threshold was set artificially to account for background cholestasis incidence. Additional drugs classified as common for induction of cholestasis according to our classification were: bosentan, ketoconazole, atorvastatin and glimepiride. Riede et al. (2017) reviewed cholestasis incidence of several drugs based on cohort and retrospective studies. In line with our classification, Riede et al. (2017) classified

cyclosporine cholestasis incidence as common and rosiglitazone as not cholestatic, but ketoconazole and atorvastatin cholestasis incidences were classified as rare in contrast to our classification system. No explanation was found for the discrepancy between atorvastatin and ketoconazole cholestasis incidence classification of these authors and that in the ADR database, hence, we used our classification system based on the European ADR database. Bosentan was classified as rare or common depending on the dose in the review of Riede et al. (2017). At therapeutic dose level, *i.e.* 125 mg twice a day, bosentan was considered a rare cause of cholestasis. Since the drugs were evaluated at their therapeutic dose level in the current study, bosentan-induced cholestasis incidence was classified as rare. Troglitazone was banned from the market and therefore not in the European ADR database, and also not in the review by Riede et al. (2017). A review of cohort studies indicated that troglitazone causes hepatocellular liver injury, with rare instances of mixed or cholestatic liver injury (Chojkier, 2005). Troglitazone cholestasis incidence was therefore classified as rare. Maximal prescribed daily dosage was used for simulations and obtained from the supplier's prescription information.

Generic PBK models for drugs

A generic PBK model was used to predict the hepatic concentrations of the selected drugs at therapeutic dose level and above. These concentrations were subsequently used to predict the inhibitory effect on hepatic bile acid efflux using a coupled bile acid PBK model (see section 2.3).

The generic drug PBK models were adapted from Punt et al. (2022). Briefly, the PBK models consisted of compartments for lung, adipose, bone, brain, heart, intestine, liver, kidney, muscle, skin, spleen, arterial and venous blood. Different compared to Punt et al. (2022) a blood:plasma ratio of 0.55 was used for acidic compounds (1-haematocrit), and 1 for neutral or basic compounds (Cubitt et al., 2009). Physicochemical properties (pKa, logP, logD, topological surface area, molecular weight) of the drugs were predicted using Chemicalize, https://chemicalize.com/ developed by ChemAxon (http://www.chemaxon.com). The physicochemical properties were subsequently used to predict tissue:plasma partition coefficients (Berezhkovskiy, 2004; Rodgers and Rowland, 2006), absorption rate constants and fractions absorbed (Hou et al., 2004).

As part of this study, several *in vitro* and *in silico* methods were evaluated to derive the tissue:plasma partition coefficients, hepatic intrinsic clearance and fraction unbound in plasma (F_{up}) (Table 1). In more detail, for the tissue:plasma partition coefficients values derived using the *in silico* methods of Rodgers and Rowland (2006) and Berezhkovskiy (2004) were compared. For the fraction unbound (F_{up}) both the *in silico* method of Lobell and Sivarajah (2003) and *in vitro* rapid equilibrium dialysis data using human plasma were evaluated. Clearance data were derived from *in vitro* hepatocyte studies or the pkCSM *in silico* tool (Pires et al., 2015). It should be noted that *in vitro* the hepatic intrinsic clearance was measured, while pkCSM predicted the total clearance, *i.e.* a combination of hepatic and renal clearance. Where possible, *in vitro* intrinsic hepatic clearance (CL_{int}) and F_{up} data were obtained from the high throughput toxicokinetic (httk) database (Pearce et al., 2017), alternatively a literature search in Scopus was conducted to obtain the *in vitro* CL_{int} (Table 2). Corrections for non-specific binding of the compounds to the hepatocytes *in vitro* were applied based on the calculation method of Kilford et al. (2008). The *in vitro* and *in silico* clearance data were scaled

to the *in vivo* situation based on a hepatocellularity of 117.5 × 10^6 hepatocytes per gram liver (Barter et al., 2007) and a liver weight of 1470 grams, or 70 kg body weight, respectively, see Eq. 1 and 2.

$$CL_{int,in\ vivo} = CL_{int,in\ vitro} \times Hep \times Vli \times 60 \times 10^{-6} \quad \text{Eq. 1}$$

$$CL_{tot,in\ vivo} = CL_{tot,in\ silico} \times BW \times 60 \times 10^{-3} \quad \text{Eq. 2}$$

Where in Eq. 1 $CL_{int,in\ vivo}$ is the intrinsic clearance *in vivo* in L min^{-1} entire $liver^{-1}$, $CL_{int,in\ vitro}$ the hepatic intrinsic clearance *in vitro* in µL min^{-1} 10^{-6} hepatocytes, Hep the hepatocellularity in 10^6 hepatocytes/g liver and Vli the weight of the liver in grams. A factor of 10^{-6} L $µL^{-1}$ and 60 min h^{-1} was applied to convert the CL_{int} to units applicable to the PBK model. Eq. 2 describes the *in silico* to *in vivo* scaling of the total clearance (CL_{tot}). $CL_{tot,in\ vivo}$ is the total clearance *in vivo* L min^{-1} entire $liver^{-1}$, $CL_{tot,in\ silico}$ the total clearance as predicted by pkCSM in mL min^{-1} kg body $weight^{-1}$, and BW the body weight in kg. Here, factors of 10^{-3} L mL^{-1} and 60 min h^{-1} were applied to convert the CL_{tot} to units applicable to the PBK model.

A literature search was performed to compile a dataset on human *in vivo* drug plasma peak concentrations (C_{max}) after a single oral dose of the selected drugs. The following key words were used for this literature study: ((TITLE ("compound name") AND ALL (bioavailability OR pharmacokinetics OR kinetics)) AND ((human OR man OR volunteer OR subject)) AND (Cmax OR "c max" OR "maximal concentration" OR "maximum concentration" OR "peak concentration")). The studies that were identified for each compound were subsequently filtered to exclude 1) results obtained for specific patient groups like patients with renal impairment or gastric by-pass, 2) studies with children, and 3) studies using slow or extended-release formulations. The results of this meta-analysis including references can be found in the Github repository[1] in the file "Invivo.xlsx".

The predicted plasma C_{max} was compared with the observed plasma C_{max} as obtained from the meta-analysis. The ratio predicted:observed C_{max} was calculated for each study and/or dose. This resulted in a number of ratios per compound. The median of this ratio was calculated per compound, and for further simulations the combination of input parameters that gave a median ratio predicted:observed C_{max} closest to 1 was selected. Only the drugs of with a median ratio predicted:observed C_{max} within 10-fold were used for further analysis (n=15). An overview of the metabolizing enzymes or transporters involved in the kinetics of the drugs was made to find explanations for over- or underpredictions. The information about the involved enzymes and transporters was obtained from literature (Wishart et al., 2018; Elsby et al., 2012; Cockshott, 2004; Hebert, 1997; Klatt et al., 2011; Treiber et al., 2007).

[1] https://github.com/Veronique-de-Bruijn/PBK-model-cholestasis.git

Table 1 Input parameters for the generic PBK model. Ka: absorption rate constant, Fa: fraction absorbed, Kpad, Kpbo, Kpbr, Kpgu, Kphe, Kpki, Kpli, Kplu, Kpmu, Kpsk, Kpsp are tissue:plasma partition coefficients for adipose tissue, bone, brain, gut, heart, kidney, liver, lung, muscle, skin and spleen, respectively. QSAR: quantitative structure activity relationship.

Process	Parameter(s)	Method	Number of drugs	Reference
Intestinal uptake	Ka, Fa	QSAR based on the topological surface area	18	Hou et al., 2004
Physicochemical parameters	pKa, logP, logD, topocological surface area, molecular weight	Chemicalize (*in silico*)	18	https://chemicalize.com/ developed by ChemAxon
Tissue:plasma partition coefficients	Kpad, Kpbo, Kpbr, Kpgu, Kphe, Kpki, Kpli, Kplu, Kpmu, Kpsk, Kpsp	*In silico*	18	Rodgers & Rowlands, 2006
		In silico	18	Berezhkovskiy, 2004
Hepatic intrinsic clearance	CL_{int}	(Cryopreserved) primary human hepatocytes (*in vitro)*	15	Data derived from the httk package (Pearce et al., 2017) or other publications (see Table 2)
Total clearance	CL_{tot}	pkCSM (*in silico*)	18	Pires et al., 2015
Fraction unbound plasma	F_{up}	Equilibrium dialysis (*in vitro)*	18	Data derived from the httk package (Pearce et al., 2017), or other publications (Hahn et al., 1973; Zaghloul et al., 1987)
		In silico	18	Lobell and Sivarajah, 2003
Blood:plasma ratio	BP	Acidic drugs: 0.55 (1-haematocrit) Neutral or basic drugs: 1	18	Cubitt et al, 2009

Table 2 Physicochemical properties, *in vitro* and *in silico* intrinsic clearance (CLint) for the 18 selected drugs

Drug	pKa1	pKa2	logP	*In vitro* CLint (µL/min/10^6 hepatocytes)	Reference	*In silico* CLint (mL/min/kg body weight)	Reference
Atorvastatin	4.31		5	0	httk	2.673	pkCSM
Bicalutamide	11.78		2.52	0	httk	3.811	pkCSM
Bosentan	5.8	1.28	5.53	2.34	httk	2.851	pkCSM
Chlorpromazine	9.2		4.56	146	(Louisse et al., 2020)	3.981	pkCSM
Cyclosporine	11.82		3.38	8.59	httk	3.656	pkCSM
Deferasirox	4.51	-0.13	5.17			3.664	pkCSM
Fluoxetine	9.4		4.19	36.7	(Chao et al., 2009)	4.786	pkCSM
Flutamide	12.81		3.4	30.4	httk	1.146	pkCSM
Glimepiride	5.62		2.93	3.67	(Hallifax et al., 2010)	4.909	pkCSM
Haloperidol	13.96	8.2	3.08	5.06	httk	12.79	pkCSM
Ketoconazole	6.42		4.28	55	httk	3.882	pkCSM
Lovastatin	14.9		3.47	0	httk	8.472	pkCSM
Pioglitazone	7.32	5.63	3.1			0.904	pkCSM
Ritonavir	13.68	2.84	5.04	8.57	httk	3.540	pkCSM
Rosiglitazone	7.37	6.4	2.86			1.297	pkCSM
Saquinavir	6.67	13.61	2.51	37.1	(Wood et al., 2018)	1.854	pkCSM
Trazodone	7.49		3.132	7.40	httk	4.688	pkCSM
Troglitazone	7.31		4.87	21.9	httk	0.382	pkCSM

Glycochenodeoxycholic acid PBK model

A PBK model describing synthesis, circulation and excretion of bile acids in healthy individuals was based on our previous work (de Bruijn et al., 2022; de Bruijn et al., 2023). The conceptual model is presented in Figure 1. The enterohepatic circulation was modelled as a circulation of GCDCA between the liver (extracellular and intracellular), gall bladder and intestine. The intestinal uptake and the hepatic uptake and efflux were described using carrier-mediated transport processes, *i.e.* ASBT, NTCP or BSEP-mediated, respectively. The NTCP-mediated hepatic uptake of GCDCA was modelled permeability-limited as described in our previous work (de Bruijn et al., 2023). The kinetic parameters for ASBT-mediated transport were obtained using Caco-2 cells cultured on permeable cell culture inserts and scaled from the *in vitro* to *in vivo* situation as described in our previous work (de Bruijn et al., 2023). GCDCA *de novo* synthesis in the liver was set equal to its excretion via the feces. GCDCA was actively transported from the liver to the common bile duct by BSEP following Michaelis–Menten kinetics. The BSEP-mediated efflux of GCDCA was described by the following equation (Eq. 1):

$$E = \frac{V_{max,BSEP} \times [Cliveriw]}{K_{m,BSEP} + [Cliveriw]} \quad \text{Eq. 1}$$

where E is the BSEP-mediated efflux in µmol/h, V_{max} is the maximum efflux rate of GCDCA in blood in µmol/entire liver/hour, [Cliveriw] the free concentration of bile acids in intracellular water in liver in

µmol/L and $K_{m,BSEP}$ the Michaelis–Menten constant in µmol/L for BSEP-mediated GCDCA efflux. The V_{max} and K_m for BSEP-mediated transport of GCDCA were obtained from a vesicular transport assay in a baculovirus-infected Sf9 system (Kis et al., 2009).

The differential model equations were encoded and solved using the deSolve package version 1.32 in R version 4.1.0 (Soetaert and Petzoldt, 2010; R Core Team, 2022). The model code can be found in the Github repository[1].

Inhibitory effect of drugs on hepatic bile acid efflux

The hepatic free concentration of the within 10-fold predicted drugs at the maximal prescribed daily therapeutic dosage was used to simulate their inhibitory effect on hepatic GCDCA efflux. The conceptual PBK model for the drugs was combined with the PBK model for GCDCA as displayed in Figure 1. The concentrations required to reduce hepatic bile acid efflux by 50% (IC_{50}) were derived from a study using suspension-cultured primary human hepatocytes (PHHs) (Zhang et al., 2016) and corrected for *in vitro* non-specific binding (Kilford et al., 2008). The IC_{50} values obtained using PHHs were for all drugs except pioglitazone lower than the IC_{50} values obtained using BSEP-transfected membrane vesicles (Supplementary Table S1). Therefore, the results obtained from suspension-cultured PHHs were used for further simulations as a worst-case estimate. Membrane vesicles and suspension-cultured PHHs provide different insights in hepatic bile acid efflux. PHHs are known to have a physiologically relevant expression of several transporters and metabolizing enzymes, rather than the exclusive BSEP expression in membrane vesicles. Hence, in contrast to membrane vesicles, the drug-induced inhibitory effect on bile acid efflux from primary suspension-cultured human hepatocytes is not necessarily caused by an exclusive inhibition of BSEP-mediated transport, but could also be caused by inhibition of the uptake, basolateral efflux by MRP3/4 or the conjugation process. Nevertheless, the net drug-induced bile acid efflux inhibition was incorporated in the equation for BSEP-mediated efflux. In the absence of specific data on the effects of all the selected drugs on bile acid efflux for GCDCA, glycocholic acid efflux was used as a surrogate for all drugs (Zhang et al., 2016). Glycocholic acid showed greater inhibition (lower IC_{50}) in assays with PHHs than GCDCA and was considered as a worst-case estimate of GCDCA efflux (Chothe et al., 2021; Yucha et al., 2017). Competitive inhibition was assumed, as this is the typical mode of drug-transporter-inhibition (Kenna et al., 2018). The following formula to calculate K_i applies for competitive inhibitors like the drugs considered here (Eq. 3) (Yung-Chi and Prusoff, 1973):

$$K_i = \frac{IC_{50}}{1 + \frac{[S]}{K_m}} \quad \text{Eq. 3}$$

Where K_i is the inhibitory constant in µM, IC_{50} the half maximum inhibitory concentration of the drug in µmol/L, [S] the substrate concentration in µM, and K_m the Michaelis-Menten constant in µM.

Subsequently, the inhibitory effect of the drugs on GCDCA efflux was incorporated in the PBK model equation describing BSEP-mediated efflux. In line with competitive inhibition, the $K_{m,BSEP}$ in the

corresponding Michaelis Menten reaction (Eq. 1) was modified to the apparent K_m ($K_{m,BSEP,app}$) as follows (Eq. 4):

$$K_{m,BSEP,app} = K_{m,BSEP} \ (1 + \frac{[I]}{K_i}) \qquad \text{Eq. 4}$$

Where $K_{m,BSEP,app}$ is the apparent Michaelis-Menten constant in µM, [I] the unbound hepatic concentration of the inhibitor (=drug) in µM and K_i the inhibitory constant in µM.

The dose-metric used to evaluate intracellular GCDCA accumulation was the area under the curve (AUC), because it has been acknowledged AUC is the most relevant for endpoints that are influenced by total dose over time resulting in an accumulation (Rietjens et al., 2019).

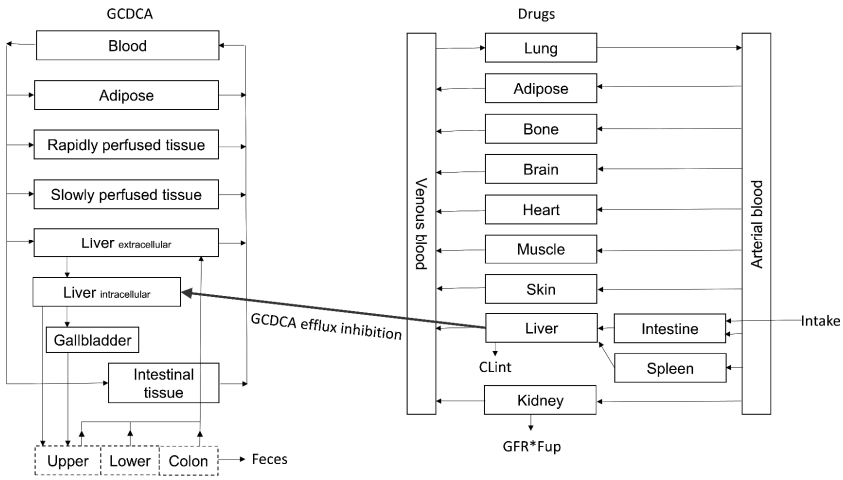

Figure 1 Conceptual model for the PBK modeling of bile acid homeostasis and the influence on this homeostasis by drugs. Conceptual model for GCDCA PBK model was taken from de Bruijn et al. (2023), conceptual model for generic drugs PBK models was taken from Punt et al. (2022). CLint=intrinsic clearance, Fup=fraction unbound plasma, GCDCA=glycochenodeoxycholic acid, GFR=glomerular filtration rate

Simulating sensitive individuals

The developed PBK approach was also employed to evaluate drug effects on intrahepatic GCDCA accumulation in sensitive individuals. For these studies cyclosporine was selected as the model drug, because the maximal prescribed daily therapeutic dose resulted in intrahepatic concentrations equivalent to the K_i for bile acid efflux inhibition, facilitating detection of changes in the bile acid accumulation. In our previous work, we established that an over 1.5-fold increased total bile acid pool size posed an individual at risk for intrahepatic bile acid accumulation as a result of BSEP-inhibition (de Bruijn et al., 2022). Furthermore, a low BSEP abundance was identified as a potential risk factor for the development of cholestasis. Therefore, as an example, the effects of cyclosporine on intrahepatic accumulation were simulated for a) a reference individual, b) an individual with a 1.5-fold increased total bile acid pool size compared to the reference individual, c) an individual with low hepatic BSEP abundance or d) an individual with an increased pool size and a low BSEP abundance. The low and reference BSEP abundances were derived from a meta-analysis of hepatic transporter abundances in healthy Caucasians (Burt et al., 2016). The *in vitro* to *in vivo* extrapolation of V_{max} was based on the

BSEP abundance. A lower BSEP abundance thus resulted in a lower *in vivo* V_{max}. The reference individual had a BSEP protein abundance of 0.84 pmoles BSEP protein per a million hepatocytes. Low BSEP abundance was set to the reported mean minus 3 times the standard deviation and amounted to 0.23 pmoles BSEP protein per million hepatocytes.

Sensitivity analysis

To assess the influence of the parameters on the model outcome, a sensitivity analysis was performed for the plasma C_{max} of the drugs and the intrahepatic GCDCA levels. The Drug's doses were set to 1 mg/kg body weight. For plasma C_{max} all potential combinations of input parameters were evaluated. The normalized sensitivity coefficients (NSC) for hepatic GCDCA levels were calculated using the combination of input parameters giving the C_{max} in closest agreement with the *in vivo* data (Supplementary Material Table S2). Based on the method reported by Evans and Andersen (2000), the normalized sensitivity coefficients (NSCs) for the model parameters were calculated as follows:

$$SC = \frac{C' - C}{P' - P} \times P/C \qquad \text{Eq. 4}$$

where C indicates the initial value of the model output, C'indicates the modified value of the model output resulting from an increase in the parameter value. P indicates the initial parameter value and P′ indicates the modified parameter value after a 5% increase of its value, keeping all other parameters at their original value.

6.3 Results

Tissue:plasma partitioning has a major impact on Cmax for acidic drugs

Figure 2 visualizes the effect of altering the method for obtaining the partition coefficients, the intrinsic clearance or F_{up} parameter, while keeping the methods for defining the other generic drug PBK model parameters unchanged. For 13 out of 18 drugs the C_{max} predictions by the generic model were within 5-fold of the observed data for at least one combination of the drug PBK model input parameters. The predicted C_{max} of atorvastatin and haloperidol were more than 5-fold but less than 10-fold overpredicted. The C_{max} of Saquinavir, flutamide and lovastatin were more than 10-fold overpredicted for all combinations of input parameters (Supplementary Material Figure S2). The largest effect on C_{max} was observed for the method used to define the partition coefficients (Figure 2A). For drugs with pKa<6, *i.e.* atorvastatin, bosentan, deferasirox and glimepiride, calculating the partition coefficients by the method of Berezhkovskiy resulted in an over 5-fold lower prediction for the C_{max} as compared to the results obtained with the method of Rodgers and Rowland. The F_{up} and clearance methods had smaller effects on plasma C_{max}. Intrinsic total clearance predicted by pkCSM resulted in slightly higher or similar C_{max} values as intrinsic hepatic clearance determined using (cryopreserved) primary hepatocytes (Figure 2B). Supported by this close agreement between the two sets of C_{max} predictions, pkCSM was employed to predict clearance for rosiglitazone, pioglitazone and deferasirox for which no *in vitro* clearance data were available. This approach resulted in C_{max} predictions within 5-fold compared to the observed pharmacokinetic data.

The hepatic free concentration of the drugs was predicted using the combination of input parameters giving the C_{max} in closest agreement with the *in vivo* data. Exemplary Figure 3 indicates which combination of input parameters gave the most accurate prediction for the C_{max} of bosentan and glimepiride. The closest agreement with *in vivo* data was achieved for bosentan and glimepiride when the C_{max} values were predicted using the method of Rodgers and Rowland for tissue partitioning and the method of Lobell and Sivarajah for calculation of F_{up}. C_{max} was predicted best when determining the clearance by the *in silico* tool pkCSM and primary hepatocytes for bosentan and glimepiride, respectively. These comparisons were made for all 18 drugs and are displayed in 6.5 Supplementary file Figure S1. In case two methods resulted in exactly the same median ratio predicted:observed, the *in silico* methods were chosen for intrinsic clearance and F_{up}. Supplementary Material Table S2 provides a tabular overview of the methods chosen for prediction of the parameters for further simulations. Flutamide, saquinavir and lovastatin were excluded from further predictions because of their >10-fold overprediction

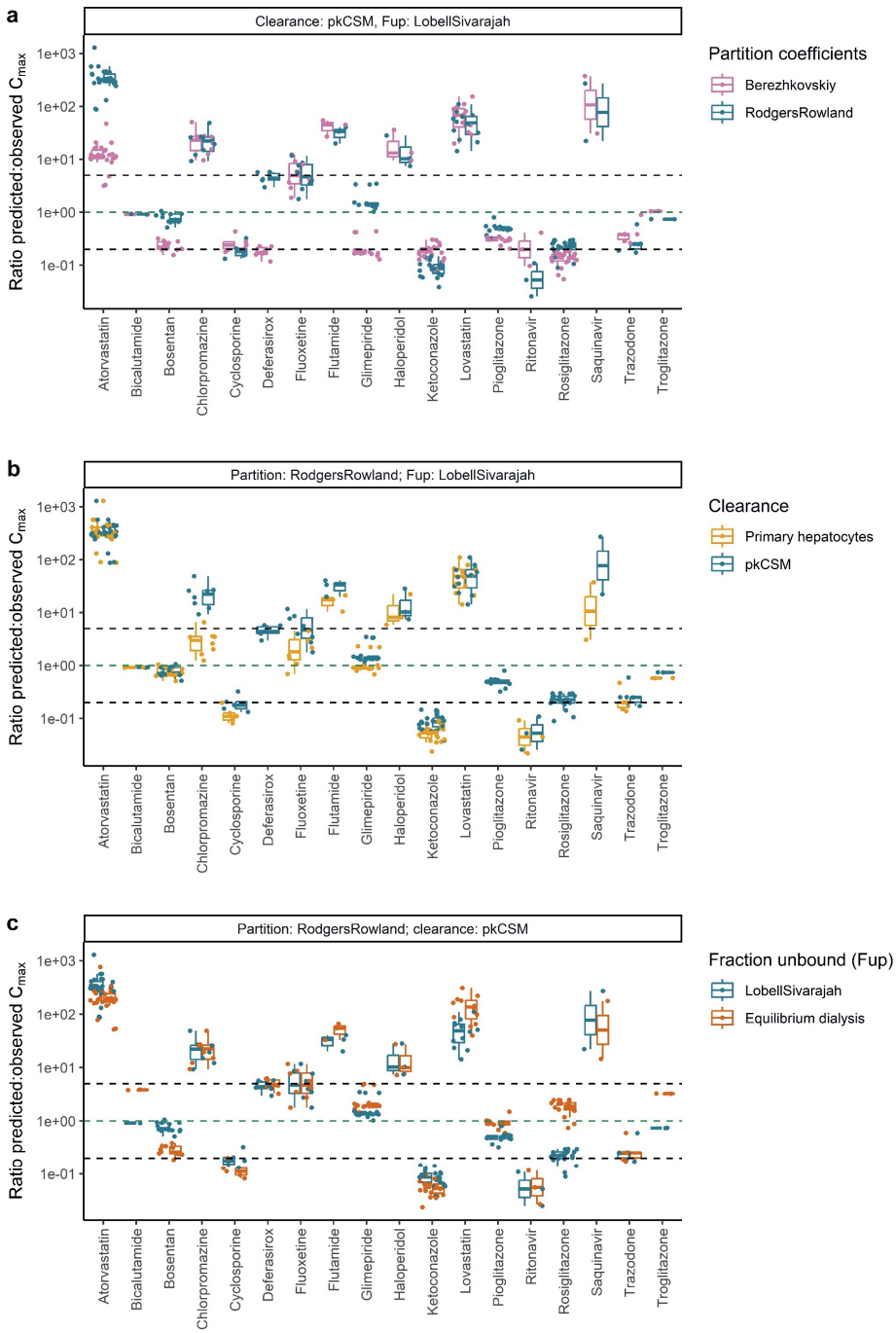

Figure 2 Ratio predicted:observed C_{max} for the 18 selected drugs using different methods to obtain the PBK model input parameters for a) partition coefficients, b) clearance and c) fraction unbound (F_{up}), while the other methods to obtain the input parameters where as indicated in the box above a, b and c). Green dashed line: ratio predicted:observed=1, lower and upper black dashed lines: ratio predicted:observed=0.2 or 5, respectively.

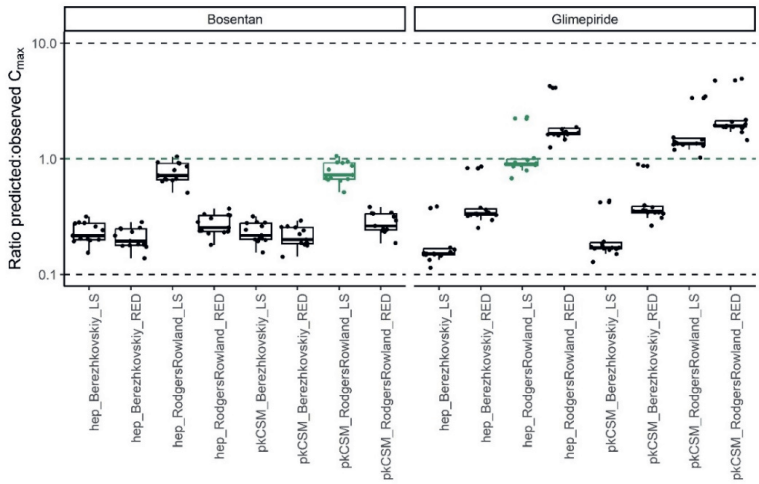

Figure 3 Ratio predicted:observed C_{max} for bosentan and glimepiride using 8 different combinations of PBK model input parameters. The green box indicates that this combination of input parameters resulted in a median ratio predicted:observed closest to 1. The combination in green is used for further simulations. Clearance: hep=primary hepatocytes, pkCSM=in silico clearance, partition coefficients: Berezhkovskiy or Rodgers and Rowlands, fraction unbound in plasma: LS=Lobell Sivarajah, RED=rapid equilibrium dialysis. Green dashed line: ratio predicted:observed=1, lower and upper black dashed lines: ratio predicted:observed=0.1 or 10, respectively

Kinetic processes involved in the kinetics of the drugs

To facilitate evaluation of potential processes that may contribute to deviations in the predicted versus observed C_{max}, an overview of the involved phase I, II or III processes in the kinetics of the 18 drugs was created (Figure 4). The color of the bullets indicates the ratio predicted:observed C_{max}. Interestingly, the C_{max} values for the statins lovastatin and atorvastatin were >5-fold overpredicted. These drugs, along with deferasirox and haloperidol, undergo phase II metabolism by several UDP-glucoronosyltransferase (UGT) enzymes. Haloperidol is also overpredicted, but deferasirox is underpredicted. Besides the UGT-enzymes, the cytochrome P450 (CYP) enzymes CYP2C8 and CYP3A4 are involved in the metabolism of lovastatin and atorvastatin. Hepatic uptake of lovastatin and atorvastatin occurs through the organic anion transporter (OATP) 1B1. The highest overprediction was observed for lovastatin. All together the overview reveals that the over- or underprediction of the C_{max} cannot be ascribed to a specific metabolic phase or enzyme since for all drugs, including the drugs with the highest level of deviation but also the drugs for which accurate predictions were obtained similar phase I, II and II metabolism and respective isoenzymes seem to be involved.

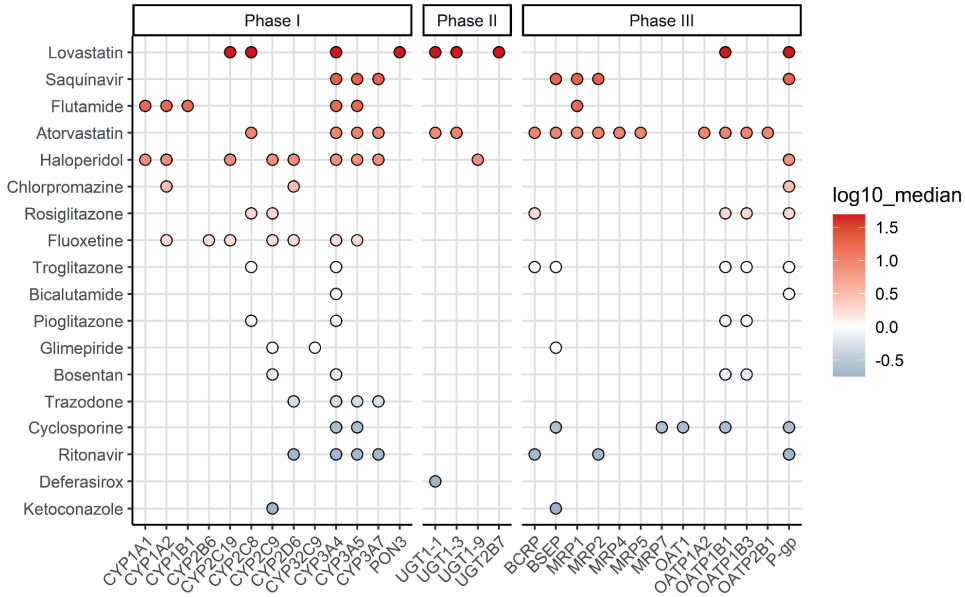

Figure 4 Phase I, II or III kinetic processes involved in the pharmacokinetics of the 18 selected drugs. To facilitate evaluation of potential parameters that may contribute to deviations in the predicted versus observed Cmax the color of the bullets indicates for the respective drug the logarithm of the median ratio predicted:observed Cmax. For the combination of input parameters used for the PBK predictions see Supplementary Material I Table S2

Drug PBK model based predictions of free hepatic concentrations at therapeutic dose levels and their comparison to the K_I for inhibition of bile acid efflux

Upon evaluation of the drug PBK model predictions for plasma C_{max} values the PBK models were used to predict maximal free hepatic concentrations of the drugs (assumed to be equal to free concentrations of the drugs in venous blood leaving the liver) at therapeutic dose levels. In Table 3 these predicted maximal free hepatic concentrations of the drugs are compared to the respective K_i values for drug-mediated inhibition of hepatic bile acid efflux by presenting the ratio between these two values. From these ratios it follows that not all drugs when dosed at their therapeutic level will result in maximal free hepatic concentrations able to reach the K_i (ratio equals at least 1) and thus will not result in effective inhibition of bile acid efflux. The PBK models can also be used to predict the dose levels required to reach maximal free hepatic concentrations of the drugs that reach the K_i, and these dose levels are also presented in Table 3. Comparison of these dose levels to the therapeutic dose levels corroborates that for some drugs therapeutic dose levels are high enough to induce maximal free hepatic concentrations in the range or above the K_i, resulting in inhibition of bile acid efflux, while for others higher than therapeutic dose levels would be needed. For cyclosporine for example, the ratio between the maximal free hepatic concentrations and the K_i amounts to 12.9 and the therapeutic dose level is 11-fold higher than what would be needed to reach the K_i while for others, like bosentan, this ratio amounts to 0.03, indicating that a 34-fold higher than therapeutic dose level would be needed to reach the K_i.

These results already explain why defining the K_i (or IC_{50}) for bile acid efflux inhibition, defines the hazard but does not predict the risk on developing cholestasis. However, it is also important to consider that not only a comparison of the maximal free hepatic concentrations to the respective K_i values is relevant to obtain insight in chances on effects on bile acid efflux and accumulation, but also the duration of this situation where free hepatic concentrations are in the range of the K_i or above.

To further study these aspects Figure 5 presents the drug PBK model based predictions for the free hepatic drug concentration over time at therapeutic dose levels including a comparison to the respective K_i values. From these results it follows that for some drugs the therapeutic dose will result in free hepatic drug concentrations over the whole 24h time frame (far) below the respective K_i in some cases not even reaching 10% of the K_i, the latter being a concentration at which for a competitive inhibitor less than 10% inhibition can be expected. The curves also reveal that for drugs for which at the therapeutic dose level the maximum free hepatic drug concentration will be reached or even exceed the K_i, the overall time frame during which concentrations in the range or above the Ki can be expected will depend on the rate of clearance. Comparison of the data for chlorpromazine and troglitazone for example, reveals that, although the ratio between the predicted maximum free hepatic concentration and the K_i is comparable for both drugs, amounting to 2.56 and 2.20 respectively, the time frame during which for troglitazone the free hepatic concentrations are in the range of the K_i is substantially larger than for chlorpromazine, due to the far more efficient clearance of chlorpromazine. This indicates that for prediction of the risk of cholestasis not the ratio between the maximum free hepatic concentration of the drug at therapeutic dose level and the K_i, but rather the ratio between the AUC of the drug compared to the K_i is of importance. Therefore, Table 3 also presents the AUC/K_i ratios at therapeutic dose levels for the different drugs.

Table 3 Therapeutic dose, inhibitory constant (K_i) for inhibition of hepatic bile acid efflux, ratio between the drug PBK model predicted maximal free hepatic concentration at therapeutic dose level (assumed to be equal to free concentration in venous blood leaving the liver) and the K_i, ratio between the drug PBK model predicted area under the curve (AUC) free hepatic concentration at therapeutic dose level, the predicted dose required to obtain a maximal free hepatic concentration of the drug equal to Ki and the AUC above the K_i.

Drug	Therapeutic dose (mg/kg body weight)[a]	K_i (nM)[b]	Ratio internal maximal liver concentration: K_i	Ratio internal liver AUC:Ki (h)	Dose required to reach K_i (mg/kg body weight)	AUC above the K_i (µmol/L x hr)
Atorvastatin	1.143	112	0.15	1.26	8.0	0.00
Bicalutamide	0.714	979	0.22	1.85	3.0	0.00
Bosentan	3.571	493	0.03	0.77	123	0.00
Chlorpromazine	28.57	460	2.56	2.20	11	0.36
Cyclosporine	15.00	4.88	12.9	253	1.2	1.12
Deferasirox	20.00	505	0.51	0.19	103	0.00
Fluoxetine	0.635	320	0.34	0.41	2.0	0.00
Glimepiride	0.086	603	0.03	0.31	2.6	0.00
Haloperidol	0.214	1134	0.11	0.28	2.0	0.00

Ketoconazole	17.14	173	5.16	26.0	3.5	1.26
Pioglitazone	0.643	631	0.91	14.8	0.7	0.00
Ritonavir	17.14	28.0	4.88	38.3	3.5	0.44
Rosiglitazone	0.114	8.18	0.47	10.8	0.3	0.00
Trazodone	8.571	1919	1.28	9.88	6.5	0.20
Troglitazone	11.43	64.0	2.20	12.4	5.0	0.12

a Therapeutic dose is the maximal prescribed daily dose and obtained from the supplier's information

b K_i is the inhibitory constant of bile acid efflux inhibition induced by the drugs. The K_i was obtained by measuring from glycocholic acid efflux in an assay using primary hepatocytes in suspension (Zhang et al., 2016).

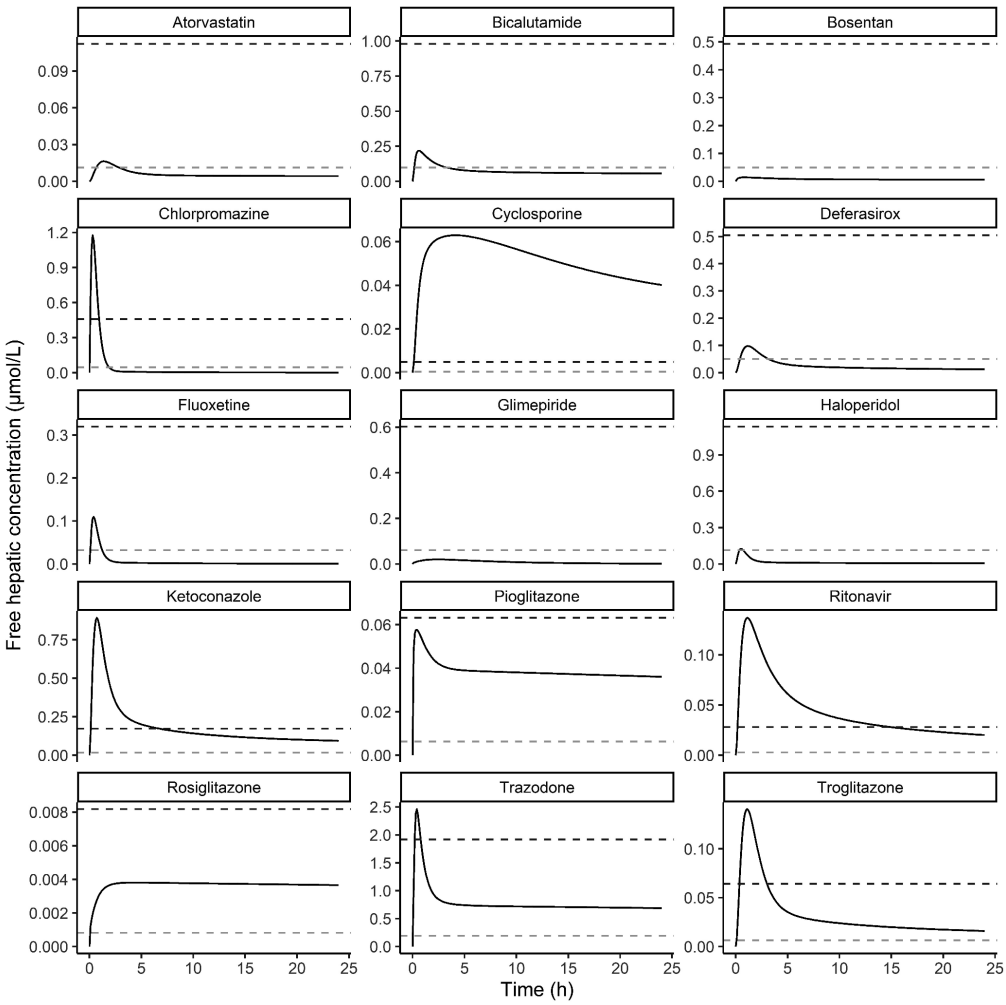

Figure 5 Free hepatic drug concentration over time at therapeutic dose level. Blue dashed line=K_i, grey dashed line=10% of K_i

PBK model predictions for drug induce bile acid accumulation

To provide insight in the consequences of the drug kinetic profiles for bile acid accumulation, PBK model predictions for drug induced bile acid accumulation were made by linking the drug PBK models to a PBK model for bile acid kinetics. Figure 6 presents the predicted GCDCA accumulation at both the therapeutic dose levels as well as at the dose levels at which the maximum free hepatic concentration was predicted to reach the K_i (Table 3). These results confirm that for several of the drugs therapeutic dose levels would not result in substantial bile acid accumulation in line with the incidence report for cholestasis are not or rarely reported. When dose levels would be at dose levels where the free maximum hepatic concentrations would be at the K_i, bile acid accumulation would be always less than 2-fold compared to the placebo and in some cases not observed at all. Of interest to note is also that only for some of the drugs for which cholestasis is observed commonly, especially cyclosporine, ritonavir and ketoconazole, bile acid accumulation at therapeutic dose levels is higher than what is predicted for the placebo (Figure 6a). Comparison to the bile acid accumulation predicted for these drugs at dose levels where the K_i is reached (Figure 6b) reveals that this higher bile acid accumulation at therapeutic dose levels can be ascribed to the fact that the therapeutic dose level is higher than the dose levels where the K_i is reached (Table 3). The results obtained also reflect that this PBK model based prediction accounts for the effects of the drug on the bile acid efflux during the whole 24h interval thus also taking into account differences in drug clearance. This is again illustrated by the differences between chlorpromazine and troglitazone for which the ratio between the predicted maximum free hepatic concentration at therapeutic dose level and the K_i is comparable (Table 3). At both simulated dose levels chlorpromazine, in spite of its ability to inhibit bile acid efflux, was predicted to not result in hepatic GCDCA accumulation while troglitazone, with less efficient clearance and a higher AUC, was predicted to result in increased hepatic bile acid levels (Figure 6). To further illustrate the importance of the size of the AUC as compared to the K_i for predicting whether bile acid accumulation is to be expected Figure 7a presents the PBK model predicted GCDCA accumulation (expressed as fold change in the AUC of GCDCA compared to the placebo) versus the ratio of the AUC of the drug versus the K_i, showing that the PBK modelling indeed adequately accounts for the effect of the varying concentration of the drug of bile acid accumulation overtime, while when using the ratio of the maximum free hepatic concentration of the drug and the K_i as the descriptive parameter no adequate prediction is obtained (Figure 7b).

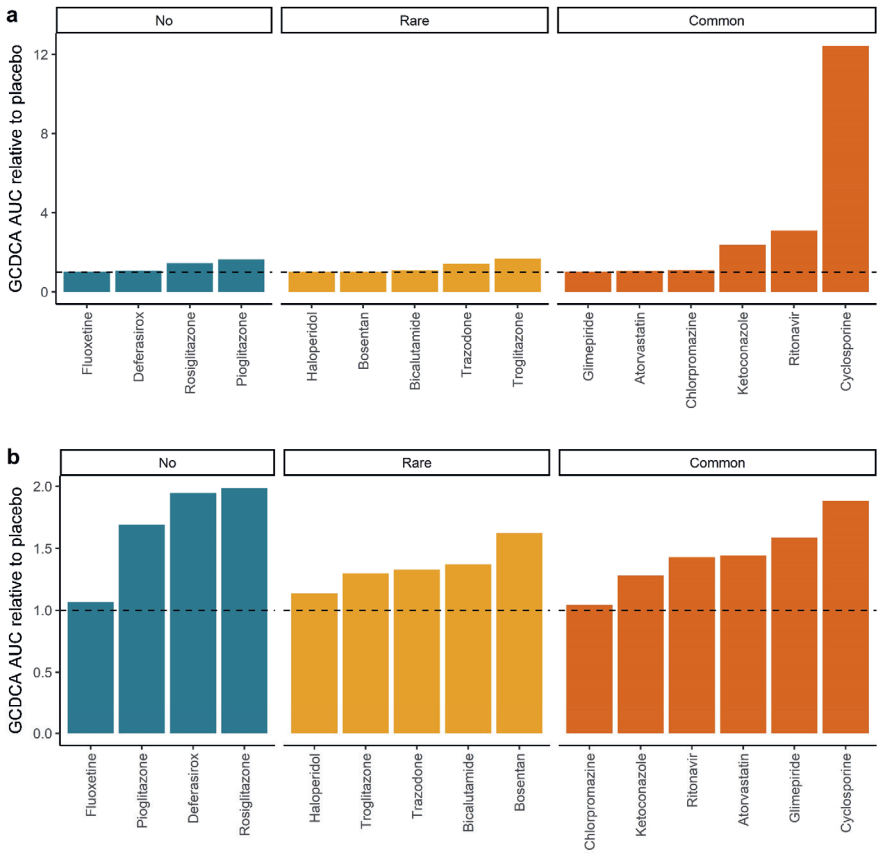

Figure 6 PBK model predicted hepatic glycochenodeoxycholic acid (GCDCA) accumulation at a) the maximal therapeutic dose level or b) the dose at which the maximum free hepatic concentration reaches the K_i (see Table 3). The dashed line indicates the placebo (set to 1). AUC=area under the curve.

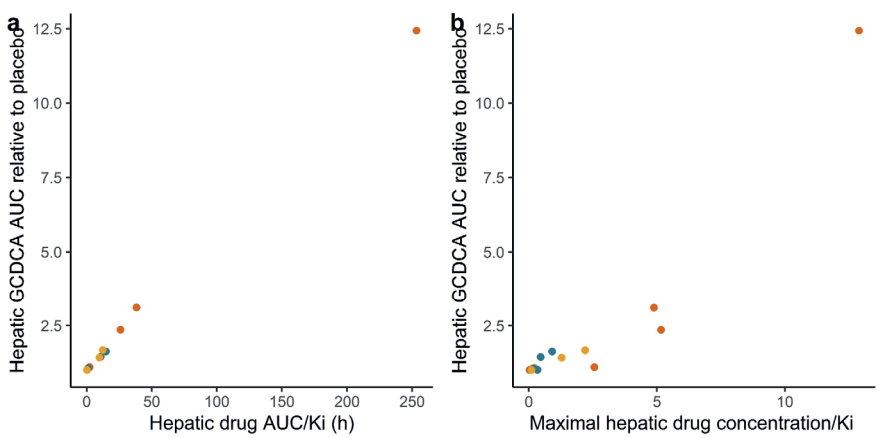

Figure 7 Hepatic glycochenodeoxycholic acid (GCDCA) area under the curve (AUC) relative to placebo versus a) the hepatic drug concentration AUC/K_i and b) maximal hepatic drug concentration/K_i. Simulations were done at therapeutic dose levels.

Finally, it is also of interest to note that the PBK model based predictions for bile acid homeostasis presented in Figure 6 do not in all cases reflect the frequency of occurrence of cholestasis at therapeutic doses of the drug. While for some compounds it is clear that therapeutic dose levels are high enough to cause bile acid accumulation, for others the therapeutic dose levels are too low to induce this effect. There are also drugs for which bile acid accumulation is predicted to occur while there is no or only rare reported incidence of cholestasis, while for some drugs for which occurrence of cholestasis is common bile acid accumulation at therapeutic dose level is limited or even absent. Of special interest is the apparent difference between the three thiazolidines troglitazone, rosiglitazone and pioglitazone. The kinetic profiles predicted for these compounds by the generic PBK model show substantial differences and especially a lack of effective clearance at prolonged time intervals for rosiglitazone and pioglitazone, resulting in potentially unrealistically high AUC levels for these drugs by the generic PBK model.

This suggests that using the AUC above the K_i as a measure to predict the occurrence of cholestasis may be a better approach. Table 3 lists these predicted AUC above K_i values for the various drugs. This would predict only the following drugs of the series of 15 drugs studied to induce cholestasis at their therapeutic dose in the order: ketoconazole > cyclosporine >> ritonavir > chlorpromazine > trazodone > troglitazone. It is of interest to note that these first 4 compounds are all listed as commonly inducing cholestasis, while trazodone and troglitazone rarely induce cholestasis. This would suggest that the AUC above the K_i might be the best parameter to predict the risk of cholestasis. The fact that this AUC above the K_i would not identify the common occurrence of cholestasis for atorvastatin and glimepiride might be related to the fact that another mode of action than inhibition of bile acid efflux is underlying the effect, since at therapeutic dose levels these two drugs were predicted to never reach free hepatic concentrations that would cause efficient inhibition of bile acid efflux.

Increased bile acid pool size and reduced BSEP abundance are potential synergistic risk factors for cholestasis

The PBK modeling of drug induced bile acid accumulation presented so far did not yet take into account factors that may cause individuals to become sensitive towards bile acid accumulation. In subsequent PBK modeling studies it was investigated to what extent an augmented bile acid pool size and low BSEP abundance are potential risk factors for the development of cholestasis upon exposure to selected drugs. To this end, first the effects of cyclosporine administration for individuals with an increased total bile acid pool or decreased BSEP levels or both were simulated (Figure 8). Cyclosporine was selected for these studies because the free intrahepatic levels of this drug were shown to meet the K_i threshold upon therapeutic dose levels. For comparison also the effects of these interindividual modifications on the hepatic GCDCA levels upon placebo treatment were calculated and are presented in Figure 8 as well. The combination of both an increased pool size and low BSEP abundance resulted in intrahepatic GCDCA levels surpassing the cumulative effects of each factor in isolation. These observations suggest a potential synergistic impact for individuals in which both risk factors are present simultaneously.

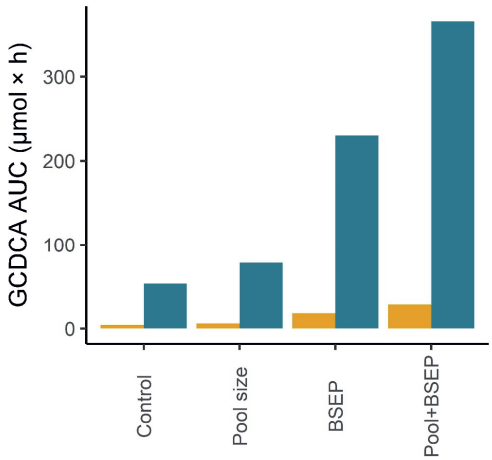

Figure 8 Area under the curve (AUC) of GCDCA levels in liver intracellular water upon administration of the maximal prescribed daily dose of cyclosporine in different sensitive individuals. Yellow=placebo, blue=cyclosporine. Control=reference individual, pool size=1.5-fold increased GCDCA pool size compared to the reference, BSEP=low BSEP abundance, Pool+BSEP=individual with a 1.5-fold increased GCDCA pool low BSEP abundance. GCDCA=glycochenodeoxycholic acid

Sensitivity analysis

The sensitivity analysis (Figure 9a) revealed that especially the fraction absorbed (Fa) and dose of the drug have strong positive influence on the plasma C_{max} of the drugs, and that the blood:plasma ratio (BP) has a strong negative influence. Cardiac output (QC) and body weight (BW) could have a positive or negative influence on the plasma C_{max} of the drugs, depending on which drug was simulated and the parametrization of the PBK model. Figure 9b revealed that the parameters related to the bile acid homeostasis typically had a stronger influence on the hepatic GCDCA AUC than drug-specific parameters. The most influential drug-specific parameters were K_i for hepatic efflux inhibition (Ki), fraction absorbed (Fa) and dose of the drug. Parameters related to the maximal rate of BSEP-mediated hepatic GCDCA efflux or its scaling had a strong influence on the hepatic GCDCA AUC. A boxplot was generated of the normalized sensitivity coefficients for all 15 drugs. Some NSC values were ±1.5× the interquartile range and thus considered an outlier. Normalized sensitivity coefficients for rosiglitazone were most often considered outliers followed by pioglitazone.

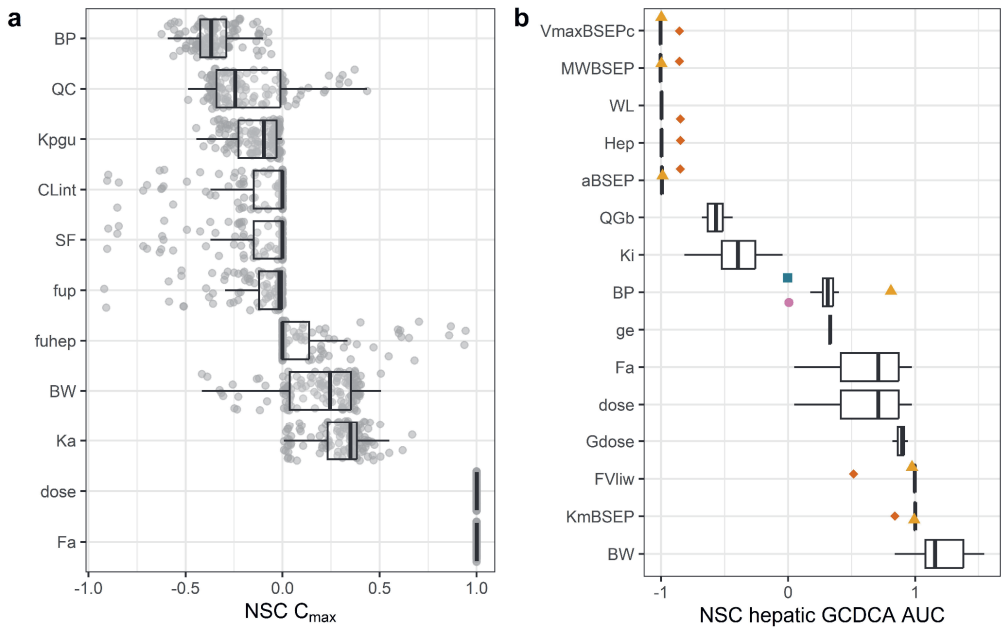

Figure 9 Sensitivity analysis for a) plasma C_{max} of 18 drugs parameterized using different combinations of input parameters and b) hepatic glycochenodoxycholic acid (GCDCA) accumulation as indicated by the area under the curve (AUC) of hepatic GCDCA after administration of 15 selected reference drugs. Outliers are colored and shaped. Parameters are included when in a) 15 or more and in b) 10 or more normalized sensitivity coefficients (NSCs) were <-0.25 or >0.25. BP=blood:plasma ratio, QC=cardiac output, Kpgu=plasma:gut partition coefficient, CLint=clearance, SF=scaling factor for clearance, fup=fraction unbound in plasma, fuhep=fraction unbound to hepatocytes, BW=body weight, Ka=absorption rate constant of the drug, dose=dose, Fa=fraction absorbed, VmaxBSEPc=maximal rate of BSEP-mediated hepatic GCDCA efflux, MWBSEP=molecular weight of BSEP, WL=weight of liver, hep=hepatocellularity, aBSEP=BSEP abundance, Qgb=fraction of GCDCA going directly to the gallbladder, Ki=inhibitory constant of hepatic bile acid efflux, ge=gall bladder ejection rate, Gdose=amount of GCDCA in gall bladder at t=0, FVliw=fraction of intracellular water in liver, KmBSEP=Michaelis-Menten constant of BSEP-mediated hepatic GCDCA efflux. ■=chlorpromazine, ●=fluoxetine, ▲=pioglitazone, ◆=rosiglitazone.

6.4 Discussion

Accurate predictions of internal dosimetry are of paramount importance in driving the acceptance of advanced (animal-free) testing methodologies for drug safety evaluations. Internal dosimetry predictions are also instrumental in bridging the gap between *in vitro* toxicity and *in vivo* dose-response relationships or drug potency data. The present study aims at development of a new approach methodology (NAM) to predict drug-induced cholestasis, as a result of hepatic efflux inhibition and subsequent bile acid accumulation. To this end, a generic PBK model was built to predict hepatic concentrations of 18 selected drugs. For 15 of these drugs, the predicted C_{max} was within 10-fold of the observed $C_{max.}$ The predicted internal hepatic dose level of these 15 drugs was incorporated in a bile acid PBK model describing the synthesis, circulation and excretion of the exemplary bile acid GCDCA. The intrahepatic GCDCA accumulation was determined as a measure for cholestatic potency.

The generic PBK models were parameterized using different *in vitro* and *in silico* input parameters and the plasma C_{max} predictions were validated with *in vivo* plasma C_{max}. Different methods were applied to define the parameters required to model the drug kinetics by the generic PBK model.

Tissue-partitioning was predicted using the quantitative-property-property relationships as described by Berezhkovskiy (2004) or Rodgers and Rowland (2006). For acidic drugs, *i.e.* pKa<6, the method used for prediction of the tissue:partition coefficients had a major effect on predicted plasma C_{max}. For 2 out of 4 strongly acidic drug in our dataset, the predictions were closest to the *in vivo* data when the method of Rodgers and Rowlands was used, while for the remaining 2 strongly acidic drugs the closest fit was achieved with Berezhkovksiy's method. These observations suggest that the most predictive approach to simulate plasma C_{max} cannot be determined by a drug's physicochemical properties alone but that model parametrization should be evaluated on a case-by-case basis, and include drug-specific processes where necessary to enhance predictive accuracy. Another interesting finding was that the *in silico* tool pkCSM resulted in C_{max} predictions similar to the predictions made with *in vitro* clearance data. If any differences were observed between the two different inputs, the pkCSM tool resulted in higher, *i.e.* more conservative, predictions than the *in vitro* clearance. These findings provide support for the use of the pkCSM tool also for pioglitazone, rosiglitazone and deferasirox for which no *in vitro* clearance data obtained from primary human hepatocytes (PHHs) were available.

The complete set of evaluated drugs consisted of 18 drugs. For 13 drugs, the predictions made by the generic PBK model were within a 5-fold range, and for 7 drugs the predictions were within a 2-fold range of the corresponding *in vivo* data. Typically, regulatory contexts demand predictions by a drug-specific PBK model within a 2-fold range of the *in vivo* data (Peters and Dolgos, 2019), however, given the large variability within reported human *in vivo* kinetic data this requirement might be excessively rigorous. Thus, deviations may in part be due to the variability within reported human *in vivo* biokinetic data. For saquinavir, for example, *in vivo* C_{max} values ranging from 5.4 to 66.1 µg/L were observed at similar dose levels (Frohlich et al., 2004; Vella and Floridia, 1998) indicating variability in the available human *in vivo* data as a potential reason for the relatively large fold differences between predicted and reported C_{max} values. Biological, technical and analytical interstudy differences could contribute to this variability, underpinning the need for harmonized *in vivo* biokinetic study protocols and the need to understand at least the main drivers of interindividual differences. Only 3 drugs (i.e. lovastatin, saquinavir and flutamide) were excluded from further analysis towards potential bile acid accumulation, because the generic PBK model overpredicted their plasma C_{max} by >10-fold. Aside from the large differences in human *in vivo* data contributing to the discrepancies, saquinavir and flutamide are multidrug resistance protein (MRP)-1 substrates and it can be speculated that by incorporating MRP-1 mediated renal and/or biliary clearance in the PBK model, the predictions would be improved. Lovastatin C_{max} is probably overestimated, because extrahepatic clearance is not (sufficiently) considered, resulting in an underprediction of total clearance. No *in vitro* lovastatin intrinsic clearance was measured using PHHs (Pearce et al., 2017), while the total *in vivo* lovastatin clearance was reported to be 451 L/hr (Zhou et al., 1995). pkCSM predicted a higher total clearance than was measured using PHHs, but the predicted clearance only amounted to 36 L/kg after extrapolation to the *in vivo* situation. pkCSM might not be suitable to accurately predict total clearance of drugs with substantial extrahepatic clearance. Lovastatin is metabolized through glucuronidation, lactonization and cytochrome P450-mediated oxidation which can take place outside the liver (Reig-Lopez et al., 2021). Glucuronidation is catalyzed by UDP-glucuronosyltransferases (UGTs) and these are widely expressed in various tissues, including liver, kidney, lung and intestine (Tukey and Strassburg, 2000;

Naritomi et al., 2015). Lactonization can occur as a spontaneous process at pH < 6 or mediated by plasmatic paraoxonase (PON) at pH > 6 (Reig-Lopez et al., 2021). Underestimation of the clearance provides a conservative estimate of the C_{max}.

Upon gaining sufficient confidence in the PBK predictions for 15 out of 18 drugs, we employed the PBK models to predict free intrahepatic drug concentrations and incorporated these into the bile acid PBK model to predict the effects of the drugs on hepatic bile acid accumulation resulting from inhibition of bile acid efflux. Hepatic accumulation at therapeutic dose levels was simulated for the commonly cholestatic drugs cyclosporine, ritonavir and ketoconazole. Interestingly, no hepatic GCDCA accumulation was predicted at therapeutic dose levels of atorvastatin, chlorpromazine and glimepiride, even though these drugs were classified as common causes of cholestasis. It is hypothesized that these drugs cause cholestasis through mechanism(s) that cannot be fully captured by the short term (1h) assay with a suspension-cultured PHH assay. The PHH assay is most suitable to study short term competitive transporter-inhibition. According to the cholestasis AOP, the mechanism(s) or molecular initiating events (MIEs) could involve transporter, hepatocellular and bile canalicular changes (Vinken et al., 2013; Gijbels et al., 2020). Chlorpromazine probably induced cholestasis through hepatocellular changes that can be observed only after several hours of incubation. It was shown that HepaRG cells exposed to 50 µM of chlorpromazine for 4h lost ~50% of hepatocellular tight junctions (Morgan et al., 2019). Glimepiride induced intrahepatic bile canalicular dilatation in a human clinical case study (Omar et al., 2009), which can impossibly be captured in a system with suspension PHHs. Atorvastatin-induced cholestasis is not fully understood, but it is has been speculated that immune-allergic reactions or ROS formation are involved (Karahalil et al., 2017). Furthermore, the different DILI patterns (hepatocellular/cholestasis/mixed) reported after atorvastatin treatment suggest that its mode of action is multifaceted and that a battery of tests is required for a NAM-based risk assessment (Averbukh et al., 2022).

In our previous study we observed a 60% increase in the liver GCDCA upon bosentan treatment, while in the current work no substantial increase was observed (de Bruijn et al., 2022). The discrepancy between the two studies can be attributed to variations in dosage and tissue partitioning, ultimately leading to a lower free intrahepatic bosentan concentration. In our earlier study, a clinical trial-like dosage of 500 mg twice a day was simulated (Fattinger et al., 2001), while in the current study the maximal prescribed daily dose of 250 mg once a day was used. Furthermore, in our previous investigation, an experimental logP value of 3.1 was employed (Meyer, 1996), while in the current study, a logP value of 5.5, predicted using Chemaxon, was used. This change, combined with a slightly higher pKa value (5.5 versus 5.8), led to a 10-fold increase in the liver:plasma partition coefficient, as calculated using the method of Rodgers and Rowlands. Besides, the *in silico* calculated fraction unbound decreased by 5-fold due to these changes in physicochemical parameters. Taking the influence of the physicochemical parameters and the dose together, this resulted in a decreased free hepatic bosentan concentration in the current manuscript compared to the previous study and thus a reduced effect on hepatic GCDCA levels. These findings stress the importance of accurate estimates of lipophilicity.

Inhibition of hepatic bile acid efflux is a hazard for cholestasis risk, but the results of the present study clearly demonstrated that predicting the risk cannot be based on the IC_{50} or K_i for inhibition of

hepatic bile acid efflux alone. PBK modeling of the intracellular hepatic drug concentration time profile and its comparison to the K_i appeared to be the best way to predict the cholestatic potential with especially the AUC above the K_i providing a better prediction than the total AUC/K_i ratio or the K_i or IC_{50} as such. This indicates that one has to take into account not only the drug's potency to inhibit the bile acid efflux, but also the external dose level and its kinetics. In addition, the individual's susceptibilities were shown to influence the risk with people with a higher bile acid pool size and low BSEP abundance being more susceptible. The developed combined drug and bile acid PBK models incorporate all this information and predict drug-induced cholestasis as a result of hepatic transporter inhibition. For a complete risk assessment of cholestasis also MIEs focusing on hepatocellular and bile canalicular changes need to be included. Future research should focus on validation and standardization of these assays and quantitatively coupling the measured MIEs to cholestasis risk. The current results provide a proof-of-principle of an animal-free PBK model to bridge the gap between *in vitro* potency to inhibit hepatic bile acid efflux and *in vivo* cholestasis risk.

Acknowledgements: We would like to thank dr.ir.Hans Bouwmeester for carefully reviewing the manuscript.

References

Ankley, G. T., Bennett, R. S., Erickson, R. J. et al. (2010). Adverse outcome pathways: A conceptual framework to support ecotoxicology research and risk assessment. Environ Toxicol Chem 29, 730-741. doi:10.1002/etc.34

Averbukh, L. D., Turshudzhyan, A., Wu, D. C. et al. (2022). Statin-induced liver injury patterns: A clinical review. J Clin Transl Hepatol 10, 543-552. doi:10.14218/JCTH.2021.00271

Barter, Z. E., Bayliss, M. K., Beaune, P. H. et al. (2007). Scaling factors for the extrapolation of in vivo metabolic drug clearance from in vitro data: Reaching a consensus on values of human micro-somal protein and hepatocellularity per gram of liver. Current drug metabolism 8, 33-45.

Bathena, S. P., Mukherjee, S., Olivera, M. et al. (2013). The profile of bile acids and their sulfate metabolites in human urine and serum. J Chromatogr B Analyt Technol Biomed Life Sci 942-943, 53-62. doi:10.1016/j.jchromb.2013.10.019

Berezhkovskiy, L. M. (2004). Volume of distribution at steady state for a linear pharmacokinetic system with peripheral elimination. J Pharm Sci 93, 1628-1640. doi:10.1002/jps.20073

Burt, H. J., Riedmaier, A. E., Harwood, M. D. et al. (2016). Abundance of hepatic transporters in caucasians: A meta-analysis. Drug Metab Dispos 44, 1550-1561. doi:10.1124/dmd.116.071183

Chao, P., Barminko, J., Novik, E. et al. (2009). Prediction of human hepatic clearance using an in vitro plated hepatocyte clearance model. Drug Metab Lett 3, 296-307. doi:10.2174/187231209790218073

Chen, M., Suzuki, A., Thakkar, S. et al. (2016). Dilirank: The largest reference drug list ranked by the risk for developing drug-induced liver injury in humans. Drug Discov Today 21, 648-653. doi:10.1016/j.drudis.2016.02.015

Chojkier, M. (2005). Troglitazone and liver injury: In search of answers. Hepatology 41, 237-246. doi:10.1002/hep.20567

Chothe, P. P., Pemberton, R. and Hariparsad, N. (2021). Function and expression of bile salt export pump in suspension human hepatocytes. Drug Metab Dispos 49, 314-321. doi:10.1124/dmd.120.000057

Cockshott, I. D. (2004). Bicalutamide: Clinical pharmacokinetics and metabolism. Clin Pharmacokinet 43, 855-878. doi:10.2165/00003088-200443130-00003

Cubitt, H. E., Houston, J. B. and Galetin, A. (2009). Relative importance of intestinal and hepatic glucuronidation-impact on the prediction of drug clearance. Pharm Res 26, 1073-1083. doi:10.1007/s11095-008-9823-9

Dawson, S., Stahl, S., Paul, N. et al. (2012). In vitro inhibition of the bile salt export pump correlates with risk of cholestatic drug-induced liver injury in humans. Drug Metab Dispos 40, 130-138. doi:10.1124/dmd.111.040758

de Bruijn, V. M. P., Rietjens, I. and Bouwmeester, H. (2022). Population pharmacokinetic model to generate mechanistic insights in bile acid homeostasis and drug-induced cholestasis. Arch Toxicol 96, 2717-2730. doi:10.1007/s00204-022-03345-8

De Bruijn, V. M. P., Te Kronnie, W., Rietjens, I. et al. (2023). Intestinal in vitro transport assay combined with physiologically based kinetic modeling as a tool to predict bile acid levels in vivo. ALTEX doi:10.14573/altex.2302011

Elsby, R., Hilgendorf, C. and Fenner, K. (2012). Understanding the critical disposition pathways of statins to assess drug–drug interaction risk during drug development: It's not just about oatp1b1. Clinical Pharmacology & Therapeutics 92, 584-598.

Fattinger, K., Funk, C., Pantze, M. et al. (2001). The endothelin antagonist bosentan inhibits the canalicular bile salt export pump: A potential mechanism for hepatic adverse reactions. Clin Pharmacol Ther 69, 223-231. doi:10.1067/mcp.2001.114667

Fontana, R. J., Bjornsson, E. S., Reddy, R. et al. (2023). The evolving profile of idiosyncratic drug-induced liver injury. Clin Gastroenterol Hepatol 21, 2088-2099. doi:10.1016/j.cgh.2022.12.040

Frohlich, M., Burhenne, J., Martin-Facklam, M. et al. (2004). Oral contraception does not alter single dose saquinavir pharmacokinetics in women. Br J Clin Pharmacol 57, 244-252. doi:10.1111/j.1365-2125.2003.01983.x

Gijbels, E., Vilas-Boas, V., Annaert, P. et al. (2020). Robustness testing and optimization of an adverse outcome pathway on cholestatic liver injury. Arch Toxicol 94, 1151-1172. doi:10.1007/s00204-020-02691-9

Hafey, M. J., Houle, R., Tanis, K. Q. et al. (2020). A two-tiered in vitro approach to de-risk drug candidates for potential bile salt export pump inhibition liabilities in drug discovery. Drug Metab Dispos 48, 1147-1160. doi:10.1124/dmd.120.000086

Hahn, I., Krieglstein, G., Krieglstein, J. et al. (1973). Distribution of chlorpromazine in a simplified blood influenced by various drugs. Naunyn-Schmiedeberg's Archives of Pharmacology 278, 35-44.

Hallifax, D., Foster, J. A. and Houston, J. B. (2010). Prediction of human metabolic clearance from in vitro systems: Retrospective analysis and prospective view. Pharm Res 27, 2150-2161. doi:10.1007/s11095-010-0218-3

Hebert, M. F. (1997). Contributions of hepatic and intestinal metabolism and p-glycoprotein to cyclosporine and tacrolimus oral drug delivery. Adv Drug Deliv Rev 27, 201-214. doi:10.1016/s0169-409x(97)00043-4

Heise, T., Schmidt, F., Knebel, C. et al. (2015). Hepatotoxic effects of (tri)azole fungicides in a broad dose range. Arch Toxicol 89, 2105-2117. doi:10.1007/s00204-014-1336-1

Hou, T. J., Zhang, W., Xia, K. et al. (2004). Adme evaluation in drug discovery. 5. Correlation of caco-2 permeation with simple molecular properties. J Chem Inf Comput Sci 44, 1585-1600. doi:10.1021/ci049884m

Kaplowitz, N. (2005). Idiosyncratic drug hepatotoxicity. Nat Rev Drug Discov 4, 489-499. doi:10.1038/nrd1750

Karahalil, B., Hare, E., Koc, G. et al. (2017). Hepatotoxicity associated with statins. Arh Hig Rada Toksikol 68, 254-260. doi:10.1515/aiht-2017-68-2994

Kenna, J. G., Taskar, K. S., Battista, C. et al. (2018). Can bile salt export pump inhibition testing in drug discovery and development reduce liver injury risk? An international transporter consortium perspective. Clinical Pharmacology & Therapeutics 104, 916-932.

Kilford, P. J., Gertz, M., Houston, J. B. et al. (2008). Hepatocellular binding of drugs: Correction for unbound fraction in hepatocyte incubations using microsomal binding or drug lipophilicity data. Drug Metab Dispos 36, 1194-1197. doi:10.1124/dmd.108.020834

Kis, E., Ioja, E., Nagy, T. et al. (2009). Effect of membrane cholesterol on bsep/bsep activity: Species specificity studies for substrates and inhibitors. Drug Metab Dispos 37, 1878-1886. doi:10.1124/dmd.108.024778

Klatt, S., Fromm, M. F. and Konig, J. (2011). Transporter-mediated drug-drug interactions with oral antidiabetic drugs. Pharmaceutics 3, 680-705. doi:10.3390/pharmaceutics3040680

Knebel, C., Sussmuth, R. D., Hammer, H. S. et al. (2022). New approach methods for hazard identification: A case study with azole fungicides affecting molecular targets associated with the adverse outcome pathway for cholestasis. Cells 11, 3293. doi:10.3390/cells11203293

Kock, K., Ferslew, B. C., Netterberg, I. et al. (2014). Risk factors for development of cholestatic drug-induced liver injury: Inhibition of hepatic basolateral bile acid transporters multidrug resistance-associated proteins 3 and 4. Drug Metab Dispos 42, 665-674. doi:10.1124/dmd.113.054304

Kostrubsky, S. E., Strom, S. C., Kalgutkar, A. S. et al. (2006). Inhibition of hepatobiliary transport as a predictive method for clinical hepatotoxicity of nefazodone. Toxicological Sciences 90, 451-459.

Leist, M., Ghallab, A., Graepel, R. et al. (2017). Adverse outcome pathways: Opportunities, limitations and open questions. Arch Toxicol 91, 3477-3505. doi:10.1007/s00204-017-2045-3

Lobell, M. and Sivarajah, V. (2003). In silico prediction of aqueous solubility, human plasma protein binding and volume of distribution of compounds from calculated pka and alogp98 values. Mol Divers 7, 69-87. doi:10.1023/b:modi.0000006562.93049.36

Louisse, J., Alewijn, M., Peijnenburg, A. et al. (2020). Towards harmonization of test methods for in vitro hepatic clearance studies. Toxicol In Vitro 63, 104722. doi:10.1016/j.tiv.2019.104722

Meyer, R., J. (1996). In vitro binding of the endothelin receptor antagonist ro 47-0203 to plasma proteins in man and animals, and red blood cell/plasma partitioning. Basel F: Hoffmann-La Roche Ltd

Morgan, K., Martucci, N., Kozlowska, A. et al. (2019). Chlorpromazine toxicity is associated with disruption of cell membrane integrity and initiation of a pro-inflammatory response in the heparg hepatic cell line. Biomedicine & Pharmacotherapy 111, 1408-1416.

Morgan, R. E., van Staden, C. J., Chen, Y. et al. (2013). A multifactorial approach to hepatobiliary transporter assessment enables improved therapeutic compound development. Toxicol Sci 136, 216-241. doi:10.1093/toxsci/kft176

Naritomi, Y., Nakamori, F., Furukawa, T. et al. (2015). Prediction of hepatic and intestinal glucuronidation using in vitro-in vivo extrapolation. Drug Metab Pharmacokinet 30, 21-29. doi:10.1016/j.dmpk.2014.10.001

Nielsen, E., Nørhede, P., Boberg, J. et al. (2012). Identification of cumulative assessment groups of pesticides. EFSA Supporting Publications 9, 269E.

Notenboom, S., Weigand, K. M., Proost, J. H. et al. (2018). Development of a mechanistic biokinetic model for hepatic bile acid handling to predict possible cholestatic effects of drugs. European Journal of Pharmaceutical Sciences 115, 175-184.

Omar, H., Kolla, J., Mangar, D. et al. (2009). Glimepiride-induced cholestasis in a man with diabetes mellitus: A case report. Journal of Medical Case Reports 3, 1-3.

Pearce, R. G., Setzer, R. W., Strope, C. L. et al. (2017). Httk: R package for high-throughput toxicokinetics. J Stat Softw 79, 1-26. doi:10.18637/jss.v079.i04

Peters, S. A. and Dolgos, H. (2019). Requirements to establishing confidence in physiologically based pharmacokinetic (pbpk) models and overcoming some of the challenges to meeting them. Clin Pharmacokinet 58, 1355-1371. doi:10.1007/s40262-019-00790-0

Pires, D. E., Blundell, T. L. and Ascher, D. B. (2015). Pkcsm: Predicting small-molecule pharmacokinetic and toxicity properties using graph-based signatures. J Med Chem 58, 4066-4072. doi:10.1021/acs.jmedchem.5b00104

Punt, A., Louisse, J., Beekmann, K. et al. (2022). Predictive performance of next generation human physiologically based kinetic (pbk) models based on in vitro and in silico input data. ALTEX 39, 221-234. doi:10.14573/altex.2108301

Reig-Lopez, J., Garcia-Arieta, A., Mangas-Sanjuan, V. et al. (2021). Current evidence, challenges, and opportunities of physiologically based pharmacokinetic models of atorvastatin for decision making. Pharmaceutics 13, 709. doi:10.3390/pharmaceutics13050709

Riede, J., Poller, B., Huwyler, J. et al. (2017). Assessing the risk of drug-induced cholestasis using unbound intrahepatic concentrations. Drug Metab Dispos 45, 523-531. doi:10.1124/dmd.116.074179

Rietjens, I. M., Ning, J., Chen, L. et al. (2019). Selecting the dose metric in reverse dosimetry based qivive: Reply to 'comment on 'use of an in vitro–in silico testing strategy to predict inter-species and inter-ethnic human differences in liver toxicity of the pyrrolizidine alkaloids lasiocarpine and riddelliine'by ning et al., arch toxicol doi: Https://doi. Org/10.1007/s00204-019-02397-7', arch toxicol doi: Https://doi. Org/10.1007/s0020 4-019-02421-w. Archives of Toxicology 93, 1467-1469.

Rodgers, T. and Rowland, M. (2006). Physiologically based pharmacokinetic modelling 2: Predicting the tissue distribution of acids, very weak bases, neutrals and zwitterions. J Pharm Sci 95, 1238-1257. doi:10.1002/jps.20502

Schmidt, F., Marx-Stoelting, P., Haider, W. et al. (2016). Combination effects of azole fungicides in male rats in a broad dose range. Toxicology 355-356, 54-63. doi:10.1016/j.tox.2016.05.018

Soetaert, K. and Petzoldt, T. (2010). Inverse modelling, sensitivity and monte carlo analysis inrusing packagefme. Journal of Statistical Software 33, 1-28. doi:10.18637/jss.v033.i03

Sundaram, V. and Bjornsson, E. S. (2017). Drug-induced cholestasis. Hepatol Commun 1, 726-735. doi:10.1002/hep4.1088

Treiber, A., Schneiter, R., Hausler, S. et al. (2007). Bosentan is a substrate of human oatp1b1 and oatp1b3: Inhibition of hepatic uptake as the common mechanism of its interactions with cyclosporin a, rifampicin, and sildenafil. Drug Metab Dispos 35, 1400-1407. doi:10.1124/dmd.106.013615

Tukey, R. H. and Strassburg, C. P. (2000). Human udp-glucuronosyltransferases: Metabolism, expression, and disease. Annu Rev Pharmacol Toxicol 40, 581-616. doi:10.1146/annurev.pharmtox.40.1.581

Vella, S. and Floridia, M. (1998). Saquinavir. Clinical pharmacology and efficacy. Clin Pharmacokinet 34, 189-201. doi:10.2165/00003088-199834030-00002

Vinken, M., Landesmann, B., Goumenou, M. et al. (2013). Development of an adverse outcome pathway from drug-mediated bile salt export pump inhibition to cholestatic liver injury. Toxicol Sci 136, 97-106. doi:10.1093/toxsci/kft177

Walker, P. A., Ryder, S., Lavado, A. et al. (2020). The evolution of strategies to minimise the risk of human drug-induced liver injury (dili) in drug discovery and development. Arch Toxicol 94, 2559-2585. doi:10.1007/s00204-020-02763-w

Wishart, D. S., Feunang, Y. D., Guo, A. C. et al. (2018). Drugbank 5.0: A major update to the drugbank database for 2018. Nucleic Acids Res 46, D1074-D1082. doi:10.1093/nar/gkx1037

Wood, F. L., Houston, J. B. and Hallifax, D. (2018). Importance of the unstirred water layer and hepatocyte membrane integrity in vitro for quantification of intrinsic metabolic clearance. Drug Metab Dispos 46, 268-278. doi:10.1124/dmd.117.078949

Yu, Y. C., Mao, Y. M., Chen, C. W. et al. (2017). Csh guidelines for the diagnosis and treatment of drug-induced liver injury. Hepatol Int 11, 221-241. doi:10.1007/s12072-017-9793-2

Yucha, R. W., He, K., Shi, Q. et al. (2017). In vitro drug-induced liver injury prediction: Criteria optimization of efflux transporter ic50 and physicochemical properties. Toxicol Sci 157, 487-499. doi:10.1093/toxsci/kfx060

Yung-Chi, C. and Prusoff, W. H. (1973). Relationship between the inhibition constant (ki) and the concentration of inhibitor which causes 50 per cent inhibition (i50) of an enzymatic reaction. Biochemical pharmacology 22, 3099-3108.

Zaghloul, I., Ptachcinski, R. J., Burckart, G. J. et al. (1987). Blood protein binding of cyclosporine in transplant patients. J Clin Pharmacol 27, 240-242. doi:10.1002/j.1552-4604.1987.tb02192.x

Zhang, J., He, K., Cai, L. et al. (2016). Inhibition of bile salt transport by drugs associated with liver injury in primary hepatocytes from human, monkey, dog, rat, and mouse. Chem Biol Interact 255, 45-54. doi:10.1016/j.cbi.2016.03.019

Zhou, L.-X., Finley, D. K., Hassell, A. E. et al. (1995). Pharmacokinetic interaction between isradipine and lovastatin in normal, female and male volunteers. Journal of Pharmacology and Experimental Therapeutics 273, 121-127.

6.5 Supplementary material

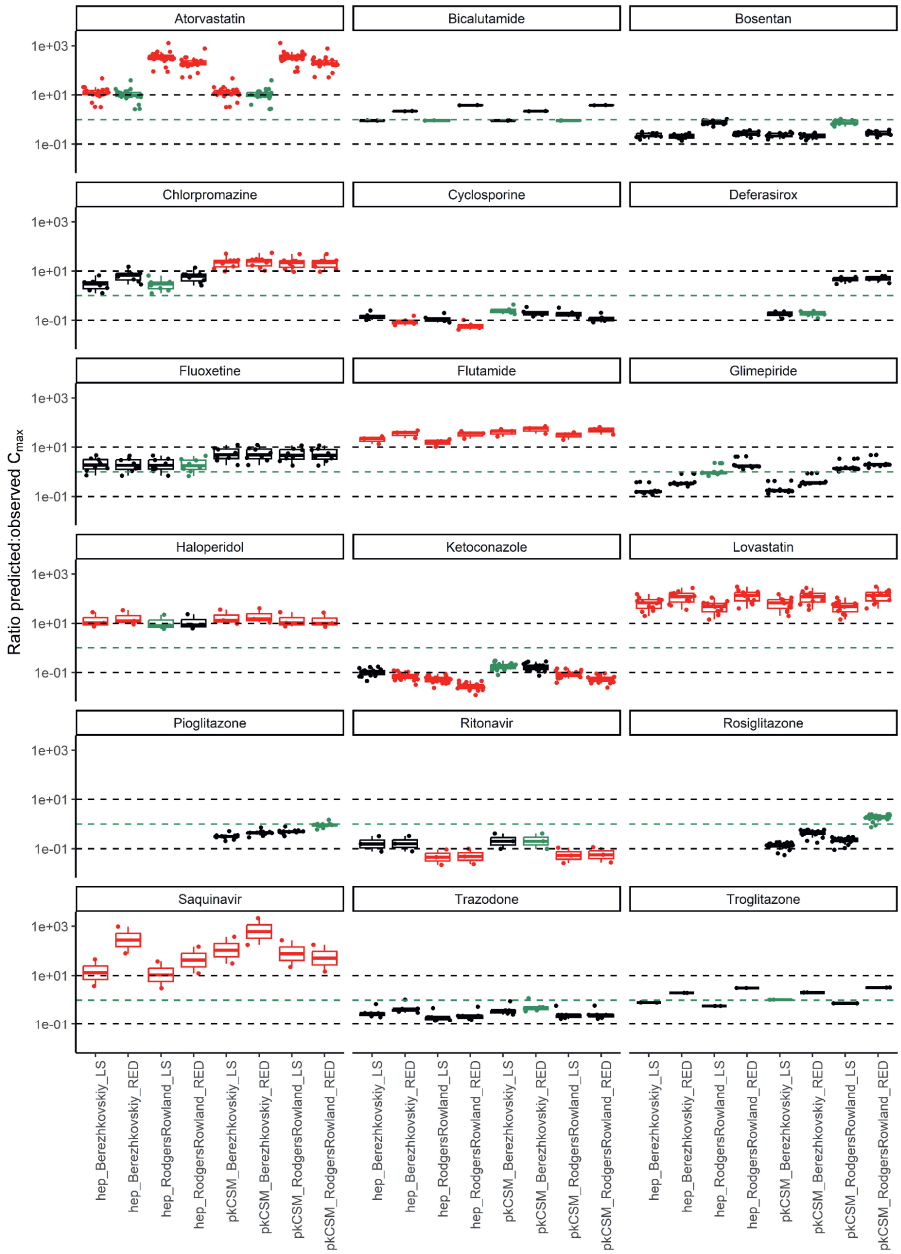

Figure S1 Ratio predicted:observed C_{max} for the selected drugs for up to 8 different combinations of input parameters. Clearance: hep=primary hepatocytes, pkCSM=in silico clearance, partition coefficients: Berezkovskiy or Rodgers and Rowlands, fraction unbound in plasma: LS=Lobell Sivarajah, RED=rapid equilibrium dialysis. Red: the median is >10 fold over- or underpredicted, black: median is within 10-fold, green: the median with the smallest fold-difference. In case two methods resulted in exactly the same method, the in silico methods were chosen for further simulations.

Table S1 IC_{50} for bile acid efflux inhibition in suspension hepatocytes or BSEP-transfected membrane vesicles.

Drug	IC_{50} SHH (μM)	Reference	IC_{50} MV (μM)	Reference
Atorvastatin	2.6	Zhang2016	13	(Morgan et al., 2013)
Bicalutamide	22.4	Zhang2016	79.6	(Morgan et al., 2013)
Bosentan	9.2	Zhang2016	23; 38.1[1]	(Morgan et al., 2013; Dawson et al., 2012)
Cyclosporine	0.1	Zhang2016	0.5; 0.5[1]	(Morgan et al., 2013; Dawson et al., 2012)
Deferasirox	11.9	Zhang2016	58.4	(Morgan et al., 2013)
Ketoconazole	3	Zhang2016	3.4; 2.9[1]	(Morgan et al., 2013; Dawson et al., 2012)
Ritonavir	0.2	Zhang2016	1.74	(Morgan et al., 2013)
Troglitazone	0.5	Zhang2016	3; 2.7[1]	(Morgan et al., 2013; Dawson et al., 2012)
Chlorpromazine	6.4	Zhang2016	>100	(Dawson et al., 2012)
Fluoxetine	5.5	Zhang2016	>100	(Hafey et al., 2020)
Glimepiride	14.1	Zhang2016	15.7	(Morgan et al., 2013)
Haloperidol	25.3	Zhang2016	>100	(Kock et al., 2014)
Pioglitazone	1.4	Zhang2016	0.3	(Dawson et al., 2012)
Rosiglitazone	0.2	Zhang2016	2.8;6.4[1]	(Morgan et al., 2013; Dawson et al., 2012)
Trazodone	43	Zhang2016	>100	(Kostrubsky et al., 2006)

1 Values from two different literature studies

Table S2 The combination of input parameters that gives an absolute median ratio predicted:observed C_{max} with the smallest fold difference. >10-fold overpredictions are excluded from further simulations.

Drug	Clearance	Partition coefficients	Fraction unbound	Median ratio predicted:observed C_{max}
Atorvastatin	pkCSM	Berezhkovskiy	Equilibrium dialysis	9.7
Bicalutamide	pkCSM	RodgersRowland	LobellSivarajah	0.9
Bosentan	pkCSM	RodgersRowland	LobellSivarajah	0.7
Cerivastatin	Primary hepatocytes	Berezhkovskiy	LobellSivarajah	1.6
Chlorpromazine	Primary hepatocytes	RodgersRowland	LobellSivarajah	3.0
Cyclosporine	pkCSM	Berezhkovskiy	LobellSivarajah	0.2
Deferasirox	pkCSM	Berezhkovskiy	Equilibrium dialysis	0.2
Fluoxetine	Primary hepatocytes	RodgersRowland	Equilibrium dialysis	1.8
Glimepiride	Primary hepatocytes	RodgersRowland	in silico	0.9
Haloperidol	Primary hepatocytes	RodgersRowland	LobellSivarajah	8.2
Ketoconazole	pkCSM	Berezhkovskiy	LobellSivarajah	0.2
Pioglitazone	pkCSM	RodgersRowland	Equilibrium dialysis	0.9
Ritonavir	pkCSM	Berezhkovskiy	Equilibrium dialysis	0.2
Rofecoxib	pkCSM	Berezhkovskiy	LobellSivarajah	0.6
Rosiglitazone	pkCSM	RodgersRowland	Equilibrium dialysis	1.9
Trazodone	pkCSM	Berezhkovskiy	Equilibrium dialysis	0.5
Troglitazone	pkCSM	Berezhkovskiy	LobellSivarajah	1.0
>10-fold overpredicted				
Flutamide	Primary hepatocytes	RodgersRowland	LobellSivarajah	17
Lovastatin	pkCSM	RodgersRowland	LobellSivarajah	49
Saquinavir	Primary hepatocytes	RodgersRowland	LobellSivarajah	20

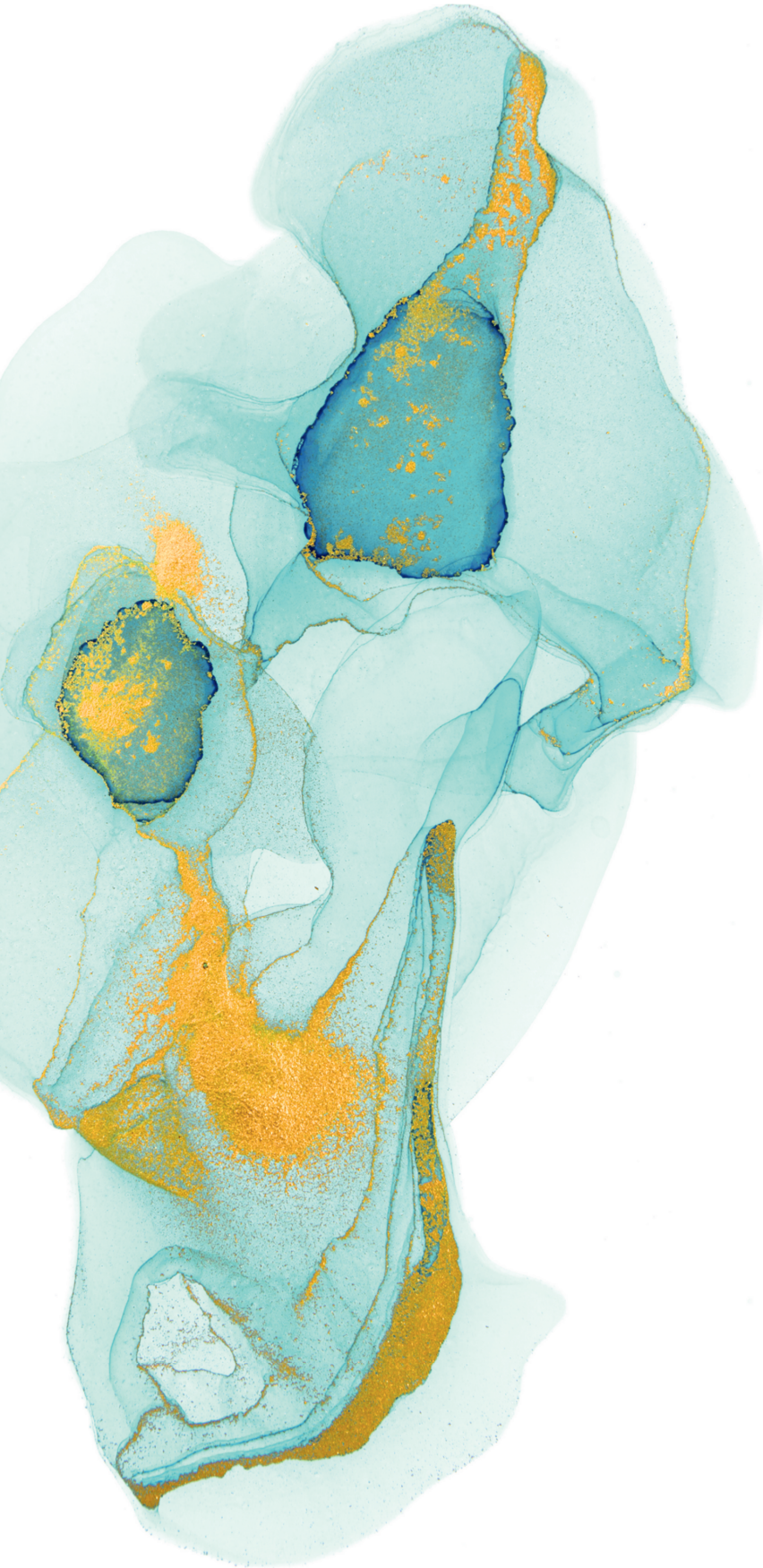

Chapter 7

General discussion

7.1 Overview of the results and main findings

The role of bile acids in human physiology has gained increasing attention over the last years. Nowadays bile acids are widely recognized as crucial signaling molecules influencing energy, glucose, and lipid metabolism, cellular proliferation, and modulating the immune system (Jia et al., 2018; Fuchs and Trauner, 2022). The maintenance of bile acid homeostasis is tightly controlled by different nuclear receptors along the gut-liver axis (Chiang, 2009). Primary bile acids are generated in the liver, and from there secreted into the intestinal lumen. These secreted primary bile acids undergo transformation into more hydrophobic secondary bile acids through modifications by the intestinal microbiome. Subsequently, they are absorbed by the intestinal epithelium and transported into the portal vein for recirculation back to the liver (Zhang et al., 2023a). Chemicals to which humans can be exposed on a daily basis, like drugs, environmental contaminants or food constituents, can interfere with bile acid homeostasis, potentially resulting in a wide range of adverse health outcomes, such as cholestasis, metabolic-associated fatty liver disease (MAFLD) or inflammatory bowel disease (Fuchs and Trauner, 2022; Arab et al., 2017). The present PhD thesis encompasses five experimental chapters focused on investigating bile acid homeostasis and its implications in the context of chemical safety assessment, cholestasis and intestinal bile acid accumulation. Due to ethical considerations and the increased demand for the use of data from human-relevant models, animal-free methods (also called new approach methodologies (NAMs)) were developed and applied to study the aim of the current thesis. The aim was to develop and apply reliable human cell based *in vitro* models and physiologically based kinetic (PBK) models to better understand and predict drug-induced disruption of bile acid homeostasis with an emphasis on cholestasis.

As the liver is a crucial organ in the biosynthesis and enterohepatic recycling of bile acids, **Chapter 2** focused on the establishment of a hepatic *in vitro* model suitable to study drug-induced effects on hepatic bile acid synthesis and secretion. Three different liver-derived *in vitro* models were compared for their ability to emulate human bile acid synthesis and secretion, firstly, sandwich cultured human hepatocytes (SCHHs), secondly, HepaRG cells (HepaRGs), and lastly hepatocyte-like intrahepatic cholangiocyte organoids (ICO-heps). Gene expression of selected target genes involved in cellular maturation status and bile acid synthesis, transport and conjugation was measured to mechanistically underpin the observed differences in bile acid synthesis and secretion. The bile acid synthesis rate was observed to be different in each model, and decreased in the order SCHHs > HepaRGs > ICO-heps. The data revealed that of the studied genes, their expression within SCHHs correlated best with that observed within material obtained from a liver biopsy. In terms of the bile acid profile produced, the bile acid profile of HepaRGs had the highest resemblance with the *in vivo* liver bile acid profile. Due to the promising results for both HepaRGs and SCHHs, the effects of bosentan and lopinavir on bile acid synthesis and secretion were evaluated in these two *in vitro* models. These two drugs were selected because of their well-known ability to inhibit hepatic bile acid efflux by inhibiting the ATP binding cassette (ABC) transporter Bile Salt Export Pump (BSEP). Lopinavir and bosentan-treatment reduced instead of increased the intrahepatic bile acid concentrations in both *in vitro* models. These findings indicate that both the HepaRG and SCHHs had a strong adaptive response and were able to counteract bile acid accumulation induced by bosentan and lopinavir. Collectively, the data revealed

important differences in phenotype and bile acid homeostasis between the three models emulating human hepatic cell functionalities. It was concluded that SCHHs and HepaRGs are powerful models for studying the effects of chemicals on bile acid homeostasis, due to the *in vivo* relevance of their bile acid profiles, the *in vivo* relevance of their gene expression of selected target genes and their responsiveness to BSEP-inhibitors.

In **Chapter 3, 4, 5** and **6** physiologically based kinetic (PBK) models were developed and applied to better understand and predict the effects of various drugs on bile acid homeostasis along the gut-liver axis. **Chapter 3** provided a first proof-of-principle of a PBK modeling approach able to predict the effects of the BSEP inhibitor bosentan on bile acid synthesis, circulation and excretion in both healthy and susceptible individuals. In the approach a PBK model for bosentan was linked to a PBK model for the bile acid glycochenodeoxycholic acid (GCDCA). In this bile acid PBK model a lumped bile acid pool consisting of only GCDCA was assumed, which was considered a fair simplification given that GCDCA is the most abundant bile acid in human serum (Bathena et al., 2013). The bile acid model consisted of separate compartments for liver, gall bladder, intestine, blood, rapidly perfused tissue, slowly perfused tissue and adipose tissue. Enterohepatic circulation was included allowing a circulation of the exemplary bile acid GCDCA between the liver, gall bladder and intestine. Given its importance in the development of cholestatic disease, BSEP-mediated transport was simulated as a process following Michaelis-Menten kinetics. The PBK model developed for bosentan was able to predict the intrahepatic concentration of bosentan upon oral administration. Subsequently, by linking the two models the consequences of the bosentan-induced inhibitory effect on BSEP for bile acid homeostasis could be predicted. In addition, variations in BSEP abundances across the population were integrated in the PBK model using Markov Chain Monte Carlo simulations, while differences in plasma bile acid levels among individuals were accounted for via empirical scaling of the total bile acid pool. Simulated high dose bosentan treatment disproportionally increased the maximum plasma bile acid concentration in individuals with a large total bile acid pool or low BSEP abundance. This PBK modeling approach, that combined bosentan and a bile acid model, provided a first proof-of-principle to estimate the safe therapeutic external dose levels of a drug with BSEP-inhibitory properties.

In **Chapter 4** the focus shifted from the liver towards the role of the intestine in bile acid homeostasis. The aim was to predict the effects of inhibiting the activity of the apical sodium-dependent bile acid transporter (ASBT) on systemic bile acid plasma levels. For this, the *in vitro* Caco-2 cell transport model was used as a model for the human intestinal epithelium. Dedicated *in vitro* bile acid transport experiments were performed using the Caco-2 model to define the relevant PBK model parameters for intestinal bile acid reabsorption. The bile acid PBK model developed in **Chapter 3** was extended to also describe ASBT-mediated ileal bile acid transport and Na^+-taurocholate cotransporting polypeptide (NTCP)-mediated hepatic uptake as transporter-mediated processes. The *in vitro* data and scaling factor for NTCP-mediated transport were obtained from a previously reported study (Notenboom et al., 2018). Furthermore, the PBK model was also extended to describe not only the biokinetics of GCDCA, but also that of glycocholic acid (GCA), glycodeoxycholic acid (GDCA) and a generic unconjugated bile acid (uBA). For this proof-of-principle study the selective ASBT-inhibitor odevixibat

was chosen as a model compound. GCA was shown to be transported over Caco-2 cells in a sodium-dependent manner, indicating the presence of functional ASBT in Caco-2 cells. While the transport of GCA, GCDCA and GDCA over the Caco-2 cells was substantially higher at 37˚C than at 4˚C, the transport of deoxycholic acid (DCA), which was used as model bile acid for uBAs, was equally high at both 4˚C and 37˚C. These findings indicate that GCA, GCDCA and GDCA transport is an active and/or facilitated process, while DCA transport is a passive process. Odevixibat inhibited GCA transport over Caco-2 cells dose-dependently. The inhibitory potency (K_i) of odevixibat was derived using GCA as a model bile acid and assumed to be similar for all conjugated bile acids. No inhibition of uBA uptake was included due to the passive nature of the transport. Upon incorporation of these data in the PBK model, the model quantitatively predicted a reduction in conjugated bile acid levels in plasma upon administration of odevixibat. The simulations matched human *in vivo* data and provided a first proof-of-principle for the incorporation of active ileal bile acid uptake in a bile acid PBK model.

To extent the scope of the developed PBK approach to different drugs, the PBK model developed in **Chapter 4** was applied in **Chapter 5** to investigate the effects of the antibiotic tobramycin on bile acid homeostasis and gain mechanistic insights in the effects of tobramycin on bile acid homeostasis reported in an *in vivo* rat study (Murali et al., 2023). This rat study showed that oral tobramycin exposure resulted in alterations in the composition and levels of bile acids in plasma and feces. These changes cannot be fully explained by alterations in the gut microbiome's metabolic capacity, hence, the effect of tobramycin on bile acid transport across Caco-2 cells and on intestinal bile acid deconjugation was investigated and the whole-body implications were simulated using the PBK model developed in **Chapter 4**. The kinetic parameters, required to describe the effects of tobramycin on intestinal bile acid reuptake and metabolism by the intestinal microbiota in the PBK model, were quantified in *in vitro* assays, using Caco-2 transport experiments and data from previously performed fecal static batch incubations (Zhang et al., 2022; Zhang et al., 2023b). Caco-2 cells were treated with tobramycin in pre- and co-exposure conditions. The pre- and co-exposure differently affected the transport of GCA, GCDCA, GDCA and DCA, the latter bile acid was again used as the model bile acid for uBA. Co-exposure affected bile acid transport in the following order: (from strongest to smallest effect) DCA > GCDCA > GDCA > GCA. For pre-exposure in the order GCA > GCDCA > GDCA > DCA. These differences can be attributed to differences in lipophilicity and thus passive transport rate of the bile acids. The lipophilicity of the bile acids can be ranked as follows: DCA > GDCA ≈ GCDCA > GCA (Roda et al., 1982). It was speculated that co-exposure affected primarily passive transport, because the largest effect was observed on the transport of the most lipophilic bile acid and the tobramycin-induced effect on bile acid transport decreased with decreasing lipophilicity of the bile acids. Pre-exposure was hypothesized to primarily affect ASBT-mediated transport (the effect decreased with increasing lipophilicity of the bile acids). The tobramycin-induced effects on passive, ASBT-mediated transport and intestinal deconjugation were incorporated in the PBK model. According to the PBK model simulations, tobramycin exposure is expected to reduce human plasma C_{max} levels of GCA, GCDCA, GDCA, and uBA by 42.4%, 27.7%, 16.9% and 75.8%, respectively. The reduction of conjugated bile acids is governed especially via an effect on ASBT-mediated intestinal uptake, and not via the effect of tobramycin on intestinal deconjugation, likely because deconjugation happens to a large

extent in the colon which has limited subsequent bile acid reuptake. The strong decrease on uBAs can be attributed to a reduction of passive transport and intestinal deconjugation rate. Overall, the PBK model proved to be a valuable tool for assessing the impact of oral exposure to xenobiotics on host bile acid homeostasis, particularly through its effects on intestinal microbial bile acid deconjugation and intestinal reuptake.

In **Chapter 6** the PBK model was applied to a set of 15 reference drugs that are known to inhibit hepatic bile acid secretion *in vitro*. These drugs are causally linked to the development of drug-induced liver injury (DILI) by the U.S. Food and Drug Administration and are classified as common, rare or no for cholestasis incidence. This classification was based on the number of cholestatic adverse drug reactions reported in the European database of suspected adverse drug reaction (ADR) reports (www.adrreports.eu). The aim of this work was to develop a NAM to predict drug-induced cholestasis, as a result of hepatic bile acid efflux inhibition and bile acid accumulation. The bile acid PBK model as described in **Chapter 4** and **5** was used, with the only adaptation to again only focus on the conjugated bile acid GCDCA. Unconjugated bile acids are mainly transported via perfusion or diffusion and thus unlikely to accumulate in the liver as a result of hepatic transport-inhibitors. In addition a generic PBK model from literature (Punt et al., 2022) was used to describe the kinetic behavior of the selected therapeutics and predict their intrahepatic concentrations The result obtained revealed that cholestasis incidence was not adequately predicted by the inhibitory constant (K_i) for inhibition of hepatic bile acid efflux, but rather by the area under the curve (AUC) above this K_i for the PBK model predicted internal hepatic drug concentration at therapeutic dose level. The approach also provided mechanistic insights in risk factors towards drug-induced cholestasis. People with slower clearance of the drug, a larger bile acid pool, reduced BSEP abundance or given higher than therapeutic dose levels are predicted to be more likely to develop drug-induced cholestasis. Combined, the results of **Chapter 3, 4, 5 and 6** show that PBK modeling of bile acids is useful to gain mechanistic as well as quantitative insights in drug-induced effects on bile acid homeostasis and cholestasis. The PBK modeling approach can also be used to identify susceptible subgroups within a population or kinetic aspects of drugs that increase their cholestasis risk.

The research presented in this PhD thesis extends the understanding of bile acid homeostasis and cholestasis in particular, while also several issues remain to be of interest for future studies on the prediction of drug or chemical-induced effects on bile acid levels throughout the body and their health consequences. These issues will be addressed in the following sections.

7.2 General discussion and future perspectives

In this section, aspects beyond the scope of the individual chapters will be discussed. The topics discussed are:

7.2.1. PBK models for drug metabolism or bile acid homeostasis.
7.2.2. Use of *in silico* data to define PBK input parameters.
7.2.3. Use of *in vitro* models to define PBK input parameters.
7.2.4. Converting *in vitro* data to the *in vivo* situation.
7.2.5. The cholestasis adverse outcome pathway (AOP).
7.2.6. The relevance of bile acids for adverse outcomes other than cholestasis.
7.2.7. Moving towards an animal-free risk assessment for cholestasis.

7.2.1. PBK models for drug metabolism or bile acid homeostasis

A chemical-specific, class-specific or generic PBK model for drug metabolism

Physiologically based kinetic (PBK) modeling is used to simulate the kinetics of a compound in different organs using mathematical equations. In this thesis, drug PBK models were developed and used to predict the concentration of a drug in the liver after oral exposure to the drug. In a next step, the intrahepatic free concentration of the drug was used to predict its effect on hepatic bile acid efflux by coupling the drug PBK model to a bile acid PBK model (the bile acid PBK models are discussed in the next paragraph). The drug PBK models in the current work were a chemical-specific model for bosentan (Chapter 3) and generic PBK models for 15 selected reference drugs (Chapter 6). A chemical-specific model is developed based on a mechanistic understanding of the absorption, distribution, metabolism and excretion (ADME) characteristics of the chemical of interest and can include several chemical-specific processes, such as renal or biliary excretion. A generic PBK model describes the kinetic aspects for all drugs in a similar way with a limited amount of input parameters. The decision to develop a chemical-specific or generic PBK model depends on the confidence needed in the predictions and the available data and resources. Chemical-specific PBK models often require experimental determination of especially the kinetic parameters for uptake, efflux and metabolism using appropriate *in vitro* assays. Generic PBK models require less parameters and are less time- and resource-consuming to develop. Therefore, generic PBK models may be used for first, quick estimates of the concentration-time profile of a chemical in several tissues. It has been indicated that it is unlikely that a single generic PBK model can fulfil regulatory requirements for use in safety assessments given the broad chemical space that needs to be covered (Najjar et al., 2022). The results in Chapter 6 corroborate that generic PBK models have a decent predictive performance, with the maximal plasma concentration (C_{max}) for 13 out of 18 drugs predicted within 5-fold compared to the *in vivo* data, but also that the predictions need to be interpreted with caution, because the C_{max} of 5 drugs were >5-fold overpredicted. The C_{max} for 3 drugs was even >10-fold overpredicted and these were excluded from further simulations, resulting in a final dataset of 15 drugs used to assess their effects on hepatic bile acid efflux and accumulation. As with chemical specific PBK models, when using generic PBK models, validation with *in vivo* data still remains necessary to obtain sufficient confidence in the PBK predictions. This presents a drawback when moving to an animal-free risk assessment. Chemical-specific models are more suitable to achieve high confidence in the predictions, which is *e.g.* required within the regulatory framework for use in safety assessment (Paini et al., 2021).

Alternatively, chemical class-specific PBK models with a well-defined chemical applicability domains appear to offer a more feasible approach than chemical-specific PBK models for the application of PBK models within the regulatory framework for use in safety assessments (Najjar et al., 2022). Class-specific PBK models require experimental determination of kinetic parameters, but instead of establishing the parameter for each chemical within the class, the parameters can be assumed to be similar for all chemicals within that class, and read-across can be applied. The example presented in Chapter 6 of the thesis reveals that generic models with *in silico* and *in vitro* defined minimal parameter sets have reached a state-of-the art where they become of value in NAMs. It can be foreseen that with further development of class-specific models and further generation of proofs-of-principle the impact of PBK modeling based approaches in modern risk and safety assessment of chemicals will become even more dominant.

PBK models for bile acid homeostasis

The drug-induced effects on bile acid homeostasis were predicted by coupling the drug PBK models to bile acid PBK models (Chapter 3-6). In this section further improvements for the bile acid PBK models will be discussed. Developing a PBK model for an endogenous metabolite is even more challenging than developing a model for a drug or food-borne chemical. To reduce model complexity, the bile acid pool was lumped into one or four selected bile acids. This can be considered an oversimplification, because *in vivo* over 20 species of bile acids are known in humans (Garcia-Canaveras et al., 2012). Further extending the number of bile acids included in the PBK model might be necessary depending on the aim of the study. Conjugated bile acids are the most important to include when studying transporter-inhibition, as was done in the current thesis, because transport of these bile acids relies on carriers for their translocation over cell membranes (Aldini et al., 1996). When adverse effects of interest are related to secondary bile acids, the PBK models may need to include a more detailed description of secondary bile acid formation through microbial bile acid metabolism. A disbalance in the secondary bile acids may occur when chemicals affect the microbiome's composition and functionality (Murali et al., 2023). Elevated colonic concentrations of bile acids can increase intestinal permeability, induce oxidative stress and related damage to DNA and enhance cell proliferation. Accordingly, a disbalance in secondary bile acids can promote (gastrointestinal) carcinogenesis (Jia et al., 2018). Reduced intestinal integrity is related to diarrhea, bacterial overgrowth and inflammatory bowel disease (Marasco et al., 2022; Miele et al., 2009).

Another aspect to consider for further refinement of the currently developed PBK model for bile acid homeostasis is the regulation of bile acid homeostasis by dynamic feedback loops mediated by several nuclear receptors, including the farnesoid-X-receptor (FXR). Inclusion of these dynamic processes would improve the physiological relevance of the bile acid homeostasis predictions. For example, when hepatic bile acid levels are increased due to a drug-induced inhibition of efflux transporters, the hepatocyte will adapt by upregulation of the basolateral efflux transporters multidrug resistance protein 3/4 (MRP3/4) and downregulation of bile acid synthesis (Chai et al., 2012). Such an adaptation was also observed in the *in vitro* models used in Chapter 2 of the thesis where inhibition of BSEP mediated hepatic bile acid efflux from SCHHs and HepaRGs by bosentan and lopinavir resulted in reduced instead of increased cellular bile acid levels. Attempts have been made to

incorporate nuclear-receptor mediated processes in a bile acid PBK model, for example, FXR-mediated autoregulation of bile acid synthesis (Voronova et al., 2020). In this study some parameters, such as the bile acid concentration inducing 50% FXR activation, were estimated because these authors did not have experimental data for this parameter. In future research, FXR activation can be determined experimentally using a FXR luminescent reporter gene assay (Suzuki et al., 2006). In the PBK model the rate constants for bile acid synthesis may be adapted accordingly with a factor based on the reporter gene data and depending on the bile acid concentration in the tissue. Additional FXR-mediated processes, such as regulation of transporter expression in the intestine and liver, were not included (Voronova et al., 2020). These could be included by adapting the rate for hepatic bile acid efflux and intestinal absorption. Inclusion of these processes would improve the physiological relevance of a bile acid PBK model, but at the same time increase model complexity and introduce the need to fit more input parameters. Real-life physiological processes often involve multiple interacting pathways and variables, each of which may require its own parameterization. Extensive use of fitting to determine input parameters makes the PBK model less suitable for extrapolation to other scenarios. Finding the right balance between complexity of the model and representing physiological relevance remains challenging in the scope of a highly dynamic process such as bile acid homeostasis. Alternatively, advanced *in vitro* models based on microfluidics may offer a tool to study dynamic interactions between multiple organs. These models will be further discussed in 7.2.6.

Probabilistic modeling

The current PBK models did not consider interindividual differences in drug metabolism and considered individual differences in bile acid kinetics only to a limited extent. Literature data, however, indicated large interindividual differences in the plasma bile acid and drug concentrations (Chapter 3-6). These differences could be explained by interindividual variabilities in ADME parameters or anatomy, but also by differences in study design and/or analytical methods between the studies. Probabilistic modeling can be used to incorporate variability in the (kinetic) parameters and thus the PBK model predictions (Maertens et al., 2022). Often, Markov Chain Monte Carlo sampling techniques are used for probabilistic PBK models and these were also applied in Chapter 3. Instead of using fixed parameter values, Markov Chain Monte Carlo simulations randomly sample parameter values from their respective probability distributions in each iteration of the simulation. By including relevant probability distributions for *e.g.* kinetic parameters or body weight, the variability in for example the response toward a drug within the human population will be described taking the interindividual differences into account and safe external dose levels for e.g. the 95th percentile of the population can be determined, thereby protecting the sensitive individuals.

Several tools are available to incorporate anatomical variability in the PBK predictions. Software applications linked to population databases can generate anatomically correct virtual populations that can be used for the simulations. This option is available in commercial software such as PK-Sim®,[2] and Simcyp™,[3], but also in freely available software such as the web-based application PopGen (McNally et al., 2014; Willmann et al., 2007). Websites can be continuously updated and

[2] https://www.open-systems-pharmacology.org/
[3] https://www.certara.com/software/simcyp-pbpk/

improved, which can change the results when the simulations are repeated at another time point. Sometimes, freely available web-based servers are turned into commercial software later on. Commercial software is typically better documented, but the high costs hamper the wide use of these platforms in academia and smaller companies (Dulsat et al., 2023).

The observed *in vivo* variation in plasma drug and bile acid levels can be attributed to variability in the kinetic parameters, but quantifying variability using *in vitro* derived kinetic parameters is laborious. The sensitivity analysis that is commonly used in evaluation the performance of PBK models should be used to identify the parameters that have a strong influence on the model outcome and guide decision-making as to variability in which parameter(s) should be studied into more detail. After identifying the most influential parameter(s), the interindividual variation in only these selected influential parameters needs to be quantified. For example, if hepatic bioactivation is an influential parameter, hepatic metabolism could be obtained using liver microsomes from different donors (Ning et al., 2019). A probability distribution for hepatic metabolism can be derived from these data and incorporated in the PBK model to simulate the kinetic behavior in a given population. These evaluations should be done on a case-by-case basis to allow for population-based PBK predictions.

Underlying reasons for interindividual variability in bile acid kinetics were investigated into more detail in the current thesis. In the modeling studies of the present thesis the total bile acid pool size was scaled by a factor 0.5 or 1.5 (Chapter 3, 5 and 6). Given that the reported bile acid concentration in bile differed 2-fold between different studies (Sips et al., 2018), this scaling of the total bile acid pool is considered realistic. Yet, this factor does not include the distribution of the bile acid pool size in the population. In combination with other variables, a large bile acid pool may not in all cases result in increased susceptibility towards adverse health outcomes like cholestasis since other factors like for example BSEP abundance may turn out to be more dominant. Work described in this thesis showed the potential of PBK modeling to study the result of these interindividual differences on bile acid homeostasis. In Chapter 3, the effect of biological variabilities in kinetic parameters on an individual's susceptibility towards hepatic bile acid accumulation was shown by using BSEP abundance randomly drawn from a log-normal distribution derived from a meta-analysis of transporter abundances in liver tissue of healthy Caucasians (Burt et al., 2016). The approach revealed that individuals with low BSEP abundance are at higher risk of drug-induced cholestasis development, because of saturation of BSEP-mediated transport. This provides a proof-of-principle of the application of Markov Chain Monte Carlo modeling for modeling bile acid homeostasis. Yet, it is preferable to further extend the probabilistic modeling to other variables within the PBK model in order to unravel their contribution to the observed highly variable plasma bile acid levels between individuals. For example, a common genetic variant of OATP1A2 was associated with a delayed postprandial increase in plasma bile acids after administration of standardized meals in 72 healthy subjects (Fiamoncini et al., 2017). It might be of interest to incorporate interindividual differences in abundance of OATP1A2 or other transporters in the bile acid PBK model.

7.2.2. Use of in silico models to define PBK input parameters

In silico predictions are faster and cheaper compared to their *in vitro* counterparts. This section discusses computational *in silico* tools that can yield PBK input parameters without the need to

perform experiments. In Chapter 6 several *in vitro* and *in silico* approaches were compared for their predictive accuracy of the C_{max} of 18 reference drugs showing that the *in silico* tools performed well. Several *in silico* tools to predict clearance are commercially available, such as the ADMET predictor®,[4] or Simcyp™,[3], but the results of the present thesis corroborated that the free online tool pkCSM also provides good estimates (Pires et al., 2015). pkCSM is a freely available web-based server and relies on learning patterns between chemical structure, similarity and pharmacokinetic and safety properties to build predictive models that can be generalized to other compounds. pkCSM is trained using 18 000 compounds for metabolism and is widely applicable to small molecules. In Chapter 6, clearance data obtained from primary hepatocytes and predicted by the pkCSM tool were compared and yielded similar PBK predictions for C_{max} of the reference drugs. If any differences in the PBK predictions were observed, the *in silico* predicted clearance resulted in a higher C_{max} prediction. A higher C_{max} is less likely to present an underestimate of the *in vivo* C_{max} and thereby can be considered more conservative. Similarly, PBK simulations for C_{max} incorporating clearance obtained using primary hepatocytes or *in silico* predicted clearance by another *in silico* tool, *i.e.* the ADMET predictor®, resulted in comparable C_{max} predictions, and if any differences were observed with the *in vitro* hepatocyte data also for the ADMET predictor the *in silico* predictions were more conservative (Punt et al., 2022). In Chapter 6, also *in vitro* and *in silico* methods for the quantification of the fraction unbound were compared and led only occasionally to different results. The calculation method of Lobell and Sivarajah (2003) was used for the *in silico* prediction of the fraction unbound.

Despite the promising results obtained with the pkCSM tool and Lobell and Sivarajah's calculation method, care needs to be taken when applying *in silico* methods. *In silico* predictions are useful for quick first estimates, but when high confidence in results is required or the PBK model output is sensitive to these parameters, the *in silico* predictions should be confirmed with experimental data to reduce the uncertainty (OECD and Magdalini, 2021). Another approach to reduce the uncertainty in the *in silico* predictions is to accompany *in silico* predictions with read-across approaches. When the *in silico* predicted clearance for a chemical is very similar to the *in vitro* observed clearance from a structurally similar compound, confidence in the accuracy of the *in silico* prediction is increased. The R package High-throughput toxicokinetics (httk) provides a clear and searchable database with *in vitro* hepatic clearances and physicochemical parameters for many different drugs and chemicals, thereby facilitating read-across (Pearce et al., 2017).

7.2.3. Use of *in vitro* models to define PBK input parameters

The drug PBK models in Chapter 3 and 6 used different *in vitro* models to obtain kinetic parameters for hepatic metabolism, *i.e.* human liver microsomes or primary hepatocytes, respectively. In the bile acid PBK models several *in vitro* models were used to determine the inhibitory effect of the drugs on the intestinal or hepatic bile acid transport. Intestinal bile acid transport is governed via both passive diffusion and ASBT (Chiang, 2009). Subsequently, the bile acids are transported to the liver via the portal vein. Bile acid uptake into hepatocytes over the sinusoidal membrane is mediated by NTCP, and to a more limited extent by members of the OATP family (Chiang and Ferrell, 2022; Kouzuki et al.,

4 https://www.simulations-plus.com/software/admetpredictor/

1998). Subsequent secretion from the hepatocytes into the canalicular capillaries, feeding into the bile ducts, is mediated by BSEP (Jia et al., 2018). Alternatively, bile acids can be secreted to the systemic circulation by MRP3/4. MRP3/4 expression is low under healthy circumstances, but transporter expression is upregulated under cholestatic conditions (Chai et al., 2012). In this section, the available *in vitro* models to determine kinetic parameters for intestinal transport and hepatic metabolism and transport will be discussed. *In vitro* to *in vivo* scaling of the kinetic parameters will be discussed in section 7.2.4.

In vitro models for intestinal transport

For intestinal bile acid transport, the *in vitro* kinetic model used in the present thesis consisted of Caco-2 cells cultured on transwells (Chapter 4). The Caco-2 model is well established and widely used for routine testing of drug absorption (Sambuy et al., 2005). As indicated in Chapter 1, Caco-2 cells possess several transporters among which 112 SLC and 20 ABC transporters were identified in a proteome analysis (Olander et al., 2016). Caco-2 cells typically present an overall estimate of transport rate, incorporating apical ASBT-mediated uptake, intracellular trafficking and basolateral efflux. Thus an overall or apparent K_m was established in the current work, which is arguably more physiologically-relevant than defining PBK model parameters for the transport mediated by ASBT alone. Although ASBT mRNA expression has been shown in Caco-2 cells (Wang et al., 2022a; van der Mark et al., 2014), ASBT protein expression in Caco-2 cells was reported to be very low or even undetectable (Olander et al., 2016; van der Mark et al., 2014). The current results corroborated that ASBT is functionally present (Chapter 4), but for future studies it would be of interest to consider a model with quantifiable ASBT protein expression to facilitate scaling to the *in vivo* situation, as will be discussed in section 7.2.5.

ASBT-transfected cell lines provide an alternative with quantifiable ASBT protein expression and activity (Balakrishnan et al., 2005), but are not commercially available and thus require (in-house) expertise in transfecting cells. Other alternatives to study ASBT-mediated transport are primary intestinal epithelial cells or induced pluripotent stem cells (iPSCs). Primary intestinal epithelial cells are hard to obtain and have low viability in culture, but mimic the human *in vivo* situation well (Kauffman et al., 2013). iPSCs are obtained by differentiating pluripotent stem cells to intestinal cell lineages. All major epithelial cell lineages are present within the iPSC-derived intestinal organoids, including enterocytes, goblet cells, Paneth cells and enteroendocrine cells (Hou et al., 2022). For several transporters in iPSC-derived intestinal organoids the mRNA levels are higher than those in the human adult intestine, but ASBT mRNA was lower than that in the human adult intestine (Onozato et al., 2018). iPSCs are typically cultured in organoid formation, but this is unsuitable for transport studies when the organoids have an inside-out configuration (Schneeberger et al., 2020). An inside-out configuration means that the basolateral side is at the outside surface of an organoid. The chemical of interest thus has limited access to the apical surface inside the organoid. The iPSC-derived intestinal cells can be adapted to a transwell configuration to make the model suitable for transport studies (Kauffman et al., 2013; Grouls et al., 2022a). However, the intricate 3D structure of the organoids is largely lost when they are cultured on a transwell, and therefore, research has been conducted towards establishing organoids with an apical-out configuration (Kakni et al., 2022). The authors successfully showed that culturing iPSC-derived intestinal organoids in a suspension system rather

than the conventional way of imbedding in a hydrogel reversed the organoid polarity and achieved an apical-out configuration. In a later study, the authors showed that FITC-dextran and a fluorescent fatty acid analogue translocated from the culture medium to the lumen of the intestinal organoids, further supporting the suitability of this system for transport studies (Kakni et al., 2023).

A major difference between the *in vitro* intestinal systems and the *in vivo* situation is the absence or limited presence of a mucus layer so that the model poorly represents this aspect of the human *in vivo* situation (Busch et al., 2023; Hilgendorf et al., 2000). The mucus layer covering the intestinal epithelium is an important extra layer that might hamper the transport and lower the apparent affinity (higher $K_{m,app}$) for ASBT or any other transporter (Veider et al., 2023). In a study with Caco-2 cells this pitfall was alleviated by applying biosimilar mucus to the apical surface of the cells (Birch et al., 2018). The mucus layer reduced the permeation rate of hydrophobic drugs, while the permeation of hydrophilic drugs was largely unaffected. Alternatively, co-cultures containing Caco-2 cells and mucus-producing HT29-MTX cells can be established to better emulate the human *in vivo* mucus layer (Lock et al., 2018; Grouls et al., 2022b). For iPSC-derived organoids protocols are being developed to stimulate the production of mucus using a physiological flow or physical motions (Sontheimer-Phelps et al., 2020; Shin and Kim, 2023). Further considerations about substrate binding to mucus or other endogenous components, its effects on apparent transporter affinity and a potential solution will be discussed in section 7.2.4.

In vitro models for hepatic transport and/or metabolism

Three types of *in vitro* models can be used to study hepatic transport and/or metabolism, *i.e.* transfected systems (cell lines, oocytes, vesicles, supersomes), whole cells such as primary hepatocytes or subcellular fractions such as microsomes or S9 (Zamek-Gliszczynski et al., 2013; Sodhi and Benet, 2021). Metabolism is commonly studied using primary human hepatocytes (Chapter 6) or subcellular fractions such as microsomes or S9 (Chapter 3). Microsomes and S9 are most often used for a low tier screen, because they are robust, easy to use and cheap compared to primary hepatocytes. Microsomes and S9 are not suitable for studying transport (inhibition). In the present thesis transfected cell lines or membrane vesicles generated from transfected cells were used to determine PBK model parameters describing BSEP- and NTCP-mediated bile acid transport kinetics (Chapter 3 - 6). Alternatively, primary human hepatocytes could have been used to get an estimate of the overall bile acid transport (uptake, *de novo* synthesis and efflux). Primary hepatocytes have a physiologically relevant enzyme and transporter expression (Hart et al., 2010), and can be used to study both hepatic metabolism and transport (Louisse et al., 2020; Yoshikado et al., 2021). It can be considered an advantage for transport studies that primary hepatocytes perform *in situ* metabolism. This is especially relevant for drugs where the metabolite, and not the parent compound, is the active inhibitor. It is of interest to note that an assay with primary human hepatocytes resulted in a more potent inhibition (lower IC_{50} and K_i) than BSEP-membrane vesicles (Chapter 6). This is probably because drugs that inhibit BSEP, often also inhibit other uptake or efflux transporters. For example, troglitazone and bosentan inhibit BSEP, but also NTCP and MRP3/4 (Funk et al., 2001; Fattinger et al., 2001; Marion et al., 2007; Morgan et al., 2013). Thus, for transport inhibition studies, primary human hepatocytes are preferred over transfected cell lines, because they provide an all-inclusive estimate of

the inhibitory potency (K_i or IC_{50}), while for the estimation of kinetic transport parameters (V_{max} and K_m) of a specific transporter, a simple transfected cell system is desirable because it gives results for a single transporter.

Several alternative whole cell models have been developed to overcome the limited availability of primary hepatocytes. The hepatocellular carcinoma cell line HepaRG provides a physiologically relevant alternative to primary human hepatocytes (Le Vee et al., 2013). A recent study showed that prototypical cholestatic drugs inhibit bile acid efflux from HepaRG cells (Le Vee et al., 2022). Only two concentrations per drug were investigated in this study. Determination of a concentration-response curve will allow for the establishment of the potency and comparison to the potency found using primary hepatocytes.

Monolayers of iPSC-derived hepatocytes have many resemblances to primary human hepatocytes in morphology and toxicity assays (Lu et al., 2015; Sirenko et al., 2014) and might provide another alternative. iPSC-derived hepatocyte-like cells were found to form functional bile canaliculi and are capable of transporting a fluorescent dye (carboxy-2′,7′-dichlorofluorescein) (Qosa et al., 2021). Shortcomings of the iPSC-derived hepatocyte-like cells for measuring effects on hepatic bile acid efflux is the relatively low expression of BSEP compared to the level in primary hepatocytes (Sakai et al., 2019). 3D cultures are suggested as a potential solution to improve polarization and transporter expression of iPSC-derived hepatocytes (Sakai et al., 2019). Here, special attention should be paid to create outside-in configurations, which can be done using 3D scaffolds or a suspension-culture rather than embedding in a hydrogel (Fiorotto et al., 2023; Kakni et al., 2022). Furthermore, other steps in the differentiation protocol should be optimized to increase transporter expression and generate iPSC-derived hepatocyte-like cells suitable for studies on drug-induced effects on bile acid efflux.

7.2.4. Converting *in vitro* kinetic data to the *in vivo* situation

Scaling factors

To incorporate *in vitro* obtained kinetic data into a PBK model, scaling factors are needed for *in vitro* to *in vivo* extrapolation. The simplest method for *in vitro* to *in vivo* scaling of kinetic parameters is empirical scaling. The scaling factor that results in the closest fit to the *in vivo* data is determined by iterative PBK simulations with different values for the scaling factor (as was done for the rate constant for intestinal transport of GCA determined in a Caco-2 transport model in Chapter 4). However, for the use in NAMs and the development of human relevant models it is preferable to parametrize PBK models without the need for any *in vivo* data. Thus, a scaling factor based on mechanistic and/or theoretical considerations on the differences between the *in vitro* model and the *in vivo* situation is preferred. A physiological scaling factor is based on the number of cells or the membrane/total protein content in the relevant tissue enabling conversion of the data obtained using the respective cells or membrane/total protein content *in vitro*. Physiological scaling factors for conversion of *in vitro* V_{max} obtained from liver S9 or microsomal incubations to a V_{max} suitable for incorporation in a PBK model have been well-established (Pelkonen and Turpeinen, 2007). A physiological scaling factor based on mg protein/entire liver enables for the conversion of *in vitro* V_{max} in pmoles/min/mg protein to *in vivo* V_{max} expressed in µmoles/hr/entire liver. Similarly, a physiological scaling factor based on the total number of cells in the liver was proven successful for defining hepatic clearance in Chapter 6.

Clearly, this physiological scaling factor based on the number of cells or mg protein per tissue cannot be applied for kinetic transport data obtained with transfected cell lines, because their transporter expression differs substantially from the *in vivo* transporter expression, obviously causing differences in activity and corresponding V_{max} values. Therefore, the relative expression factor (REF) and relative activity factor (RAF) have been introduced to correct for differences in gene expression/protein abundance or activity between the *in vitro* model and the *in vivo* situation (Jamei et al., 2014). REF and RAF can also be used to correct for a decreased expression and/or activity of transporters or metabolizing enzymes upon culturing cells *in vitro,* which is typically observed with primary hepatocytes (Elaut et al., 2006). The REF and RAF approach for *in vitro* to *in vivo* extrapolation of transport or metabolism kinetics has been increasingly applied (Chan et al., 2019; Zou et al., 2013; Kumar et al., 2021).

The REF is based on relative expression or if possible, protein abundance in the cells of interest and in human primary tissue. It is preferable that these measurements are performed in the same lab to prevent technical study differences. Post-translational modifications may alter transport activity, but are not covered by a REF. The RAF offers a potential solution to this problem. For establishment of a RAF, not only *in vitro* activity but also *in vivo* activity is needed and the latter can be determined based on the quantification of the drug of interest in the organs *in vivo*, using *e.g.* positron emission tomography (PET) imaging of radiolabeled drugs (Storelli et al., 2022). PET imaging is expensive and not all drugs can be radiolabeled, so this cannot be routinely performed. PET imaging can be used to obtain a universal RAF based on a selected number of reference drugs. Primary hepatocytes are often used as a surrogate model for quantification of the kinetic parameters for *in vivo* transport and metabolism (Izumi et al., 2018; Mitra et al., 2018; Chan et al., 2019). Determination of the RAF value for conversion of the data obtained using a transfected model system to data in hepatocytes allows subsequent use of the physiological scaling factor to convert the data to the *in vivo* situation. To facilitate future use of these REF and RAF scaling factors more proofs-of-principle should be generated. The obtained *in vitro* kinetic parameters should be scaled to the *in vivo* situation based on the REF and/or RAF value, and the predicted and observed concentration-time profiles need to be compared. Upon gaining accurate predictions for sufficient chemicals and transporters, the REF and/or RAF can be used to predict concentration-time profiles for chemicals for which no *in vivo* data are available.

In the current work BSEP- and NTCP-mediated transport were scaled based on a REF value, but intestinal transport was scaled empirically (Chapter 4). Even though the plasma bile acid concentration-time profiles in plasma were accurately predicted, this does not necessarily mean that the application of the REF values gave accurate estimates of the *in vivo* transport. Any flaws might have been inherently corrected by empirical scaling of intestinal transport. An important underlying assumption in the scaling approaches applied in the present thesis is that the apparent affinity ($K_{m,app}$) is identical *in vitro* and *in vivo*. This is however not always the case due to differences between the nominal and free concentration and this will be discussed in some more detail in the following section.

Differences between nominal and free concentration

According to the "free drug hypothesis" only free, unbound drug is available to interact with biological targets. A drug or chemical bound to macromolecules is not available for transport, resulting in a lower apparent affinity (higher $K_{m,app}$), since higher nominal concentrations will be required to reach saturation of the transporter or metabolic enzyme. The important role of protein binding is underscored by the finding that OATP-mediated hepatic uptake of rosuvastatin can be well predicted upon using transfected cells and a REF scaling factor, but only when plasma proteins were included in the *in vitro* studies (Kumar et al., 2021).

Differences between the nominal and free concentration *in vitro* might be due to binding to medium constituents and/or cell culture materials (Kramer et al., 2015). Especially lipophilic drugs are likely to bind to the cell culture materials, thereby reducing the free concentration (Dimitrijevic et al., 2022). Mass balance recovery tests should be routinely performed to investigate this. For example, when 500 pmoles of a chemical are added to the culture medium, at the end of the experiment, 500 pmoles should be recovered from the culture medium and the cells combined. When a substantial (typically >20%) amount of the chemical is missing, this indicates that the chemical has bound to the culture material and corrections are necessary. Chemical distribution models provide computational tools to perform these corrections (Proenca et al., 2021). Yet, when the chemical does not bind to the plastic, this does not necessarily mean that the drug is available to the cell. Some drugs or chemicals bind non-specifically to the cell surface and/or their transport is hampered by a hydrodynamic barrier called the unstirred water layer. Computational methods to correct for these processes were applied in Chapter 4 and 6 (Kilford et al., 2008; Balakrishnan et al., 2007).

It is especially challenging to determine the free concentration that reaches the enterocytes *in vivo* and this has sofar received limited research interest in PBK modeling. It is speculated that the large difference between the *in vitro* $K_{m,app}$ and *in vivo* $K_{m,app}$ of taurocholic acid transport in ASBT-transfected oocytes, Caco-2 cells, ASBT-transfected cells and a human perfusion can be attributed to differences in the free concentration and/or passive transport (Krag and Phillips, 1974; Zhu et al., 2021). Potentially, the *in vivo* $K_{m,app}$ was higher than the *in vitro* $K_{m,app}$ because of the presence of microbes, food components and/or the mucus layer *in vivo* but not *in vitro*. Chemicals have to diffuse over the mucus layer to reach the enterocyte. When the mucus layer tends to bind the chemical this process will increase the $K_{m,app}$, as was also discussed in section 7.2.3.. To estimate the free concentration that reaches the enterocytes *in vivo* and delineate the true K_m, the fraction unbound in caecum or other intestinal contents and the passive diffusion over the intestine *in vivo*, including the mucus layer, have to be determined. Precision cut intestinal slices can be used as a surrogate to study passive intestinal transport *in vivo* by performing experiments at 4˚C, although it is technically challenging to work with precision cut intestinal slices due to their limited availability and short life span. Human precision cut intestinal slices established a $K_{m,app}$ of 140 µM for taurocholic acid (Li et al., 2018), which is already closer to the data obtained by *in vivo* perfusion studies (600 µM) than the *in vitro* values obtained from Caco-2 cells (22.4 µM) (Chapter 4). These findings indicate that the mucus layer and/or differences in cell membrane permeability are partially responsible for the discrepancies between *in vivo* and *in vitro* $K_{m,app}$. Further discrepancies can be attributed to binding to components in the intestinal lumen and should be studied in the future. It is proposed that a better understanding

of the free available concentrations, both *in vitro* and *in vivo*, will improve the concordance between *in vitro* and *in vivo* $K_{m,app}$.

Chemical distribution within tissues

An important consideration in using PBK modeling to convert *in vitro* data to the *in vivo* situation is the chemical distribution over the liver and how that influences the concentration available for transport and metabolism. In PBK models, tissues/organs are generally represented as perfusion-limited, well-stirred models. This means that it is assumed that the chemical is homogenously distributed over the tissues/organs (Rietjens et al., 2011). However, when a chemical is taken up by a carrier, the membrane permeability, and not the perfusion, is the rate-limiting factor. This implies that the conventional tissue:plasma partition coefficient is not suitable to describe transport and distribution to a permeability-limited organ and specific kinetic parameters for the transport should be determined. The guidance document of the Organisation for Economic Cooperation and Development (OECD) on the characterization, validation and reporting of Physiologically Based Kinetic (PBK) models for regulatory purposes states that it is necessary to use a permeability-limited organ structure to mechanistically account for the action of transporters in PBK models (OECD and Magdalini, 2021). In line with this recommendation, a permeability-limited model was constructed in order to be able to incorporate hepatic active uptake of bile acids in the PBK model (Chapter 4). To this end, the liver was divided in an extra- and intracellular compartment. The extracellular compartment is perfused, and carriers are responsible for the transport of the drug from the extracellular to the intracellular compartment (Jamei et al., 2014). Even more detailed compartmentalized liver models are available that might even better recapitulate the gradual decrease in tissue concentrations along the organ (*e.g.* from periportal to perivenous regions of the liver), such as the parallel tube model or a 5-compartment liver model (Pang et al., 2019). Increasing model complexity is only favorable when it increases predictivity and does not introduce too many uncertainties.

7.2.5. Cholestasis adverse outcome pathway (AOP)

In recent years numerous adverse outcome pathways (AOPs) have been developed as a conceptual framework to support the construction of non-animal based testing approaches for chemical safety assessment. AOPs consist of a molecular initiating event (MIE), one or more key event(s) (KEs) and an adverse outcome (AO), which represent biological effects at different levels of biological organization. The general principle of AOPs is that a limited set of KEs and Key Event Relationships (KERs) can sufficiently describe and predict the interaction of a toxicant on the biological pathway resulting in an adverse outcome (Villeneuve et al., 2014).

Cholestasis refers to an impairment of bile acid excretion causing accumulation of bile acids in the liver and/or the systemic circulation (Noor, 2015). At the molecular level, inhibition of BSEP-mediated transport is considered the MIE of the AOP for cholestasis (Vinken et al., 2013). Several nuclear receptors, especially the constitutive androstane receptor (CAR), the pregnane-X-receptor (PXR), and the FXR are activated as an adaptive response to counteract bile acid accumulation (Vinken et al., 2013). At the same time, deteriorative responses such as mitochondrial dysfunction, oxidative stress and inflammation take place. These deteriorative responses lead to apoptosis, necrosis and

ultimately cholestasis. The cholestasis AOP was already described and visualized in Figure 3 of Chapter 1 of this thesis.

In Chapter 6, the aim was to predict cholestasis as a result of bile acid efflux inhibition by therapeutic drugs. The kinetic data for inhibition of hepatic bile acid efflux were derived from literature where the IC_{50} for inhibition of bile acid efflux was quantified in a short-term assay with primary human hepatocytes (Zhang et al., 2016). The assay was not specific to BSEP-inhibition, but transporter inhibition in general. This is in line with the more recent insights on cholestasis that also inhibition of other transporters than BSEP can lead to cholestasis (Gijbels et al., 2020). Using generic PBK models, the intrahepatic drug concentrations were derived. These were subsequently used to predict the drug's effect on hepatic bile acid efflux and bile acid accumulation. The PBK modeling approach led to true positive predictions for cyclosporine, ritonavir and ketoconazole, but false negative predictions for chlorpromazine, atorvastatin and glimepiride. A literature search indicated that the latter compounds induce cholestasis through other mechanisms than inhibition of (BSEP-mediated) hepatic bile acid efflux (see Chapter 6 for references). While the approach provided a proof-of-principle of an animal-free PBK model to bridge the gap between *in vitro* potency to inhibit hepatic bile acid efflux and *in vivo* cholestasis risk, it also clearly indicated that other MIEs and/or KEs need to be considered for a complete risk assessment of cholestasis. Here, these MIEs and NAMs to study them will be discussed in some more detail. These additional MIEs for AOPs leading to cholestasis include hepatocellular changes and bile canalicular changes (Gijbels et al., 2019).

Cellular changes in response to chemical-exposure can be studied at mRNA levels using sequencing. Sequencing aids the cholestasis hazard assessment when biomarker genes have been identified. A recent study compared the transcriptomic profiles of HepG2 cells exposed to nine cholestatic and nine non-cholestatic drugs. Using machine learning approaches, 13 genes were identified that were up or downregulated under cholestatic conditions. Importantly, most of these genes fulfill a biological function that overlaps with KEs that play a role in the development of cholestasis. 9 Of these 13 genes were involved in one or more KEs, *i.e.* bile acid synthesis, bile flow disruption, oxidative stress, inflammation, endoplasmic reticulum stress and apoptosis. Two genes related to the adaptive response to counteract hepatic bile acid accumulation were elevated (*i.e. TSKU* and *ALAS1).* The functionality of the remaining two genes is less well understood, but their putative functions correlate with bile flow disruption and autophagy (Jiang et al., 2023). Transcriptomics analysis is useful for qualitative hazard identification and elucidating which KEs are involved, but for risk assessment, the KEs, and especially the KE affected at the lowest dose levels, need to be investigated in a quantitative way. In a weight-of-evidence approach, transcriptomic profiling can inform the further steps as for what endpoint a quantitative *in vitro* concentration-response experiment should be performed. A concentration-response curve can be used to determine the benchmark dose (BMD or BMDL) as the point of departure (PoD) for risk assessments.

The MIE of hepatocellular changes leading to cholestasis can be quantified through various relatively simple assays, such as lactate dehydrogenase (LDH) or glucose 6-phosphate dehydrogenase (G6PD) assays. These assays provide no insight in the mode of action underlying the toxicity and are late markers of toxicity. Therefore, the drug-induced cholestasis (DIC) assay has been proposed to test the hepatocyte functionality in the presence of potentially cholestatic drugs. Briefly, primary human

hepatocytes or HepaRG cells are exposed to test compounds in the absence or presence of a physiologically relevant mixture of bile acids. Urea secretion or cell viability is measured in co-exposure (test compound and bile acids) and just the test compound. The ratio between cell viability or urea secretion under these two conditions is calculated. In case a cholestatic compound is present, bile acids from the medium will accumulate in the cells and this results in reduced urea secretion, and ultimately a reduction of cell viability. The ratio in cell viability or urea secretion in the test compound + bile acids / test compound will thus decrease when a compound is cholestatic. A ratio below the cut-off value of 0.78 can be used to flag for increased cholestasis risk. The cut-off value is chosen based on experimental data and has no mechanistic basis (Van Brantegem et al., 2020). After optimizing the cut-off values, the assay using primary human hepatocytes resulted in 83% sensitivity and 67% specificity. The assay was initially developed for primary human hepatocytes (Hendriks et al., 2016; Oorts et al., 2016) and has been recently adapted to HepaRG cells (Gijbels et al., 2020). In Chapter 2, HepaRG cells were shown to have human-relevant expression of genes related to bile acid homeostasis and synthesized and secreted a bile acid profile similar to the human situation. A major advantage of HepaRG cells over primary hepatocytes is that they are readily available and they have less batch-to-batch variability, which makes the assay suitable for high-throughput studies.

Bile canalicular changes represent another MIE in the cholestasis AOPs. Cholestatic drugs can either result in early constriction or dilation of the canalicular lumen. The techniques to study bile canalicular changes are less well defined than those for hepatocellular changes. Primary human hepatocytes cultured in a sandwich-configuration and HepaRG cells are suitable *in vitro* models, because they polarize and have functional bile canaliculi (Rowe et al., 2013; Le Vee et al., 2013). Alternatively, intrahepatic cholangiocyte organoids (ICO) can be used to study chemical-induced effects on the bile canaliculae. ICOs are derived from cholangiocytes from human liver biopsies and are considered bipotential (Huch et al., 2015). In Chapter 2, these ICOs were differentiated towards hepatocyte-like cells, but they can also be differentiated towards mature cholangiocyte-like cells (Chen et al., 2018). A recent study showed that ICOs can be cultured on hollow-fiber membranes to generate 3D bile duct structures. Here, they showed several key characteristics of cholangiocytes, such as P-glycoprotein mediated transport in a polarized fashion and FXR-dependent functions (Wang et al., 2022b). Microscopic time-lapse imaging can be used to assess morphological changes in the bile canaliculi (Burbank et al., 2016). Manually analyzing these data is laborious and prone to human errors. Automated algorithms able of identifying the canalicular space and quantifying its surface at different timepoints should be developed. Automated algorithms make the assessment of dynamic bile canalicular changes more attainable on a routine-basis.

7.2.6. The relevance of bile acids for adverse outcomes other than cholestasis

The current thesis focused primarily on cholestasis, which is a relatively well-understood pathology, as is illustrated by the availability of an AOP (aopwiki.org). Bile acids are involved in several physiological functions, including an altered nuclear receptor-mediated signaling, immune responses, intestinal integrity and/or microbiome's composition and functionality (Jia et al., 2018). A disruption of bile acid homeostasis is implicated in various other pathologies, including liver diseases such as metabolic associated fatty liver disease (MAFLD) and hepatocellular and cholangiocellular carcinoma, but also

diseases that affect the intestine such as inflammatory bowel disease (Fuchs and Trauner, 2022). This section discusses the role of a disruption of bile acid homeostasis in adverse outcomes other than cholestasis, using MAFLD as an example, and potential models to study these adverse outcomes.

MAFLD patients have a different plasma bile acid pool compared to healthy individuals (Puri et al., 2018) and several processes regulated by bile acids are disrupted in MAFLD (Rodriguez-Duque et al., 2023; Jia et al., 2018). The following paragraph will further explain what alterations to the bile acid pool are observed in MAFLD and how these changes relate to MAFLD pathology. MAFLD disease progression and fibrosis state is related to increased ratios of primary:secondary bile acids and conjugated:unconjugated bile acids in plasma (Puri et al., 2018; Jahn and Geier, 2018). Increased concentrations of conjugated cholic acid species and species derived from DCA in serum is associated with liver fibrosis (Puri et al., 2018). Given that the gut microbiome is responsible for the conversion of primary bile acids into secondary bile acids, such as DCA, it was hypothesized that the microbiome played a crucial role in MAFLD progression (Smirnova et al., 2022). In a follow-up study, the aim was to link the observed differences in bile acid profile associated with increasing MAFLD disease severity to the microbiome's composition. 16S rRNA sequencing elucidated a decreased bacterial diversity with increasing disease severity. Specifically, *Bacteroidetes* and several genera of Lachnospiraceae family containing the ability to produce DCA increased with increasing disease severity, whereas the abundance of several potentially beneficial microbes decreased (Smirnova et al., 2022). So, patients with MAFLD exhibit an altered microbiome's composition that can be linked to an altered microbiome's functionality and bile acid profile. The aforementioned changes in the bile acid profile lead to a more hydrophobic bile acid pool, which is inversely related to FXR agonism (Cai et al., 2022). Through a reduced FXR activity, alterations in lipid and glucose metabolism and inflammation might occur, which are all involved in MAFLD pathology. Furthermore, the microbiome is implicated in regulating gut motility and gut permeability. Increased gut permeability enhances translocation of toxicants to the liver and is a risk factor for liver injury and MAFLD (Cani et al., 2007).

To predict the development of MAFLD or other adverse outcomes related to a disturbed bile acid homeostasis upon chemical exposure, a system that captures the dynamic crosstalk between gut epithelium, gut microbiome and liver should be established (see also section 7.2.1.). In doing so AOPs may provide a useful approach to identify MIEs, KEs and KERs leading to the adverse outcome. Within this context, NAMs can provide useful tools to gain mechanistic insights in disease development and establishment of KEs. Advanced *in vitro* models are needed to capture the multidirectional interactions between intestinal epithelium, liver, and gut microbiome in a human relevant situation. Organ-on-chip (OoC) devices can be used to couple chambers with cells recapitulating different organs based on microfluidics. Several OoC platforms are available that allow the connection of two different organs, *e.g.* gut epithelium and liver (Yang et al., 2023). Given that the microbiome fulfils crucial dynamic processes in the bile acid homeostasis, the microbiome should be included in these investigations. Incorporating the microbiome in a OoC platform is challenging, because of the opposite needs of mammalian cells and the microbiome in terms of oxygen supply which requires advanced culturing techniques (Jalili-Firoozinezhad et al., 2019). Yet, *in vitro* microfluidic devices exist that connect the intestinal epithelium and the microbiome, *e.g.* the human-microbial crosstalk model (HuMiX) or Dynamic42 Biochip platform (Shah et al., 2016; Maurer et al., 2019). A recent study

introduced neuronal cells in the HuMiX model and showed that this allowed for a co-culture of two types of mammalian cells and bacterial cells. The cell types are separated by semi-permeable membranes, but can still communicate with each other through soluble factors (Sedrani et al., 2023). These devices can then be used to unravel the complex interplay along the gut-liver axis in the onset of several diseases, establish causal KEs and generate AOPs. Future efforts should be directed towards incorporating the intestinal epithelium, gut microbiome and liver in the same microfluidics device, preferably also incorporating intestinal and hepatic immune cells (Lucchetti et al., 2021). Upon development of an AOP and elucidating the relevant dynamic processes, these dynamic processes could be incorporated in the bile acid PBK model to define a so-called physiologically based dynamic (PBD) model. To this end, a quantitative understanding of what magnitude and/or duration of change in the upstream KE is needed to evoke some magnitude of change in the downstream KE is required (OECD, 2017). A PBD model will aid to study the effects of chemicals on both kinetic and dynamic processes involved in bile acid homeostasis leading to *e.g.* MAFLD in a quantitative way.

7.2.7. Moving towards an animal-free risk assessment for cholestasis

As discussed in the previous sections a large number of NAM-based tools is available to study the MIEs and KEs involved in cholestasis. But how can we move from an animal-centered risk assessment towards a mechanistic human physiology NAM-based risk assessment for cholestasis? What do we need to gain sufficient trust in the predictive reliability of an animal-free risk assessment for cholestasis? Toxicologists often consider the lack of organismal complexity and toxicokinetic context as major limitations of a NAM-based risk assessment. The current thesis provides a proof-of-principle for the use of PBK modeling to incorporate toxicokinetic context into a NAM-based risk assessment for cholestasis that results from inhibition of hepatic bile acid transport and subsequent hepatic bile acid accumulation (Chapter 6). Data from an *in vitro* model alone defining the IC_{50} or K_i for inhibition of bile acid transport in an assay with primary hepatocytes was not able to adequately predict hepatic bile acid accumulation for the selected cholestatic compounds. Combining these data with outcomes of the PBK model resulted in the parameter AUC above the K_i that better predicted the cholestasis risk. Some drugs were identified as false-negative for cholestasis, but this can be explained as they cause cholestasis through other MIEs (hepatocellular or canalicular changes) and/or that the therapeutic dose levels are low enough to not result in intrahepatic concentrations that reach the K_i for inhibition of bile acid transport. These findings stress that a battery of *in vitro* tests combined with PBK modeling should be included to study the other dynamic MIEs/KEs. In order to predict a PoD for risk assessment it is important to establish a quantitative understanding between the MIEs/KEs leading to cholestasis. The focus should be on the human-relevance of the selected *in vitro* tests and ensuring that changes in the critical and most sensitive MIE/KE can be detected. The approach should gain enough information to confidently assess the likelihood of an adverse effect in humans rather than full coverage of the AOP (Schmeisser et al., 2023). It is crucial to realize that the default of animal data is also highly variable and not per se predictive of human toxicity (Pham et al., 2020; Olson et al., 2000). The research community, industry and risk assessors should strive to protect human health, not to predict animal toxicity.

7.3 Conclusion

The current thesis combined human cell based *in vitro* models and PBK models to better understand and predict drug-induced disruption of bile acid homeostasis with emphasis on cholestasis. PBK models describing the synthesis, distribution and excretion of bile acids were developed. Given that carrier-mediated processes are crucial for bile acid homeostasis, these processes were incorporated in the PBK models. The PBK modeling approach, combining drug and bile acid PBK models, was shown to enable quantitative prediction of the alterations in bile acid homeostasis upon drug-exposure. Transporter inhibition is only one of the MIEs in the cholestasis AOP, and future research has to elucidate which other MIEs/KEs should be studied and what would be adequate assays to do so. HepaRGs and SCHHs were shown in the present thesis to provide suitable cell models to study MIEs/KEs in AOPs for cholestasis, because they were shown to be able to emulate the liver functionality to synthesize and secrete bile acids, and have functional bile canaliculi. Future efforts should be directed towards a better understanding of the drug-induced dynamic changes in bile acid homeostasis, their health consequences and the use of NAMs to study these processes aiming at replacement, reduction and refinement (3Rs) of animal experimentation.

References

Aldini, R., Roda, A., Montagnani, M. et al. (1996). Relationship between structure and intestinal absorption of bile acids with a steroid or side-chain modification. *Steroids 61*, 590-597. doi:10.1016/s0039-128x(96)00119-5

Arab, J. P., Karpen, S. J., Dawson, P. A. et al. (2017). Bile acids and nonalcoholic fatty liver disease: Molecular insights and therapeutic perspectives. *Hepatology 65*, 350-362. doi:10.1002/hep.28709

Balakrishnan, A., Sussman, D. J. and Polli, J. E. (2005). Development of stably transfected monolayer overexpressing the human apical sodium-dependent bile acid transporter (hasbt). *Pharm Res 22*, 1269-1280. doi:10.1007/s11095-005-5274-8

Balakrishnan, A., Hussainzada, N., Gonzalez, P. et al. (2007). Bias in estimation of transporter kinetic parameters from overexpression systems: Interplay of transporter expression level and substrate affinity. *J Pharmacol Exp Ther 320*, 133-144. doi:10.1124/jpet.106.107433

Bathena, S. P., Mukherjee, S., Olivera, M. et al. (2013). The profile of bile acids and their sulfate metabolites in human urine and serum. *J Chromatogr B Analyt Technol Biomed Life Sci 942-943*, 53-62. doi:10.1016/j.jchromb.2013.10.019

Birch, D., Diedrichsen, R. G., Christophersen, P. C. et al. (2018). Evaluation of drug permeation under fed state conditions using mucus-covered caco-2 cell epithelium. *Eur J Pharm Sci 118*, 144-153. doi:10.1016/j.ejps.2018.02.032

Burbank, M. G., Burban, A., Sharanek, A. et al. (2016). Early alterations of bile canaliculi dynamics and the rho kinase/myosin light chain kinase pathway are characteristics of drug-induced intrahepatic cholestasis. *Drug Metab Dispos 44*, 1780-1793. doi:10.1124/dmd.116.071373

Burt, H. J., Riedmaier, A. E., Harwood, M. D. et al. (2016). Abundance of hepatic transporters in caucasians: A meta-analysis. *Drug Metab Dispos 44*, 1550-1561. doi:10.1124/dmd.116.071183

Busch, M., Brouwer, H., Aalderink, G. et al. (2023). Investigating nanoplastics toxicity using advanced stem cell-based intestinal and lung in vitro models. *Front Toxicol 5*, 1112212. doi:10.3389/ftox.2023.1112212

Cai, J., Rimal, B., Jiang, C. et al. (2022). Bile acid metabolism and signaling, the microbiota, and metabolic disease. *Pharmacol Ther 237*, 108238. doi:10.1016/j.pharmthera.2022.108238

Cani, P. D., Amar, J., Iglesias, M. A. et al. (2007). Metabolic endotoxemia initiates obesity and insulin resistance. *Diabetes 56*, 1761-1772. doi:10.2337/db06-1491

Chai, J., He, Y., Cai, S.-Y. et al. (2012). Elevated hepatic mrp3/abcc3 expression in human obstructive cholestasis is mediated through tnfα and jnk/sapk signaling pathway. *Hepatology (Baltimore, Md.) 55*, 1485.

Chan, J. C., Tan, S. P., Upton, Z. et al. (2019). Bottom-up physiologically-based biokinetic modelling as an alternative to animal testing. *ALTEX-Alternatives to animal experimentation 36*, 597-612.

Chen, C., Jochems, P. G. M., Salz, L. et al. (2018). Bioengineered bile ducts recapitulate key cholangiocyte functions. *Biofabrication 10*, 034103. doi:10.1088/1758-5090/aac8fd

Chiang, J. Y. (2009). Bile acids: Regulation of synthesis. *J Lipid Res 50*, 1955-1966. doi:10.1194/jlr.R900010-JLR200

Chiang, J. Y. L. and Ferrell, J. M. (2022). Discovery of farnesoid x receptor and its role in bile acid metabolism. *Mol Cell Endocrinol 548*, 111618. doi:10.1016/j.mce.2022.111618

Dawson, S., Stahl, S., Paul, N. et al. (2012). In vitro inhibition of the bile salt export pump correlates with risk of cholestatic drug-induced liver injury in humans. *Drug Metab Dispos 40*, 130-138. doi:10.1124/dmd.111.040758

Dimitrijevic, D., Fabian, E., Nicol, B. et al. (2022). Toward realistic dosimetry in vitro: Determining effective concentrations of test substances in cell culture and their prediction by an in silico mass balance model. *Chemical Research in Toxicology 35*, 1962-1973.

Dulsat, J., Lopez-Nieto, B., Estrada-Tejedor, R. et al. (2023). Evaluation of free online admet tools for academic or small biotech environments. *Molecules 28*, 776. doi:10.3390/molecules28020776

Elaut, G., Henkens, T., Papeleu, P. et al. (2006). Molecular mechanisms underlying the dedifferentiation process of isolated hepatocytes and their cultures. *Current drug metabolism 7*, 629-660.

Fattinger, K., Funk, C., Pantze, M. et al. (2001). The endothelin antagonist bosentan inhibits the canalicular bile salt export pump: A potential mechanism for hepatic adverse reactions. *Clin Pharmacol Ther 69*, 223-231. doi:10.1067/mcp.2001.114667

Fiamoncini, J., Yiorkas, A. M., Gedrich, K. et al. (2017). Determinants of postprandial plasma bile acid kinetics in human volunteers. *Am J Physiol Gastrointest Liver Physiol 313*, G300-G312. doi:10.1152/ajpgi.00157.2017

Fiorotto, R., Mariotti, V., Taleb, S. A. et al. (2023). Cell-matrix interactions control biliary organoid polarity, architecture, and differentiation. *Hepatol Commun 7*, e0094. doi:10.1097/HC9.0000000000000094

Fuchs, C. D. and Trauner, M. (2022). Role of bile acids and their receptors in gastrointestinal and hepatic pathophysiology. *Nat Rev Gastroenterol Hepatol 19*, 432-450. doi:10.1038/s41575-021-00566-7

Funk, C., Pantze, M., Jehle, L. et al. (2001). Troglitazone-induced intrahepatic cholestasis by an interference with the hepatobiliary export of bile acids in male and female rats. Correlation with the gender difference in troglitazone sulfate formation and the inhibition of the canalicular bile salt export pump (bsep) by troglitazone and troglitazone sulfate. *Toxicology 167*, 83-98. doi:10.1016/s0300-483x(01)00460-7

Garcia-Canaveras, J. C., Donato, M. T., Castell, J. V. et al. (2012). Targeted profiling of circulating and hepatic bile acids in human, mouse, and rat using a uplc-mrm-ms-validated method. *J Lipid Res 53*, 2231-2241. doi:10.1194/jlr.D028803

Gijbels, E., Vilas-Boas, V., Deferm, N. et al. (2019). Mechanisms and in vitro models of drug-induced cholestasis. *Arch Toxicol 93*, 1169-1186. doi:10.1007/s00204-019-02437-2

Gijbels, E., Vilas-Boas, V., Annaert, P. et al. (2020). Robustness testing and optimization of an adverse outcome pathway on cholestatic liver injury. *Arch Toxicol 94*, 1151-1172. doi:10.1007/s00204-020-02691-9

Grouls, M., Janssen, A. W., Duivenvoorde, L. P. et al. (2022a). Differential gene expression in ipsc-derived human intestinal epithelial cell layers following exposure to two concentrations of butyrate, propionate and acetate. *Scientific Reports 12*, 13988.

Grouls, M., van der Zande, M., de Haan, L. et al. (2022b). Responses of increasingly complex intestinal epithelium in vitro models to bacterial toll-like receptor agonists. *Toxicology in Vitro 79*, 105280.

Hafey, M. J., Houle, R., Tanis, K. Q. et al. (2020). A two-tiered in vitro approach to de-risk drug candidates for potential bile salt export pump inhibition liabilities in drug discovery. *Drug Metab Dispos 48*, 1147-1160. doi:10.1124/dmd.120.000086

Hart, S. N., Li, Y., Nakamoto, K. et al. (2010). A comparison of whole genome gene expression profiles of heparg cells and hepg2 cells to primary human hepatocytes and human liver tissues. *Drug Metab Dispos 38*, 988-994. doi:10.1124/dmd.109.031831

Hendriks, D. F., Fredriksson Puigvert, L., Messner, S. et al. (2016). Hepatic 3d spheroid models for the detection and study of compounds with cholestatic liability. *Sci Rep 6*, 35434. doi:10.1038/srep35434

Hilgendorf, C., Spahn-Langguth, H., Regardh, C. G. et al. (2000). Caco-2 versus caco-2/ht29-mtx co-cultured cell lines: Permeabilities via diffusion, inside- and outside-directed carrier-mediated transport. *J Pharm Sci 89*, 63-75. doi:10.1002/(SICI)1520-6017(200001)89:1<63::AID-JPS7>3.0.CO;2-6

Hou, Z., Meng, R., Chen, G. et al. (2022). Distinct accumulation of nanoplastics in human intestinal organoids. *Sci Total Environ 838*, 155811. doi:10.1016/j.scitotenv.2022.155811

Huch, M., Gehart, H., van Boxtel, R. et al. (2015). Long-term culture of genome-stable bipotent stem cells from adult human liver. *Cell 160*, 299-312. doi:10.1016/j.cell.2014.11.050

Izumi, S., Nozaki, Y., Kusuhara, H. et al. (2018). Relative activity factor (raf)-based scaling of uptake clearance mediated by organic anion transporting polypeptide (oatp) 1b1 and oatp1b3 in human hepatocytes. *Mol Pharm 15*, 2277-2288. doi:10.1021/acs.molpharmaceut.8b00138

Jahn, D. and Geier, A. (2018). Bile acids in nonalcoholic steatohepatitis: Pathophysiological driving force or innocent bystanders? *Hepatology 67*, 464-466. doi:10.1002/hep.29543

Jalili-Firoozinezhad, S., Gazzaniga, F. S., Calamari, E. L. et al. (2019). A complex human gut microbiome cultured in an anaerobic intestine-on-a-chip. *Nat Biomed Eng 3*, 520-531. doi:10.1038/s41551-019-0397-0

Jamei, M., Bajot, F., Neuhoff, S. et al. (2014). A mechanistic framework for in vitro-in vivo extrapolation of liver membrane transporters: Prediction of drug-drug interaction between rosuvastatin and cyclosporine. *Clin Pharmacokinet 53*, 73-87. doi:10.1007/s40262-013-0097-y

Jia, W., Xie, G. and Jia, W. (2018). Bile acid-microbiota crosstalk in gastrointestinal inflammation and carcinogenesis. *Nat Rev Gastroenterol Hepatol 15*, 111-128. doi:10.1038/nrgastro.2017.119

Jiang, J., van Ertvelde, J., Ertaylan, G. et al. (2023). Unraveling the mechanisms underlying drug-induced cholestatic liver injury: Identifying key genes using machine learning techniques on human in vitro data sets. *Arch Toxicol 97*, 2969-2981. doi:10.1007/s00204-023-03583-4

Kakni, P., Lopez-Iglesias, C., Truckenmuller, R. et al. (2022). Reversing epithelial polarity in pluripotent stem cell-derived intestinal organoids. *Front Bioeng Biotechnol 10*, 879024. doi:10.3389/fbioe.2022.879024

Kakni, P., López-Iglesias, C., Truckenmüller, R. et al. (2023). Psc-derived intestinal organoids with apical-out orientation as a tool to study nutrient uptake, drug absorption and metabolism. *Frontiers in Molecular Biosciences 10*, 1102209.

Kauffman, A. L., Gyurdieva, A. V., Mabus, J. R. et al. (2013). Alternative functional in vitro models of human intestinal epithelia. *Front Pharmacol 4*, 79. doi:10.3389/fphar.2013.00079

Kilford, P. J., Gertz, M., Houston, J. B. et al. (2008). Hepatocellular binding of drugs: Correction for unbound fraction in hepatocyte incubations using microsomal binding or drug lipophilicity data. *Drug Metab Dispos 36*, 1194-1197. doi:10.1124/dmd.108.020834

Kock, K., Ferslew, B. C., Netterberg, I. et al. (2014). Risk factors for development of cholestatic drug-induced liver injury: Inhibition of hepatic basolateral bile acid transporters multidrug resistance-associated proteins 3 and 4. *Drug Metab Dispos 42*, 665-674. doi:10.1124/dmd.113.054304

Kostrubsky, S. E., Strom, S. C., Kalgutkar, A. S. et al. (2006). Inhibition of hepatobiliary transport as a predictive method for clinical hepatotoxicity of nefazodone. *Toxicological Sciences 90*, 451-459.

Kouzuki, H., Suzuki, H., Ito, K. et al. (1998). Contribution of sodium taurocholate co-transporting polypeptide to the uptake of its possible substrates into rat hepatocytes. *Journal of Pharmacology and Experimental Therapeutics 286*, 1043-1050.

Krag, E. and Phillips, S. F. (1974). Active and passive bile acid absorption in man. Perfusion studies of the ileum and jejunum. *J Clin Invest 53*, 1686-1694. doi:10.1172/JCI107720

Kramer, N. I., Di Consiglio, E., Blaauboer, B. J. et al. (2015). Biokinetics in repeated-dosing in vitro drug toxicity studies. *Toxicology in vitro 30*, 217-224.

Kumar, V., Yin, M., Ishida, K. et al. (2021). Prediction of transporter-mediated rosuvastatin hepatic uptake clearance and drug interaction in humans using proteomics-informed ref approach. *Drug Metab Dispos 49*, 159-168. doi:10.1124/dmd.120.000204

Le Vee, M., Noel, G., Jouan, E. et al. (2013). Polarized expression of drug transporters in differentiated human hepatoma heparg cells. *Toxicol In Vitro 27*, 1979-1986. doi:10.1016/j.tiv.2013.07.003

Le Vee, M., Moreau, A., Jouan, E. et al. (2022). Inhibition of canalicular and sinusoidal taurocholate efflux by cholestatic drugs in human hepatoma heparg cells. *Biopharm Drug Dispos 43*, 265-271. doi:10.1002/bdd.2333

Li, M., Vokral, I., Evers, B. et al. (2018). Human and rat precision-cut intestinal slices as ex vivo models to study bile acid uptake by the apical sodium-dependent bile acid transporter. *Eur J Pharm Sci 121*, 65-73. doi:10.1016/j.ejps.2018.05.005

Lobell, M. and Sivarajah, V. (2003). In silico prediction of aqueous solubility, human plasma protein binding and volume of distribution of compounds from calculated pka and alogp98 values. *Mol Divers 7*, 69-87. doi:10.1023/b:modi.0000006562.93049.36
Lock, J. Y., Carlson, T. L. and Carrier, R. L. (2018). Mucus models to evaluate the diffusion of drugs and particles. *Adv Drug Deliv Rev 124*, 34-49. doi:10.1016/j.addr.2017.11.001
Louisse, J., Alewijn, M., Peijnenburg, A. et al. (2020). Towards harmonization of test methods for in vitro hepatic clearance studies. *Toxicol In Vitro 63*, 104722. doi:10.1016/j.tiv.2019.104722
Lu, J., Einhorn, S., Venkatarangan, L. et al. (2015). Morphological and functional characterization and assessment of ipsc-derived hepatocytes for in vitro toxicity testing. *Toxicol Sci 147*, 39-54. doi:10.1093/toxsci/kfv117
Lucchetti, M., Kaminska, M., Oluwasegun, A. K. et al. (2021). Emulating the gut-liver axis: Dissecting the microbiome's effect on drug metabolism using multiorgan-on-chip models. *Curr Opin Endocr Metab Res 18*, 94-101. doi:10.1016/j.coemr.2021.03.003
Maertens, A., Golden, E., Luechtefeld, T. H. et al. (2022). Probabilistic risk assessment - the keystone for the future of toxicology. *ALTEX 39*, 3-29. doi:10.14573/altex.2201081
Marasco, G., Cremon, C., Barbaro, M. R. et al. (2022). Pathophysiology and clinical management of bile acid diarrhea. *J Clin Med 11*, 3102. doi:10.3390/jcm11113102
Marion, T. L., Leslie, E. M. and Brouwer, K. L. (2007). Use of sandwich-cultured hepatocytes to evaluate impaired bile acid transport as a mechanism of drug-induced hepatotoxicity. *Mol Pharm 4*, 911-918. doi:10.1021/mp0700357
Maurer, M., Gresnigt, M. S., Last, A. et al. (2019). A three-dimensional immunocompetent intestine-on-chip model as in vitro platform for functional and microbial interaction studies. *Biomaterials 220*, 119396.
McNally, K., Cotton, R., Hogg, A. et al. (2014). Popgen: A virtual human population generator. *Toxicology 315*, 70-85. doi:10.1016/j.tox.2013.07.009
Miele, L., Valenza, V., La Torre, G. et al. (2009). Increased intestinal permeability and tight junction alterations in nonalcoholic fatty liver disease. *Hepatology 49*, 1877-1887. doi:10.1002/hep.22848
Mitra, P., Weinheimer, S., Michalewicz, M. et al. (2018). Prediction and quantification of hepatic transporter-mediated uptake of pitavastatin utilizing a combination of the relative activity factor approach and mechanistic modeling. *Drug Metab Dispos 46*, 953-963. doi:10.1124/dmd.118.080614
Morgan, R. E., van Staden, C. J., Chen, Y. et al. (2013). A multifactorial approach to hepatobiliary transporter assessment enables improved therapeutic compound development. *Toxicol Sci 136*, 216-241. doi:10.1093/toxsci/kft176
Murali, A., Giri, V., Zickgraf, F. M. et al. (2023). Connecting gut microbial diversity with plasma metabolome and fecal bile acid changes induced by the antibiotics tobramycin and colistin sulfate. *Chemical Research in Toxicology* doi:10.1021/acs.chemrestox.2c00316
Najjar, A., Punt, A., Wambaugh, J. et al. (2022). Towards best use and regulatory acceptance of generic physiologically based kinetic (pbk) models for in vitro-to-in vivo extrapolation (ivive) in chemical risk assessment. *Arch Toxicol 96*, 3407-3419. doi:10.1007/s00204-022-03356-5
Ning, J., Rietjens, I. M. C. M. and Strikwold, M. (2019). Integrating physiologically based kinetic (pbk) and monte carlo modelling to predict inter-individual and inter-ethnic variation in bioactivation and liver toxicity of lasiocarpine. *Arch Toxicol 93*, 2943-2960. doi:10.1007/s00204-019-02563-x
Noor, F. (2015). A shift in paradigm towards human biology-based systems for cholestatic-liver diseases. *J Physiol 593*, 5043-5055. doi:10.1113/JP271124
Notenboom, S., Weigand, K. M., Proost, J. H. et al. (2018). Development of a mechanistic biokinetic model for hepatic bile acid handling to predict possible cholestatic effects of drugs. *European Journal of Pharmaceutical Sciences 115*, 175-184.
OECD (2017). *Guidance document for the use of adverse outcome pathways in developing integrated approaches to testing and assessment (iata)*. Vol. OECD Publishing.

OECD and Magdalini, S. (2021). Guidance document on the characterisation, validation and reporting of physiologically based kinetic (pbk) models for regulatory purposes.
Olander, M., Wisniewski, J. R., Matsson, P. et al. (2016). The proteome of filter-grown caco-2 cells with a focus on proteins involved in drug disposition. *J Pharm Sci 105*, 817-827. doi:10.1016/j.xphs.2015.10.030
Olson, H., Betton, G., Robinson, D. et al. (2000). Concordance of the toxicity of pharmaceuticals in humans and in animals. *Regul Toxicol Pharmacol 32*, 56-67. doi:10.1006/rtph.2000.1399
Onozato, D., Yamashita, M., Nakanishi, A. et al. (2018). Generation of intestinal organoids suitable for pharmacokinetic studies from human induced pluripotent stem cells. *Drug Metab Dispos 46*, 1572-1580. doi:10.1124/dmd.118.080374
Oorts, M., Baze, A., Bachellier, P. et al. (2016). Drug-induced cholestasis risk assessment in sandwich-cultured human hepatocytes. *Toxicol In Vitro 34*, 179-186. doi:10.1016/j.tiv.2016.03.008
Paini, A., Tan, Y.-M., Sachana, M. et al. (2021). Gaining acceptance in next generation pbk modelling approaches for regulatory assessments–an oecd international effort. *Computational Toxicology 18*, 100163.
Pang, K. S., Han, Y. R., Noh, K. et al. (2019). Hepatic clearance concepts and misconceptions: Why the well-stirred model is still used even though it is not physiologic reality? *Biochemical Pharmacology 169*, 113596.
Pearce, R. G., Setzer, R. W., Strope, C. L. et al. (2017). Httk: R package for high-throughput toxicokinetics. *J Stat Softw 79*, 1-26. doi:10.18637/jss.v079.i04
Pelkonen, O. and Turpeinen, M. (2007). In vitro-in vivo extrapolation of hepatic clearance: Biological tools, scaling factors, model assumptions and correct concentrations. *Xenobiotica 37*, 1066-1089. doi:10.1080/00498250701620726
Pham, L. L., Watford, S. M., Pradeep, P. et al. (2020). Variability in in vivo studies: Defining the upper limit of performance for predictions of systemic effect levels. *Computational Toxicology 15*, 100126.
Pires, D. E., Blundell, T. L. and Ascher, D. B. (2015). Pkcsm: Predicting small-molecule pharmacokinetic and toxicity properties using graph-based signatures. *J Med Chem 58*, 4066-4072. doi:10.1021/acs.jmedchem.5b00104
Proenca, S., Escher, B. I., Fischer, F. C. et al. (2021). Effective exposure of chemicals in in vitro cell systems: A review of chemical distribution models. *Toxicol In Vitro 73*, 105133. doi:10.1016/j.tiv.2021.105133
Punt, A., Louisse, J., Beekmann, K. et al. (2022). Predictive performance of next generation human physiologically based kinetic (pbk) models based on in vitro and in silico input data. *ALTEX 39*, 221-234. doi:10.14573/altex.2108301
Puri, P., Daita, K., Joyce, A. et al. (2018). The presence and severity of nonalcoholic steatohepatitis is associated with specific changes in circulating bile acids. *Hepatology 67*, 534-548. doi:10.1002/hep.29359
Qosa, H., Ribeiro, A. J., Hartman, N. R. et al. (2021). Characterization of a commercially available line of ipsc hepatocytes as models of hepatocyte function and toxicity for regulatory purposes. *Journal of pharmacological and toxicological methods 110*, 107083.
Rietjens, I. M. C. M., Louisse, J. and Punt, A. (2011). Tutorial on physiologically based kinetic modeling in molecular nutrition and food research. *Mol Nutr Food Res 55*, 941-956. doi:10.1002/mnfr.201000655
Roda, A., Cappelleri, G., Aldini, R. et al. (1982). Quantitative aspects of the interaction of bile acids with human serum albumin. *J Lipid Res 23*, 490-495.
Rodriguez-Duque, J. C., Calleja, J. L., Iruzubieta, P. et al. (2023). Increased risk of mafld and liver fibrosis in inflammatory bowel disease independent of classic metabolic risk factors. *Clin Gastroenterol Hepatol 21*, 406-414 e407. doi:10.1016/j.cgh.2022.01.039
Rowe, C., Gerrard, D. T., Jenkins, R. et al. (2013). Proteome-wide analyses of human hepatocytes during differentiation and dedifferentiation. *Hepatology 58*, 799-809. doi:10.1002/hep.26414

Sakai, Y., Iwao, T., Susukida, T. et al. (2019). In vitro bile acid-dependent hepatocyte toxicity assay system using human induced pluripotent stem cell-derived hepatocytes: Current status and disadvantages to overcome. *Drug Metab Pharmacokinet 34*, 264-271. doi:10.1016/j.dmpk.2019.04.004

Sambuy, Y., De Angelis, I., Ranaldi, G. et al. (2005). The caco-2 cell line as a model of the intestinal barrier: Influence of cell and culture-related factors on caco-2 cell functional characteristics. *Cell biology and toxicology 21*, 1-26.

Schmeisser, S., Miccoli, A., von Bergen, M. et al. (2023). New approach methodologies in human regulatory toxicology–not if, but how and when! *Environment international* 108082.

Schneeberger, K., Sanchez-Romero, N., Ye, S. et al. (2020). Large-scale production of lgr5-positive bipotential human liver stem cells. *Hepatology 72*, 257-270. doi:10.1002/hep.31037

Sedrani, C., Gomez-Giro, G., Grandmougin, L. et al. (2023). A gut-on-a-chip model to study the gut microbiome-nervous system axis. *J Vis Exp* doi:10.3791/64483

Shah, P., Fritz, J. V., Glaab, E. et al. (2016). A microfluidics-based in vitro model of the gastrointestinal human-microbe interface. *Nat Commun 7*, 11535. doi:10.1038/ncomms11535

Shin, W. and Kim, H. J. (2023). In vitro morphogenesis and differentiation of human intestinal epithelium in a gut-on-a-chip. In (eds.), *Intestinal differentiated cells: Methods and protocols*. Springer.

Sips, F. L. P., Eggink, H. M., Hilbers, P. A. J. et al. (2018). In silico analysis identifies intestinal transit as a key determinant of systemic bile acid metabolism. *Front Physiol 9*, 631. doi:10.3389/fphys.2018.00631

Sirenko, O., Hesley, J., Rusyn, I. et al. (2014). High-content assays for hepatotoxicity using induced pluripotent stem cell-derived cells. *Assay Drug Dev Technol 12*, 43-54. doi:10.1089/adt.2013.520

Smirnova, E., Muthiah, M. D., Narayan, N. et al. (2022). Metabolic reprogramming of the intestinal microbiome with functional bile acid changes underlie the development of nafld. *Hepatology 76*, 1811-1824. doi:10.1002/hep.32568

Sodhi, J. K. and Benet, L. Z. (2021). Successful and unsuccessful prediction of human hepatic clearance for lead optimization. *J Med Chem 64*, 3546-3559. doi:10.1021/acs.jmedchem.0c01930

Sontheimer-Phelps, A., Chou, D. B., Tovaglieri, A. et al. (2020). Human colon-on-a-chip enables continuous in vitro analysis of colon mucus layer accumulation and physiology. *Cell Mol Gastroenterol Hepatol 9*, 507-526. doi:10.1016/j.jcmgh.2019.11.008

Storelli, F., Yin, M., Kumar, A. R. et al. (2022). The next frontier in adme science: Predicting transporter-based drug disposition, tissue concentrations and drug-drug interactions in humans. *Pharmacol Ther 238*, 108271. doi:10.1016/j.pharmthera.2022.108271

Suzuki, T., Nishimaki-Mogami, T., Kawai, H. et al. (2006). Screening of novel nuclear receptor agonists by a convenient reporter gene assay system using green fluorescent protein derivatives. *Phytomedicine 13*, 401-411. doi:10.1016/j.phymed.2005.09.003

Van Brantegem, P., Chatterjee, S., De Bruyn, T. et al. (2020). Drug-induced cholestasis assay in primary hepatocytes. *MethodsX 7*, 101080. doi:10.1016/j.mex.2020.101080

van der Mark, V. A., de Waart, D. R., Ho-Mok, K. S. et al. (2014). The lipid flippase heterodimer atp8b1–cdc50a is essential for surface expression of the apical sodium-dependent bile acid transporter (slc10a2/asbt) in intestinal caco-2 cells. *Biochimica et Biophysica Acta (BBA)-Molecular Basis of Disease 1842*, 2378-2386.

Veider, F., Knoll, P., Jorgensen, A. M. et al. (2023). Oral drug delivery: Influence of mucus on cellular interactions and uptake of lipid-based nanocarriers in caco-2 cells. *Acta Biomater 167*, 416-424. doi:10.1016/j.actbio.2023.06.005

Villeneuve, D. L., Crump, D., Garcia-Reyero, N. et al. (2014). Adverse outcome pathway (aop) development i: Strategies and principles. *Toxicol Sci 142*, 312-320. doi:10.1093/toxsci/kfu199

Vinken, M., Landesmann, B., Goumenou, M. et al. (2013). Development of an adverse outcome pathway from drug-mediated bile salt export pump inhibition to cholestatic liver injury. *Toxicol Sci 136*, 97-106. doi:10.1093/toxsci/kft177

Voronova, V., Sokolov, V., Al-Khaifi, A. et al. (2020). A physiology-based model of bile acid distribution and metabolism under healthy and pathologic conditions in human beings. *Cell Mol Gastroenterol Hepatol 10*, 149-170. doi:10.1016/j.jcmgh.2020.02.005

Wang, J., Bakker, W., Zheng, W. et al. (2022a). Exposure to the mycotoxin deoxynivalenol reduces the transport of conjugated bile acids by intestinal caco-2 cells. *Arch Toxicol 96*, 1473-1482. doi:10.1007/s00204-022-03256-8

Wang, Z., Faria, J., van der Laan, L. J. W. et al. (2022b). Human cholangiocytes form a polarized and functional bile duct on hollow fiber membranes. *Front Bioeng Biotechnol 10*, 868857. doi:10.3389/fbioe.2022.868857

Willmann, S., Höhn, K., Edginton, A. et al. (2007). Development of a physiology-based whole-body population model for assessing the influence of individual variability on the pharmacokinetics of drugs. *Journal of pharmacokinetics and pharmacodynamics 34*, 401-431.

Yang, J., Hirai, Y., Iida, K. et al. (2023). Integrated-gut-liver-on-a-chip platform as an in vitro human model of non-alcoholic fatty liver disease. *Communications Biology 6*, 310.

Yoshikado, T., Lee, W., Toshimoto, K. et al. (2021). Evaluation of hepatic uptake of oatp1b substrates by short term-cultured plated human hepatocytes: Comparison with isolated suspended hepatocytes. *J Pharm Sci 110*, 376-387. doi:10.1016/j.xphs.2020.10.041

Zamek-Gliszczynski, M. J., Lee, C. A., Poirier, A. et al. (2013). Itc recommendations for transporter kinetic parameter estimation and translational modeling of transport-mediated pk and ddis in humans. *Clin Pharmacol Ther 94*, 64-79. doi:10.1038/clpt.2013.45

Zhang, J., He, K., Cai, L. et al. (2016). Inhibition of bile salt transport by drugs associated with liver injury in primary hepatocytes from human, monkey, dog, rat, and mouse. *Chem Biol Interact 255*, 45-54. doi:10.1016/j.cbi.2016.03.019

Zhang, J., Lyu, A. and Wang, C. (2023a). The molecular insights of bile acids homeostasis in host diseases. *Life Sciences* 121919.

Zhang, N., Wang, J., Bakker, W. et al. (2022). In vitro models to detect in vivo bile acid changes induced by antibiotics. *Arch Toxicol 96*, 3291-3303. doi:10.1007/s00204-022-03373-4

Zhang, N., Zheng, W., Bakker, W. et al. (2023b). In vitro models to measure effects on intestinal deconjugation and transport of mixtures of bile acids. *Chem Biol Interact 375*, 110445. doi:10.1016/j.cbi.2023.110445

Zhu, Q., Komori, H., Imamura, R. et al. (2021). A novel fluorescence-based method to evaluate ileal apical sodium-dependent bile acid transporter asbt. *J Pharm Sci 110*, 1392-1400. doi:10.1016/j.xphs.2020.11.030

Zou, P., Liu, X., Wong, S. et al. (2013). Comparison of in vitro-in vivo extrapolation of biliary clearance using an empirical scaling factor versus transport-based scaling factors in sandwich-cultured rat hepatocytes. *J Pharm Sci 102*, 2837-2850. doi:10.1002/jps.23620

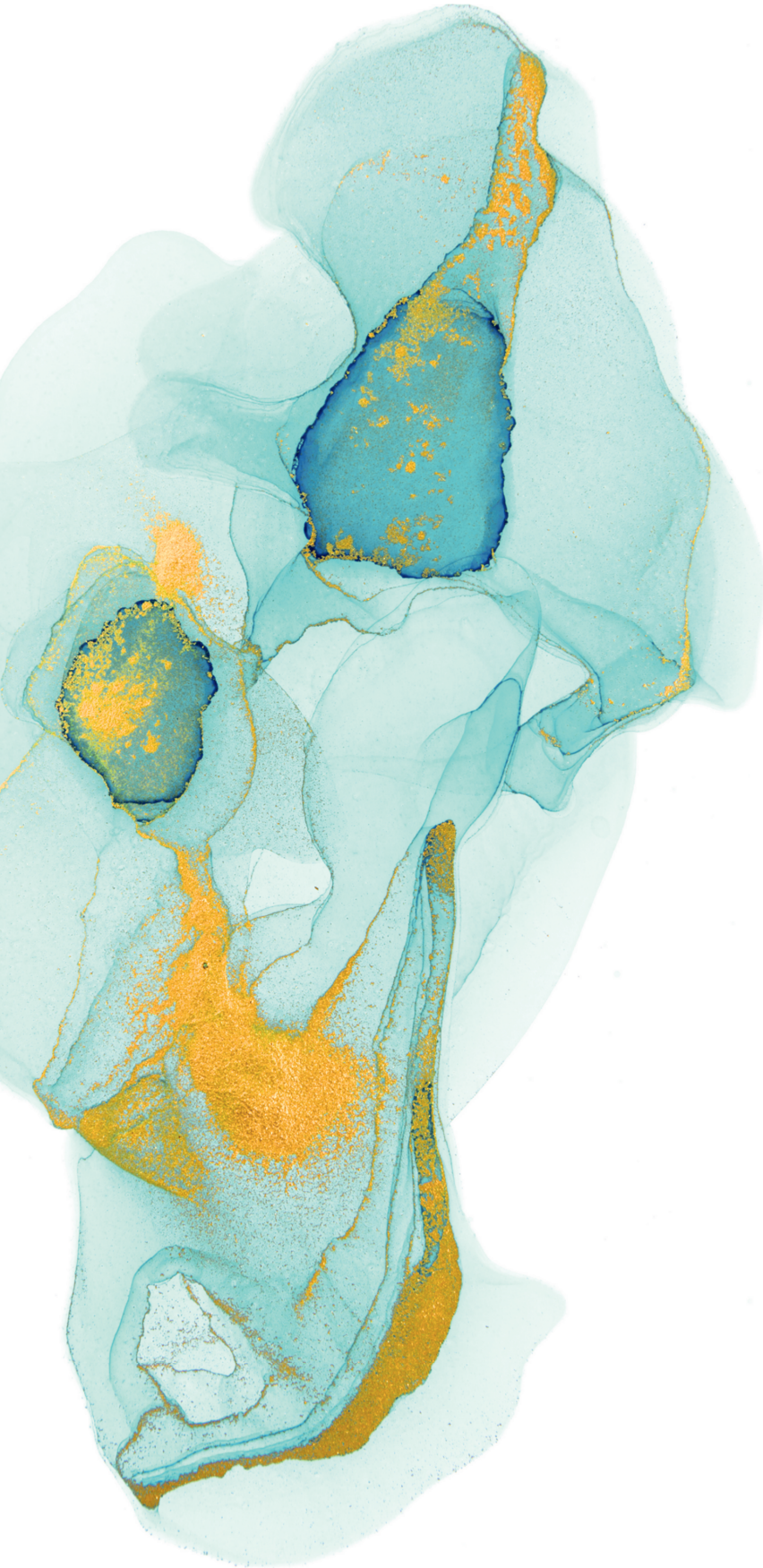

Summary

The significance of bile acids within human physiology has received substantial attention in recent years. Bile acids are now acknowledged as pivotal signaling molecules with profound implications for energy homeostasis, glucose regulation, lipid metabolism, cellular proliferation, and immune modulation. Primary bile acids are synthesized in the liver and secreted into the intestinal lumen, where they undergo modifications by the intestinal microbiome to evolve into more hydrophobic secondary bile acids. Subsequently, these intestinal bile acids are efficiently absorbed across the intestinal epithelium and transported via the portal vein for reuptake by the liver. Various xenobiotics encountered in everyday life, including pharmaceuticals, environmental pollutants, and dietary constituents, possess the capacity to perturb bile acid homeostasis. Such perturbations can give rise to an array of adverse health outcomes, encompassing cholestasis, metabolic-associated fatty liver disease (MAFLD), and inflammatory bowel disease. The aim of the present thesis was to develop and apply reliable human cell based *in vitro* models and physiologically based kinetic (PBK) models to better understand and predict drug-induced disruption of bile acid homeostasis with an emphasis on cholestasis. Upon gaining a better understanding of the relationship between specific disruptions in bile acid homeostasis and adverse outcomes, measurement of these disruptions *in vitro* and translation of these data to the *in vivo* situation using PBK modeling can serve as an indicator of toxicity or potency for selected adverse outcomes. In the thesis a proof-of-principle was provided focusing on the endpoint cholestasis and data-rich chemicals (drugs). Cholestasis refers to an impaired hepatic bile acid secretion and subsequent hepatic bile acid accumulation and increased bile acid levels in the systemic blood circulation. The symptoms include jaundice, pruritus and fever.

Chapter 1 introduces the physiological roles and enterohepatic circulation of bile acids, the role of inhibition of the hepatic bile salt export pump (BSEP) in the development of cholestasis and the health consequences of inhibition of the apical sodium-dependent bile acid transporter (ASBT). Furthermore, the effects of antibiotics and other drugs on bile acid homeostasis and New approach methodologies (NAMs) to study these effects are introduced, along with the aim and outline of the thesis.

Chapter 2 compares the capacity of three different hepatic *in vitro* systems to emulate human liver functionality to synthesize and secrete bile acids. Bile acid synthesis rates and profiles, responsiveness to selected BSEP-inhibitors and selected target genes were analyzed for hepatocyte-like intrahepatic cholangiocyte organoids (ICO-heps), sandwich cultured human hepatocytes (SCHH) and HepaRG cells (HepaRGs). To this end, basal bile acid production of SCHHs, HepaRG cells and ICO-heps were analyzed, and the effect of the known BSEP-inhibitors bosentan and lopinavir on bile acid disposition in SCHHs and HepaRG cells was quantified. RT-qPCR of selected target genes involved in maturation status, synthesis, transport and conjugation of bile acids was performed to mechanistically underpin the observed differences in bile acid homeostasis. The bile acid synthesis rate was observed to be different in each model, and decreased in the order SCHHs > HepaRGs > ICO-heps. Surprisingly, the bile acid levels in the HepaRG and SCHH lysates decreased upon treatment with bosentan and lopinavir, indicating that both treatments triggered strong adaptive responses to counteract intracellular bile acid accumulation. The data revealed that of the studied genes, their expression

within SCHHs correlated best with that observed within material obtained from a liver biopsy. In terms of the bile acid profile produced, the bile acid profile of HepaRGs had the highest resemblance with the *in vivo* liver bile acid profile. Collectively, the data revealed important differences in phenotype and bile acid homeostasis between the three human hepatic *in vitro* systems tested.

Chapter 3 develops a PBK model that provides a tool to predict dose-dependent bile acid accumulation in humans upon treatment with the BSEP-inhibitor bosentan. To this end, three mutually connected PBK models were developed, consisting of a PBK model for a) bosentan, b) RO 47-8634 (the active metabolite of bosentan) and c) bile acids. The bile acid PBK model was developed using glycochenodeoxycholic acid (GCDCA) as an exemplary bile acid. The bosentan and RO 47-8634 PBK models were used to predict their concentrations at the target organ for BSEP-inhibition, *i.e.* the liver. The PBK model kinetic parameters for BSEP-mediated transport were obtained from a literature study reporting BSEP-mediated GCDCA uptake in membrane vesicles. The scaling factor required to convert the *in vitro* kinetic data to the *in vivo* situation was based on the relative BSEP expression in the membrane vesicles and *in vivo* tissue. The effects of *in vivo* variabilities in transporter BSEP abundance and bile acid pool size on plasma and liver bile acid concentrations were also simulated. The PBK model developed adequately predicted the *in vivo* postprandial bile acid kinetics. Both the Markov Chain Monte Carlo simulations based on a distribution of BSEP abundances and empirical scaling of the total bile acid pool readily described the variations in plasma bile acid concentrations within and between human volunteers. Bosentan treatment disproportionally increased the maximum bile acid plasma concentration in individuals with a large total bile acid pool or low BSEP abundance. Especially individuals having a large total bile acid pool size and a low BSEP abundance were predicted to be at risk for rapid saturation of BSEP and subsequent intrahepatic bile acid accumulation. The PBK model provided a first proof-of-principle for coupling a drug and bile acid PBK model to predict drug-induced effects on bile acid postprandial kinetics.

Chapter 4 simulates the effects of ileal ASBT-inhibition on intestinal and systemic plasma bile acid levels, because disturbing ileal bile acid uptake was expected to substantially affect intestinal and systemic bile acid levels. The model from the previous chapter was extended to describe not only GCDCA, but also glycocholic acid (GCA) and glycodeoxycholic acid (GDCA) and unconjugated bile acids. Caco-2 cells were used to gain insights in the underlying mechanisms of bile acid transport, and to obtain kinetic transport parameters for GCA. While the transport of GCA, GCDCA and GDCA over the Caco-2 cells was substantially higher at 37 ˚C than at 4 ˚C, the transport of deoxycholic acid (DCA), which was used as model bile acid for unconjugated bile acids, was equally high at both 4 ˚C and 37 ˚C. These findings indicate that GCA, GCDCA and GDCA transport is an active and/or facilitated process, while DCA transport is a passive process. The drug and selective ASBT-inhibitor odevixibat inhibited GCA transport dose-dependently. The inhibitory potency (K_i) of odevixibat was derived using GCA as a model bile acid and assumed to be similar for all conjugated bile acids. No inhibition of unconjugated bile acid uptake was included due to the passive nature of their transport. Upon incorporation of these data in the PBK model, the model quantitatively predicted a reduction in conjugated bile acid levels in plasma upon administration of odevixibat. The simulations matched human *in vivo* data and

provided a first proof-of-principle for the incorporation of ileal bile acid uptake in a bile acid PBK model.

Chapter 5 applies the newly developed PBK model to investigate the effect of the antibiotic tobramycin on bile acid homeostasis. Inhibition of intestinal bile acid transport was studied using Caco-2 cells. Inhibition of intestinal deconjugation was based on previous studies using fecal static batch incubations. Two exposure conditions, pre-exposure and co-exposure to tobramycin, revealed distinct effects on bile acid transport. Co-exposure primarily affected transport in the order of DCA > GCDCA > GDCA > GCA, while pre-exposure had the greatest impact on GCA followed by GCDCA, GDCA, and DCA. Based on the differences in lipophilicity and thus passive transport rate, it was speculated that co-exposure primarily affected passive transport, because it had the strongest effect on the most lipophilic bile acid, *i.e.* DCA. Conversely, pre-exposure was speculated to primarily impact ASBT-mediated transport. These data were incorporated in the PBK model to predict tobramycin's impact on plasma bile acid levels, resulting in a predicted reduction in maximal plasma levels of GCA, GCDCA, GDCA and unconjugated bile acids by 42.4%, 27.7%, 16.9%, and 75.8%, respectively. The reduction in conjugated bile acids was primarily attributed to ASBT-mediated intestinal uptake, while the decrease in unconjugated bile acids was linked to reduced passive transport and intestinal deconjugation rates. In summary, the PBK model demonstrated its utility as a valuable tool for evaluating the influence of oral xenobiotic exposure on host bile acid homeostasis, with a specific focus on its effects on intestinal microbial bile acid deconjugation and transport processes.

Chapter 6 applies the newly developed PBK model to a set of 15 reference drugs. These drugs are known to inhibit hepatic bile acid efflux and are causally linked to development of drug-induced liver injury, but are classified as common, rare or no cholestasis incidence. The bile acid PBK model as described in Chapter 4 and 5 was used, with the only adaptation to again only focus on the conjugated bile acid GCDCA. Unconjugated bile acids are mainly transported via perfusion or diffusion and thus unlikely to accumulate in the liver as a result of hepatic transport-inhibitors. The intrahepatic drug concentrations were predicted with generic PBK models and incorporated in the bile acid PBK models along with their inhibitory effect on hepatic bile acid efflux, which was obtained from a literature study using a short-term incubation with primary hepatocytes. The result obtained revealed that cholestasis incidence was not adequately predicted by the inhibitory constant (K_i) for inhibition of hepatic bile acid efflux, but rather by the area under the curve (AUC) above this K_i for the PBK model predicted internal hepatic drug concentration at therapeutic dose level. The approach also provided mechanistic insights in risk factors towards drug-induced cholestasis. People with slower clearance of the drug, a larger bile acid pool, reduced BSEP abundance or given higher than therapeutic dose levels are predicted to be more likely to develop drug-induced cholestasis.

Chapter 7 gives an overview of the main findings in this thesis and provides a general discussion on points beyond the scope of the individual chapters. The chapter further discusses the PBK models for drug metabolism and bile acids, *in vitro* and *in silico* tools to define PBK input parameters, converting *in vitro* data to the *in vivo* situation, the cholestasis adverse outcome pathway and the relevance of

bile acids for adverse outcomes other than cholestasis. To finalize, a discussion is provided about the paradigm shift towards an animal-free risk assessment for cholestasis.

Taken together, the present thesis integrated human cell-based *in vitro* models with PBK modeling to understand and predict drug-induced effects on bile acid homeostasis, focusing on cholestasis. It was shown that it is feasible to apply new approach methodologies (NAMs) to predict drug-induced cholestasis as a result of hepatic bile acid efflux inhibition and to predict the whole-body effects of inhibition of ileal bile acid absorption. Thereby, the current work contributes to the 3Rs (reduction, refinement, replacement) of experimental animal studies.

Samenvatting

De afgelopen jaren heeft de rol van galzuren in de menselijke fysiologie aanzienlijke aandacht gekregen. Galzuren worden gezien als essentiële signaalmoleculen met belangrijke implicaties voor energiehomeostase, glucose en vetmetabolisme, cellulaire proliferatie en immuunmodulatie. Primaire galzuren worden in de lever gesynthetiseerd en uitgescheiden in de darm, waar ze door de darmmicrobiota worden omgezet tot beter wateroplosbare secundaire galzuren. Vervolgens worden deze galzuren efficiënt geabsorbeerd door het darmepitheel en via de poortader getransporteerd voor heropname door de lever. Diverse lichaamsvreemde stoffen waar we in het dagelijks leven mee in aanraking komen, waaronder geneesmiddelen, milieuverontreinigende stoffen en voedingsbestanddelen, kunnen de galzuurhomeostase verstoren. Dergelijke verstoringen kunnen leiden tot verschillende ziektebeelden, waaronder cholestase, metabool-geassocieerde vette leverziekte en inflammatoire darmaandoeningen. Het doel van dit proefschrift was het ontwikkelen en toepassen van betrouwbare *in vitro* modellen gebaseerd op menselijke cellen en fysiologisch gebaseerde kinetische (physiologically based kinetic) (PBK) modellen om de door geneesmiddelen veroorzaakte verstoring van galzuurhomeostase beter te begrijpen en te voorspellen, met de nadruk op cholestase. Een beter begrip van de relatie tussen specifieke verstoringen in de galzuurhomeostase en verschillende ziektebeelden maakt het mogelijk om deze verstoringen *in vitro* te meten en vervolgens de resultaten te vertalen naar de *in vivo* situatie met een PBK-model. Deze aanpak kan dan vervolgens dienen als een indicator van de toxische potentie van een bestaand of nieuw ontwikkeld geneesmiddel voor de inductie van de geselecteerde ziektebeelden. Dit proefschrift biedt een zogenoemde “proof-of-principle” gefocust op het eindpunt cholestase en chemicaliën waar veel data over beschikbaar zijn (geneesmiddelen). Cholestase is een ziektebeeld veroorzaakt door verstoring van de hepatische galzuuruitscheiding en opeenvolgende opstapeling van galzuren in de lever en de systemische bloed circulatie. De symptomen zijn geelzucht, jeuk en koorts.

Hoofdstuk 1 introduceert de fysiologische functies en enterohepatische circulatie van galzuren, de rol van remming van de hepatische galzout-exportpomp (bile salt export pump) (BSEP) in de ontwikkeling van cholestase en de gezondheidsgevolgen van remming van de apicale natriumafhankelijke galzuurtransporter (apical sodium-dependent bile acid transporter) (ASBT). Verder worden de effecten van antibiotica en andere geneesmiddelen op galzuurhomeostase en “New Approach Methodologies” (NAMs) om deze effecten te bestuderen geïntroduceerd samen met het doel en de opzet van het proefschrift.

Hoofdstuk 2 vergelijkt de capaciteit van drie verschillende *in vitro* systemen voor hepatocyten om de functionaliteit van de menselijke lever na te bootsen op het gebied van synthese en uitscheiding van galzuren. Galzuurproductie en -uitscheiding, respons op geselecteerde BSEP-remmers en geselecteerde doelgenen werden geanalyseerd voor leverorganoïden, primaire hepatocyten en cellen van de veelgebruikte cellijn HepaRG. De basale galzuurproductie door leverorganoïden, primaire hepatocyten en HepaRG-cellen werd geanalyseerd, en het effect van de bekende BSEP-remmers bosentan en lopinavir op galzuren in het medium en lysaat van primaire hepatocyten en HepaRG-cellen werd gekwantificeerd. RT-qPCR van geselecteerde doelgenen die betrokken zijn bij de

celdifferentiatie, en bij synthese, transport en conjugatie van galzuren werd uitgevoerd om de waargenomen verschillen in galzuurhomeostase mechanistisch te onderbouwen. De galzuursynthesesnelheid bleek verschillend te zijn in elk model en nam af in de volgorde primaire hepatocyten > HepaRG-cellen > leverorganoïden. Onverwacht resulteerde behandeling van de cellen met de BSEP-remmers bosentan en lopinavir in een daling in plaats van een stijging van de galzuurniveaus in de cellysaten van HepaRG en primaire hepatocyten. Dit geeft aan dat beide behandelingen sterke adaptieve reacties veroorzaakten om intracellulaire ophoping van galzuren tegen te gaan. De gegevens toonden aan dat van de bestudeerde genen de expressie in primaire hepatocyten het beste correleerde met die waargenomen in materiaal verkregen uit een leverbiopsie. Wat betreft het geproduceerde galzuurprofiel vertoonde het galzuurprofiel van HepaRG-cellen de grootste gelijkenis met het *in vivo* galzuurprofiel van de lever. Gezamenlijk toonden de gegevens belangrijke verschillen aan in fenotype en galzuurhomeostase tussen de drie geteste *in vitro* lever modellen.

Hoofdstuk 3 beschrijft de ontwikkeling van een PBK-model dat de dosisafhankelijke ophoping van galzuren in mensen kan voorspellen bij behandeling met de BSEP-remmer bosentan. Hiervoor werden drie onderling verbonden PBK-modellen ontwikkeld, bestaande uit een PBK-model voor a) bosentan, b) RO 47-8634 (actieve metaboliet van bosentan) en c) galzuren. Het PBK-model voor galzuren werd ontwikkeld voor glycochenodeoxygalzuur (glycochenodeoxycholic acid) (GCDCA) als model galzuur. De bosentan- en RO 47-8634 PBK-modellen werden gebruikt om hun concentraties te voorspellen in het doelorgaan voor BSEP-remming, namelijk de lever. De kinetische parameters voor BSEP-gemedieerd transport werden verkregen uit een literatuurstudie met geïsoleerde membraanblaasjes. De schalingsfactor die nodig was om de *in vitro* kinetische gegevens naar de *in vivo* situatie om te zetten was gebaseerd op de relatieve hoeveelheid BSEP-transportereiwit (BSEP-abundantie) in de membraanblaasjes ten opzichte van een leverbiopsie. Ook werden de effecten van *in vivo* variatie in BSEP-abundantie en in de omvang van de galzuurpool op plasma- en leverconcentraties van galzuren gesimuleerd. Het ontwikkelde PBK-model voorspelde de *in vivo* postprandiale kinetiek van galzuren adequaat. De variatie binnen en tussen de testpersonen werd goed voorspeld op basis van BSEP-abundantie en empirische schaling van de omvang van de galzuurpool. Vooral individuen met een grote galzuurpool en een lage BSEP-abundantie werden voorspeld risico te lopen op saturatie van BSEP en daaropvolgend ophoping van galzuren in de lever. Het PBK-model leverde een eerste voorbeeld over het koppelen van een geneesmiddel- en galzuur-PBK-model om de effecten van geneesmiddelen op de postprandiale kinetiek van galzuren te voorspellen.

Hoofdstuk 4 voorspelt de effecten van remming van ASBT-gemedieerd galzuurtransport in de darm op de gehalten van galzuren in darm en plasma, omdat werd verwacht dat verstoring van de galzuuropname in de darm aanzienlijke invloed zou hebben op galzuurgehaltes in zowel de darm als het plasma. Het galzuur-PBK-model ontwikkeld in hoofdstuk 3 werd uitgebreid om niet alleen GCDCA, maar ook de gehalten van twee andere geconjugeerde galzuren, glycogalzuur (glycocholic acid) (GCA) en glycodeoxygalzuur (glycodeoxycholic acid) (GDCA), en van ongeconjugeerde galzuren te beschrijven. Caco-2 cellen werden gebruikt om inzicht te krijgen in het onderliggende mechanisme

van galzuurtransport en om kinetische transportparameters te verkrijgen voor GCA. Terwijl het transport van de geconjugeerde galzuren substantieel hoger was bij 37 ˚C dan bij 4 ˚C, was het transport van deoxygalzuur (deoxycholic acid) (DCA), wat als modelstof diende voor ongeconjugeerde galzuren, even hoog bij 37 ˚C en 4 ˚C. Deze resultaten duidden erop dat het transport van de geteste geconjugeerde galzuren een actief en/of gefaciliteerd proces is, terwijl het transport van DCA een passief proces is. Het geneesmiddel odevixibat is een selectieve ASBT-remmer en zorgde voor een dosis-afhankelijk remming van GCA-transport over de Caco-2 cellen. De remmingsconstante (K_i) van odevixibat werd bepaald voor de remming van het transport van GCA als model galzuur en er werd aangenomen dat deze remmingsconstante gelijk was voor alle geconjugeerde galzuren. Remming van het transport van ongeconjugeerde galzuren werd niet meegenomen, omdat dit een passief proces is. Nadat deze data in het galzuur-PBK-model waren opgenomen, voorspelde het model de reductie in geconjugeerde galzuurgehaltes in plasma na toediening van odevixibat kwantitatief. De simulaties waren in overeenstemming met humane *in vivo* data en toonden een eerste bewijs voor het feit dat het mogelijk is galzuuropname te beschrijven in een galzuur-PBK-model.

Hoofdstuk 5 past het nieuw ontwikkelde PBK-model toe om het effect van het antibioticum tobramycine op galzuurhomeostase te onderzoeken. De kinetische parameters voor remming van galzuurtransport in de darm door tobramycine werden bepaald met Caco-2 cellen. De remming van galzuurdeconjugatie door de darmmicrobiota werd beschreven gebaseerd op een voorgaande studie waar gebruik werd gemaakt van een statische incubatie met humane feces. Twee blootstellingsscenario's, namelijk blootstelling aan tobramycine vooraf of tijdens het transport van de galzuren, onthulden verschillende effecten op het galzuurtransport. Gelijktijdige blootstelling aan tobramycine en galzuren had voornamelijk effect op het transport in de volgorde DCA > GCDCA > GDCA > GCA, terwijl tobramycineblootstelling voorafgaand aan de galzuurblootstelling het grootste effect had op GCA gevolgd door GCDCA, GDCA en DCA. Gebaseerd op de verschillen in lipofiliciteit en daarmee de snelheid van passief transport, en het feit dat het effect het sterkst was voor het meest lipofiele galzuur, d.w.z. DCA, werd aangenomen dat gelijktijdige blootstelling vooral effect heeft op passief transport. Aan de andere kant heeft blootstelling van de Caco-2 cellen vooraf waarschijnlijk het meeste effect op ASBT-gemedieerd transport, omdat in dit geval transport van DCA het minst geremd werd. Deze data waren ingebouwd in het galzuur-PBK-model om het effect van tobramycine op plasma galzuurgehaltes te voorspellen. Dit resulteerde in een voorspelde reductie in de maximale galzuurgehaltes in plasma van GCA, GCDCA, GDCA en ongeconjugeerde galzuren met respectievelijk 42.4%, 27.7%, 16.9%, and 75.8%. De reductie in de geconjugeerde galzuren werd voornamelijk toegeschreven aan ASBT-gemedieerd transport in de darm, terwijl de reductie in ongeconjugeerde galzuren was gelinkt aan een vermindering van het passieve transport en een reductie in deconjugatie door de darmmicrobiota. Alles bijeen laten de resultaten zien dat het galzuur-PBK-model een nuttig instrument is voor het verkrijgen van inzicht in de invloed van orale blootstelling aan lichaamsvreemde stoffen op galzuurhomeoastase, met een specifieke focus op de effecten veroorzaakt door veranderingen in de deconjugatie door de darmmicrobiota en transportprocessen.

Hoofdstuk 6 past het nieuw ontwikkelde PBK-model toe op een set van 15 geselecteerde geneesmiddelen. Het was bekend dat deze geneesmiddelen hepatische galzuuruitscheiding remmen en dat deze geneesmiddelen causaal gelinkt zijn aan ontwikkeling van leverschade veroorzaakt door geneesmiddelen. Het galzuur-PBK-model zoals beschreven in hoofdstuk 4 en 5 werd gebruikt, met een focus op het geconjugeerde galzuur GCDCA. Ongeconjugeerde galzuren worden voornamelijk getransporteerd door perfusie of diffusie en opstapeling in de lever als resultaat van remming van hepatische galzuurefflux is dus onwaarschijnlijk. De leverconcentratie van de geneesmiddelen werd voorspeld aan de hand van een generiek PBK-model en gekoppeld aan het galzuur-PBK-model in combinatie met het remmende effect (K_i) op galzuuruitscheiding. Deze laatste parameter werd gekwantificeerd op basis van een literatuurstudie met primare hepatocyten. De PBK-uitkomsten onthulden dat cholestase-incidentie niet adequaat voorspeld kan worden op basis van de K_i voor remming van de hepatische galzuuruitscheiding, maar wel door het gebied onder de curve (de integraal) van de voorspelde interne leverconcentratie boven deze K_i bij een therapeutische dosering. De aanpak bood ook mechanistische inzichten in risicofactoren voor het ontwikkelen van door geneesmiddelen veroorzaakte cholestase. Individuen met een langzame klaring van het geneesmiddel, een grote totale galzuurpool, een verminderde BSEP-abundantie en/of die hoger dan therapeutische doseringen toegediend hebben gekregen hebben een grotere kans op het ontwikkelen van door geneesmiddelen veroorzaakte cholestase.

Hoofdstuk 7 geeft een overzicht van de belangrijkste bevindingen in dit proefschrift en een algemene discussie over punten die de inhoud van de afzonderlijke hoofdstukken overstijgen. Het hoofdstuk bediscussieert de PBK-modellen voor geneesmiddelen en galzuren, *in vitro* en *in silico* manieren om PBK-inputparameters te bepalen, het omzetten van *in vitro* data naar de *in vivo* situatie, de "Adverse Outcome Pathway" (AOP) voor cholestase en de relevantie van galzuren voor andere negatieve gezondheidseffecten dan cholestase. Als laatste wordt de paradigmaverschuiving naar dierproefvrije risicobeoordeling voor cholestase bediscussieerd.
Kortom, dit proefschrift integreert *in vitro* modellen gebaseerd op menselijke cellen in PBK-modellen om de effecten van geneesmiddelen op galzuurhomeostase te begrijpen en te voorspellen, met de nadruk op cholestase. Er werd aangetoond dat het haalbaar is om deze NAMs toe te passen voor het voorspellen van door geneesmiddelen veroorzaakte cholestase die het resultaat is van remming van hepatische galzuuruitscheiding en om de effecten van remming van galzuuropname in de darm op galzuurconcentraties in de darm en het plasma te voorspellen. Daarmee draagt het huidige werk bij aan de 3 V's (vermindering, verfijning en vervanging) van dierproeven.

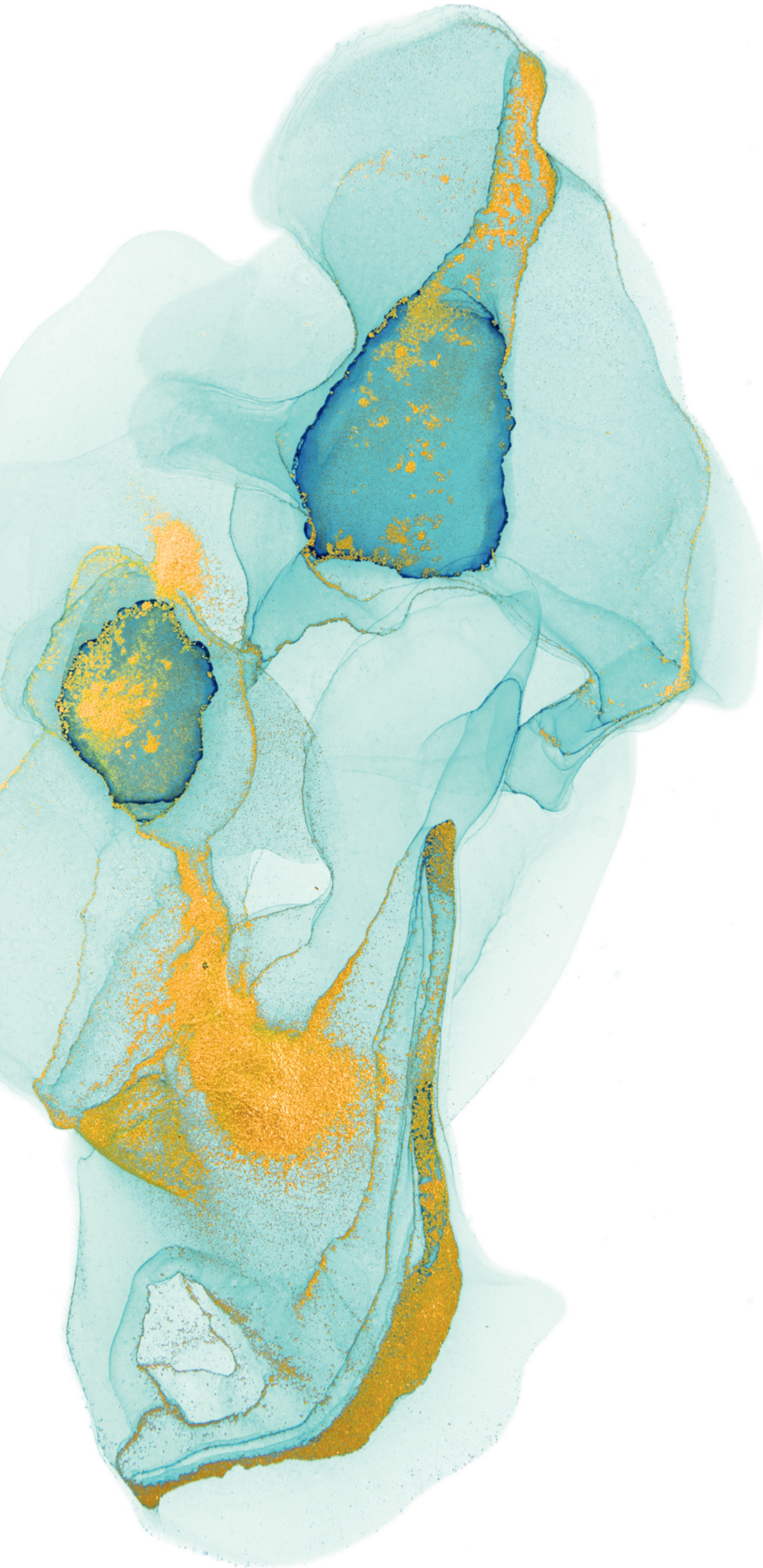

Appendix

Acknowledgements

Here it finally is: my PhD thesis! It fulfills me with happiness and pride that after over 4 years of dedicated and hard work this project has successfully come to an end. It was an exciting and rewarding journey full of personal and professional growth, but also a challenging time with setbacks and insecurities. Luckily, I was surrounded by all of you who believed in me, made me smile and helped me in so many different ways. I will express my gratitude and appreciation to you in these pages!

First, I would like to thank my supervisors Hans and Ivonne. Thanks to your excellent supervision I have always believed that this project would come to a good end. I am deeply grateful that you both encouraged me to discuss any challenges with you and would always take the time to come to a solution together. Your feedback, guidance, support and trust have been incredibly important to me over the last 4 years. Hans, thank you for your critical questions, new perspectives and approachability. I am grateful that your door was always open for me. Thank you for consistently encouraging me to explore my own ideas and follow my own path. Ivonne, thank you for sharing your incredible and inexhaustible expertise with me. I am deeply impressed by your ability to give sharp, detailed and swift comments. Your guidance and solution-driven mindset has repeatedly given me direction when I needed it.

I gratefully acknowledge the members of the thesis committee for their time to evaluate my thesis. I highly appreciate your efforts to guarantee the quality of this thesis.

I would like to extend my gratitude to all the co-authors who contributed to this work. Thank you for your contribution to the experimental work and valuable discussions. Zhenguo and Bart, thank you for introducing me into the world of organoids and your help with the organoid work. Thank you Willem for your help with the Caco-2 experiments. Thank you Wouter and Weijia for your help with setting up the LC-MS/MS method. I also gratefully acknowledge Jacques, who is unfortunately no longer with us, for his help with the LC-MS/MS method. To Nina, thank you for your contribution to the experimental work with the Caco-2 cells and the writing of Chapter 5.

To everyone at TOX-WUR: thanks for making this journey so much fun! You are such heartwarming people and I am happy that I got to know all of you. Thanks go to Carla, Gerda and Letty for your (administrative) support over the past years. Thank you Lidy for your warm welcome when I first came to TOX. I would like to thank the current and former staff: Alexandros, Bert, Birol, Hans (van den B.), Laura, Marco, Matthias, Nico, Nacho, Naomi, Nynke, Sebas and Wouter. Thank you for all the fun talks and support over the last years. This work would not have been possible without the expertise technical help of all the TOX technicians. You really do amazing work to make everything in and around the lab go smoothly. Here, special thanks go to Wouter and Sebas for being the troubleshooting superheroes for the LC-MS/MS! Your endless optimism and each your sense of humor made it fun to work in the lab. I couldn't have measured all those samples without your tips and tricks. Thank you Laura for your warm and joyful personality and your technical guidance with cell culture and setting up experiments. Your encouragement and ability to put things into perspective helped me

to deal better with several setbacks. I miss our coffee talks, but I'm very happy that you are enjoying your retirement so much! To Naomi, I miss your happy smile every morning in the lab! The lab work became much smoother and easier when you came to TOX to take care of the day-to-day lab business, thank you so much for that. To Bert and Hans, thank you for our good and fun talks and your technical assistance during the first phase of my PhD. You both made me more confident in the lab and ready to make a good start. To Nynke, thank you for your enthusiasm during the PhD trip to the UK last spring. Your incredible expertise in kinetics and much more is so inspiring! To Nico, thank you for our fun coffee talks, laughter and fresh insights from time to time.

To my dear paranymphs, Merel and Aafke, what a ride it has been! We have been in this PhD journey from (more or less) the start together and I'm happy and grateful to have such positive and encouraging colleagues to share ups and downs and beers with. Merel, you are such an optimist and I admire your contagious smile! I will miss our chats and peptalks. Aafke, it's lovely to talk to someone with so much "nuchtere boerenverstand" and resilience. I'm happy that you have become such a dear friend! ☺ Let's finish our HP "marathon" soon (if we haven't already by the time of the defence)!

To my offices: Aafke, Akanksha, Katja, Qianrui and Yiming: thank you for your support and fun chats! To Chrysanthi, Germaine and Donovan: you started your PhDs when I was in my final year and I hope that I didn't scare you away with my stressed out typing. I'm happy to have been part of the most cultural office that even goes to operas together. I wish you all lots of success for your PhDs!

To the SOT-girls: Annelies, Katja and Tessa: we had so much fun in San Diego! This trip was really a highlight of my PhD. Relaxing in the loft after a day of science, exploring the beautiful beach, having over-priced tequilla at the Sevilla salsa club and of course the elevator that brought us right into the comedy club. Thank you!

To the members PhD trip committee: Germaine, Hugo, Jingxuan, Katharina, Liang and Thijs. I'm so proud of how we organized this big trip for our department to the UK! It was somewhat a logistical challenge, but we managed and made a big success of it. Germaine, you are our designer-hero: thanks for that! Hugo, thank you for your endless enthusiasm and willingness to take up almost everything. Jingxuan, without your note-taking we would have been nowhere close as organized as we were. Katharina, thanks for the enormous efforts you put in making this happen. And thank you for being such a fun roomie in London! Liang and Thijs, thanks for taking up so much of the logistical challenges. Why did the Londoners need to strike when we were there?! Thanks for all the fun we had drinking tea, eating scones, enjoying neck oil and being kicked out of the pub at bed time!

To the current TOX-PhDs: Edith, Frances, Gijs, Ghaliya, Jiaqi, Kiri, Matteo, Quihui, Shivani, Tanne, Tom, Xiyu, Xukun and Yasser, we have had many wonderful moments together during coffee breaks, lab work, BBQs, after-work drinks, lunches, Christmas dinners and of course the PhD trip to the UK. Thanks for making the last 4 years unforgettable! I would like to extend my gratitude to the former TOX-PhDs and TOX-postdocs: you know who you are!

To my MSc students: Gialam, Lize, Yumeng, Willem and Aurore: thank you for your contribution to my PhD project. Thanks for trusting me and I have learned a lot about being a good supervisor by working with all of you.

Voor iedereen die er de afgelopen jaren voor me geweest is: Roos, we kennen elkaar al sinds de zandbak op de basisschool en ik ben zo blij dat we elkaar nooit uit het oog verloren zijn. Jouw droge humor brengt altijd een lach op mijn gezicht. Myrna en Xian, bedankt voor de pizza-avondjes en theetjes de afgelopen jaren en reden om nog af en toe carnaval te vieren! Aan mijn lieve AID-zusje en bestuurgenootje: Cindy, ik ben blij en dankbaar om een vriendin als jij in mijn leven te hebben met je altijd nuchtere en positieve kijk op het leven. Fijn dat we de PhD-struggles de afgelopen jaren konden delen, gedeelde smart is halve smart! Hilde: onze fietsritjes deze zomer hebben er voor gezorgd dat ik het allemaal volhield. De laatste loodjes wogen voor ons allebei zwaar, maar het is ons gelukt! Wie had dat gedacht toen we meer dan 10 jaar geleden samen in de collegebankjes zaten voor ons eerste college. Ik ben ontzettend blij om zo'n lieve en sterke vriendin als jij in mijn leven te hebben. Merle, bedankt voor al onze gezellige groenteburger-dates. Jouw kijk op het leven heeft er meer dan eens voor gezorgd dat ik dingen heel anders bekeek. En het moederschap staat je goed! Paul & Lisa, bedankt voor de gezellige etentjes en drankjes met trompet-muziek op de achtergrond! En natuurlijk voor de hulp met het bedenken van stellingen. ☺ Aan Romy, Marna, Nicole, Marit, Regina, Olga, Julianne, Carola en Esmer: bedankt dat jullie zo'n leuke en gezellige teamies zijn! Niks leidt beter af dan een goede pot volleybal!

Aan de familie Beckers-Koek-van Putten-Rote-van Vliet: jullie zijn de leukste schoonfamilie die ik me kan wensen! Altijd gezellig om met jullie (te lange) verjaardagsliedjes te zingen, (te veel) pannenkoeken te eten of (te fanatiek) spelletjes te doen! Aan de komkommers, bedankt voor jullie gezelligheid, warmte en vrolijkheid!

Aan papa en mama, bedankt dat jullie altijd voor een fijn en warm nest hebben gezorgd en me altijd gestimuleerd hebben om te studeren. Zonder jullie steun was dit natuurlijk nooit gelukt! Fijn dat ik altijd kan bellen voor een peptalk of als ik even mijn ei kwijt moet. Aan Emiel, Natasja, Carlijn, Matthijs, Brigitte, Pieter-Paul en natuurlijk ook Ties, Renske, Stijn, Giel en alvast ??, heel erg bedankt voor jullie steun en/of afleiding de afgelopen jaren. Brigitte, bedankt voor je nuchterheid, optimisme en luisterend oor als de cellen weer eens niet deden wat ze moesten doen. Ik ben blij dat je het PhD-avontuur nog steeds aandurft en weet zeker dat dat helemaal goed gaat komen! Wie weet heb jij ook wel leuke conferenties op de planning waar een roadtripje achteraan kan. ;)

Aan Arjen, wat ben ik blij dat jij die ene avond mijn leven binnen kwam gewandeld! Bedankt voor je liefde, warmte en steun. Jij weet altijd een lach op mijn gezicht te brengen en het leven luchtiger en kleurrijker te maken. Vooral tijdens de laatste hectische maanden van mijn PhD was je een rots in de branding voor me met altijd een warme maaltijd voor me als ik eindelijk tijd had om te eten. Het was echt heerlijk om deze periode samen af te sluiten met onze prachtige reis door Australië. Ik kan niet wachten op de volgende stap met jou!

About the author

Véronique de Bruijn was born on August 4th 1995 in Boxmeer, the Netherlands. She completed her Bachelor's Nutrition & Health at Wageningen University and Research in 2016. During her bachelor's programme she followed a minor programme in Microbiology & Infection biology and Stockholm University. She continued with the Master programmes Applied Food Safety and Molecular Nutrition & Toxicology at Wageningen University and Research. During her MSc studies, she performed her internship at BASF SE, Ludwigshafen, Germany at the department of Experimental toxicology & ecology. In 2019 she started her PhD at the Division of Toxicology under supervision of prof.dr.ir. Ivonne M.C.M. Rietjens and dr. Hans Bouwmeester. During her PhD, she followed the postgraduate education programme in Toxicology which facilitates her to register as a European Toxicologist (ERT). Currently, she is employed at the National Institute for Public Health and the Environment (RIVM) at the department of Innovative Testing Strategies.

List of publications

This thesis

de Bruijn, V. M. P., Wang, Z., Bakker, W., Zheng, W., Spee, B. & Bouwmeester, H. (2022b). Hepatic bile acid synthesis and secretion: Comparison of in vitro methods. *Toxicology Letters 365*, 46-60. doi:10.1016/j.toxlet.2022.06.004

de Bruijn, V. M. P., Rietjens, I.M.C.M. & Bouwmeester, H. (2022a). Population pharmacokinetic model to generate mechanistic insights in bile acid homeostasis and drug-induced cholestasis. *Archives of Toxicology 96*, 2717-2730. doi:10.1007/s00204-022-03345-8

de Bruijn, V. M. P., te Kronnie, W., Rietjens, I. M. C. M. & Bouwmeester, H. (2023). Intestinal *in vitro* transport assay combined with physiologically based kinetic modeling as a tool to predict bile acid levels *in vivo 40*. *ALTEX - Alternatives to animal experimentation* doi:10.14573/altex.2302011

N. Zhang, Rietjens, I.M.C.M. & **de Bruijn, V.M.P.** Application of physiologically based (PBK) modelling to quantify the effect of the antibiotic tobramycin on bile acid levels in human plasma. *Submitted*

de Bruijn, V.M.P. & Rietjens, I.M.C.M. From hazard to risk: a case study to predict drug-induced cholestasis using New Approach Methodologies (NAMs). *Submitted*

Other publications

de Bruijn, V.M.P., Behr, C., Sperber, S, Walk, T., Ternes, P., Slopianka, M., Haake, V., Beekmann, K. & van Ravenzwaay, B. (2020). Antibiotic-induced changes in microbiome-related metabolites and bile acids in rat plasma. *Metabolites 10*, doi:10.3390/metabo10060242

Zhang, N., **de Bruijn, V.M.P.**, Zheng, W., Bakker, W., van Ravenzwaay, B. & Rietjens, I.M.C.M., Antibiotics reduce intestinal bile acid reuptake in an *in vitro* model system. *Submitted*

Wang, J., **de Bruijn, V.M.P.**, Rietjens, I.M.C.M, Kramer, N.I. & Bouwmeester, H., Use of physiologically based kinetic modeling to predict deoxynivalenol metabolism and its role in intestinal inflammation and bile acid kinetics in humans. *Submitted*

Overview of completed training activities

Discipline specific courses

Cellular toxicology	PET	2020
Environmental toxicology	TOX-WUR	2020
Organ toxicology	PET	2021
Toxicogenomics	PET	2021
Molecular toxicology	PET	2021
Pathobiology & toxicological pathology	PET	2021
Immunotoxicology	PET	2023

General courses

VLAG PhD week	VLAG	2019
The Essentials of Scientific Writing & Presenting	WGS	2020
Reviewing a scientific manuscript	WGS	2020
Brain friendly working and writing	VLAG	2020
Critical thinking and argumentation	WGS	2020
Applied statistics	VLAG	2020
Quantitative methods for biology (EdX)	Harvard University	2020
Supervising BSc and MSc thesis students	ESD	2021

Optional courses and other activities

Preparation of research proposal	TOX-WUR	2019
Organisation TOX PhD excursion to the United Kingdom	TOX-WUR	2022-2023
Participation TOX PhD excursion to the United Kingdom	TOX-WUR	2023
Weekly scientific presentations	TOX-WUR	2019-2023

Conferences and meetings

Science with impact	Wageningen PhD symposium	2019
Towards animal free innovations	VU Amsterdam	2019
In vitro studies of the human intestinal microbiota	MIB/VLAG	2020
ASCCT Annual meeting	American Society for Cellular and Computational Toxicology (ASCCT)	2020
61st Annual meeting Society of Toxicology and ToxExpo, poster	Society of Toxicology (SOT)	2022
Annual meeting Dutch Society of Toxicology, poster	Nederlandse Vereniging Toxicologie (SOT)	2022

The research described in this thesis was financially supported by the division of Toxicology at Wageningen University & Research.

Financial support from Wageningen University for printing this thesis is gratefully acknowledged.

Cover design by Arjen van Putten and Véronique de Bruijn
Printed by ProefschriftMaken